The present work was submitted to the Institute of Geology and Geochemistry of Petroleum and Coal, RWTH Aachen University

MASTER THESIS

_____

Carbon degradation and potential greenhouse gas production in a changing Arctic thermokarst landscape – a case study from drained lake basins on the Yukon Coastal Plain, Canada

Kohlenstoffdegradation und potentielle Treibhausgasproduktion in einer dynamischen arktischen Thermokarstlandschaft - eine Fallstudie aus drainierten Seebecken auf der Yukon Coastal Plain, Kanada

_____

presented by: Verena Bischoff

                    Matriculation number: 368402

1st supervisor: Prof. Dr. rer. nat. Jan Schwarzbauer

                    RWTH Aachen University

2nd Supervisor: Dr. Juliane Wolter

                    University of Potsdam

Aachen, November 23, 2023

Content

List of Figures

List of Tables

Abbreviations and Nomenclature

Notation	meaning
ACL	Average chain length
ae	Aerobic
AL	Active layer
an	Anaerobic
ANOVA	Analysis of variance
ASE	Accelerated solvent extraction
bp	Before present
CFE	Climate forcing effect (CO_2-equivalents)
CH_4	methane
CO_2	Carbon dioxide
CPI	Carbon preference index
dw	Dry weight
eC	Electrical conductivity
EOPD	Even-over-odd predominance
GHG	Greenhouse gas
HPA	Higher plant alcohol Index
LGM	Last Glacial Maximum
OC	Organic carbon
OEPD	Odd-over-even predominance
OM	Organic matter
P_{aq}	Aquatic proxy
PF	Permafrost
pH	Potential of hydrogen
P_{wax}	Terrestrial proxy
RCF	Relative climate forcing
rpm	Revolutions per minute
TL	Transition layer
TC	Total carbon
TIC	Total inorganic carbon
TN	Total nitrogen
TOC	Total organic carbon
VPDB	Vienna PeeDee Belemnite

Abstract

Permafrost carbon pools are vulnerable to a warming climate and bear the potential to alter the terrestrial carbon cycle. In the extensive drained lake basin wetlands that cover Arctic lowlands, enhanced degradation of organic-rich deposits upon permafrost thaw could lead to greenhouse gas emissions to the atmosphere. This study investigates processes and intensity of organic matter decomposition and associated potential greenhouse gas production in thawed sediment from drained lake basins on the Yukon Coastal Plain in the western Canadian Arctic.

We conducted three-month low-temperature (4 °C) incubation experiments, assessing the greenhouse gas production potential in the active layer, transition layer, and permafrost of sediment cores from two adjacent drained lake basins under aerobic and anaerobic conditons. The study was supplemented by comprehensive geochemical and biomarker analyses before and after the incubation experiments.

Our findings revealed a higher carbon turnover of up to 2.7 % of the available organic carbon to CO_2 under aerobic conditions. Carbon loss from mineral permafrost layers matched that of surface peat samples, whereas nitrogen limitation constrained short-term carbon mineralization in pioneer peat layers that accumulated shortly after lake drainage.

The GHG production under anaerobic conditions exhibited a high depth-dependency, with permafrost layer samples deviating from the otherwise observed high methanogenesis in active and transition layer samples within the short incubation period. High contributions of the potent greenhouse gas methane of up to 94 % enhanced the climate forcing effect of anaerobic emissions.

Consequently, the determined relative climate forcing is higher under anaerobic compared to aerobic conditions in active and transition layers, suggesting that waterlogged conditions within drained lake basins are more unfavorable in the short term.

While established degradation proxies C:N, $\delta^{13}C$ and CPI did not distinctly trace significant degradation of terrestrial organic matter, we observed major shifts in lipid composition, reflected in increasing concentrations of *n*-alkanols and *n*-alkanes.

Zusammenfassung

Die Erwärmung der Arktis kann gravierende Veränderungen des im Permafrost gespeicherten Kohlenstoffspeichers bewirken, und somit des globalen terrestrischen Kohlenstoffkreislaufs beeinflussen. Eine verstärkte Zersetzung kohlenstoffreichen Ablagerungen in den drainierten Seebecken Arktischer Tiefebenen birgt beim Tauen des Permafrostbodens das Potential, Treibhausgase in die Atmosphäre zu emittieren. Diese Studie untersucht die Intensität der Zersetzung organischen Materials sowie die damit verbundene potenzielle Treibhausgasproduktion in getautem Sediment aus drainierten Seebecken auf der Yukon Coastal Plain in der westlichen kanadischen Arktis.

In zwei Sedimentkernen wurde im Rahmen von dreimonatigen aeroben und anaeroben Inkubationsexperimenten bei 4 °C wurde das Treibhausgasbildungspotenzial im oberflächennahen Active Layer, dem Transition Layer und dem ganzjährig gefrorenen Permafrost untersucht. Die Studie wurde durch umfassende geochemische und Biomarker-Analysen vor und nach den Inkubationsversuchen ergänzt.

Unsere Ergebnisse zeigten eine höhere Kohlenstoff Konversionsrate unter aeroben Bedingungen von bis zu 2,7 % des verfügbaren organischen Kohlenstoffs zu CO_2. Der Kohlenstoffabbau in mineralischen Ablagerungen entsprach dem der oberflächennahen Torfe. In den ersten Torfablagerungen nach drainieren des Sees kann Stickstoffmangel die mikrobielle Aktivität und demnach die Kohlenstoffmineralisation Organik-reicher Schichten bremsen.

Die Treibhausgasproduktion unter anaeroben Bedingungen hingegen zeigte sich in dem kurzen Zeitraum stark abhängig von der Tiefe der Probe. Die Methanproduktion in Permafrostschichten entsprach nicht den hohen Konzentrationen, die in der aktiven und der Übergangsschicht gemessen wurden. Hohe Beiträge des potenten Treibhausgases Methan zum Emissionspotential von bis zu 94 % verstärkten die klimawirksame Wirkung der Emissionen unter anaeroben Bedingungen.

Folglich ist die ermittelte relative Klimawirksamkeit der Treibhausgasproduktion in der Aktiven Schicht und der Übergansschicht unter anaeroben Bedingungen kurzfristig höher als unter aeroben Bedingungen. Demnach sind feuchtere Bedingungen in drainierten Seebecken kurzfristig ungünstiger. Während die etablierten Abbauproxys C:N, $\delta^{13}C$ und CPI keine signifikante Degradation des terrestrischen organischen Materials nachweisen konnten, zeigte sich eine starke Veränderung der Zusammensetzung der Lipide, was sich in steigenden Konzentrationen von *n*-Alkanolen und *n*-Alkanen widerspiegelte.

1. Introduction

1.1. Scientific relevance and background

The high-latitude regions experience near-surface air temperature warming at a rate more than twice the global average, a phenomenon known as 'Arctic Amplification' (Graversen et al. 2008; Masson-Delmotte et al. 2021). The Arctic permafrost soils, covering approximately 14 % (21×10^6 km^2) of the global land surface (Obu et al. 2019), are particularly vulnerable to this rapid warming (Schuur et al. 2013). As a consequence, widespread permafrost degradation is evident, including thickening of the annually thawing surficial active layer, erosion and deeper drainage of permafrost-affected soils (Oechel et al. 1993; Sushama et al. 2007; Romanovsky et al. 2010; Schaefer et al. 2011; Harden et al. 2012; Elberling et al. 2013). The transformation of Arctic tundra ecosystems induced by climate warming has profound implications for the carbon balance of permafrost soils (Ping et al. 2015). Frozen conditions in permafrost-affected soils inhibit the microbial decomposition of organic matter. As a result, the permafrost carbon pool is currently estimated to account for over 30 % of global soil organic carbon pool (Schuur et al. 2015).

Upon thaw, the once perennially frozen organic matter becomes mobilized and accessible for microbial decomposition (Schuur et al. 2015). The mineralization of organic carbon to carbon dioxide (CO_2) and methane (CH_4) and release of these potent climate-relevant trace gases into the atmosphere contributes to global warming (Schaefer et al. 2014). This permafrost carbon feedback is recognized as one of the most substantial terrestrial feedbacks to anthropogenic climate change (Schuur et al. 2015). However, these ecosystems also have the potential to act as carbon sinks through the storage of carbon in vegetation and peat (Tarnocai et al. 2009; Hugelius et al. 2014). Whether an Arctic tundra ecosystem acts as a net carbon sink or source is highly individual and dynamic (Oechel et al. 1993), influenced by changes in hydrology, vegetation productivity, and overall soil characteristics (Schuur et al. 2015; Schädel et al. 2016; Voigt et al. 2017; Turetsky et al. 2020; Chen et al. 2021).

The amount and form of carbon that is emitted from permafrost ecosystems depends on the prevailing conditions in permafrost soils. Aerobic carbon decomposition produces exclusively CO_2 while fermentative and syntrophic processes contribute to an additional methane (CH_4) release under anaerobic conditions (Schuur et al. 2015; in 't Zandt et al. 2020). Previous studies, encompassing laboratory incubations and in situ flux measurements, suggested that carbon decomposition is higher under aerobic conditions but is potentially more climatically unfavorable under anaerobic conditions (Elberling et al. 2013; Olefeldt et al. 2013; Lawrence et al. 2015). The total amount of carbon that may be released into the atmosphere due to permafrost thaw as well as the climate forcing effect of these emissions is subject to large uncertainties (IPCC 2013; Ernakovich et al. 2022).

Recent studies stressed the pressing need to assess permafrost ecosystem transitions and accompanying changes in biogeochemical cycles (Lee et al. 2012; Lawrence et al. 2015; Treat et al. 2015; Olefeldt et al. 2021; Jones et al. 2022). Thermokarst, the permafrost thaw-induced surface collapse, and associated lake formation as well as the opposing thermokarst lake drainage pose major shifts in landcover and soil hydrology (Lehner & Döll 2004; Olefeldt et al. 2016; Bouchard et al. 2020; Jones et al. 2022). Both thermokarst lake initiation and lake drainage events have increased in past decades in the highly dynamic lowland lake – drained lake basin environments (Lindgren et al. 2021). Induced changes in the oxic state of soils as it has implications for Greenhouse Gas (GHG) emission potentials and composition in the Lake-Drained Lake Basin (L-DLB) system (Bring et al. 2016; Schädel et al. 2016; Walvoord & Kurylyk 2016; Lafrenière & Lamoureux 2019; van Huissteden 2020). Still, the carbon degradation and greenhouse gas emission potentials of the heterogenous drained lake basin sediments are largely unstudied (Zona et al. 2012).

1.2. Research objectives

This master thesis project aims to determine the impact of permafrost thaw on organic carbon stored in drained lake basin sediments of the Yukon Coastal Plain in the western Canadian Arctic, an ice-rich lowland area that is vulnerable to thaw in a warming climate.

Research objectives in this thesis include:

1. Tracing and assessing the decomposition of organic carbon upon thaw within one summer period under trajectories of drained (aerobic) resp. waterlogged (anaerobic) conditions within the soils using geochemical parameters and lipid biomarkers.

2. Determining the greenhouse gas production potential associated with carbon mineralization and comparing the production potential under drained (aerobic) and waterlogged (anaerobic) conditions within the sediment, focusing on

    a. carbon degradation behavior in the heterogenous sediments (organic, mineral, cryoturbated sediment) and

    b. carbon degradation behavior across the current permafrost thermal regimes (active layer, transition layer, perennially frozen permafrost layers).

2. Research background

2.1. Permafrost

2.1.1. Definition of permafrost

Modern definitions of the term Permafrost evolved beyond its initial definition of being "permanently frozen". Presently, the definition officially approved by the International Permafrost Association (IPA) refers to "ground (soil or rock and included ice and organic material) that remains at or below 0 °C for at least two consecutive years" (van Everdingen 1998). The definition relies solely on a temperature criterion, thereby considering the physical state of the ground substrate, regardless of the material composition (Brown & Kupsch 1974; French 2007). Certain forms of ice, such as glacier ice and buried ice, are deliberately excluded from this delineation (van Everdingen 1998).

2.1.2. Development of permafrost

The change of seasons brings forth a cycle of alternating heat and cold that penetrates the ground surface. In cold environments, permafrost aggradation occurs when the extend of ground freezing during winter surpasses the extend of thawing in the summer. In a cooling climate setting, the initially thin ground layer that persists over the summer progressively increases in thickness over the years.

The permafrost base is established by the constant geothermal heat flux, which increases with lithosphere depth. In contrast, the permafrost table is affected by the seasonal fluctuating ground surface temperatures (Figure 1). The negative heat balance facilitates permafrost aggradation, whereas a positive heat balance in summer acts to degrade permafrost. As a result of summer warming, temperatures in the surface layer of permafrost soil exceed 0 °C. This annually thawing surface layer is known as the active layer (Burn 1998). The depth of the active layer in sediments depends on soil properties such as heat capacity and heat permeability, exhibiting high variability (French 2007; French 2013). There is a transition zone between the active layer and the underlying permafrost zone that occasionally thaws, but not every summer (Shur et al. 2005; French & Shur 2010). Most ecological, hydrological, biochemical and pedogenical processes are restricted to the active layer in periglacial environments (Hinzman et al. 1991). The annual thawing and freezing in the active layer of permafrost soils heavily affects soil structure, and whole horizons may be shifted, warped or displaced in a processes termed cryoturbation (Ping et al. 2015; Beer et al. 2022). Because the underlying permafrost impedes subsurface drainage, thawed active layer soils are often waterlogged (Ping et al. 2015).

The insulating characteristics of vegetation and peat covers (Brown 1966; Seppälä 1986) can affect active layer depth by shielding the underlying permafrost from insulation during summer, thus limiting thaw to a shallow layer. Aside from the severity and duration of winter freezing, the snow cover plays a significant role in permafrost development. Its insulating properties can both weaken winter freezing

and disrupt vegetation assimilation, potentially providing a shield for the ground surface (Williams & Smith 1991a; van Huissteden 2020). Consequently, low precipitation and vegetation assembly contribute to permafrost aggradation. As ground temperature is highly influenced by climatic conditions, active layer depth may change over time (Dobinski 2011). Layers of perenially unfrozen ground (taliks) can form as the result of local heat anomalies e.g. underneath lakes (Ling & Zhang 2003; Chadburn et al. 2017) when lake depth exceeds a threshold depth and does not freeze to the bottom (Arp et al. 2011).
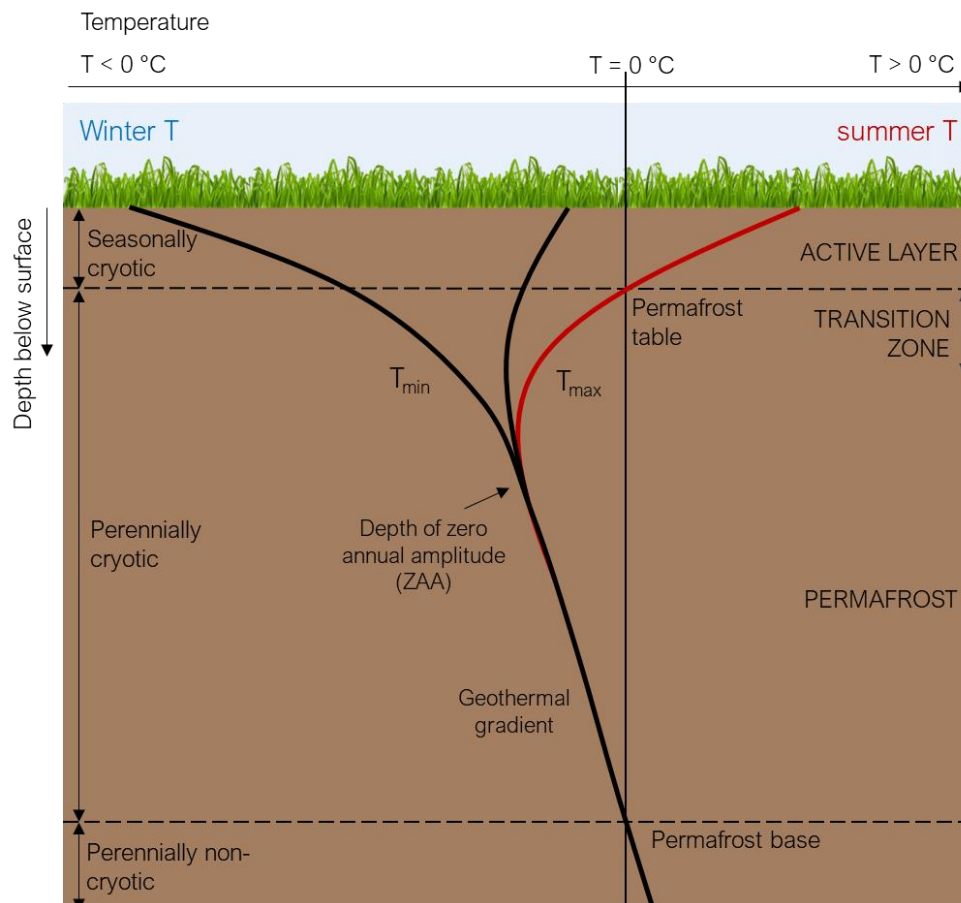
Figure 1: Thermophysical model of permafrost in a periglacial environment, after Dobinski (2011).

2.1.3. Past and present distribution of permafrost environments

Permafrost is typically associated with periglacial environments (van Everdingen 1998; Dobinski 2011). Conversely, periglacial environments extend beyond areas of permafrost prevalence or a proximity to glacial environments of the Pleistocene. Instead, they are delineated by the climatic conditions, geomorphological processes and landforms within cold, yet non-glacial environments (Dylik & Rybczynska 1964; Washburn 1979; French 1987).

Much of the present-day permafrost is relict and potentially older than the Last Glacial Maximum (LGM), extending back to the Pleistocene (Burn 1994). Still, its temperature and thickness has since strongly varied with climatic fluctuations throughout the Quaternary period (Lunardini 1995). The permafrost-affected areas of the northern hemisphere have undergone numerous cycles of expansion

and retreat (Burn 1994). Widespread permafrost thaw occurred at the termination of the Last Glacial (Burn 1997; Walter et al. 2007).

By today, an expanse of approximately 18.7×10^6 km^2 is influenced by permafrost in the northern hemisphere (Hugelius et al. 2013), equalling approximately 23.9 % of the total land mass (Zhang et al. 2008). Based on spatial continuity, areas affected by permafrost are classified into areas of isolated (≤ 10 % of the land surface underlain by permafrost), sporadic (10 – 50 %), discontinuous (50 – 90 %) and continuous (≥ 90 %) permafrost occurrence (Heginbottom et al. 1993).

The low temperatures necessary for permafrost aggradation can arise from low solar energy supply at high latitudes as well as the low heat capacity of air in high altitude mountainous environments (Dobinski 2011). Arctic and boreal permafrost dominates over mountain permafrost, with lowland regions (< 300 m asl) situated above 60 °N accounting for approximately 60 % of the total permafrost affected area (Zhang et al. 1999; Jones et al. 2022).

2.1.4. Future of permafrost environments

As a consequence of global warming, the mean annual air temperature in the Arctic has risen by 2.7 °C since 1971 (Box et al. 2019) and warming is expected to further accelerate in forthcoming decades (Masson-Delmotte et al. 2021). This warming trend is particularly pronounced in high-latitude environments, where temperatures are increasing at twice the rate of the global average (IPCC, 2001). This escalated warming of polar regions is termed "Artic Amplification" (Graversen et al. 2008). The ongoing warming extends the period of thaw during summer, thereby causing the active layer to deepen (Romanovsky et al. 2010; Walvoord & Kurylyk 2016; Biskaborn et al. 2019) (Figure 2).
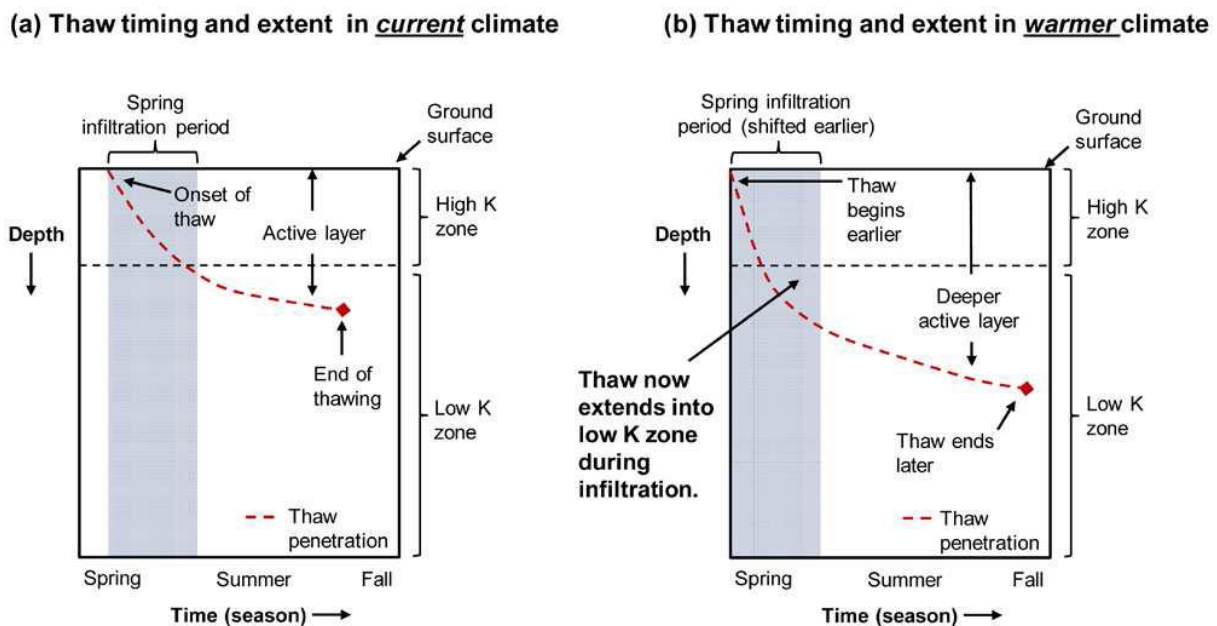
Figure 2: Permafrost thaw model in current and warmer climate. Timing of spring infiltration and seasonal thaw penetration in a typical high over low hydraulic conductivity (K) soil profile for a (a) current and (b) warmer climate. (Walvoord and Kurylyk, 2016).

Elevated precipitation levels will lead to thicker snow cover, which acts as an insulator for the ground surface (French 2017; van Huissteden 2020). This effect may be offset by the reduced snow cover duration and thickness by enhanced melting triggered by warmer air temperatures (van Huissteden 2020). This shift has major implications for the soil's hydrologic storage capacity, particularly in the deeper zones characterized by lower hydraulic conductivity (K) (Walvoord & Kurylyk 2016). On the contrary, thawing of ice-rich permafrost and ground ice will contribute to wetter conditions in lowland permafrost regions (Jorgenson et al. 2006; Schädel et al. 2016).

As a result of climate warming, amplified in the Arctic, 40 % of permafrost is expected to thaw within the next decades, even if the targeted global mean temperature rise is limited to 2 °C (Camill 2005; Chadburn et al. 2017; Biskaborn et al. 2019). The near-surface permafrost cover will be reduced by over 90 % by the end of the century (Lawrence et al. 2008; in 't Zandt et al. 2020).

2.2. Thermokarst lakes and drained lake basins

Around a quarter of Earth's lakes are located in northern high latitudes (Lehner & Döll 2004). Most of them formed in depressions that were created by bedrock erosion during Pleistocene glaciations. Further, many lakes in sedimentary lowlands emerge as a consequence of permafrost thaw-induced surface collapse, known as thermokarst (Lehner & Döll 2004; Olefeldt et al. 2016; Bouchard et al. 2020). Thermokarst landscapes are characteristic features in lowland permafrost regions as they cover approximately 20 % of the northern permafrost area (Olefeldt et al. 2016) (Figure 3).
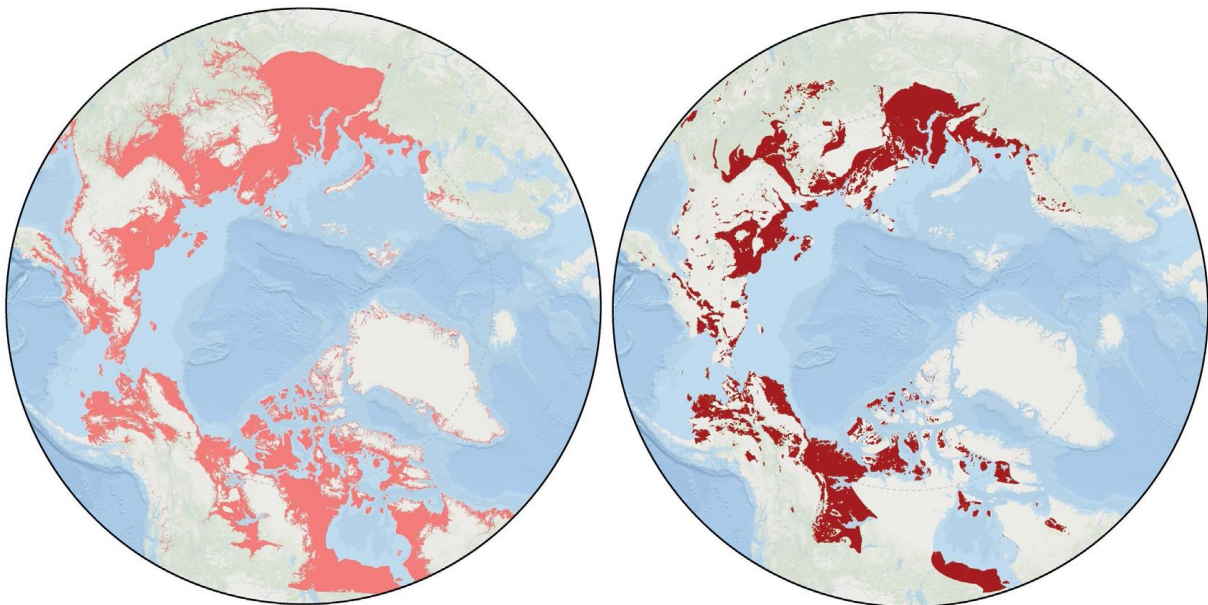
Figure 3: The Artic and boreal lowland permafrost region. Left: lowland permafrost regions (< 300 m a.s.l.) of the northern hemisphere (Amante & Eakins 2009). Right: northern circumpolar permafrost regions showing low – very high thermokarst lake coverage (Olefeldt et al. 2016). From Jones et al. (2022).

2.2.1. Evolution of thermokarst lakes

With permafrost aggradation, the freezing pore water expands and thus enlarges the pore space within a soil. When the aggregated ground ice melts, accompanied by a decrease in volume, those

soils loose internal structure, and the soil surface becomes susceptible to collapse. This process of new landform development initiated by thawing of permafrost or melting of ground ice is referred to as thermokarst (Grosse et al. 2013). Thermokarst favours pond and lake formation as water accumulates in the created depressions (Hopkins 1949; Hinkel et al. 2007; Bowden 2010; Arp et al. 2020). Once initiated, the coalescence of emerging isolated subsidence ponds becomes self-enhancing, ultimately resulting in the formation of a lake (Grosse et al. 2013; Bouchard et al. 2020). As lake depth increases, it surpasses the maximum ice cover thickness determined by ponded water's heat capacity. Consequently, the formation of local perenially unfrozen layers, so-called taliks (see chapter 2.1.2.), is fostered and the lake begins to fill in with silty sediments (Lachenbruch 1962; Bouchard et al. 2020).

Apart from the processes involved in their initiation, thaw lakes and non-thaw lakes interact similarly with the surrounding terrain, including expansion through degradation of underlying and surrounding permafrost (Jones et al. 2022). Thermal and mechanical erosion of the lake bed and banks can increase the lateral extent of a lake by 0.1 to 1.0 m per year (Williams & Smith 1991b; Ling & Zhang 2003; West & Plug 2008, 2009; Arp et al. 2011; Jones et al. 2011). Erosion rates tend to be higher in ice-rich permafrost degraded by thaw lakes than in ice-poor surroundings with non-thaw lakes (Jones et al. 2011; Roy-Leveillee & Burn 2017).

2.2.2. Evolution of drained lake basins

Complete thermokarst lake drainage can occur within hours (Mackay 1981) as the result of bank overtopping (Marsh et al. 2009; Grosse et al. 2013), snow damming (Mackay 1988; Marsh & Neumann 2001; Arp et al. 2020), river channel migration (Jones & Arp 2015), underground piping (Marsh et al. 2009), coastal erosion (Arp et al. 2010; Jones et al. 2022), expansion towards drainage gradients (Mackay 1988), and human disturbance (Hinkel et al. 2007). Apart from local permafrost properties such as high ice contents, warm temperatures, and high active layer thickness (Hinkel et al. 2007), high water levels, the topography (drainage gradient, proximity to rivers, lakes or coastline), and climate, can increase an individual thaw lake's vulnerability to drainage (Mackay 1988; Grosse et al. 2013; Jones et al. 2020).

After lake drainage, without the heat storage capacity of ponded water, the freshly exposed taliks are prone to permafrost aggradation (Jones et al. 2011). Peat formation may be initiated by highly productive plants such as grasses and sedges on the freshly exposed surface while decomposition remains retarded in waterlogged soils (Hinkel et al. 2003; Jones et al. 2012; Loiko et al. 2020). Peat accumulation ceases over time (Jones et al. 2012). Ecosystems reorganize accompanying this process of substantial changes in hydrology, vegetation composition and biogeochemical cycling (Olefeldt et al. 2016).

2.2.3. The dynamics of lake – drained lake basin systems

A cyclicity in lake-permafrost dynamics has been observed in Artic lowlands, referred to as the "thaw lake cycle" (Mackay 1988; Burn & Smith 1990; Hinkel et al. 2005; Jorgenson & Shur 2007). Over the course of the Holocene, two significant periods of extensive lake initiation have been identified. The first of these took place during the Bølling–Allerød warming around 14.7 thousand years before present (ka bp) and extended until the Younger Dryas period (Figure 4a). A second phase occurred during a warm and wet interval in the early Holocene, spanning from 11.5 to 9.0 ka (Lenz et al. 2016; Bouchard et al. 2017; Brosius et al. 2021) (Figure 4b). During the middle and late Holocene, the formation of new lakes slowed down, while the expansion and drainage of existing lakes progressed (Hinkel et al. 2003; Jones et al. 2012; Loisel et al. 2014; Treat & Jones 2018; Brosius et al. 2021). Only sporadic episodes of lake formation occurred thereafter (Burn & Smith 1990; Brosius et al. 2021).
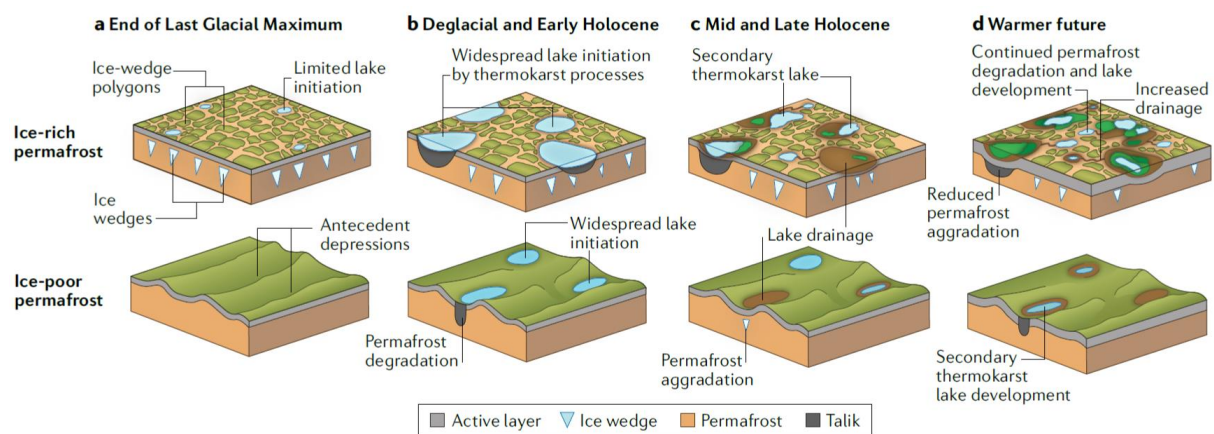
Figure 4: Development and future trajectory of the lake and drained lake basin system. Conceptual depiction of lake initiation and drainage in ice-rich and ice-poor permafrost lowland Arctic regions from the deglacial period, through the Holocene and in a warmer future (Jones et al. 2022).

These thermokarst lake and drained lake basin (L-DLB) environments currently represent a prominent 49 % of lowland permafrost regions (< 300 m asl), equivalent to 21 % of the total permafrost region (Grosse et al. 2013; Olefeldt et al. 2016). L-DLB regions exhibit significant landscape diversity across ice-rich and ice-poor terrains (Jones et al. 2022). The combined presence of lakes and drained lake basins can account for over 75% of the landscape, with drained lake basins commonly outnumbering contemporary, extant lakes. The ratio of drained lake basins to lakes typically ranges from 1.1 to 16 (Bergstedt et al. 2021), as identified by remote sensing imagery (Smith et al. 2005; Nitze et al. 2017; Lindgren et al. 2021).

Representative studies of Lindgren et al. (2021) reported a significant lake area decrease within the continuous permafrost region from the 1970s to the 2010s. Despite a noteworthy increase in the initiation of new lakes (+ 9.4 %) during these decades, this expansion is unable to counterbalance the drainage of medium-sized (10 to 50 ha) to very large lakes (> 100 ha) (Figure 5). Notably, the surge in lake formation observed during the transition from the Pleistocene to the Holocene is not anticipated to repeat itself amid ongoing anthropogenic warming (Brosius et al. 2021).
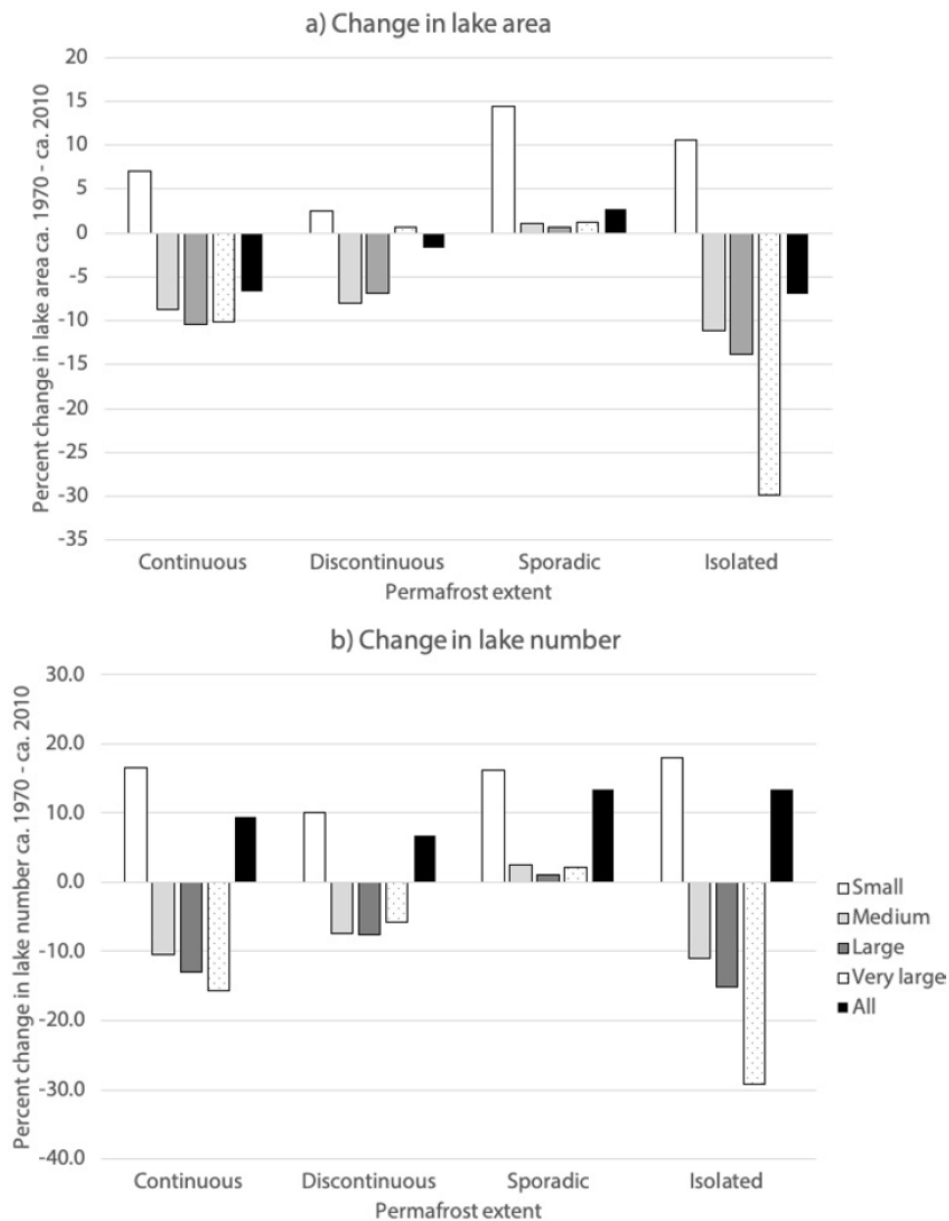
Figure 5: Recent changes in lake number and lake area in the permafrost environment. Summary of lake area (a) and number (b) changes across the different permafrost zones in the study domain from ca. 1970s to 2010s, from Lindgren et al. (2021).

Consequently, L-DLB landscapes within lowland permafrost regions are progressively being characterized by the prevalence of drained lake basins (DLBs) (Jones et al. 2011; van Huissteden et al. 2011; Nitze et al. 2018; Walter Anthony et al. 2018; Swanson 2019; Lindgren et al. 2021) (Figure 4c). In regions where annual mean air temperatures exceed 0 °C, permafrost aggradation on freshly exposed surfaces after lake drainage occurs at a slower pace or might not occur at all (Jones et al. 2022) (Figure 4d). The development of persistent taliks within DLBs carries significant implications for the ecosystem's hydrological and carbon fluxes (Jones et al. 2022). This transition, in turn, affects hydrology, carbon and nutrient cycling, and consequently, the vegetative cover (Walter et al. 2007; Jones et al. 2012; Walter Anthony et al. 2014).

9

2.3. Carbon pools and feedbacks in permafrost ecosystems

2.3.1. The carbon cycle in permafrost ecosystems

The general carbon storage of ecosystems is the net result of carbon dioxide (CO_2) uptake by plants from the atmosphere via photosynthesis (gross primary production (GPP)) and the opposed decomposition of organic C by plants via autotrophic respiration (R_A) and by MO by heterotrophic respiration (R_H) as CO_2. The difference between uptake and respiration is referred to as the net ecosystem production (NEP) (Woodwell & Whittaker 1968; Chapin et al. 2006) (Figure 6).
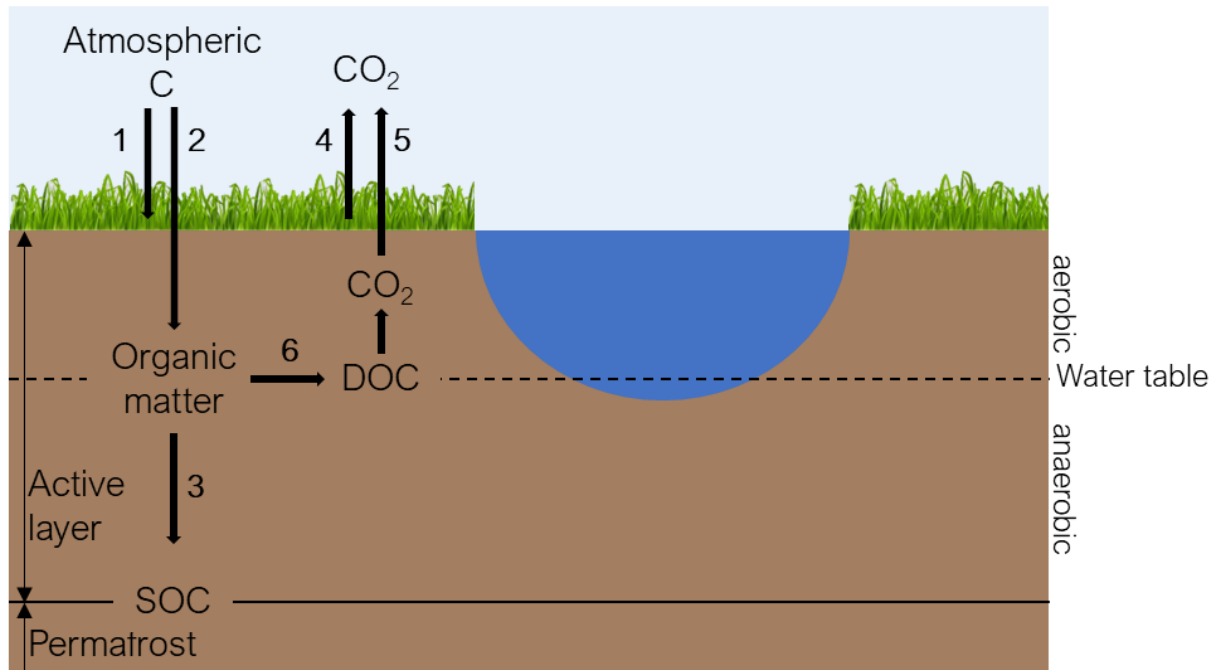
1 Gross primary productivity (GPP)
2 Net primary productivity (NPP)
3 Net ecosystem production (NEP)
4 Autotrohpic respiration (R_A)
5 Heterotrophic respiration (R_H)
6 Hydrolysis & fermentation

Figure 6: The terrestrial carbon cycle. After Christensen & Cox (1995) and Chapin et al. (2006).

Primary production rates (GPP) are generally low within cold periglacial environments, resulting in low carbon transfer to the soil through litter fall and the root system (van Huissteden 2020). However, in wetland environments, peat formation (Jones et al. 2012; Palmtag et al. 2015) and accumulation in lake sediments (Walter Anthony et al. 2014) enhance carbon sequestration into the ecosystem.

Microbial communities in permafrost environments have evolved to withstand harsh conditions of sub-zero temperatures, limited water and nutrient availability, and rapid phase changes accompanying permafrost thaw (Vishnivetskaya et al. 2011; Ernakovich et al. 2022). Tundra soils exhibit a wide range of microorganisms, including bacteria, archaea, yeasts, algae and mycelial fungi (D'Amico et al. 2006; Vishnivetskaya et al. 2011). Still, microbial activity faces physical constraints due to low temperatures and prevailing anaerobic conditions in waterlogged permafrost lowlands and wetlands (Oechel et al.

1998). The low heterotrophic respiration rates (R_H) of buried plant remains and other organic materials results in high preservation of carbon in the soils (Schaefer et al. 2011; Zona et al. 2012), implying a high net ecosystem production (NEP). The process of vertical soil mixing through cryoturbation processes further facilitates the movement of organic matter to deeper soil layers, significantly enhancing the preservation potential of the organic material (Walker et al. 2004; Bockheim 2007; Schuur et al. 2008). Consequently, the majority of carbon that accumulated in the system as dust, flood plain sediments and other organic and plant debris since the last glacial has remained stored in soils (Zimov et al. 2006a; Zimov et al. 2006b; Schuur et al. 2008). The Northern Circumpolar Soil Carbon Database (NCSCD) currently estimates a total of 1 300 – 1 370 Gt of carbon being stored in permafrost soils (Hugelius et al. 2014; van Huissteden 2020). This constitutes a large portion of the carbon stored within the upper 3 meters of global soils (2 344 Gt) (Jobbágy & Jackson 2000; Strauss et al. 2017). Moreover, this carbon stock in permafrost soils surpasses the current amount of carbon in the atmosphere (829 Gt) and exceeds the carbon stored in global vegetation (520 Gt) (Ciais et al. 2014; Strauss et al. 2017).

The form of carbon release to the atmosphere is primarily determined by the soil's oxygen status (Schuur et al. 2008). The production of methane (methanogenesis) occurs exclusively under anoxic soil conditions and is attributed to specialized methanogenic *Euryarchaeota* in permafrost-affected soils. (Rivkina et al. 1998; Kobabe et al. 2004; Wagner 2008; Vishnivetskaya et al. 2011). Methanogenesis starts with hydrolysis of polysaccharides, followed by the fermentation of sugars into fatty acids, acetate, H_2 and CO_2, which serve as terminal electron acceptors for methanogenesis (Conrad 2005). This process involves either the reduction of carbon dioxide to methane (autotrophy) by hydrogenotrophic methanogens or via the fermentation of acetate to methane (heterotrophy) by acetoclastic methanogens (Conrad et al. 1989; Conrad & Klose 1999; Heslop et al. 2020) (Figure 7).

Acetoclastic methanogenesis: $CH_3COOH \rightarrow CH_4 + CO_2$ (Figure 7, arrow 7)
Hydrogenotrophic methanogenesis: $CO_2 + 4\,H_2 \rightarrow CH_4 + 2\,H_2O$ (Figure 7, arrow 8)

The specific methane production pathway utilized depends on physiochemical parameters and substrate availability (Walter et al. 2008). While globally, acetate decarboxylation is the dominant pathway of CH_4 production (Lovley & Klug 1986; Conrad 2009), the CO_2 reduction pathway prevails in northern peatlands (Hornibrook et al. 1997; Horn et al. 2003; Lee et al. 2012). The methane produced is released into the atmosphere through diffusion and ebullition, with ebullition constituting 80 – 95 % of total CH_4 emissions in Arctic lakes (Walter et al. 2006; Sepulveda-Jauregui et al. 2015).

However, methane oxidation acts as a biological filter that mitigates methane emissions while migrating through soils (Knoblauch et al. 2008; in 't Zandt et al. 2020). Within the active-layer, methanotrophy typically takes place at the interface between oxic and anoxic zone, in the rhizosphere of vascular plants, and in submerged mosses (Liebner et al. 2011; Vishnivetskaya et al. 2011). The enzyme methane monooxygenase enables methane oxidizing *Proteobacteria* (MOP) to use methane as the sole source of carbon and energy (Bowman 2006; Vishnivetskaya et al. 2011).

11

In aerobic conditions, O_2 acts as the preferred electron acceptor for methane oxidation.

Aerobic methane oxidation: $CH_4 + 2\,O_2 \rightarrow CO_2 + 2\,H_2O$ (Figure 7, arrow 10)
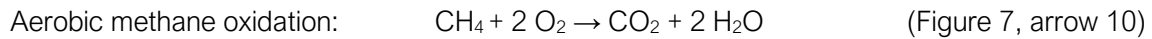
Under anaerobic conditions, methanotrophic archaea and bacteria may use alternative electron acceptors for methane oxidation, preferentially NO_3 and NO_2^- as in terrestrial environments (Knief 2019; Heslop et al. 2020).

AOM: $CH_4 + 4\,NO_3 \rightarrow CO_2 + 4\,NO_2^- + 2\,H_2O$ (Figure 7, arrow 9)

AOM: $3\,CH_4 + 8\,NO_2^- + 8\,H^+ \rightarrow 3\,CO_2 + 4\,N_2 + 10\,H_2O$ (Figure 7, arrow 9)
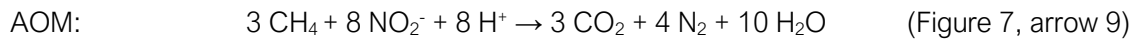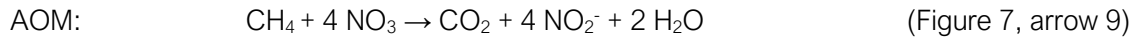
Methane oxidation has the potential to reduce CH_4 emissions to the atmosphere by 100 % in aerobic settings (Roslev & King 1996; Popp et al. 2000; Whalen & Reeburgh 2000). As a result, only CO_2 is released from oxic soils (Schuur et al. 2008).

1 Gross primary productivity (GPP)
2 Net primary productivity (NPP)
3 Net ecosystem production (NEP)
4 Autotrohpic respiration (R_A)
5 Heterotrophic respiration (R_H)
6 Hydrolysis & fermentation
7 Acetoclastic methanogenesis
8 Hydrogenotrophic methanogenesis
9 anaerobic oxidation of methane (AOM)
10 aerobic methane oxidation
11 diffusion
12 ebullition
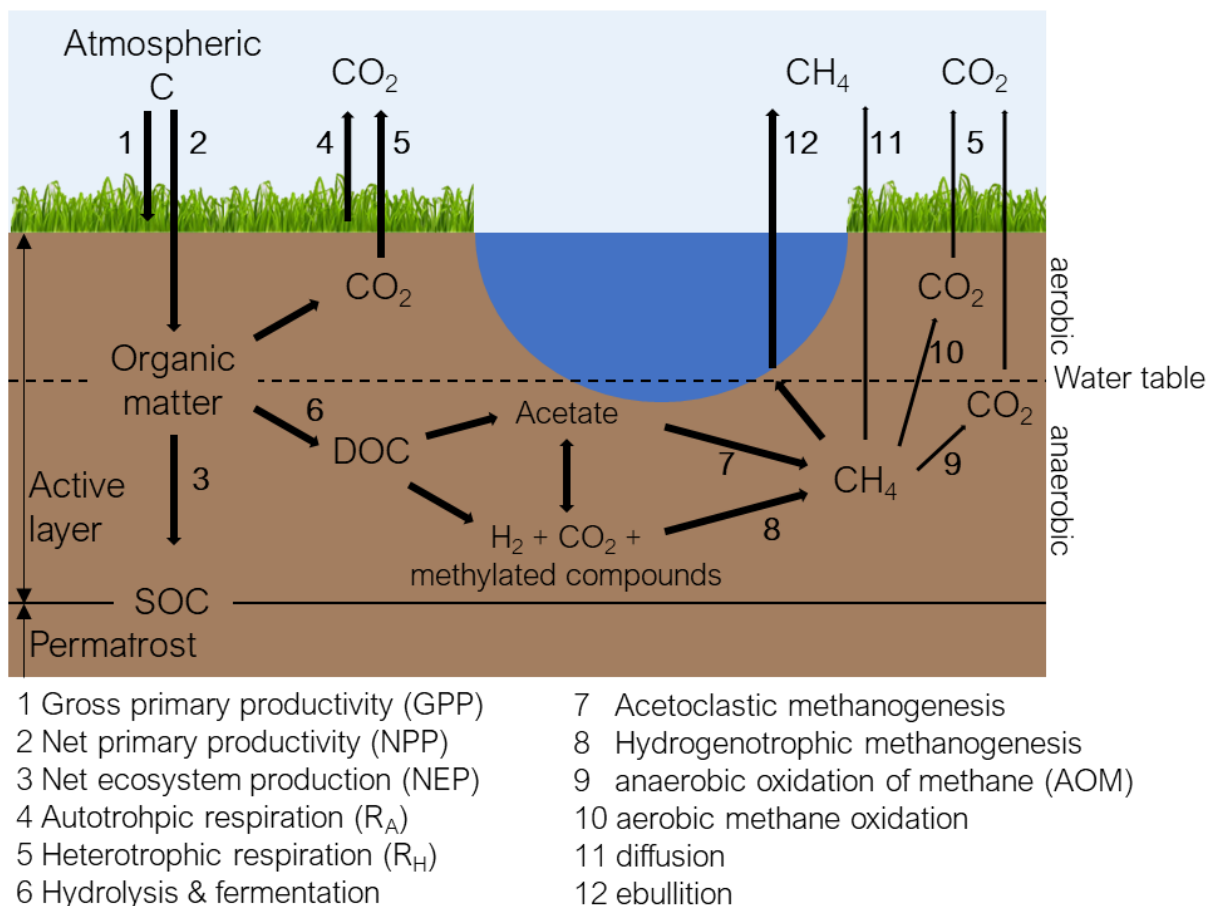
Figure 7: Methane production and consumption pathways in permafrost-affected soils. According to Christensen & Cox (1995); Wagner & Liebner (2009); in 't Zandt et al. (2020).

2.3.2. The permafrost carbon feedback

Near-surface temperatures in the Arctic have warmed twice the global average over the past 50 years, a disproportionate warming that is known as 'Arctic amplification' (Graversen et al. 2008; IPCC 2013). The deepening of permafrost active layers due to Arctic climate warming implies that the permafrost carbon pool becomes progressively available for microbial decomposition as warmer temperatures accelerate microbial metabolism (Schuur et al. 2015). This feedback loop of thawing

permafrost intensifying the decomposition of organic matter and leading to increased greenhouse gas (GHG) emissions is termed the "permafrost carbon feedback" (Schuur et al. 2008, 2013, 2015; Schaefer et al. 2014; van Huissteden 2020). With respect to the size of the permafrost carbon pool, even small changes in C dynamics could significantly increase the atmospheric CO_2 concentration (Koven et al. 2011; Schuur et al. 2013) (Figure 8).
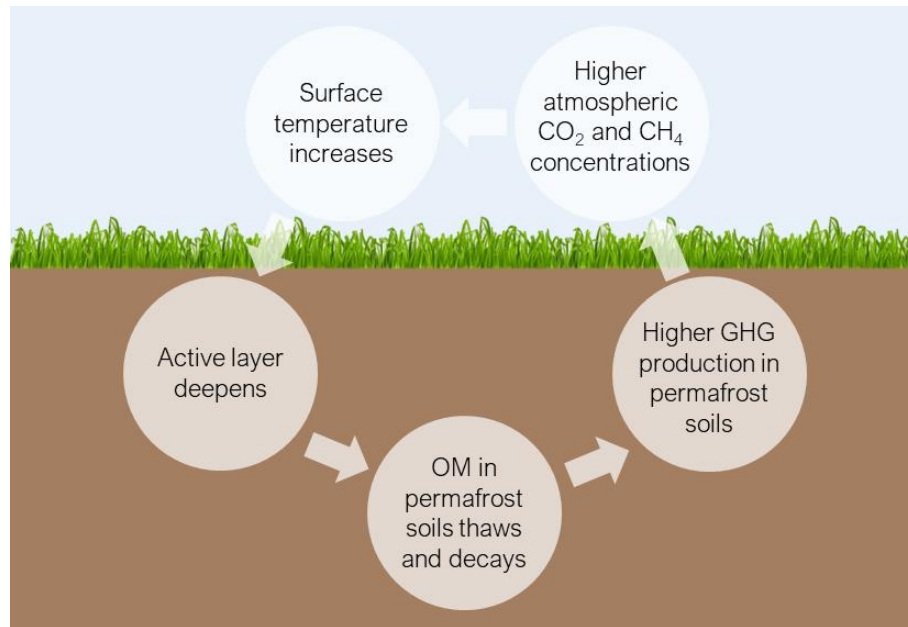
Figure 8: The Permafrost Carbon Feedback (Schaefer et al. 2014).

The immediate response of microbial activity to seasonal temperature increases predicts a rapid influence of Arctic warming on nutrient cycles (Vishnivetskaya et al. 2011). However, shifts in microbiome structure render it challenging to assess microbial community responses (Coolen et al. 2011; Mackelprang et al. 2011; Coolen & Orsi 2015; Barbato et al. 2022; Ernakovich et al. 2022; in 't Zandt et al. 2020). Further, climatic changes affect microbial community establishment (Bischoff et al. 2013; Holm et al. 2020).

The key uncertainty in evaluating the carbon feedback of permafrost ecosystem dynamics in a warming Arctic is the balance between the effects of changing subsurface hydrology, oxygen availability, and the vegetation cover (Schädel et al. 2016).

The impact of vegetation composition changes on carbon cycling introduces additional uncertainty to the system (Chapin et al. 1995; McGuire et al. 2018). Increased nutrient availability (Chapin et al. 1995), and a warmer and prolonged growing season (Sistla et al. 2013; Natali et al. 2014) will alter plant species composition (Chapin et al. 1995; Olefeldt et al. 2013) and promote plant growth ((Rustad et al. 2001; Hobbie et al. 2002), contributing to enhanced plant CO_2 uptake and storage in vegetation and soils (Schädel et al. 2016).

In terms of hydrology, permafrost ecosystems can experience either decreasing wetness (lake drainage, drying wetlands) (Smith et al. 2005; Koch et al. 2014; Lindgren et al. 2021) or heightened wetness (thermokarst) (Zona et al. 2012; Polishchuk et al. 2015; Jorgenson & Grosse 2016) with rising temperatures. These shifts in moisture regimes impact organic matter turnover and

subsequently influence the quantity and composition of greenhouse gas release (Kwon et al. 2017). Lower soil moisture and associated enhanced oxygen availability in drying ecosystems create favourable conditions for microbial carbon decomposition via heterotrophic respiration and thus CO_2 release (Chapin et al. 1995; Walter et al. 2006; E. A.G. Schuur et al. 2015; Schädel et al. 2016). Conversely, water-saturated, anoxic environments promote microbial carbon fermentation and inhibit methanotrophy, leading to slower, but concurrent CO_2 and CH_4 release (Vishnivetskaya et al. 2011). Laboratory experiments revealed that aerobic conditions yield around 3.4 times higher C release compared to anaerobic conditions (Schädel et al. 2016).

Assessing the permafrost carbon feedback of L-DLB systems is complex. Within thermokarst lakes, continual input of organic matter stimulates microbial decomposition and contributes to anoxic conditions at the lake bottom (Deshpande et al. 2017). Thermokarst lakes exhibit a strong positive climate feedback (Walter et al. 2007; Schuur et al. 2008; Schaefer et al. 2011; Walter Anthony et al. 2016; Walter Anthony et al. 2018), attributed to high CH_4 emissions via ebullition (Zimov et al. 1997; Walter et al. 2006; Matveev et al. 2016; Walter Anthony et al. 2016; Yao et al. 2021) and the rapid release of old, long-term stored carbon (in 't Zandt et al. 2020; Turetsky et al. 2020).

Emissions from drained lake basins are generally one to three orders of magnitude lower than from lakes as a consequence of talik refreezing and vegetation colonization (Zona et al. 2010; Walter Anthony et al. 2018). After lake drainage, atmospheric CO_2 is taken up by pioneer vegetation colonising the basin floor. Initially high CH_4 emissions arising from the water-saturated, organic soils decline over time as drying progresses and peat accumulation slows (Zona et al. 2010; Zona et al. 2012; Olefeldt et al. 2013; Lawrence et al. 2015; Treat et al. 2021). Over a time period of many years, the warming effect of the emitted short-lived CH_4 may be compensated by incorporation of long-lived CO_2 from the atmosphere in the vegetation succession in drained lake basins (Oechel et al. 2000; Whiting & Chanton 2001; Jones et al. 2012). Due to the differing greenhouse gas lifetimes, DLBs may turn to net carbon sinks over time (Dorrepaal et al. 2009; McGuire et al. 2009; Neubauer & Megonigal 2015).

Assessing the ratio of emitted greenhouse gases is crucial as CH_4 bears a significantly higher radiative forcing with a global warming potential (GWP) 28 times that of CO_2 on a 100-year scale (Schuur et al. 2008; IPCC 2013; Schuur et al. 2013; E. A. G. Schuur et al. 2015; Treat et al. 2015; Schädel et al. 2016). Nonetheless, total GHG emissions expressed in CO_2-C equivalents from aerobic soils are reportedly 2.3 times higher than from anaerobic soils (Schädel et al. 2016). These variations in GWP can result in ecosystems contributing to climate warming even when carbon storage outweighs carbon release (van Huissteden 2020).

In total, the expected emissions by permafrost regions are unlikely to cause abrupt climate change on short time scales but have the potential to steadily fuel global warming on a decade-to-century timescale (Schuur et al. 2015). This contribution may not be linear, but weaken over time when labile carbon pools are exhausted (Luo et al. 2001; Knoblauch et al. 2013; Sistla et al. 2013).

3. Study area

The study area is situated within the Yukon Coastal plain in the Western Canadian Arctic (Figure 9). A lowland region extending over approximately 282 km, stretching from the Mackenzie River delta in the east to the Alaskan border in the west. It is a relatively narrow plain, with a width ranging from 10 - 40 km. The landscape gently slopes from the inland British Mountains toward the Canadian Beaufort Sea. The Yukon Coastal Plain is primarily characterized by tundra, accounting for approximately 80 % of its land cover. Additionally, lakes and wetlands make up the remaining 20 % of the land cover (Smith et al. 2004). A research station that is permanently staffed during the summer months from April to October is located on Herschel Island.
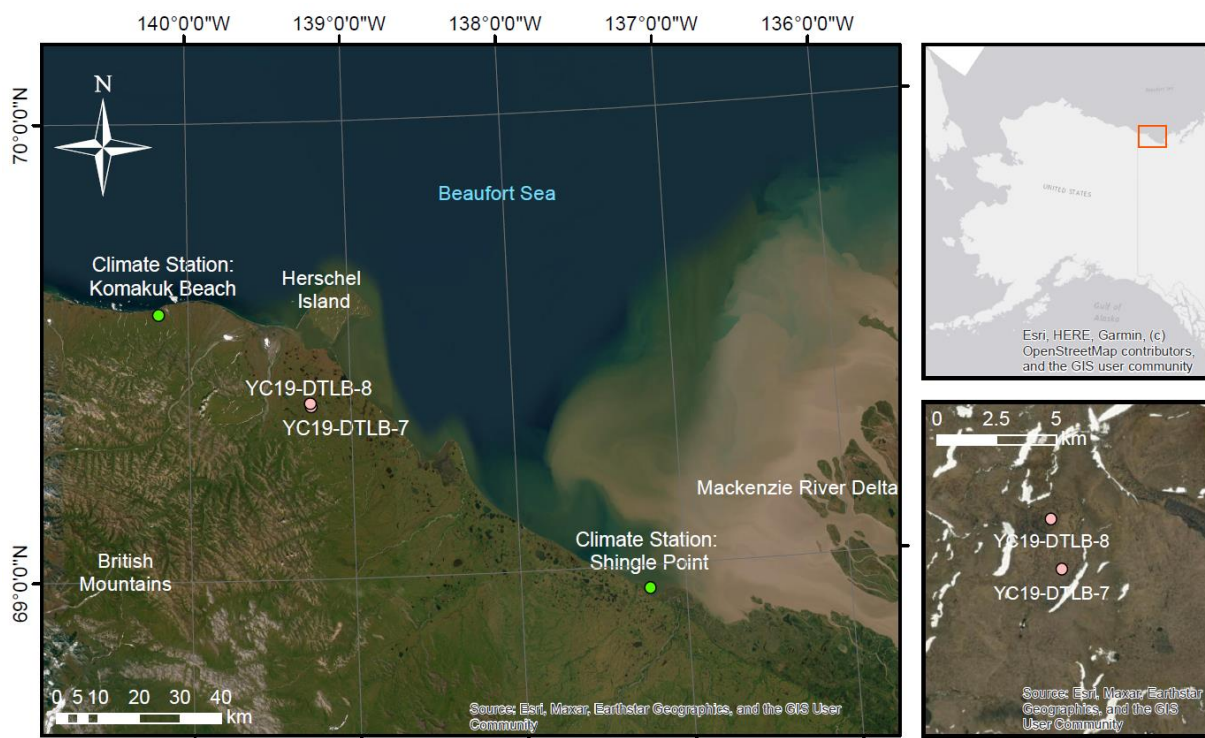
Figure 9: Satellite image of the study area along the Yukon Coastal Plain, Canada.

3.1. Geology and geomorphology

The bedrock of the coastal plains in this region is primarily composed of slates and shale, with ages ranging from Palaeozoic through Early Tertiary. These rock formations underwent erosion during the Late Tertiary period under non-periglacial climate conditions (Smith et al. 2004). During the Wisconsinan Glaciation, which occurred approximately 23 000 – 18 000 cal a BP, the Yukon Coastal Plain experienced partial glaciation (Hughes et al. 1981; Blasco et al. 1990; Duk-Rodkin & Hughes 1995). The Laurentian ice sheet covered a substantial portion of the Canadian Arctic and terminated just west of Herschel Island (Rampton 1982; Duk-Rodkin 1999). As a result, the surface sediment of the Yukon Coastal Plain is comprised of a mixture of glacial morainic deposits and coarse-grained glaciofluvial material as well as fine-grained lacustrine and fluvial sediments (Rampton 1982; Smith et al. 2004; Couture 2010) (Figure 10). This sediment is overlain by a layer of organic soil. Peat beds are

15

a common feature in lacustrine basins and can vary in thickness from 0.5 to 3.5 meters. The accumulation is fostered by poor drainage and a flat landscape with low slope gradients towards the Canadian Beaufort Sea (Rampton 1982).
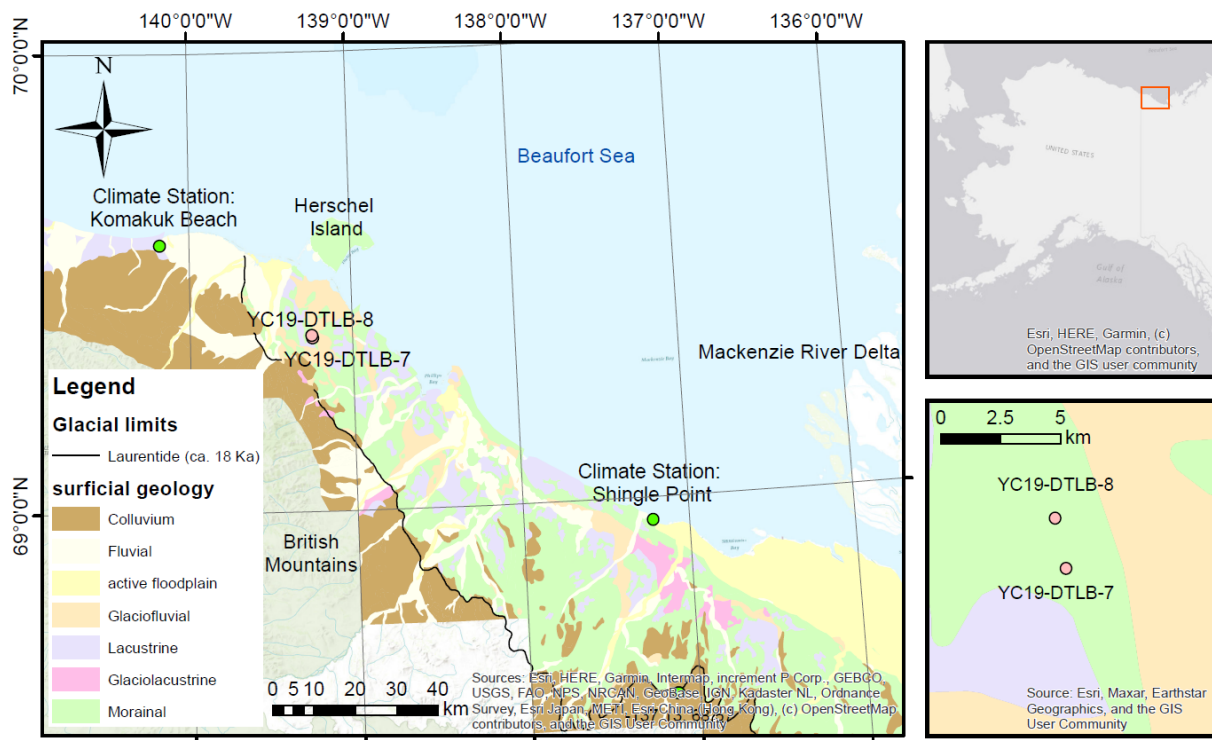
Figure 10: Distribution of Pleistocene and Holocene sediments along the Yukon Coastal Plain, Canda, based on Rampton (1982).

The Yukon Coastal Plain is located within the continuous permafrost zone (Nguyen et al. 2009). In most of the Yukon Coastal Plain, permafrost depths extend to approximately 100 meters. Only within the Mackenzie Delta region, permafrost depths can reach up to 500 meters (Burn & Kokelj 2009). The coastal lowland is characterized by shallow active layers of 0.3 – 1.5 meters (MacKenzie et al. 2022). During the early Holocene, around 8 000 years BP, active layers were up to 2.5 times thicker (Mackay 1978; Ritchie 1984; Kokelj et al. 2002; Burn 2011). The region's soils tend to be poorly drained due to several factors, including the presence of fine-textured soils, the insulating effects of vegetation cover, the accumulation of organic surface horizons, and low heat accumulation. Consequently, many coastal soils are waterlogged, with limited oxygen supply, which is indicated by the presence of gleyed or strongly mottled horizons (MacKenzie et al. 2022). The Yukon Coastal Plain is one of the most ice-rich areas of the Arctic (Rampton 1982). Some coastal segments have reported volumetric ground ice contents as high as 74 % in the upper portion of permafrost (Couture & Pollard 2017). This large share of ground ice plays a significant role in accelerating thermoerosional processes, such as thermokarst, and the development of retrogressive thaw slumps (Pollard 1990; Lantuit & Pollard 2005; Lantuit & Pollard 2007; Wolter et al. 2016).

3.2. Local climate

The prevailing polar tundra climate is marine in summer but shifts to a continental climate for most of the year when sea ice covers the Beaufort Sea (Hill et al. 1991; Galley et al. 2016). Mean annual air temperatures of - 11 °C and - 9.9 °C were recorded at Komakuk Beach and Shingle Point. During the long winter season, average temperatures fall below - 20 °C. Snowmelt only commences around May as temperatures climb above 0 °C. Even during the summer months, average temperatures rarely exceed 10 °C (Rampton 1982). Precipitation levels are relatively low, with Komakuk Beach receiving around 161.3 mm and Shingle Point approximately 253.9 mm of precipitation. The precipitation shows a summer maximum, hence the reported monthly averaged depths of the snow cover during the winter months (Dec-Apr) range only from 21 - 26 cm at Komakuk Beach and 34 – 36 cm at Shingle Point. All climate data was provided by the Government of Canada for the period from 1971 to 2000 (Government of Canada 2011). Ice-free conditions in the Beaufort Sea prevail for only three to four months per year. The semi-diurnal tides fluctuate in the microtidal range (0.3 – 0.5 m) (Héquette et al. 1995). Highest storm surges of the season occur in autumn just before the Beaufort Sea freezes over (Hill 1990; Hudak & Young 2002). The dominant wind-direction on the plain is north-west (Hill 1990). Temperature increases in both mean air and permafrost temperatures have been observed at Herschel Island. Between the periods 1899 – 1905 to 1995 – 2006, mean air temperatures rose by 2.5°C, and permafrost temperatures increased by 2.6 °C (Burn & Zhang 2009). As a consequence of the associated longer open water season in the Beaufort Sea, coastal erosion has accelerated (Lantuit & Pollard 2007; Jones et al. 2009; Stroeve et al. 2014), contributing to higher carbon fluxes to the sea (0.036 Tg/a) (Obu et al. 2016; Couture et al. 2018). Current estimates suggest that the region is experiencing sea level rise at a rate of approximately 3.5 ± 1.1 mm per year (Manson & Solomon 2007). Furthermore, the Yukon Coastal Plain is situated in a submergent area (Forbes 1980).

3.3. Local vegetation

Low and dwarf shrub tundra covers the Yukon Coastal Plain that is situated approximately 100 km north of the tree line (Ritchie 1984; Wolter et al. 2016; MacKenzie et al. 2022). The vegetation has adapted to high variability in sunlight insolation and harsh temperature conditions (He et al. 2016). Productivity is strongly restricted to a short growing season (van Huissteden 2020). The local vegetation composition is highly dependent on hydrological conditions, soil properties and morphological features. Vegetation is dominated by sedges, mosses and dwarf-shrubs in lowlands and cotton grass (*Eriophorum scheuzeri*) and tussock (*Eriophorum vaginatum* and *Bryophytes*) tundra where the soil is better drained (Mackay 1963). Arctic willow (*Salix arctica*), dryas (*Dryas integrifolia*) and vetch (*Astragalus umbellatus/alpinus*) are the dominating species in well-drained uplands (MacKenzie et al. 2022). Along streams and lakes, willow and birch shrubs (*Alnus sp., Betula glandulosa, Salix sp.*) occur (Rampton 1982).

4. Methods

4.1. Field work

The two permafrost sediment cores YC19-DTLB-7 (Figure 11) and YC19-DTLB-8 (Figure 12) analysed in this thesis were taken on the Yukon Coast 2019 expedition in spring 2019 under chief scientist Prof. Hugues Lantuit and Dr. George Tanski (Table 1). A total of 24 drained lake sites on the Yukon Coastal Plain were identified prior to the expedition by remote sensing imagery. One sediment core per drained lake basin was taken with a SIPRE corer during the expedition under P.I. Dr. Juliane Wolter. As the sediment was frozen to the top, little drilling mud was generated in the process and a first core description was possible immediately. As a downside, associated depths of the active layer as well as the vegetative cover could not be determined on site due to the prevailing snow cover. The two drained lake basins DTLB-7 and DTLB-8 cover respective areas of approximately 1.10 and 0.22 km^2.

Table 1: Sampling information for permafrost sediment cores YC19-DTLB-7 and YC19-DTLB-8.

Sampling date	Sample ID	Sampling coordinates	Elevation [m a.s.l.]	Distance to coast [km]
April 25th, 2019	YC19-DTLB-7	69.37662 °N 139.24631 °W	50	11.5
April 25th, 2019	YC19-DTLB-8	69.38322 °N 139.25035 °W	50	11.2

Figure 11: Sediment core YC19-DTLB-7 on April 25th, 2019.
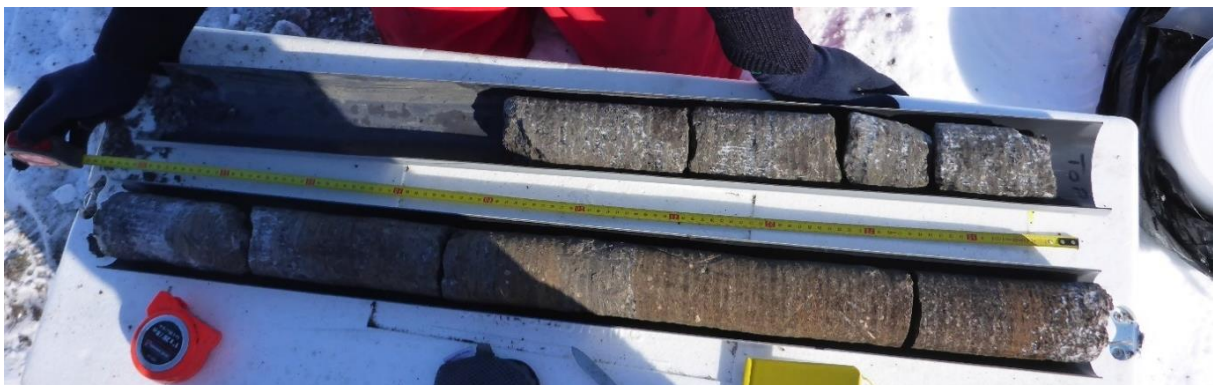
Figure 12: Sediment core YC19-DTLB-8 on April 25th, 2019.

Cores were wrapped in aluminum and plastic foil and were stored and transported in styrofoam boxes, ensuring sub-zero temperatures until arrival at the cold room (- 15 °C) at Alfred Wegener Institute Helmholtz Centre for Polar- and Marine Research (AWI) in Potsdam.

4.2. Laboratory work

Laboratory analyses were performed at AWI in Potsdam (Figure 13). Splitting and subsampling of the sediment cores was carried out in a climate chamber at - 8 °C to prevent thawing. Both cores were split into halves lengthwise using a Makita band saw. As a first step, they were cleaned and lithologically described (Table 2 & Table 3). Pictures were taken. The working halves of the two studied permafrost sediment cores YC19-DTLB-7 and YC19-DTLB-8 were described and subsampled at even intervals for biogeochemistry and grain size analysis by Juliane Wolter at AWI Potsdam on June 28th, 2021.
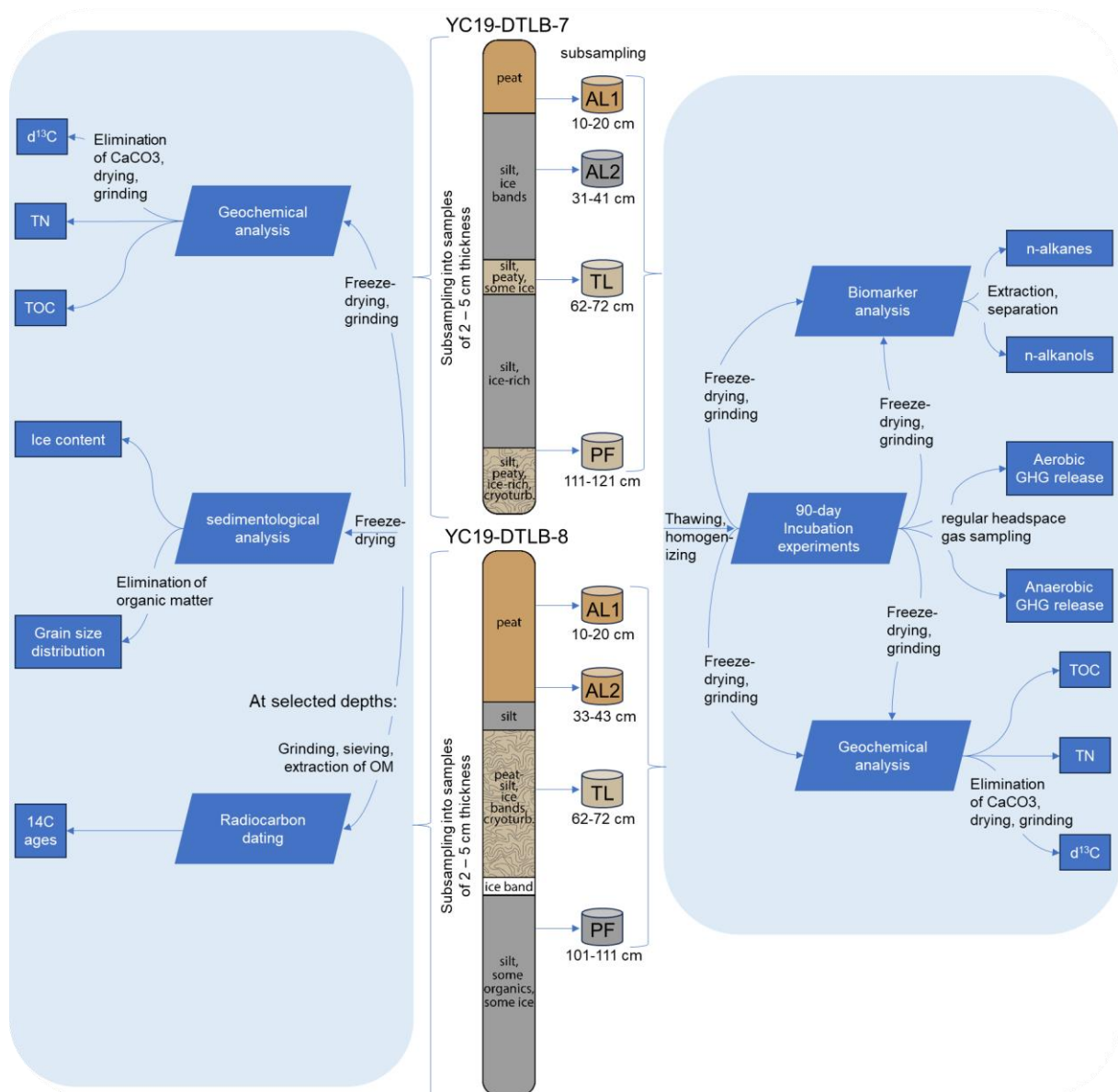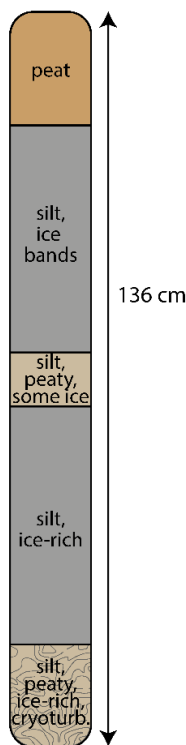
Figure 13: Flowchart of laboratory analyses.

Table 2: Sedimentological core description of YC19-DTLB-7.

depth (cm)	core description
0 - 2	live vegetation
2 - 21	medium-brown peat, few roots 3 mm, structureless
21 - 27	grey silt, two vertical ice veins 5 mm wide with 1 horizontal connection, through entire section
27 - 31	core loss with crumbled pieces, suspended silt in ice matrix
31 - 64	suspended silt, ice with few vertical bubble trains, roots (few) 2 mm, 59 - 64 ice layers
64 - 136	cryoturbated silt, peat and ice, peat lenses 7 cm ice-rich, few roots 1 - 2mm

Table 3: Sedimentological core description of YC19-DTLB-8.

depth (cm)	core description
0 - 5	ice-rich fresh peat
5 - 9	reddish ice-rich peat
9 - 26	medium-brown peat, roots up to 3 mm, structureless cryostructure
26 - 43	porous peat (dried? Sediment?), roots up to 4mm, colour as above
43 - 50	brownish-grey silt, roots up to 3 mm, horizontal layered cryostructure, some vertical bubble veins, lowest cm is structureless
50 - 76	slightly cryoturbated, medium-brown peat with some silt-ice layers (58, 60 - 63), roots 4 mm above 62 cm, above 58 finely layered horizontal cryostructure, below 63 cm structureless
76 - 91	ice with peat and silt, vertical bubble trains
91 - 96	ice lens with some silt, vertical bubble trains
96 - 138	suspended silt, ice with vertical bubble trains, ice bands (111 - 114, 116 - 117, 127 - 129), below 123 individual roots up to 3 mm
138 - 155	ice-rich brownish-grey silt with many roots 4 mm, visible organics, ice lenses up to 5mm, irregular

Samples for radiocarbon dating were taken at chosen depths. The second, archive half is meant to be kept intact for long term storage. Due to the multitude of analyses, the archive was subsampled for incubation and biomarker analyses at four chosen sampling depths. The large amount of material necessary for these analyses required that layers of 10 cm thickness were sampled and homogenized.

4.2.1. Ice content

The ice content was determined as the weight difference between the frozen and freeze-dried samples and was expressed in weight percentage (wt. %) (Equation 1).

$$ice\ content\ [wt.\%] = \frac{m_w - m_d}{m_w} * 100$$

Equation 1

m_w [g]   weight of the wet sample material
m_d [g]   weight of the dried sample material

4.2.2. Grain size distribution

Grain size analysis was performed to evaluate the origin of the sediment and provides insights into transportation processes and deposition mechanisms. The analysis was applied for all mineral samples whilst it was not feasible to implement a grain size analysis for peaty samples that contained little to no sediment.

In preparation for grain size analysis, a deliberate removal of organic matter from the samples was conducted to prevent result distortion. For this purpose, 100 ml of 3 % hydrogen peroxide (H_2O_2) were added to the 400 ml beakers containing the sample material. In addition, approximately 4 ml of 32 % ammonia were added for pH modification. The samples were then subjected to constant agitation at 60 °C on an Edmund Bühler GmbH heated shaker for four weeks in order to enhance reaction. Starting 24 h after initiation, further 10 ml of 30 % H_2O_2 were added 4 - 5 times a week throughout the procedure. To maintain the optimal near-neutral pH conditions (6 - 8), ammonia or acetic acid were intermittently introduced. When pH stability was achieved within the neutral range, the addition of 30 % H_2O_2 was increased to 20 ml. Once foam and bubble formation ceased, indicating the full removal of organic matter, samples were washed with de-ionised water to remove the added H_2O_2.

Subsequently, the samples were centrifuged using a Heraeus Cryofuge 8500i (5050 rpm, 10 min, 20 °C) and a Heraeus Megafuge 40 (both Thermo Scientific), and the separated solid sample material was freeze dried and homogenized. Plastic jars were filled with 0.6 – 0.7 g of sample material, along with a dispersing agent (0.5 g tetra-sodium pyrophosphate 10-hydrate ($Na_4P_2O_7 * 10\ H_2O$)). Deionized water was added before placing the jar in a Gerhardt Laboshake overhead shaker for a minimum of 24 h. Each sample was divided into 8 equal subsamples with a particle concentration ranging from 5 - 15 % using a Fritsch laborette 27 Rotary Sample Divider. Particles exceeding 1 mm were removed through sieving to prevent laser device damage but were weighed and later incorporated into the grain size distribution if significant.

The final grain size distribution was determined using a Malvern Mastersizer 3000 (Malvern Instruments, UK) equipped with a Malvern Hydro LV wet-sample dispersion unit. The suspended samples are exposed to a red laser (633 nm wavelength) and a blue LED (470 nm wavelength), with particle refraction quantified by multiple scatter light detectors. Grain sizes were calculated based on the light impulses on each detector. A minimum of three subsamples were measured per sample, until the standard deviation in each grain size class was < 5 %. Grain sizes are presented according to ISO 14688-1:2017 standards, describing grain size on a scale from clay (particles < 2 μm), silt (< 63 μm), sand (< 2 mm), gravel (< 64 mm) to boulder sized clasts (Appendix 1). Grain size statistics were processed using GRATISTAT software.

4.2.3. Total carbon and total nitrogen

Biogeochemical parameters such as total nitrogen (TN), total carbon (TC), and total organic carbon (TOC) were analysed to serve as key indicators for shifts in organic matter composition. These analyses provided insights into paleoenvironmental conditions during deposition. Total amounts of carbon (TC) and nitrogen (TN) were determined based on pyrolysis. Homogenization of the samples was achieved through grinding using a planetary mill (Pulverisette 5, Fritsch). Approximately 50 mg of the grinded sample material was weighted into steel crucibles using a Mettler Toledo XS105 dual range analysis scale (accuracy of ± 0.1 mg). The carbon fractions total organic carbon (TOC), residual organic carbon (ROC) and total inorganic carbon (TIC) were determined individually via pyrolysis according to DIN19539 in a Soli TOC® cube (Elementar Analysensysteme GmbH) (Figure 14a).
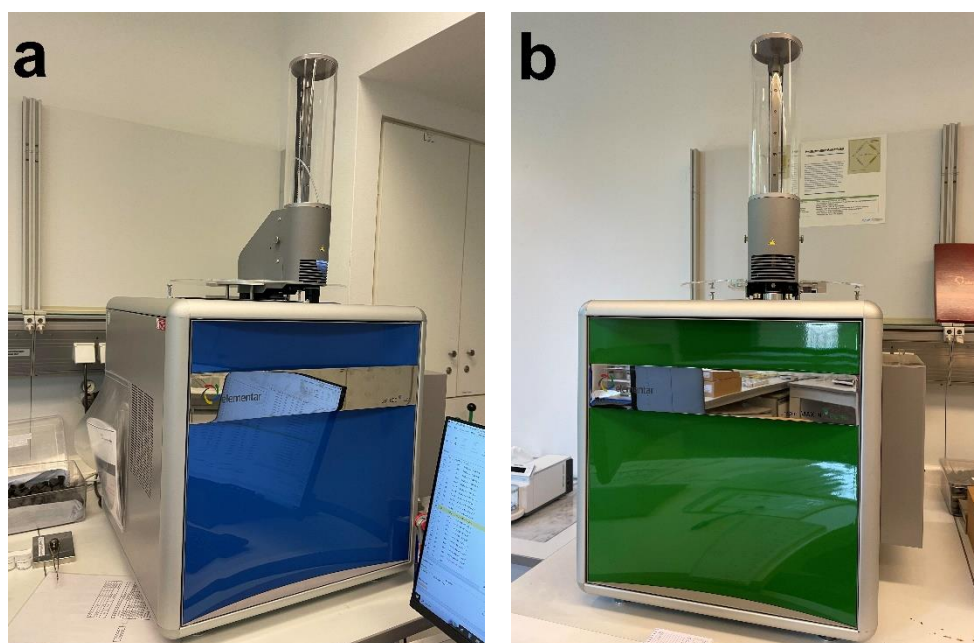
Figure 14: Laboratory devices for determination of carbon and nitrogen. (a) The Soli TOC® cube and (b) the Rapid max N exceed (both Elementar Analysensyteme) in the carbon & nitrogen lab at AWI Potsdam.

Following a heat ramp, samples were heated at a rate of 70 °K/min to 400, 600 and 900 °C with holding times of 230, 120 and 150 s, respectively. Prior to the sediment samples, three empty

crucibles were inserted for background detection, followed by calibration standards consisting of 3 x 20 mg of 6 % calcium carbonate (TC = 6 %), 3 x 50 mg of IVA 2176 (TOC = 15.52 %), 1 x 15 mg of 12 % calcium carbonate (TC = 12 %) and 1 x 100 mg of EDTA 5:45 (TOC = 4.11 %). A control sequence was measured after 37 samples, consisting of 1 x 15 mg of 12 % calcium carbonate and 1 x 100 mg of EDTA 5:45. To ensure measurement quality, each sample was measured twice.

Total nitrogen (TN) determination was carried out using a Rapid Max N exceed (Elementar Analysensysteme GmbH) (Figure 14b). Again, approximately 50 mg of the grinded sample material was weighed into steel crucibles using a Sartorius micro M2P laboratory scale (accuracy of $\pm$ 0.001 mg). Samples were heated to 900 °C. O_2 was introduced at a flow rate of 160 ml/min for 2 min for samples > 15 wt. % TOC and at a flow rate of 120 ml/min for 2 min for samples < 15 wt. % TOC. Prior to the sediment samples, three empty crucibles were inserted for background detection, followed by calibration standards consisting of 4 x 50 mg EDTA 5:45 (N = 0.960 %), 1 x 50 mg of soil standard 1 (N = 0.216 %), 1 x 50 mg of soil standard 2 (N = 0.064 %), 1 x 50 mg of IVA 2150 (N = 0.490 %) and 1 x 50 mg of IVA 2156 (N = 1.360 %). A control sequence was measured after 37 samples, consisting of soil standard 1 and 2, IVA 2150 and IVA 2156, 50 mg each. The accuracy of the results is $\pm$ 0.1 wt. % according to the manufacturer, equalling the detection limit for C and N of the device. Both analyses were carried out once again with the substrate of one of the two opened incubation vials after three months of incubation.

The relative contents of organic carbon and nitrogen (subsequently referred to as C:N ratio) can further provide information on the source as well as the degree of degradation of the organic matter. High degrees of preservation are indicated by high C:N ratio values, while low values imply considerable mineralization of the organic material (Meyers 1994; Stevenson 1994; Schirrmeister et al. 2011).

4.2.4. Stable Carbon Isotopes

Further information on the origin and degradation of organic matter could be derived from the carbon stable isotope composition. Stable isotopic compositions reflect the origin of organic matter, altered by degradation processes.

The high TOC contents throughout the entire core allowed stable isotope analysis of every sample. Prior to the carbon stable isotope analysis, inorganic carbon was removed from the samples by addition of 20 ml of 1.3 molar hydrochloric acid (HCl). Reaction was supported by heating the conical flask to 50 °C on a hotplate for three hours under occasional stirring. The carbonate-free sample was then neutralized back to a pH of 7 and a chloride (Cl) content of < 500 parts per million (ppm) by repeated addition and decantation of distilled water. The samples were filtered using a glass microfiber filter (Whatman Grade GF/B, nominal particle retention of 1.0 µm) to fully separate sediment from the liquid. Finally, the residues were dried at 50 °C in a compartment dryer and grinded.

The amount of substrate required for the following simultaneous C and N stable isotope analysis was determined depending on the individual TOC content of a sample according to the isotope laboratory of AWI Potsdam (Equation 2 & Equation 3).

$$\delta^{13}C: \quad \text{target weight [mg] = 20 / TOC [wt. \%]}$$ *Equation 2*

$$\delta^{15}N: \quad \text{target weight [mg] = 10 / TOC [wt. \%]}$$ *Equation 3*

The calculated amount of sample was weighed into tin capsules using a Sartorius micro M2P laboratory scale (accuracy of $\pm$ 0.001 mg) with a maximum deviation of $\pm$ 0.02 mg in reference to the target weight. The determination of the carbon isotopic composition was carried out by the Stable Isotope Laboratory of the Alfred Wegener Institute Helmholtz Centre for Polar and Marine Research (ISOLAB Facility Potsdam). The carbon isotopic composition was determined using a Delta-V-Advantage gas mass spectrometer (Thermo Fisher Scientific) equipped with a FLASH elemental analyser EA 2000 and a CONFLO IV gas mixing system. To transfer organic carbon and nitrogen into the gaseous state, samples were combusted at 1020 °C in an O_2 atmosphere with chrome dioxide (CrO_2) serving as an oxidant. As CO_2 and several nitrogen oxides (NO_x) formed, CO_2 was separated from other gases in the reduction tube and the elemental analyser. For carbon isotope measurements, the CO_2 gas was transferred with Helium as a carrier gas via the CONFLO IV gas mixing system and a capillary to the mass spectrometer, where the carbon isotope composition was determined relative to laboratory standards of known isotopic composition. Calibration runs were performed before, and control runs in between the measurement runs to ensure quality of the results. Some samples were measured in duplicate in order to estimate the quality and the reproducibility of the measurements. Stable carbon isotope analysis was carried out again with the substrate of one of the two opened incubation vials after three months of incubation.

The ratio between the two stable carbon isotopes is noted as $\delta^{13}C$ and expressed in permille relative to Vienna Pee Dee Belemnite (VPDB), a calibrated standard produced by the International Atomic Energy Agency in Vienna (Equation 4). The standard deviation (1 σ) is generally better than $\delta^{13}C = \pm$ 0.15 ‰.

$$\boldsymbol{\delta^{13}C} \, [‰ \, vs. VPDB] = \frac{R_{Sample} - R_{Standard}}{R_{Standard}} * 1000$$ *Equation 4*

R   [-]   Ratio between heavy and light isotope ($^{13}C/^{12}C$)

4.2.5. Geochronology

Radiocarbon dating was performed in order to establish a geochronological record of the drained lake basin strata. Samples for radiocarbon dating were taken from the bulk material subsamples and analyzed using acceleration mass spectrometry (AMS) with a Mini Carbon Dating System (MICADAS) at AWI in Bremerhaven. Preparation of the samples involved the removal of nitrogen (^{14}N) and hydrocarbon ($^{12}CH_2$ and $^{13}CH_1$), compounds that share the same mass as ^{14}C (acid-alkali-acid sample preparation). Afterwards, the weight-dependent deviation radii could be distinctly assigned to the

three carbon isotopes. To express the obtained dates in calibrated kilo years BP (cal. ka BP), further processing was required. This calibration was achieved using the open-source software Calib 8.20 (Calib 8.2 n.d.) along with the IntCal20 calibration curve (Stuiver et al. 1998; Reimer 2020).

4.2.6. Microbiology

A microbiological analysis will be conducted on the sampling material but results are not included here as they were not within the scope of this thesis and not available at the time of writing.

4.2.7. Incubation

Laboratory incubations were conducted to assess the greenhouse gas production potential of drained lake basin sediments upon thaw. Subsamples of 10 cm thickness were taken from four selected sampling depths of both frozen sediment cores at - 8 °C in a cold lab at AWI Potsdam. The chosen core depths were selected to be representative of different thermal regimes. Two samples were obtained from the annually thawing active layer (AL), one from the occasionally thawing transition layer (TL), and another from the perennially frozen permafrost zone (PF). For comparability of greenhouse gas (GHG) production, corresponding core depths were chosen in both sediment cores. Given the locally highly variable hydrologic conditions in DLB environments, GHG production was investigated under both aerobic and anaerobic conditions. An incubation temperature of 4 °C was chosen to simulate a realistic scenario of a mid-term moderate sediment warming as well as current realistic summer active layer temperatures at the chosen depths.

Sediment incubations closely followed the procedures outlined by Strauss et al. (2015) and Jongejans et al. (2021). In preparation for the incubation, 120 ml glass vials were first rinsed with milli-Q water, then dried in an oven at 60 °C, and subsequently heated in a Muffle furnace at 500 °C to eliminate any potential contamination. The frozen sediment samples were thawed at 7 °C overnight in a nitrogen (N_2) atmosphere within a glovebox at GFZ Potsdam. After the thawed samples had been homogenized, four replicate incubation vials, each containing 15 g_{ww} sample material, were prepared in the glovebox for the anaerobic incubation experiment. Concurrently, four additional replicates for each sample were prepared under aerobic conditions in a sterile workbench. In addition to these, two blank samples were prepared, resulting in a total of 66 incubation vials. One exception is sample YC19-DTLB-8 AL2, where material constraints resulted in a sample weight of 12.9 g_{ww} each. The sediment samples were kept at field moisture conditions. The prepared incubation vials were sealed with autoclaved butyl stoppers and secured with aluminium caps. The headspace gas within the sealed vials was replaced with synthetic air (20 % O_2, 80 % N_2) for the aerobic vials, and N_2 for the anaerobic vials by flushing with synthetic air resp. N_2 for three minutes. Thereby, it was assured that any dissolved oxygen from the soil, water, and headspace is removed from the anaerobic vials. The remaining sediment material was utilized for the determination of pH, total organic carbon (TOC), total nitrogen (TN), and carbon isotopic composition in the sediment prior to the incubation experiment. All

prepared incubation vials were then stored in an incubator at AWI, where they were maintained at a temperature of 4 °C in darkness (Figure 15).

Figure 15: Incubation vials of anaerobic incubation experiment stored in a fridge at AWI Potsdam.

CO_2 and CH_4 concentrations in the headspace were analysed by gas chromatography using an Agilent GC 7890A. The device is equipped with an Agilent HP-PLOT Q column to separate the gases before quantification. CH_4 was quantified using a flame ionization detector (FID) while CO_2 was measured with a thermal conductivity detector (TCD). The instrument settings involved a temperature of 45 °C at both the injector and oven, with the detector set at 250 °C. Helium was used as the carrier gas for the chromatographic analysis. Gas subsamples of 250 µl were extracted from the vial headspace for the gas chromatographic measurement using a Hamilton gas tight syringe. During the course of the aerobic incubation, the headspace of the incubation vials was flushed with synthetic air whenever the CO_2 concentrations exceeded values of about 0.3 % (3 000 ppm), complying with the last calibration point of the GC. After flushing, the headspace concentrations were measured again to ensure a viable calculation of the cumulative greenhouse gas production over the incubation period. CO_2 concentrations after flushing were generally well below 200 ppm.

The experiment commenced with daily measurements for the initial five days of incubation. Due to the high emissions and the need for headspace gas flushing, measurement intervals for the aerobic incubation were kept at 3 - 4 days for the first two months. In the subsequent weeks of the experiment, the measurement interval was extended to a once-a-week frequency. The measurement interval for the anaerobic vials was set to a once-a-week schedule three weeks after starting the experiment. After 90 days of incubation, two out of the four replicates were removed from the incubation experiment for determination of pH and electrical conductivity, TOC, TN and $\delta^{13}C$ assessment as well as biomarker analysis. The incubation experiment continued for an additional nine months for the two remaining replicates, which is not within the scope of this thesis.

The concentrations of CO_2 and CH_4 in the incubation vial headspace were calculated from the measured gas concentrations, headspace volume, incubation temperature, and pressure using Henry's law (Knoblauch et al. 2013; Walz et al. 2018) (Equation 5).

$$c_{gas}\left[\frac{\mu mol}{g_{dw}}\right] = \frac{\rho * V * X}{R * T * m_d}$$

Equation 5

ρ	[Pa]	pressure inside the incubation vial
V	[m³]	gas volume in the incubation vial of ~ 103 ml resp. 0.000103 m³
X	[µmol mol⁻¹]	measured gas concentration
R	[Pa*m³ mol⁻¹ K⁻¹]	gas constant of 8.3144 Pa*m³ mol⁻¹ K⁻¹
T	[K]	incubation temperature of 277.15 °K
m_d	[g]	weight of the dried sample material

Under the given incubation conditions, part of the produced CH_4 becomes dissolved in pore water within the wet sample material. This dissolved CH_4 is not accounted for when measuring the concentrations in the headspace. To address this, the amount of CH_4 dissolved in water is calculated using the Bunsen solubility coefficient of 0.0022 mol l⁻¹ at 1 bar (Yamamoto et al. 1976) (Equation 6).

$$c_{CH4-aq}\left[\frac{\mu mol}{g_{dw}}\right] = \frac{S_{CH4} * \frac{m_w * wc}{1\,000} * X_{CH4} * \frac{\rho}{100\,000}}{m_d}$$

Equation 6

S_{CH4}	[mol l⁻¹ at 1 bar]	Bunsen solubility coefficient of 0.0022 mol CH_4 l⁻¹ at 1 bar
m_w	[g]	weight of the wet sample material
m_d	[g]	weight of the dried sample material
wc	[ml g_ww⁻¹]	water content
ρ	[Pa]	pressure in the incubation vial
X_{CH4}	[µmol mol⁻¹]	measured concentration in parts per million (ppm) or µmol/mol

Similarly, it is essential to account for the amount of CO_2 that is dissolved in water when assessing cumulative CO_2 production in the sediment. The solubility of CO_2 in water at 4 °C is notably high, approximately 0.065 mol l⁻¹, as defined by Carroll et al. (1991). It is important to recognize that the dissociation of carbonic acid in water at low pH levels can influence the concentration of dissolved inorganic carbon (DIC) in water. Hence the calculation was adjusted to include pH-dependent dissociation constants according to Millero et al. (2007) (Appendix 2, Equation 7).

$$c_{DIC-aq}\left[\frac{\mu mol}{g_{dw}}\right] = \frac{(S_{CO2} * \rho * X) * \left(1 + \left(\frac{K1}{10^{-pH}}\right)\right) + \left(\left(\frac{K1 * K2}{(10^{-pH})^2}\right)\right) * wc}{m_d}$$

Equation 7

S_{CO2}	[mol l⁻¹ at 1 bar]	solubility coefficient of CO_2 in water
K1	[mol kg⁻¹ bar⁻¹]	stoichiometric constants for the dissociation of carbonic acid in NaCl solutions
K2	[mol kg⁻¹ bar⁻¹]	stoichiometric constants for the dissociation of carbonic acid in NaCl solutions
m_d	[g]	weight of the dried sample material

However, only part of the dissolved inorganic carbon is constituted of CO_2, as DIC summarizes dissolved carbon dioxide (CO_2), hydrogencarbonate (HCO_3^-) and carbonate (CO_3^{2-}). Therefore, further calculations have to be applied to obtain only the dissolved CO_2 (Equation 8).

$$c_{CO2-aq}\left[\frac{\mu mol}{g_{dw}}\right] = \frac{cDIC}{\left(1 + \left(\frac{K1}{10^{-pH}}\right) + \left(\frac{K1 * K2}{(10^{-pH})^2}\right)\right)} * 1$$

Equation 8

c_{DIC}	[µmol g_dw⁻¹]	concentration of dissolved inorganic carbon
K1	[mol kg⁻¹ bar⁻¹]	stoichiometric constants for the dissociation of carbonic acid in NaCl solutions
K2	[mol kg⁻¹ bar⁻¹]	stoichiometric constants for the dissociation of carbonic acid in NaCl solutions

The total amount of CO_2 resp. CH_4 produced in the incubation vials is further transferred (Equation 9).

$$c_{CH4\text{-}C} \left[\frac{\mu g}{g_{dw}}\right] = (c_{gas} + c_{CH4-aq}) * M_C \qquad \textit{Equation 9}$$

C_{gas}	[µmol g_{dw}^{-1}]	concentration of CH_4 in headspace gas
$C_{CH4\text{-}aq}$	[µmol g_{dw}^{-1}]	concentration of CH_4 dissolved in water
M	[µg µmol^{-1}]	Molar mass of carbon of 12 µg/µmol

From the concentrations, mean CH_4 and CO_2 production of the four replicates were calculated, expressed in µg CH_4-C and CO_2-C $g_{dry\ weight}^{-1}$ and g_{OC}^{-1}. A linear regression was fitted through the four latest production measurements to obtain daily CH_4 and CO_2 production rates over time.

Further, when expressing individual production rates as a share of the maximum production rate, the relative decrease in CH_4 production can be described (Treat et al. 2015). After log-transformation of the data, a linear regression (forced through zero) was fitted to obtain κ, the exponential decay rate of production rates following the maximum production rate. Further, this could be converted to a percentage decay rate per day (Equation 10).

$$decay \, [\% \, d^{-1}] = (1 - exp(\kappa)) * 100) \qquad \textit{Equation 10}$$

As described in chapter 2.3.2., the higher global warming potential (GWP) of methane on a 100-year timescale had to be taken into account when evaluating the climate forcing effect of the cumulative carbon release. As such, the observed methane production under anaerobic conditions was corrected for its higher climate forcing by expressing it in CO_2 equivalents by multiplying the CH_4 concentration by 28 to assess the climate forcing effect (CFE) of the produced greenhouse gases (IPCC 2013) (Equation 11).

$$Climate \, Forcing \, Effect \left[\frac{mg \, CO_2\text{-}C \, eq}{g_{OC}}\right] = 1 * c_{CO2} + 28 * c_{CH4} \qquad \textit{Equation 11}$$

c_{CO2}	[mg CO_2-C g_{dw}^{-1}]	concentration of CO_2 produced in the incubation vial
c_{CH4}	[mg CH_4-C g_{dw}^{-1}]	concentration of CH_4 produced in the incubation vial

The relative climate forcing as introduced by Schuur et al. (2008) further aims to compare the climate impact of cumulative greenhouse gas production in aerobic and anaerobic conditions of an incubation experiment and hence the prevailing oxic state of the source environment. It was determined by dividing the cumulative aerobic CO_2 production by the cumulative anaerobic CO_2 and CH_4 production expressed in CO_2 equivalents (all else being equal) (Equation 12).

$$Relative \, climate \, forcing = \frac{cumulative \, production \, of \, aerobic \, CO_2}{cumulative \, production \, of \, anaerobic \, CO_2 + (28 * cumulative \, production \, of \, anaerobic \, CH_4)}$$

$$\textit{Equation 12}$$

Here, values < 1 indicated a higher total climate impact of the greenhouse gas release in anaerobic settings compared to aerobic settings and vice versa (Schuur et al. 2008).

4.2.8. Biomarker analysis

The organic matter composition and degradation of the permafrost sediment samples was studied in more detail by analysing the lipid composition in a comprehensive biomarker analysis. Biomarkers are stable structures that can be unambiguously linked with biological precursor compounds, and are therefore used to ascertain origin and type of organic matter (Gagosian et al. 1981; Otto & Simpson 2005; Amelung et al. 2008). Even tough posing a minor share of OM, lipids in soils have been described to be highly resistant to biodegradation (Dinel et al. 1990) and have been established as viable biomarkers. In this study, we focused on the analysis of *n*-alkanes, *n*-alkanols, and *n*-fatty acids. These compounds represent aliphatic side chains in immature organic matter that were previously covalently linked to the complex organic matrix via ether or ester bonds (Glombitza et al. 2009). Lipids are effectively insoluble in water but are extractable by solvents that dissolve fats (Killops & Killops 2013). Biomarker analysis was performed following the methods outlined in Schulte et al. (2000) and Strauss et al. (2015). For the analysis, we obtained four samples from the selected sampling depths (see chapter 4.2.) in both sediment cores. We conducted biomarker analysis on the original substrate that was left over from the preparation of the incubation vials. Additionally, we conducted biomarker analysis on the sediment from the incubation vials after three months of aerobic and anaerobic incubation respectively.

Firstly, 0.84 to 4.17 g of freeze-dried sample material were weighed into extraction cells, and an ASE 200 extractor (Dionex) was used for the extraction process (Figure 16). For the accelerated solvent extractions (ASE), a mixture of dichloromethane and methanol (DCM/MeOH) in a ratio of 99:1 (v/v) was used as the extraction solvent. The extraction process began with a gradual temperature increase to 75 °C over a span of 5 min. The temperature was maintained at this level for 20 min, while the pressure was held constant at 5 MPa. Following extraction, the dissolved compounds were concentrated using a TurboVap® closed-cell evaporation system (Biotage) or a Rocket Synergy vacuum evaporator (Genevac SP Scientific), operating at 42 °C. Further evaporation was carried out using nitrogen gas (N_2).

Figure 16: The ASE 200 extractor (Dionex).

To enable relative quantification of the results, internal standards were added to the samples. These internal standards had a specific concentration of 100 µg/ml and were introduced into the samples in varying volumes, ranging from 80 to 500 µl depending on their TOC content (Table 4). 5α-androstane was used as the internal standard for the aliphatic fraction, ethylpyrene for the aromatic fraction, 5α-androstan-17-on for the nitrogen-, sulfur, and oxygen- (NSO-) containing compounds, and erucic acid for NSO fatty acid fraction.

Table 4: TOC dependent internal standard addition to biomarker sample extracts.

Sample TOC content	Internal standard addition
[wt. %]	[µg]
< 10	8
10 – 25	20
> 25	50

Subsequently, the samples were separated into unpolar (aliphatic and aromatic hydrocarbons) and polar (hetero (NSO-) compounds) fractions using medium-pressure liquid chromatography (MPLC) (Radke et al. 1980) (Figure 17).

Figure 17: The Medium-pressure liquid chromatography (MPLC).

Samples were dissolved in min 500 µl n-hexane before 300 µl of the extracts were injected into the MPLC system. Some samples required a higher dilution factor to keep the amount of injected sample below 50 mg. In the MPLC system, the samples were initially passed through a pre-column filled with silica gel, where the aliphatic and aromatic fractions were eluted using n-hexane. The polar NSO fraction remained on the column and was subsequently eluted with dichloromethane (DCM). The NSO fraction was further split into an alcohol and a fatty acid fraction. To recover the alcohols, the NSO sample, dissolved in 1 ml 99:1 vol. % DCM:Methanol, was lead through a KOH-impregnated silica gel column using 120 ml of DCM. Thereafter, the addition of 50 ml of formic acid allowed the elution of fatty acids using another 100 ml of DCM.

The lipids were identified and quantified using gas chromatography and mass spectrometry (GC-MS) via a coupled Trace GC Ultra and DSQ MS system (both Thermo Electron Corporation) (Figure 18). Prior to GC-MS analysis, *n*-fatty acids were methylated with diazomethane, and *n*-alkanols were silylated with N-methyl-N-trimethylsilyltrifluoroacetamide (MSTFA). After samples were injected in splitless mode, they were vaporized by heating from 50 °C to 300 °C with a defined heating rate of 10 °C s^{-1}, and held at 300 °C for 10 minutes. The mix of the vaporized sample and the carrier gas helium (1 ml min^{-1}) was then led through a BPX5 (SGE) capillary column. For the measurement, the GC oven was heated after 1 min of isothermal holding at its initial temperature of 50 °C to 310 °C with a heating rate of 3 °C s^{-1}, followed by an isothermal holding time of 30 minutes. The GC analysis was followed by compound analysis in the coupled MS. Full-scan mass spectra were obtained from the MS was operated in electron impact ionization mode at 230 °C. Homologue compounds of *n*-alkanes, *n*-fatty acids and *n*-alkanols were identified and quantified using the software Xcalibur™ (Thermo Fisher Scientific).

Figure 18: The Coupled Trace GC Ultra and DSQ MS (Thermo Fisher Corporation).

Total lipid concentrations (C$_{tot}$) were calculated as the sum of the whole range of detected *n*-alkane homologues C$_{11}$ - C$_{35}$ resp. for the range from C$_{12}$ to C$_{32}$ for *n*-alkanols and *n*-fatty acids. All total concentrations were reported in µg g$_{TOC}$$^{-1}$. Apart from total lipid concentrations, the obtained GS-MS data could be used to calculate various biomarker concentration ratios. A multitude of reliable biomarker indices have been proposed to reveal the source of OM and its degradation more precisely by depicting prominent patterns and ratios in the biomarker concentrations.

The fundamentals of *n*-alkane, *n*-alkanol and *n*-fatty acid biomarker indices are the predominance of specific chain lengths in different organic matter types. The occurrence of shorter chain lengths (< C$_{20}$) in *n*-alkanes and *n*-alkanols hint to an origin of from bacteria, fungi, plankton and aquatic algae (Weete 1976; Harwood & Russell 1984; Otto & Simpson 2005), whereas longer chain *n*-alkanes (> C$_{20}$) indicate an input from terrestrial vascular plant waxes (Barnes & Barnes 1978; Cranwell 1984;

Kolattukudy & Espelie 1989) (Figure 19). More precise source correlations have been summarized by Zheng et al. (2007); Amelung et al. (2008) and Schaefer et al. (2016) and can be found in Appendix 3.

Figure 19: Predominating n-alkane chain lengths in different organisms, modified after Killops & Killops (2009), from Strauss et al. (2015).

Hence, established biomarker indices include the average chain length (ACL), that can be applied to *n*-alkanes, *n*-alkanols and *n*-fatty acids (Boreddy et al. 2018) (Table 5, Equation 13, Equation 18, Equation 22). Further common biomarker indices relying on the presence and ratio of certain chain-length *n*-alkanes are the aquatic organic matter proxy (P_{aq}) (Ficken et al. 2000) (Equation 14), reflecting the relative proportions of waxy hydrocarbons derived from emergent and submerged macrophytes to total hydrocarbons. Further, the P_{wax} index (Zheng et al. 2007) (Equation 15), reflects the relative proportion of waxy hydrocarbons derived from terrestrial plants to total hydrocarbons.

n-Fatty acids and *n*-alkanols typically show a pronounced even-over-odd predominance (EOPD) (Rieley et al. 1991; Zheng et al. 2007) (Equation 19). In the decarboxylation process of *n*-fatty acids to *n*-alkanes, one C is split off, thereby creating the characteristic odd-numbered *n*-alkane chain-lengths (Killops & Killops 2013). Hence, *n*-alkanes typically show a distinct odd-over even predominance in carbon chain lengths. This is described by both, the odd-over-even predominance (OEPD / EOPD) (Eglinton & Hamilton 1967) (Equation 16), as well as the refined carbon preference index (CPI) (Bray & Evans 1961; Marzi et al. 1993) (Equation 17). *n*-Alkanes from epicuticular waxes of vascular plants reportedly give high CPI values (> 5), whereas CPI values from bacteria and algae can be significantly lower (≈ 1) (Gelpi et al. 1970; Cranwell 1981, 1987; Andersson & Meyers 2012). As more abundant homologues of *n*-alkanes, *n*-alkanols and *n*-fatty acids are preferentially decomposed by biota, the gap of odd- and even-numbered homologues is decreasing with progressing decomposition, indicated by lower OEPD and CPI (Glombitza et al. 2009; Andersson & Meyers 2012). As such, OEPD and CPI are commonly used as biomarkers for the degradation of organic matter. Poynter (1989) introduced the higher plant alcohol index (HPA), reflecting the share of long-chain *n*-alkanols over the sum of major odd alkanes and even alcohols (Equation 21). Similarly, Strauss et al. (2015) developed the higher plant patty acid index (HPFA), reflecting the share of long-chain *n*-fatty acids over the sum of major odd alkanes and even fatty acids (Equation 23).

Table 5: Selected lipid biomarker indices: n-alkanes.

Biomarker index	Equation	
Average Chain Length	$$ACL_{n-alkanes} = \frac{\sum i * C_i}{\sum C_i}$$ i = carbon number (index), C = concentration	*Equation 13*
Aquatic organic matter proxy	$$P_{aq} = \frac{C_{23} + C_{25}}{C_{23} + C_{25} + C_{29} + C_{31}}$$	*Equation 14*
P$_{wax}$	$$P_{wax} = \frac{C_{27} + C_{29} + C_{31}}{C_{23} + C_{25} + C_{27} + C_{29} + C_{31}}$$	*Equation 15*
Odd-over-even predominance	$$OEPD = \frac{\sum odd\ C_{27} - C_{33}}{\sum even\ C_{26} - C_{32}}$$	*Equation 16*
Carbon preference index	$CPI_{n-alkanes}$ $$= \frac{(C_{23} + C_{25} + C_{27} + C_{29} + C_{31}) + (C_{25} + C_{27} + C_{29} + C_{31} + C_{33})}{2 * (C_{24} + C_{26} + C_{28} + C_{30} + C_{32})}$$	*Equation 17*

Table 6: Selected lipid biomarker indices: n-alkanols.

Biomarker index	Equation	
Average Chain Length	$$ACL_{n-alkanols} = \frac{\sum i * C_i}{\sum C_i}$$ i = carbon number (index), C = concentration	*Equation 18*
EOPD	$$EOPD = \frac{\sum even\ C_{12} - C_{32}}{\sum odd\ C_{13} - C_{33}}$$	*Equation 19*
Carbon Preference Index	$CPI_{n-alkanols}$ $$= \frac{(C_{20} + C_{22} + C_{24} + C_{26} + C_{28}) + (C_{22} + C_{24} + C_{26} + C_{28} + C_{30})}{2 * (C_{21} + C_{23} + C_{25} + C_{27} + C_{29})}$$	*Equation 20*
Higher Plant Alcohol Index	$$HPA = \frac{(C_{24} + C_{26} + C_{28})_{alkanol}}{(C_{24} + C_{26} + C_{28})_{alkanol} + (C_{25} + C_{27} + C_{29})_{alkane}}$$	*Equation 21*

Table 7: Selected lipid biomarker indices: n-fatty acids.

Biomarker index	Equation	
Average Chain Length	$$ACL = \frac{\sum i * C_i}{\sum C_i}$$ i = carbon number (index), C = concentration	*Equation 22*
Higher Plant Fatty Acid Index	$HPFA$ $$= \frac{(C_{24} + C_{26} + C_{28})_{n\text{-}fatty\ acids}}{(C_{24} + C_{26} + C_{28})_{n\text{-}fatty\ acids} + (C_{27} + C_{29} + C_{31})_{n\text{-}alkanes}}$$	*Equation 23*

4.3. Statistical analyses

We performed statistical analyses to test correlations and interdependencies between the GHG production characteristics, geochemical parameters and biomarker indices using R version 4.2.2 (R development team 2022).

4.3.1. Pearson's correlation coefficients

Pearson's correlation coefficients (r) were explored to assess associations between variables in a comprehensive correlation analysis. This statistical measure examines the strength and direction of a linear relationship between two variables. The determined correlation coefficient 'r' varies between - 1 (perfect negative correlation) and 1 (perfect positive correlation), with 0 denoting no linear correlation (Table 8).

Table 8: Strength of relationships of Pearson's correlation coefficients

Absolute value of r	Strength of relationship
r < 0.3	None or very weak
0.3 < r < 0.5	Weak
0.5 < r < 0.7	Moderate
r > 0.7	Strong

A probability value (p-value) of < 0.05 (assuming data normality) indicates strong evidence of a significant correlation, providing assurance that the observed correlation is not due to sampling variability. Notably, correlation does not imply causation, and the two tested variables may not necessarily influence each other.

4.3.2. Paired t-test

To answer the first research objective, assessing if geochemical and biomarker parameters have significantly changed during the 90-day incubation experiments, we conducted paired t-tests on the t_0 and t_{90} measurements. The paired t-test examines the mean difference between the paired observations, with a low p-value suggesting that the observed difference is unlikely to be due to random chance alone (Hsu & Lachenbruch 2005; Kim 2015). Consequently, for parameters displaying a p-value < 0.05 or < 0.1, it can be inferred that there is a statistically significant difference between the t_0 and t_{90} measurements of the parameter.

Prior to the analysis, Shapiro-Wilk tests were performed to verify that the parameter changes within the incubation period were normally distributed (indicated by p-values exceeding the significance level of 0.05) (Kim 2015), which was visually confirmed using Q-Q plots. Additionally, the effect size (Cohen's d) for the paired t-test was calculated to quantify the magnitude of the difference between the two paired groups (Cohen 1988) (Equation 24). A larger Cohen's d value indicates a larger effect size. The original classification defined a small effect size as d = 0.2, a medium effect size as d = 0.5,

and a large effect size as d = 0.8 (Cohen 1988), although these values are not strict thresholds and can vary depending on the field of study (Gignac & Szodorai 2016).

$$d = \frac{\bar{x}_1 - \bar{x}_2}{2}$$ *Equation 24*

$\bar{x}_1$ mean group 1
$\bar{x}_2$ mean group 2
s   standard deviation

4.3.3. Analysis of variance

Analysis of variance (ANOVA) can provide valuable insights into the complex relationships among multiple categorical factors and a continuous outcome variable. It is commonly used in experimental research to assess the combined impact of different treatments or conditions, or categorical variables, on a particular outcome. In this study, one-way ANOVAs were conducted to examine whether the categorical classes soil type or the permafrost thermal regime are predictors of Greenhouse Gas release under both aerobic and anaerobic conditions, part of the second research objective (Table 9).

Table 9: Categorical factors tested in one-way ANOVAs

Categorical factor	Sediment Type	Permafrost Thermal Regime
categories	Organic	Active layer
	Mineral	Transition layer
	Cryoturbated	perennial permafrost

Assumptions of ANOVA analyses include independence of observations, normality, and homogeneity of variances that have to be tested first (Ståhle & Wold 1989). Normality was assessed using the Shapiro-Wilk test (Shapiro & Wilk 1965) and visually inspected via a Q-Q plot (D'Agostino 1986), while homogeneity of variances was examined using Bartlett's tests for each combination (Bartlett 1936; Arsham & Lovric 2011). Even when passing the tests, it is essential to interpret the results of the tests cautiously due to the small sample size in our study.

5. Results

5.1. Bulk geochemical parameters

Laboratory analyses revealed sedimentological and geochemical properties of the two permafrost sediment cores YC19-DTLB-7 and YC19-DTLB-8. A continuous record throughout the total core depth could be provided for the total organic carbon (TOC) and total nitrogen (TN) contents as well as ice contents. From these parameters, lithological units of peat, silt, and cryoturbated layers were defined in the cores. They correspond to terrestrial (peat) and lacustrine (silt) depositional environments of sediment. The last lake drainage event was marked by the uppermost silt – peat interface, located at 21 cm depth in YC19-DTLB-7 and at 43 cm depth in YC19-DTLB-8. The samples YC19-DTLB-7 AL1 and YC19-DTLB-8 AL2 were taken right above that interface to reflect the pioneer vegetation assembling in the freshly drained lake basin. YC19-DTLB-8 AL1 is the only sample of a more mature peaty soil.

All eight samples were in the acidic range, with the peat samples exhibiting more acidic pH values (4.59 – 5.06) than the silt samples (6.23 – 6.50) (Figure 20a & Figure 21a). The cryoturbated sample YC19-DTLB-8 TL showed an intermediate pH value of 5.43. In the absence of saltwater intrusion into the DLBs, the electrical conductivity (eC) of pore water was low (62.4 – 172 µS/cm) and appeared to be increasing with depth (Figure 20b & Figure 21b). Not enough pore water could be obtained from sample YC19-DTLB-7 AL1 for eC analysis. The drained lake basins showed very moist sediments, revealed by high ice contents of > 80 wt. % in the top layer peat and 39.31 – 63.57 wt. % in silts (Figure 20c & Figure 21c). The peat samples just above the uppermost peat – silt interface showed very high and highly similar gravimetric ice contents of 83.65 resp. 83.68 wt. %. Gravimetric ice content was even higher in established peat sample YC19-DTLB-8 AL1 (91.74 wt. %).

Silt was the dominant grain size present in the sediment cores, making up ~ 75 vol. % in YC19-DTLB-7 and ~ 80 vol. % in YC19-DTLB-8 of the mineral fraction, followed by clay contributing ~ 15 vol. % of the sediment composition (Figure 20e & Figure 21e). The mean grain size was consistent throughout the sediment core, fluctuating in a narrow range from 8.76 – 10.94 µm in YC19-DTLB-7 and 5.98 – 11.93 µm in YC19-DTLB-8. Pure peat lithologies were excluded from grain size analysis.

Peat and silt were easily distinguishable by their TOC contents, which are > 40 wt. % in peat samples and < 10 wt. % in silt samples (Figure 20f & Figure 21f). Intervals of fluctuating TOC values characterize the cryoturbated samples. Contributions of TIC, originating from calcium carbonate ($CaCO_3$) in arctic soils, were < 0.1 % in all samples. Peats were further characterized by higher TN values of 1.78 – 2.30 wt. % compared to silt samples with only 0.35 – 0.75 wt. % (Figure 20g & Figure 21g). The ratio of organic carbon and nitrogen in the sediment is reflected in the C:N ratio, and ranged from 13.31 in YC19-DTLB-7 AL2 to 24.14 in YC19-DTLB-7 AL1 (Figure 20h & Figure 21h). The

carbon isotopic signature of δ¹³C values was very consistent throughout the two cores, ranging only from - 27.69 to – 28.48 ‰ vs. VPDB (Figure 20i & Figure 21i).

A radiocarbon age of 2 989 cal a BP was determined at a core depth of 132 - 134.5 cm in YC19-DTLB-7 (Figure 20d). Sediment core YC19-DTLB-8 covers a longer sediment accumulation period, as it exhibited a calibrated radiocarbon age of 8 105 cal a BP at 150 - 151.5 cm core depth (Figure 21d). Radiocarbon samples were taken above the peat-silt interface to estimate onset of terrestrial conditions in the basins. It was revealed that terrestrial conditions in DTLB-7 prevail for a longer time, with a corrected median radiocarbon age of the pioneer peat of 949 cal a BP compared to 600 cal a BP in DTLB-8. Further results of radiocarbon dating are provided in Appendix 4.
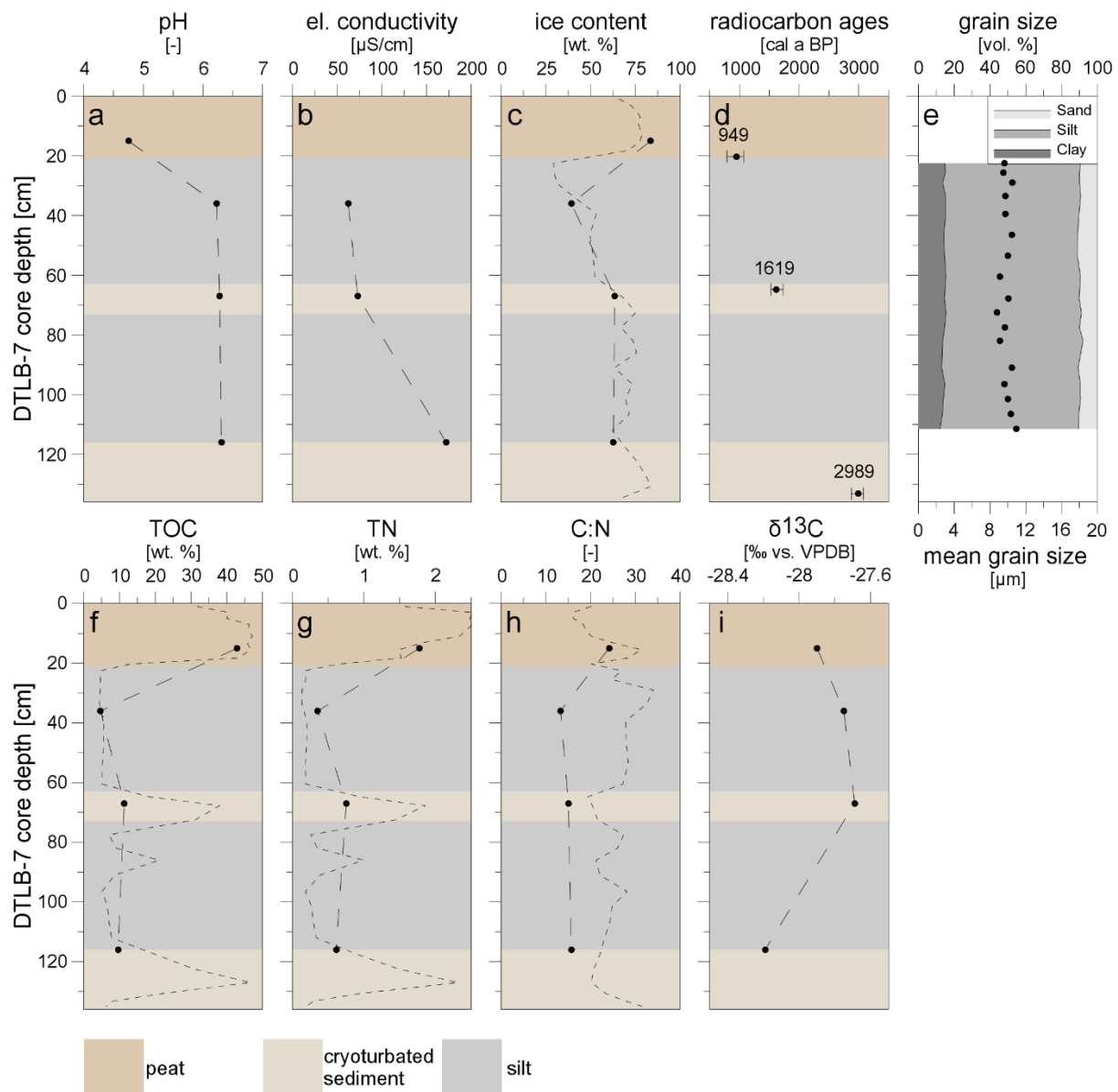
Figure 20: Records of selected sedimentological and biogeochemical parameters (a) pH, (b) eC, (c) gravimetric ice content, (d) ¹⁴C ages, (e) volumetric grain size distribution, (f) TOC, (g) TN, (h) C:N, and (i) δ¹³C of permafrost sediment core YC19-DTLB-7 -AL1, -AL2, -TL, and -PF. Continuous records can be provided for TOC, TN and C:N (dashed line). Note that depths of radiocarbon dating samples differ from geochemical analysis sampling depths.
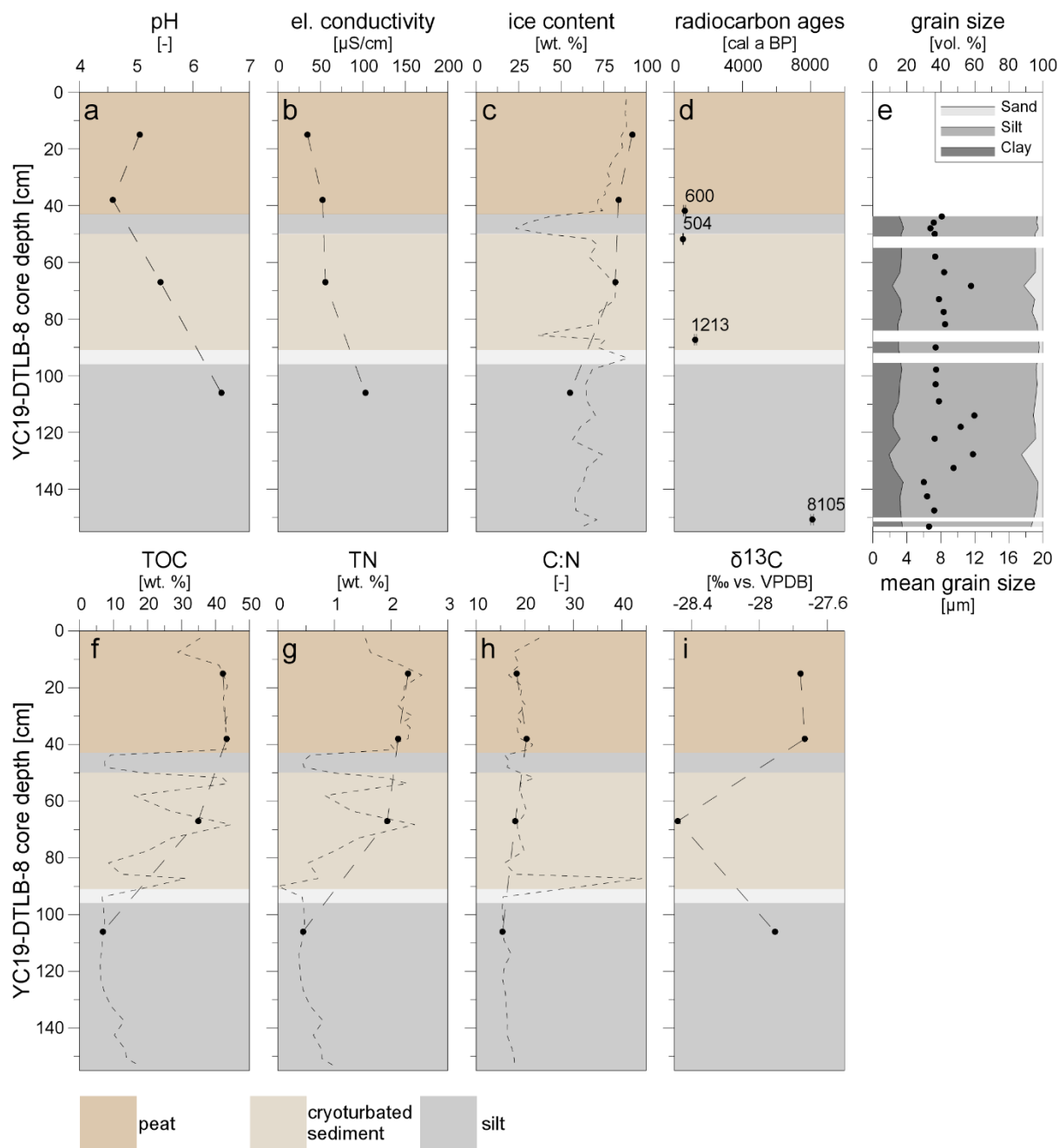
Figure 21: Records of selected sedimentological and biogeochemical parameters (a) pH, (b) eC, (c) gravimetric ice content, (d) ^{14}C ages, (e) volumetric grain size distribution, (f) TOC, (g) TN, (h) C:N, and (i) $\delta^{13}C$ of permafrost sediment core YC19-DTLB-8 -AL1, -AL2, -TL, and -PF. Continuous records can be provided for TOC, TN and C:N (dashed line). Note that depths of radiocarbon dating samples differ from geochemical analysis sampling depths.

The highly heterogenous lithology in the sediment cores could mask depth trends of these parameters in the cores, as observations are likely related to changes in sediment composition. In summary, geochemical analysis of both cores revealed similar features. Peaty organic layers were more moist, more acidic and exhibited higher TOC and TN values than silty mineral layers (Appendix 5).

5.2. Incubation experiments

5.2.1. Anaerobic incubation experiment

The cumulative CO_2 and CH_4 production per gram dry weight (g_{dw}) after 90 days of anaerobic incubation was highly variable and ranged from 0.01 ± 0.00 mg C g_{dw}^{-1} in YC19-DTLB-8 PF to 0.48 ± 0.01 mg C g_{dw}^{-1} in YC19-DTLB-8 AL1 (Figure 22, Appendix 6). Greenhouse gas production was dominated by methane in all samples except for the permafrost samples, where no significant methane production occurred so far. Production per g_{dw} was four times higher in peaty compared to silty samples within the active layer, and equal within the transition layer.
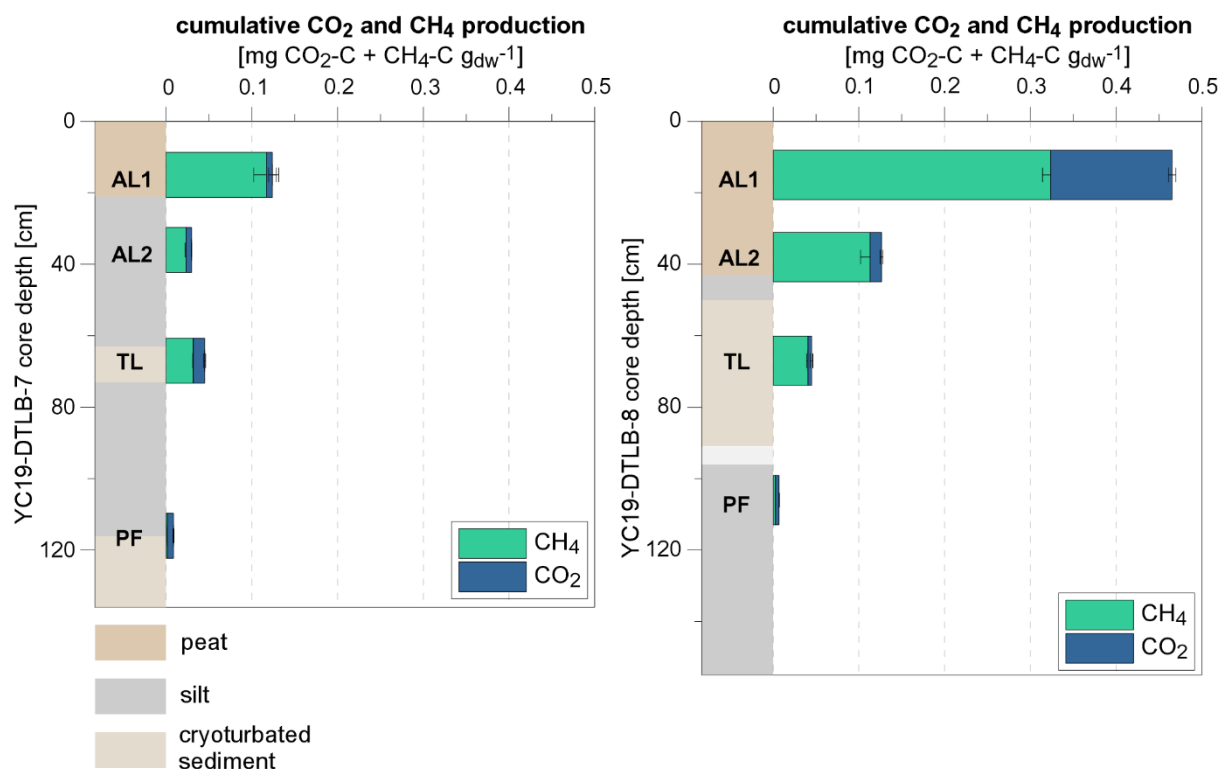
Figure 22: Cumulative greenhouse gas production (CO_2: blue, CH_4: green) per gram dry weight (g_{dw}) within the anaerobic incubation experiment (90 days, 4 °C, N_2 atmosphere) in YC19-DTLB-7 (left) and YC19-DTLB-8 (right).

The cumulative CH_4 production per g_{dw} was highly dependent on the organic carbon (OC) content in the sediment. Thus, the differences in organic carbon content in the heterogeneous sediment cores may mask trends. A normalization to gram organic carbon (g_{OC}) instead of gram soil removed that bias and enabled the assessment of the lability of the organic matter and turnover rates. Cumulative production per g_{OC} was highest in established peat sample YC19-DTLB-8 AL1 (1.14 ± 0.02 mg C g_{OC}^{-1}) (Figure 23, Appendix 6). The observed GHG production was similar in pioneer peat of YC19-DTLB-7 AL1 (0.29 ± 0.02 mg C g_{OC}^{-1}) and YC19-DTLB-8 AL2 (0.29 ± 0.02 mg C g_{OC}^{-1}). PF samples showed low CH_4 production over 90 days of anaerobic incubation.

By day 90 of anaerobic incubation, high shares of the total GHG production was constituted of methane (Figure 22 & Figure 23). It contributed ≥ 67.3 % of total GHG production in active and transition layer samples, but ≤ 38.7 % in permafrost samples.

Relatively high carbon conversion rates (% C_{ini}) in mineral samples are masked by low TOC contents when normalized to g_{dw}. This accounted for silty active layer sample YC19-DTLB-7 AL2, marking the second highest production per g_{OC} of the eight samples. Overall, low shares of the total organic carbon content of the samples were respired by microorganisms to CH_4 and CO_2 within the incubation experiment, equalling only 0.01 – 0.15 wt. % OC (Figure 23).

Figure 23: Cumulative greenhouse gas production (CO_2: blue, CH_4: green) per gram organic carbon (g_{OC}) within the anaerobic incubation experiment (90 days, 4 °C, N_2 atmosphere) in YC19-DTLB-7 (left) and YC19-DTLB-8 (right).

In all eight samples, CH_4 production started immediately with the start of the incubation experiment and production rates increased over time until reaching peak production rates after 14 – 34 days (Figure 24, Table 10, Appendix 6). The timing between the start of the incubation and maximum production rates will be referred to as 'lag time', as proposed by Treat et al. (2015). In the PF samples, the production rate peaks did not exceed the initial CH_4 production rate at the beginning of the experiment. Thus, the initial CH_4 production starting the experiment equivalated the highest production rate of the 90-day experiment (Table 10).

Maximum CH_4 production rates normalized to g_{OC} ranged from 1.34 ± 0.28 µg CH_4-C g_{OC}^{-1} d^{-1} in YC19-DTLB-7 PF at day 2 to 19.24 ± 0.45 µg CH_4-C g_{OC}^{-1} d^{-1} in mature peat layer YC19-DTLB-8 AL1 at day 17 (Appendix 6). After the production rate peak, production rates decreased for the remainder of the 90-day incubation period. The decline in production rates appeared to be steeper in mineral samples, resulting in narrower peaks as opposed to broader peaks in organic samples. These narrow peaks in production rates were also reflected in the maximum-to-mean production rate ratio, being high (> 4) in silty samples (DTLB-7 AL2, -PF, DTLB-8 PF) and lower in peaty samples (~ 2) (Appendix 6). Still, the entire peak was mapped in the incubation period of 90 days for both sediment types. The

mean daily production rates scaled with the cumulative production after 90 days and ranged from 0.16 ± 0.01 µg CH_4-C g_{OC}^{-1} d^{-1} in YC19-DTLB-7 PF to 8.54 ± 0.22 µg CH_4-C g_{OC}^{-1} d^{-1} in YC19-DTLB-8 AL1 (Appendix 6).
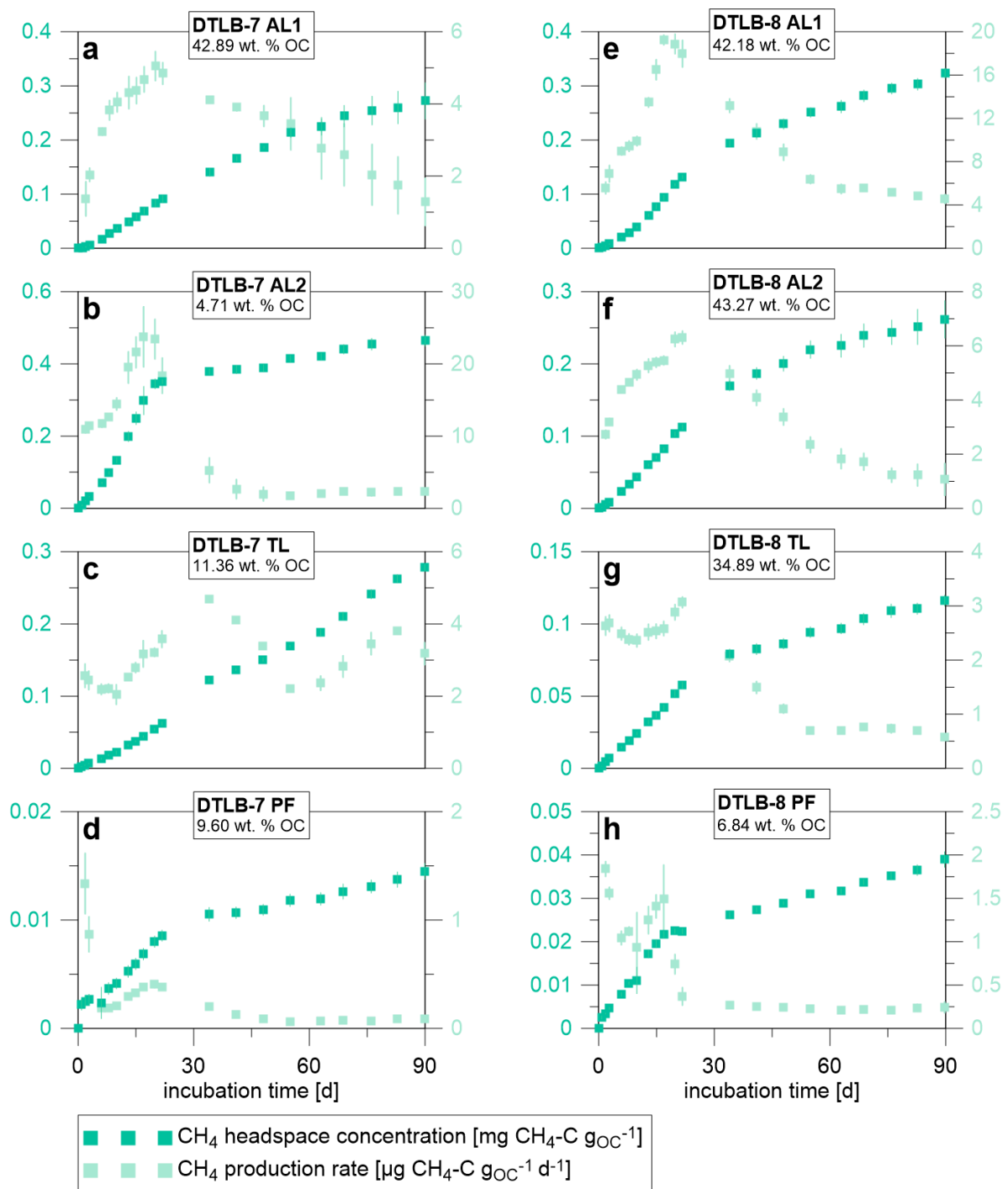
Figure 24: Mean CH_4 headspace concentration and corresponding mean CH_4 production rates during the anaerobic incubation experiment (90 days, 4 °C, N_2 atmosphere) in (a-d) YC19-DTLB-7 and (e-h) YC19-DTLB-8. Error bars show ranges of four replicates.

Further, when expressing individual production rates as a share of the maximum production rate, the relative decrease in CH_4 production can be described. After log-transformation of the data, a linear regression could be fitted to obtain κ, the exponential decay rate of production rates following the maximum production rate, as described in chapter 4.2.7.. Expressed in percentage decay rate per

day, the observed production rate decay was highest in mineral YC19-DTLB-7 AL2 (8.77 ± 1.46 % d^{-1}) and lowest in organic YC19-DTLB-7 AL1 (1.80 ± 1.02 % d^{-1}), in accordance with the observed maximum-to-mean production ratios (Table 10).

Table 10: Course of CH_4 production within anaerobic incubation experiment. Mean lag times of maximum CH_4 production and decay of CH_4 production rates following the maximum CH_4 production rate.

Sample ID	Soil type	Lag time of maximum CH_4 production rate [d]	CH_4 production rate decay [% d^{-1}]
YC19-DTLB-7 AL1	Organic	20 ± 0	1.80 ± 1.02
YC19-DTLB-7 AL2	Mineral	17 ± 2	8.77 ± 1.46
YC19-DTLB-7 TL	Cryoturbated	34 ± 18	3.05 ± 0.12
YC19-DTLB-7 PF	Mineral	20 ± 1	4.82 ± 0.36
YC19-DTLB-8 AL1	Organic	17 ± 1	2.16 ± 0.26
YC19-DTLB-8 AL2	Organic	22 ± 1	2.85 ± 0.36
YC19-DTLB-8 TL	Cryoturbated	22 ± 0	3.79 ± 0.42
YC19-DTLB-8 PF	Mineral	14 ± 2	5.59 ± 0.99

Mean production rates of CO_2 ranged from 0.14 ± 0.05 µg CO_2-C g_{OC}^{-1} d^{-1} in YC19-DTLB-8 TL to 4.30 ± 0.30 µg CO_2-C g_{OC}^{-1} d^{-1} in YC19-DTLB-8 AL1 (Figure 25, Appendix 6). Production rates were highly diverse within the 90-day incubation period. Maximum CO_2 production rates were measured within the first week of the experiment in all samples, reaching up to 139.33 ± 8.61 µg CO_2-C g_{OC}^{-1} d^{-1} in YC19-DTLB-7 AL2 and equalled up to the 278-fold of the mean production rate in sample YC19-DTLB-8 TL (Appendix 6). There was evidence for CO_2 consumption within the incubation vials as headspace concentrations declined for a period of time in each sample, implying negative production rates. Hence, the CO_2 concentration in the vial headspace was variable throughout the experiment. While peak concentrations ranged from 70.55 ± 7.17 mg CO_2-C g_{OC}^{-1} in YC19-DTLB-7 AL1 to 430.19 ± 52.99 µg CO_2-C g_{OC}^{-1} in YC19-DTLB-8 AL1, the headspace concentrations after 90 days were only 12.24 ± 4.27 µg CO_2-C g_{OC}^{-1} in DTLB-8 TL to 372.80 ± 15.17 µg CO_2-C g_{OC}^{-1} YC19-DTLB-8 AL1 (Appendix 6). Hence, we observed fluctuating CO_2 to CH_4 production ratios during 90 days of anaerobic incubation.
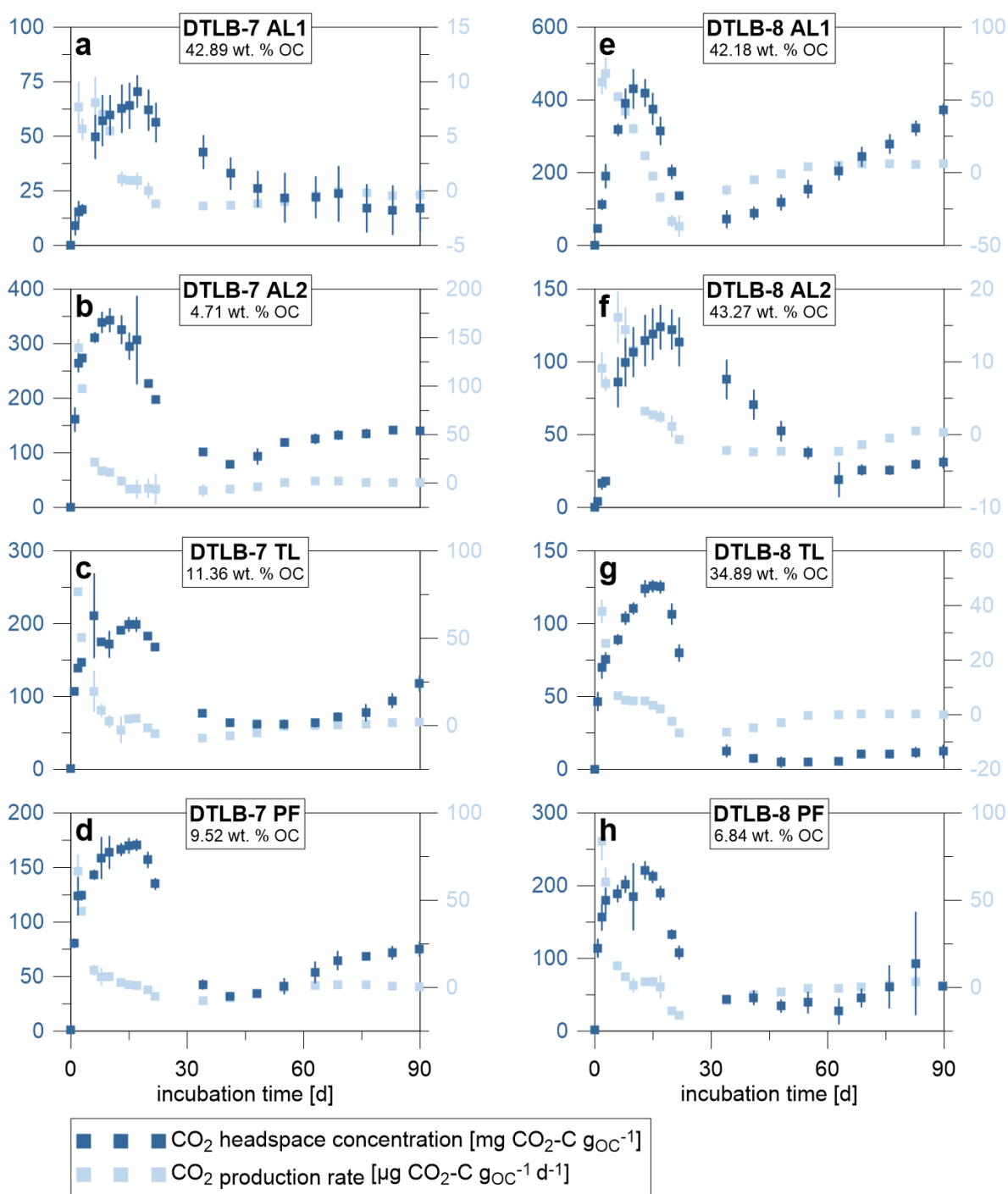
Figure 25: Mean CO_2 headspace concentration and corresponding mean CO_2 production rates during the anaerobic incubation experiment (90 days, 4 °C, N_2 atmosphere) in (a-d) YC19-DTLB-7 and (e-h) YC19-DTLB-8. Error bars show ranges of four replicates.

5.2.2. Aerobic incubation experiment

The GHG production per gram dry sediment (g_{dw}) in the aerobic incubation experiment is dominated by peaty samples due to their high OC contents (Figure 26). The observed cumulative production of CO_2 per g_{dw} is highest in YC19-DTLB-8 AL1 (4.91 ± 0.20 mg CO_2-C g_{dw}^{-1}) and lowest in silty YC19-DTLB-7 AL2 (0.41 ± 0.00 mg CO_2-C g_{dw}^{-1}) (Appendix 7). No significant CH_4 production was detected under aerobic incubation conditions.

43
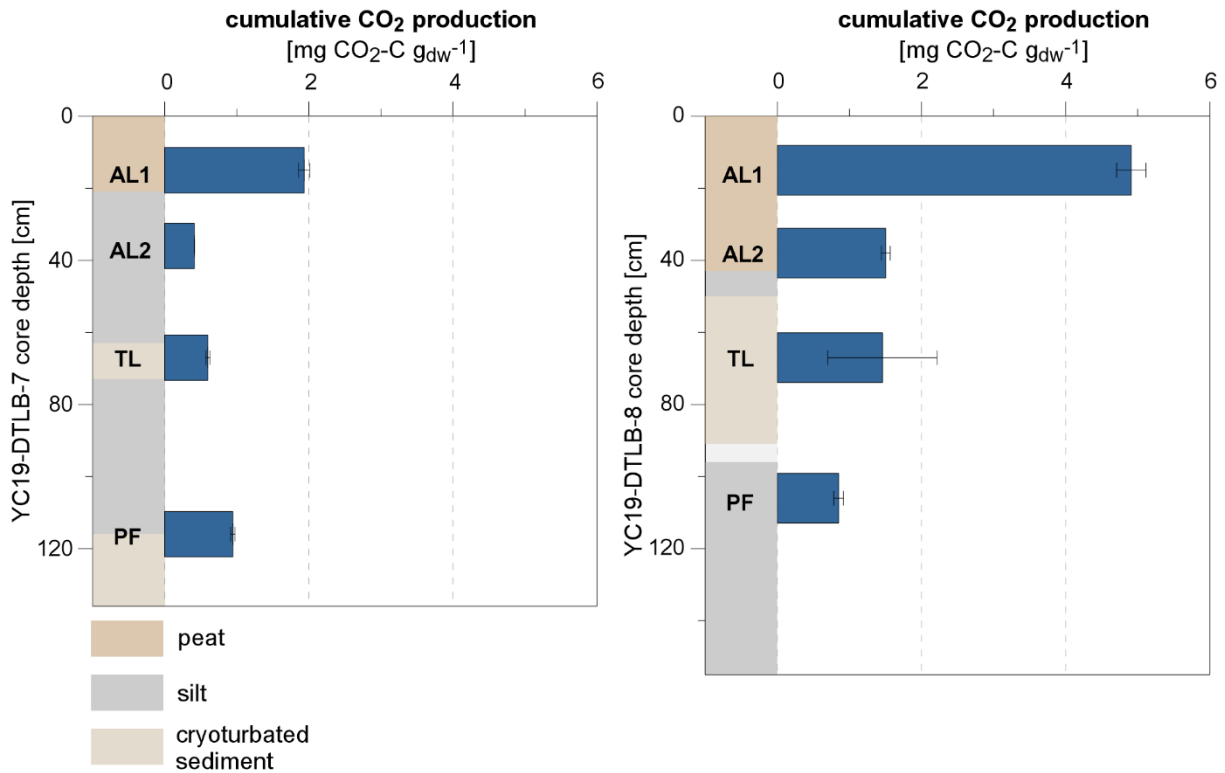
Figure 26: Cumulative greenhouse gas production (CO$_2$: blue, CH$_4$: green) per gram dry weight (g$_{dw}$) within the aerobic incubation experiment (90 days, 4 °C, synthetic air atmosphere) in YC19-DTLB-7 (left) and YC19-DTLB-8 (right).

The three mineral samples showed high CO$_2$ production per gram organic carbon (g$_{OC}$) in of 8.77 ± 0.07 to 12.45 ± 0.97 mg CO$_2$-C g$_{OC}^{-1}$ within the range observed in established peat sample YC19-DTLB-8 AL1 (11.64 ± 0.18 mg CO$_2$-C g$_{OC}^{-1}$) (Figure 27, Appendix 7).
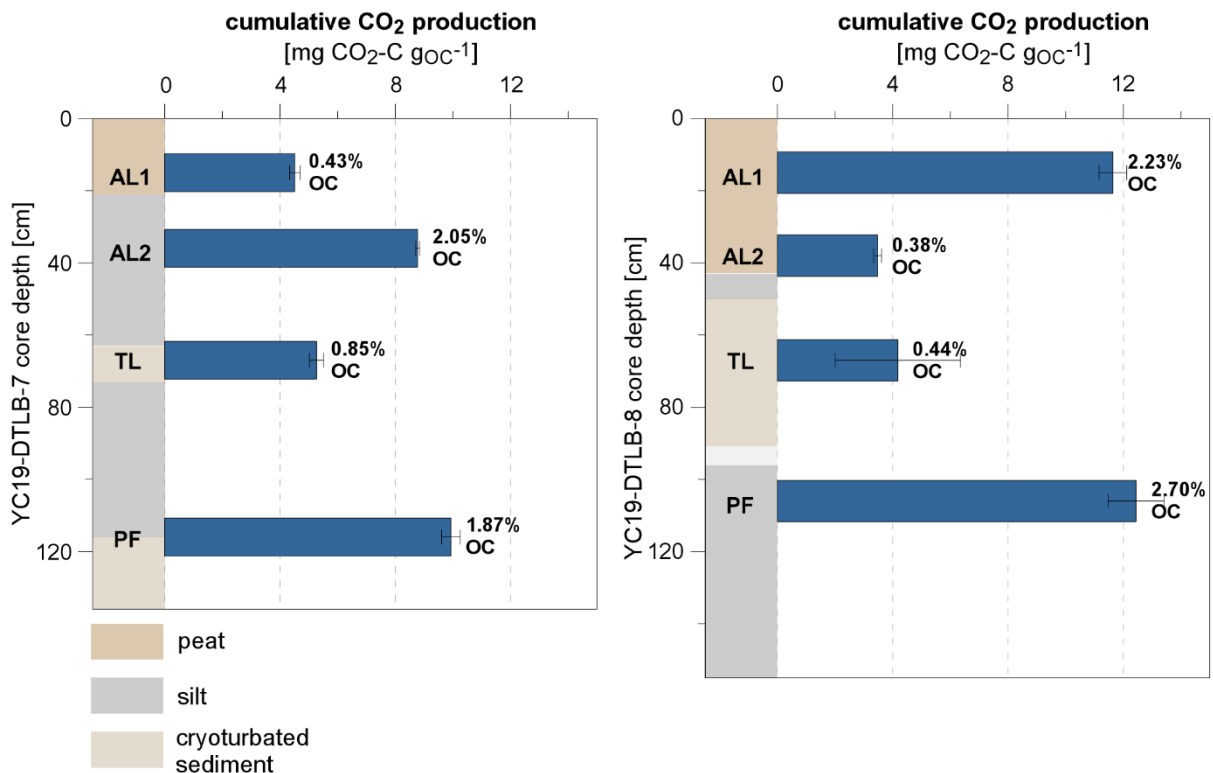
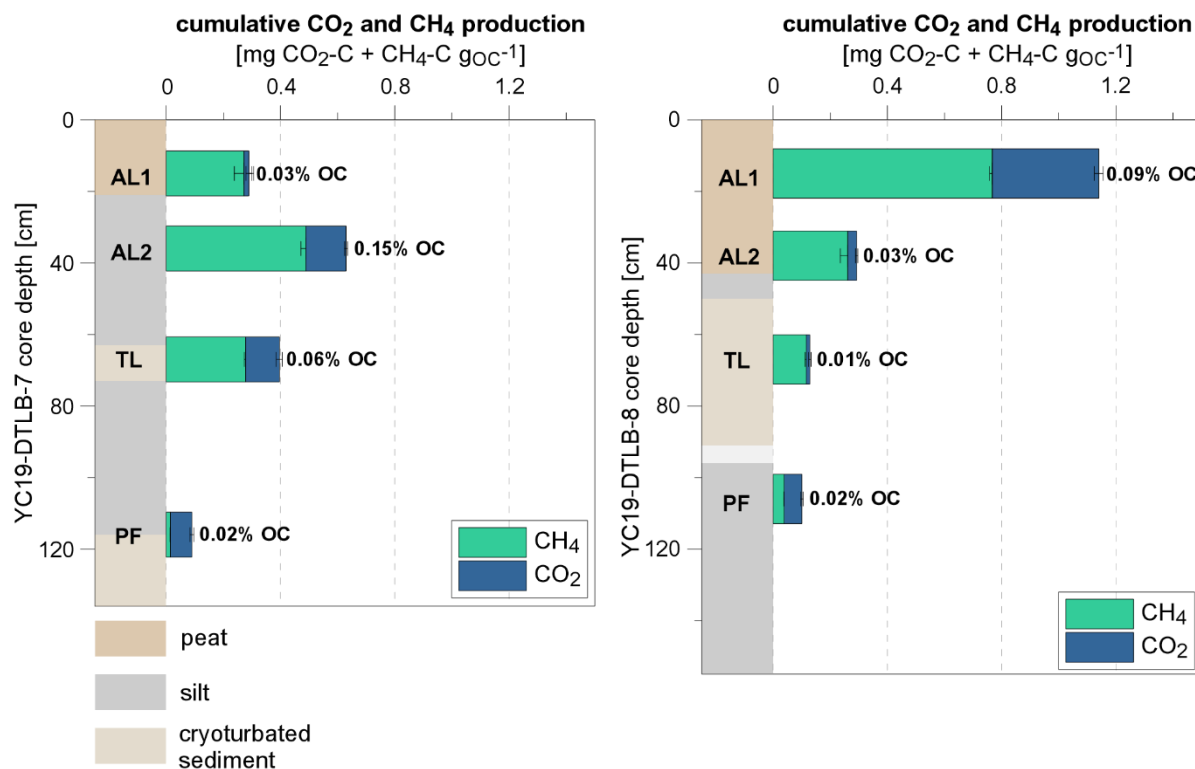*Figure 27: Cumulative greenhouse gas production (CO$_2$: blue, CH$_4$: green) per gram organic carbon (g$_{OC}$) within the aerobic incubation experiment (90 days, 4 °C, synthetic air atmosphere) in YC19-DTLB-7 (left) and YC19-DTLB-8 (right).*

There was considerably lower carbon turnover in the pioneer peat samples YC19-DTLB-7 AL1 (4.51 ± 0.18 mg CO_2-C g_{OC}^{-1}) and YC19-DTLB-8 AL2 (3.48 ± 0.18 mg CO_2-C g_{OC}^{-1}). Up to 2.7 % of the initial carbon content was mineralized within the short incubation period, highest in mineral samples and the established peat sample (Figure 27).

Corresponding mean CO_2 production rates ranged from 38.78 ± 1.56 µg CO_2-C g_{OC}^{-1} d^{-1} in YC19-DTLB-8 AL2 to 138.66 ± 10.85 µg CO_2-C g_{OC}^{-1} d^{-1} in YC19-DTLB-8 PF (Figure 28, Appendix 7). Initially high production rates at the start of the incubation decreased until reaching a second peak with maximum production rates of 88.82 ± 4.20 to 211.30 ± 11.89 µg CO_2-C g_{OC}^{-1} d^{-1} in all but two samples. The second peak was lower than the initial production rate in YC19-DTLB-8 PF and barely equalled initial production rate in YC19-DTLB-8 TL and YC19-DTLB-7 PF. The lag time for the second peak in production rates varied from 13 (YC19-DTLB-7 AL1) to 45 days (YC19-DTLB-8 PF) (Table 11, Appendix 7). Again, the ratio between maximum and mean production rate was highly variable. Similar to anaerobic CH_4 production, the maximum to mean production ratio was higher in silty samples (1.71 - 4.63) than in peaty samples (~ 2) (Appendix 7). This observation was also reflected in a steeper production rate decay after the maximum CO_2 production rate in mineral samples ($3.95 - 5.15$ % d^{-1}) compared to organic samples ($1.26 - 2.11$ % d^{-1}) (Table 11).

Table 11: Course of CO_2 production within aerobic incubation experiment. Mean lag times of maximum CO_2 production and decay of CO_2 production rates following maximum CO_2 production rates.

| Sample ID	Soil type	Lag time of maximum CO_2 production rate	CO_2 production rate decay
		[d]	[% d^{-1}]
YC19-DTLB-7 AL1	Organic	12 ± 1	1.26 ± 0.10
YC19-DTLB-7 AL2	Mineral	2 ± 0	3.30 ± 0.07
YC19-DTLB-7 TL	Cryoturbated	2 ± 0	4.60 ± 0.29
YC19-DTLB-7 PF	Mineral	42 ± 10	4.21 ± 0.21
YC19-DTLB-8 AL1	Organic	22 ± 0	1.57 ± 0.06
YC19-DTLB-8 AL2	Organic	15 ± 0	2.11 ± 0.12
YC19-DTLB-8 TL	Cryoturbated	44 ± 6	2.36 ± 0.97
YC19-DTLB-8 PF	Mineral	44 ± 2	5.15 ± 1.50
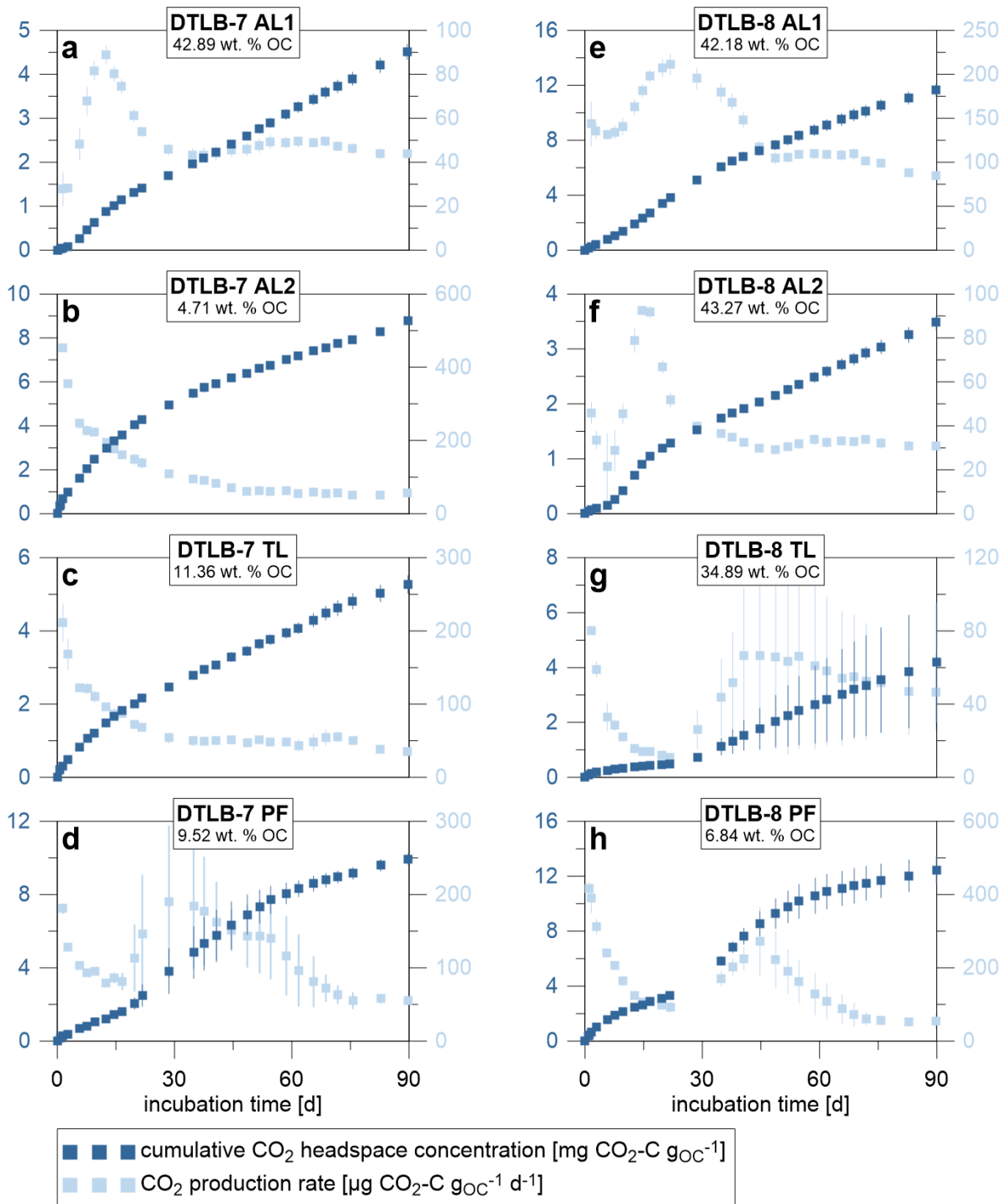
Figure 28: Mean cumulative CO₂ headspace concentration and corresponding mean CO₂ production rates during the aerobic incubation experiment (90 days, 4 °C, syn. air atmosphere) in (a-d) YC19-DTLB-7 and (e-h) YC19-DTLB-8. Error bars show ranges of four replicates.

5.2.3. Effects of incubation experiments on OM

When comparing greenhouse gas production between the anaerobic and aerobic incubation experiments, a significantly higher production could be reported for aerobic incubation conditions (Figure 29). Aerobic versus anaerobic GHG production ratios ranged from 10.2 – 32.6 in active and transition layer samples. This effect was even more pronounced in the permafrost layer samples (ae:an > 100).
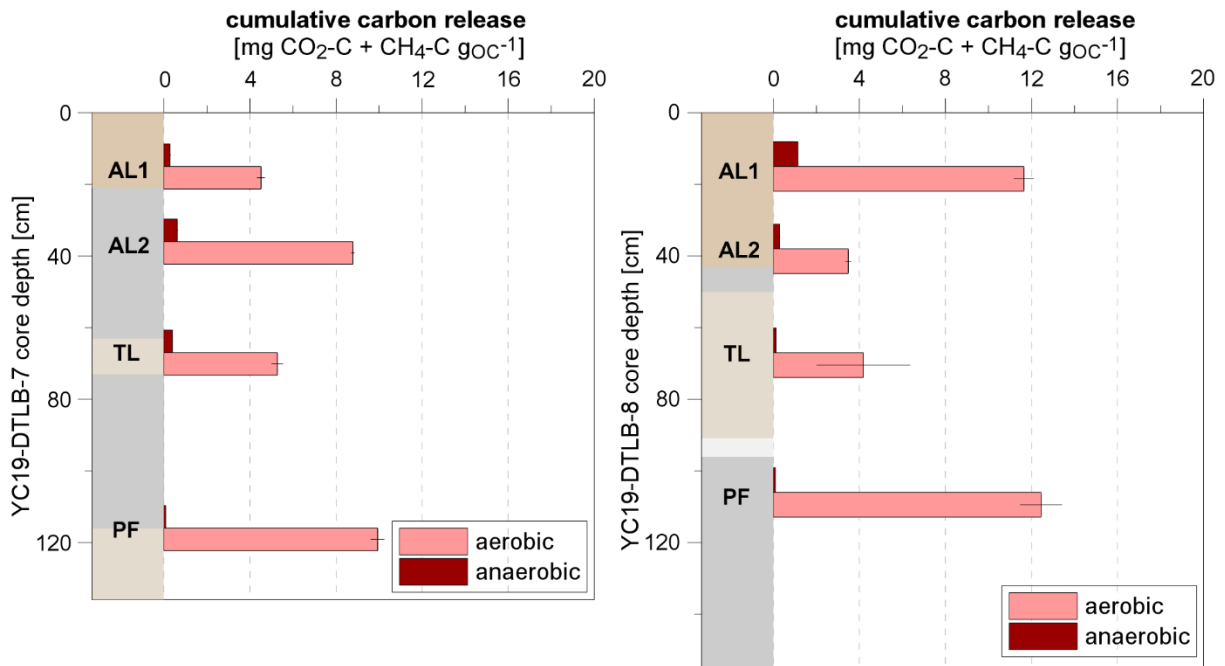
Figure 29: Cumulative greenhouse gas production in YC19-DTLB-7 (left) and YC19-DTLB-8 (right) after 90 days of anaerobic (red) and aerobic (pink) incubation conditions.

Contributions of CH_4 to the greenhouse gas production under anaerobic conditions are of high importance when assessing the climate forcing effect of GHG emissions concerning the different global warming potential of CO_2 and CH_4 (see chapter 2.3.2.). Because of the high contribution of highly climate-relevant CH_4 under anaerobic conditions, the climate forcing effect of the GHG production within the anaerobic incubation experiment exceeded the climate forcing effect of aerobic GHG production in all but the PF and one of the TL samples (Figure 30).
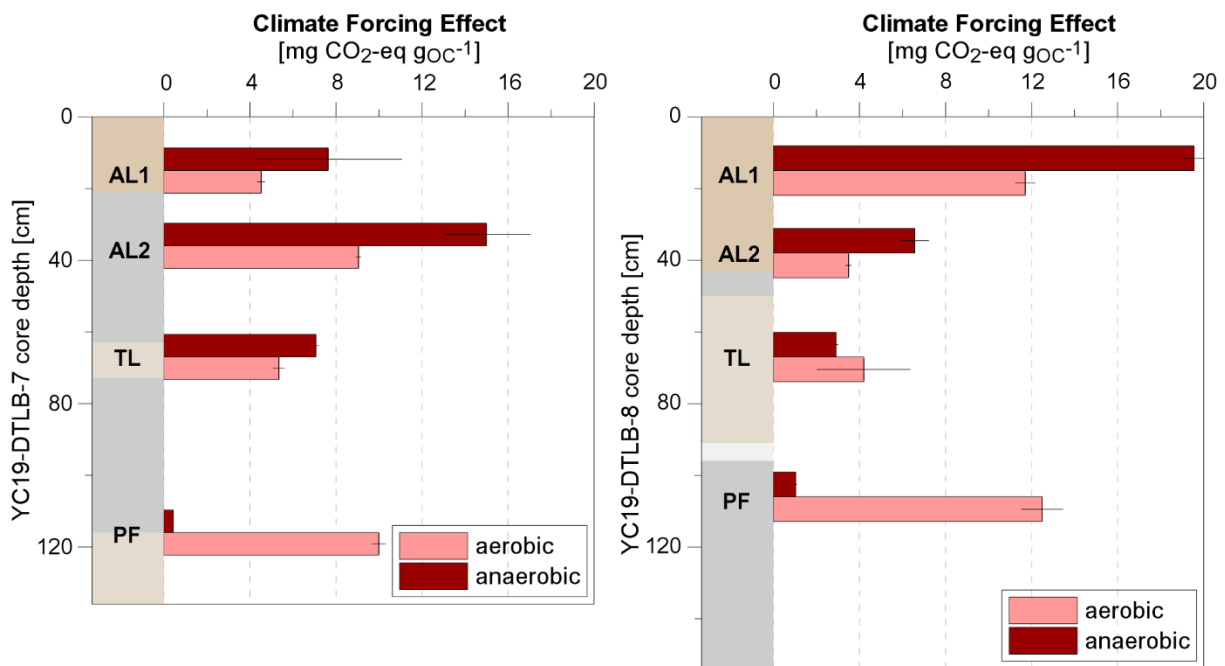
Figure 30: Climate forcing effect of cumulative greenhouse gas production in YC19-DTLB-7 (left) and YC19-DTLB-8 (right) under anaerobic (red) and aerobic (pink) incubation conditions.

47

Strikingly, the resulting relative climate forcing values were highly similar in active layer samples (0.53 – 0.60), higher in TL samples (0.75 – 1.43) and highest in PF samples (12.01 – 22.69), where the total GHG production under anaerobic conditions was generally very low.

5.2.4. Changes in geochemical parameters

We detected minor changes in geochemical parameters after 90 days of anaerobic and aerobic incubation at 4 °C, especially in the permafrost layers that experienced the lowest carbon conversion (Figure 31 & Figure 32). Greenhouse gas production was accompanied by a strong decrease in pH values in the sediment pore water. The extent of pH decline was higher under anaerobic incubation conditions and particularly in silty sediment samples, while peaty top layers remained nearly unaltered.
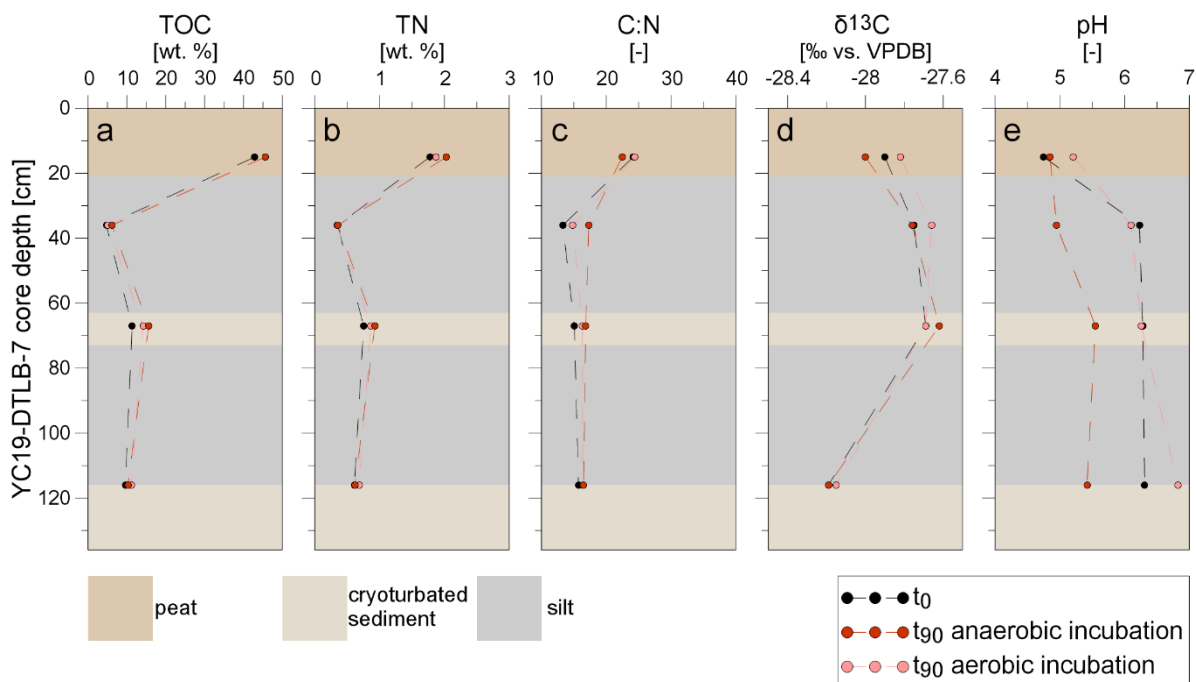
Figure 31: Changes of geochemical parameters within the aerobic and anaerobic incubation experiment. (a) TOC, (b) TN, (c) C:N, (d) $\delta^{13}C$, and (e) pH within permafrost sediment core YC19-DTLB-7 after 90 days of anaerobic (red) and aerobic (pink) incubation.
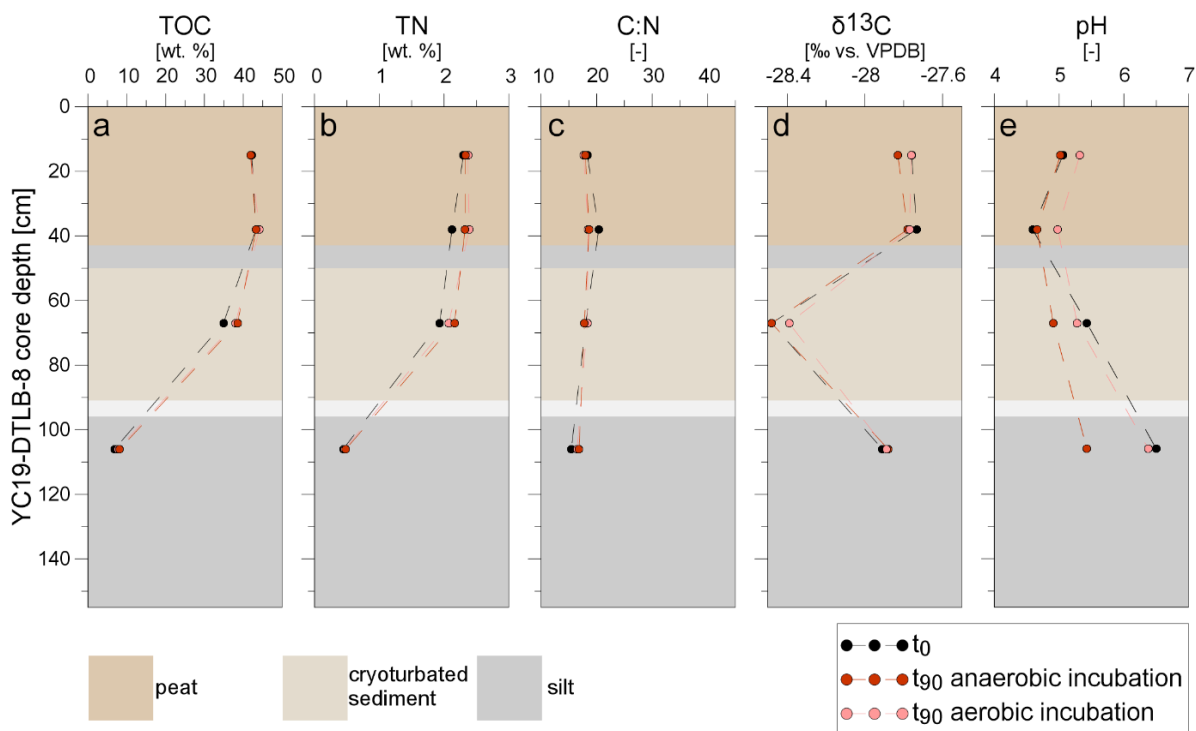
Figure 32: Changes in geochemical parameters within the aerobic and anaerobic incubation experiments. (a) TOC, (b) TN, (c) C:N, (d) $\delta^{13}C$, and (e) pH within permafrost sediment core YC19-DTLB-8 after 90 days of anaerobic (red) and aerobic (pink) incubation.

5.3. Biomarker analysis

Despite lipid biomarkers constituting only a minor fraction of the overall bulk organic matter in all samples, crucial information on the OMs sources, decomposition and hence paleoenvironmental conditions could be derived from their composition.

5.3.1. Saturated lipids

The total n-alkane concentration (C_{tot}) displayed high variations across the samples, ranging from 138.49 to 361.08 μg g_{OC}^{-1} (Figure 33 & Figure 34). The highest concentrations in both cores were observed just above the interface between peat and mineral soil.

The distribution patterns of n-alkanes exhibited similarities between the two cores. Analysed samples revealed the presence of carbon numbers spanning from 11 to 35, with distinct prominence of the odd-numbered long-chain n-alkanes n-C$_{27}$, n-C$_{29}$, and n-C$_{31}$. The unimodal distribution patterns shifted within the heterogeneous sediment core YC19-DTLB-7, the predominant homologue (c_{max}) being n-C$_{31}$ in the surface peat, to n-C$_{29}$ in silty AL2 and TL below, to n-C$_{27}$ in the permafrost sample. In DTLB-8, n-alkane concentrations peaked in n-C$_{27}$ in DTLB-8 AL1, -AL2 and -TL, while the permafrost sample peaked in n-C$_{31}$. The lower carbon number n-alkanes $< n$-C$_{20}$ made up less than 5 % of the total n-alkane concentration in peaty samples while up to 12 % in mineral samples.

We observed increases of up to 180 % in n-alkane concentration at t$_{90}$ of anaerobic and aerobic incubation in mineral samples. The total n-alkane concentration decreased in YC19-DTLB-7 TL as well as YC19-DTLB-8 AL1 and AL2.

49

While *n*-alkane concentrations severely changed with incubation, distribution patterns remained highly similar. Composition of newly formed or introduced *n*-alkanes apparently did not diverge from the already present lipids. The predominant *n*-alkane homologue remained the same in all samples of YC19-DTLB-8, while it shifted to lower (AL1 and PF) or higher carbon numbers (AL2) within the YC19-DTLB-7 sediment core.
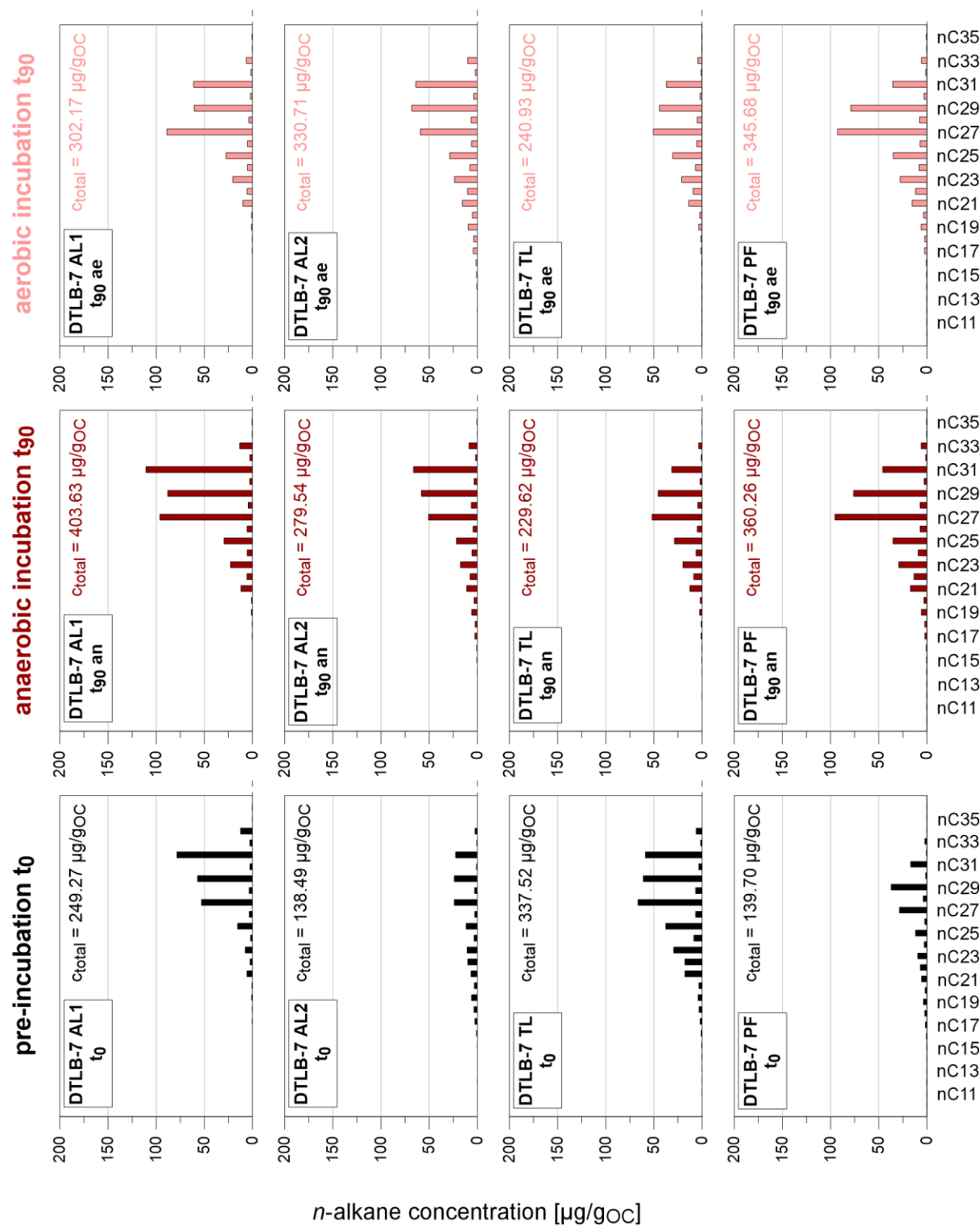
Figure 33: n-Alkane distribution patterns before and after incubation experiments in YC19-DTLB-7. Results of biomarker analysis at t_0 (black) and at t_{90} of anaerobic (red) and aerobic (pink) incubation.
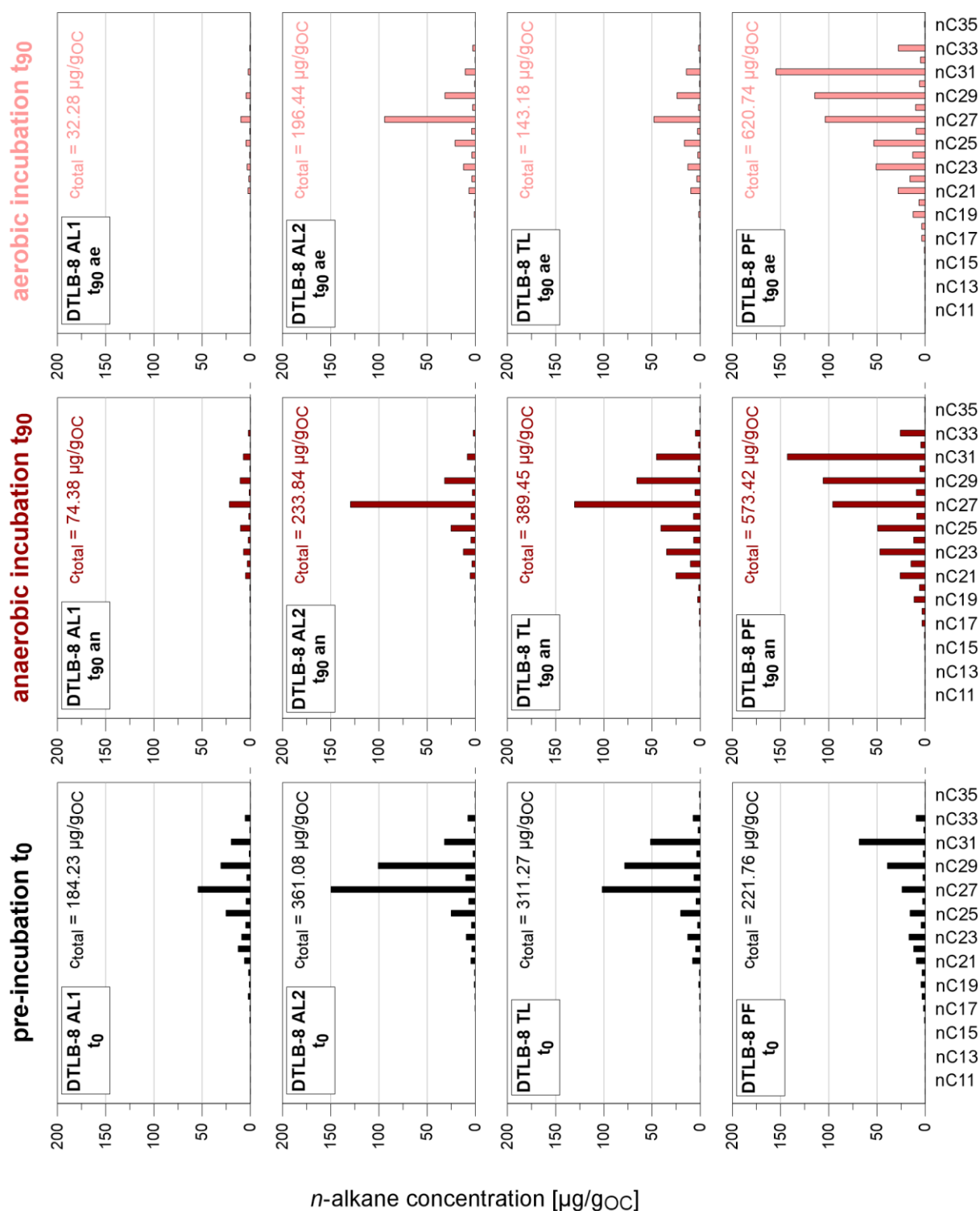
Figure 34: n-Alkane distribution patterns before and after incubation experiments in YC19-DTLB-8. Results of biomarker analysis at t₀ (black) and at t₉₀ of anaerobic (red) and aerobic (pink) incubation.

5.3.2. Functional lipids

n-Alkanols were detected in the range between *n*-C_{12} and *n*-C_{32} and exhibited a strong even-over-odd carbon number predominance (Figure 35 & Figure 36). They showed highly similar bimodal distribution patterns in the samples with maxima at short-chain *n*-C_{20} and long-chain *n*-C_{28} though ranging in total concentrations between 15.82 (YC19-DTLB-7 PF) to 285.29 (YC19-DTLB-7 AL1)

µg g_{OC}^{-1}. Within the two cores, they were highly abundant in peaty samples above the peat – mineral soil interface.
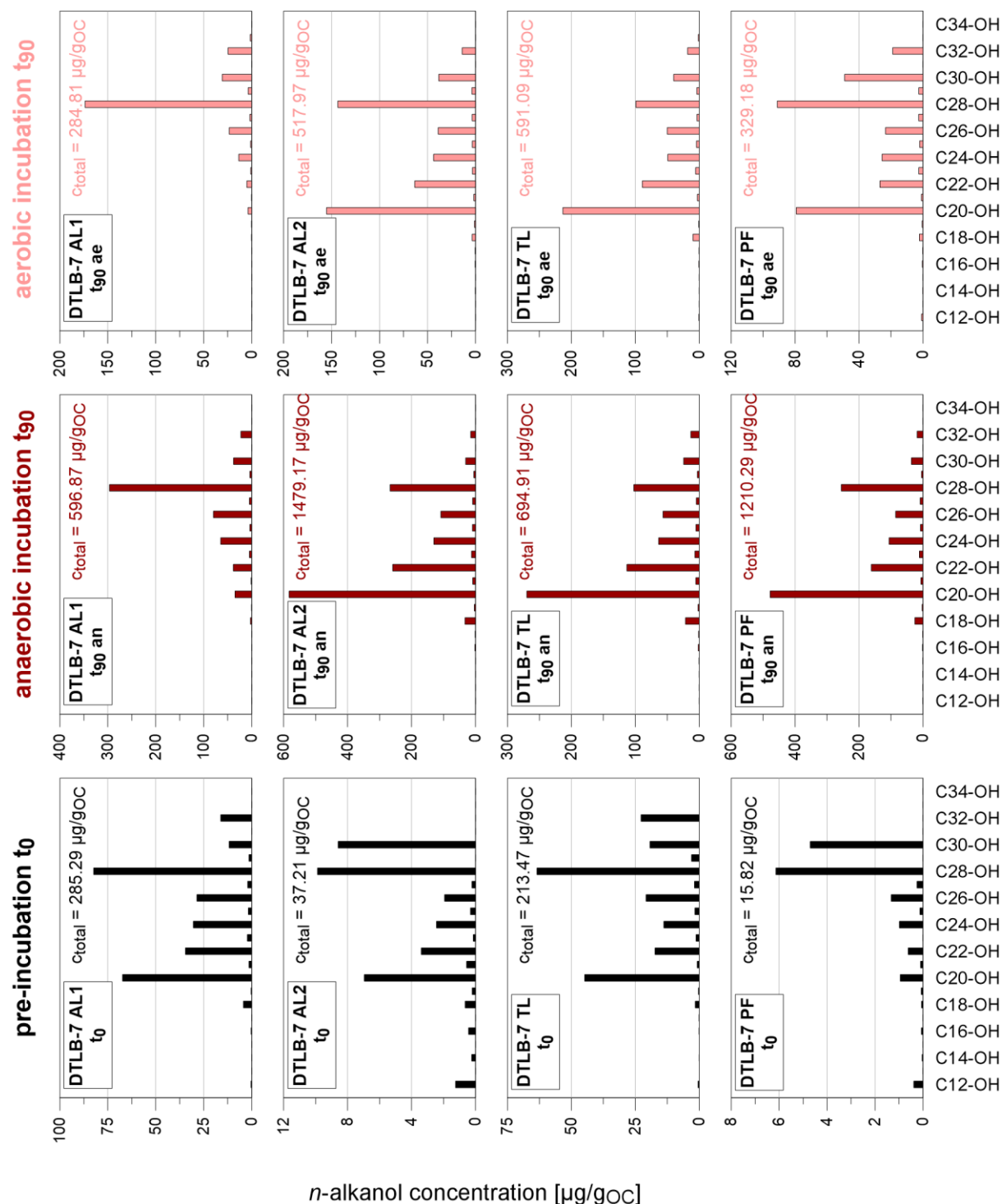
Figure 35: n-Alkanol distribution patterns before and after incubation experiments in YC19-DTLB-7. Results of biomarker analysis at t_0 (black) and at t_{90} of anaerobic (red) and aerobic (pink) incubation.
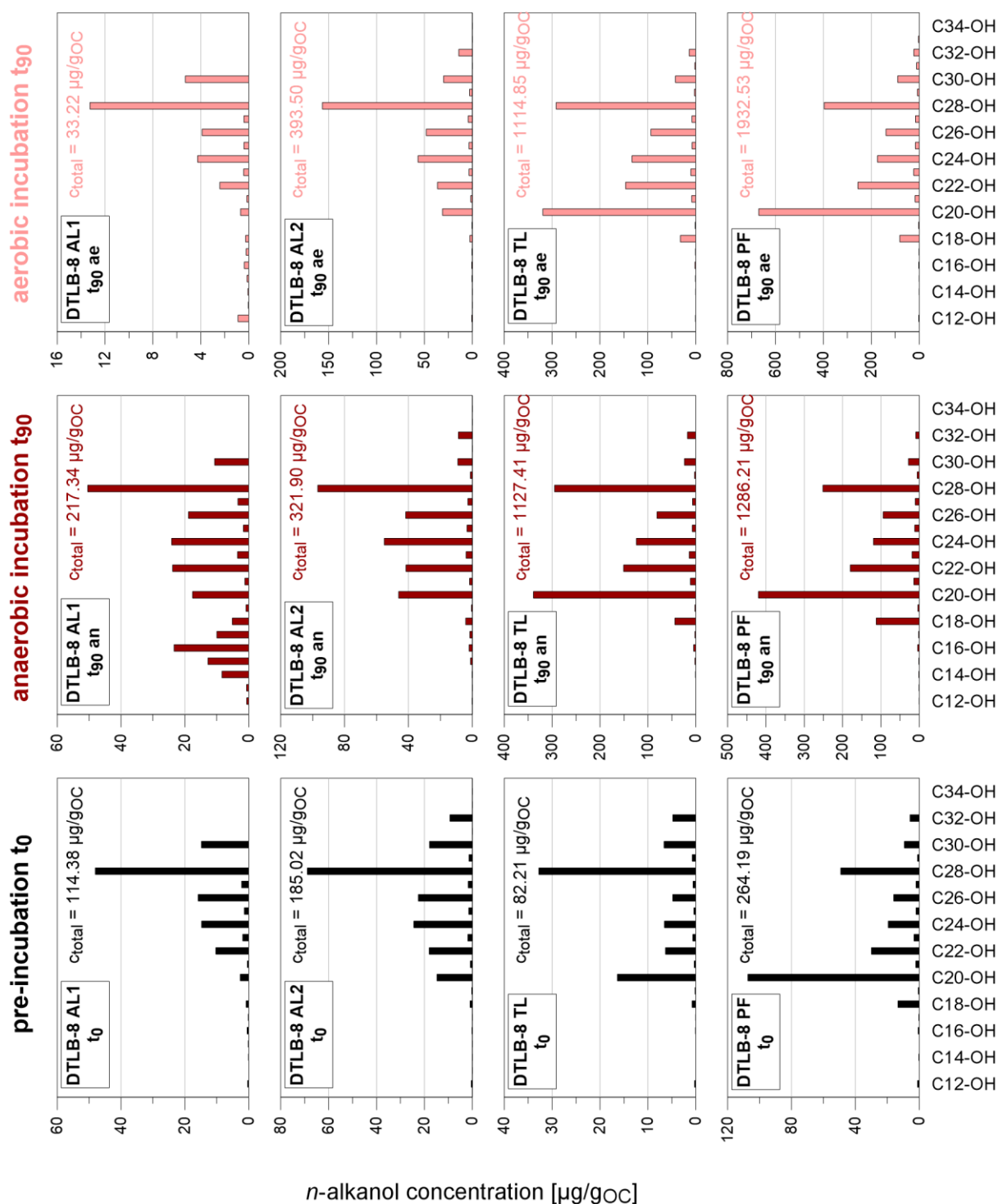
Figure 36: n-Alkanol distribution patterns before and after incubation experiments in YC19-DTLB-8. Results of biomarker analysis at t_0 (black) and at t_{90} of anaerobic (red) and aerobic (pink) incubation.

Increases in total concentrations of *n*-alkanes and *n*-alkanols were observed in all samples within the 90-day anaerobic incubation experiment (Appendix 13). This accumulation was considerably higher in mineral samples (+ 282 to + 909 %) compared to organic samples (- 2.31 to + 87 %), with the cryoturbated samples showing intermediate values (+ 67 to + 285 %). Lipid preservation was lower within the aerobic incubation in all sediment types (organic: - 78.07 to + 9.81 %, mineral: + 333 to + 425 %, cryoturbated: + 51 to + 219 %).

Because the euric acid standard was defective, no total concentrations of *n*-fatty acids in the samples could be evaluated. *n*-Fatty acids cannot be evaluated here as the chromatograms of the NSOs fraction were not yet available.

5.3.3. Biomarker indices

n-Alkanes and *n*-alkanols constituted for < 0.06 % of organic carbon content in all samples (Figure 37a & Figure 38a). All samples exhibited a high *n*-alkane ACL > 27 (Figure 37b & Figure 38b). The range of observed ACL values was narrow, only varying from 27.49 in YC19-DTLB-8 AL1 to 28.92 in YC19-DTLB-7 AL1. The ACL decreased within both aerobic and anaerobic incubation experiments, in a similar manner in all samples except YC19-DTLB-7 AL2, where it slightly increased. For *n*-alkanols, ACL values were > 24 in all samples (Figure 37c & Figure 38c). The ACL of *n*-alkanols showed a decreasing trend with depth in YC19-DTLB-8 but an increasing trend in YC19-DTLB-7. ACL of *n*-alkanols experienced stronger alteration during the incubation period compared to the ACL of *n*-alkanes. With incubation experiments, ACL values generally decreased in all samples except YC19-DTLB-7 AL1, where values strongly increased (anaerobic incubation: + 1.87, aerobic incubation: + 3.22). Anaerobic incubation conditions resulted in a stronger alteration of the *n*-alkanol ACL compared to aerobic conditions. P_{aq} und P_{wax} naturally showed opposing trends. In conformity with high *n*-alkane ACL values, P_{wax} values are very high (0.73 – 0.89) (Figure 37e & Figure 38e) while P_{aq} are low (0.15 – 0.40) (Figure 37d & Figure 38d) in all samples.

Indices describing the ratio of odd-and-even carbon chain length homologues are used as proxies of the degradation of the organic matter. Odd-numbered *n*-alkanes were 10 - 16 times more abundant in the samples compared to even numbered *n*-alkanes as described by the odd-over-even predominance (OEPD) (Figure 37f & Figure 38f). The same circumstance was also reflected in the high (> 5) carbon preference index (CPI) (Figure 37g & Figure 38g). In YC19-DTLB-7, the highest CPI and OEPD values could be found in peaty surface layer AL1, while samples from the other sampling depths AL2, TL and PF exposed consistent values of ~ 5 and ~ 10 respectively. In a slightly higher level, the consistency of OEPD and CPI values in AL2, TL and PF could also be observed in YC19-DTLB-8. Here, the AL1 sample showed significantly lower odd-over-even patterns. Both degradation proxies did not show high deviations after the incubation experiments, except for high increases of both proxies in YC19-DTLB-8 AL2 and decreases in YC19-DTLB-8 PF. CPI of *n*-alkanols in the range of *n*-C_{20}-OH to *n*-C_{30}-OH revealed similar patterns to the CPI of *n*-alkanes, but the predominance of, in this case, even numbered homologues was even more pronounced (Figure 37i & Figure 38i). This is also reflected in the even-over-odd predominance (EOPD) of *n*-alkanols (Figure 37h & Figure 38h)

The higher plant alcohol index (HPA) was generally < 0.5, implying a generally higher prevalence of dominant *n*-alkane homologues n-C_{27} to n-C_{31} than dominant *n*-alkanol homologues *n*-C_{24} to *n*-C_{28} (Figure 37j & Figure 38j). The highest shares of dominant *n*-alkanols compared to *n*-alkanes were

found in the near-surface samples and in YC19-DTLB-8 PF. HPA values considerably changed within the incubation experiments. Strong relative increases of the dominant even-numbered *n*-alkanols were observed in all samples, higher under anaerobic conditions in YC19-DTLB-7 but higher under aerobic conditions in YC19-DTLB-8.
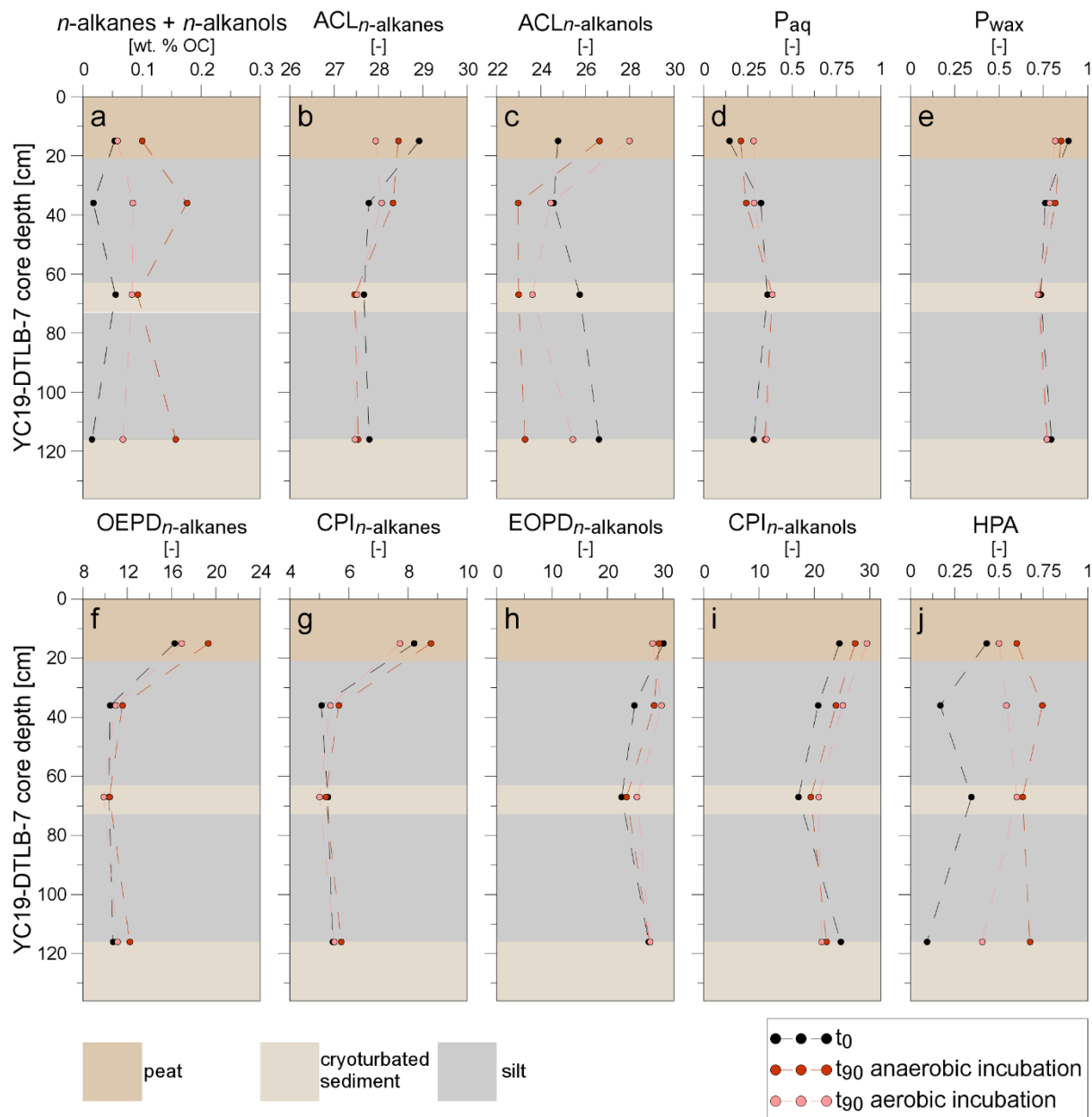
Figure 37: Changes of biomarker indices within the aerobic and anaerobic incubation experiments. Contribution of lipids to the sediment organic carbon content (a) and biomarker indices (b) ACL of n-alkanes, (c) ACL of n-alkanols, (d) P_aq, (e) P_wax, (f) OEPD of n-alkanes, (g) CPI of n-alkanes, (h) EOPD of n-alkanols, (i) CPI of n-alkanols, and (j) HPA in permafrost sediment core YC19-DTLB-7 at t_0 (black) and at t_90 of anaerobic (red) and aerobic (pink) incubation.
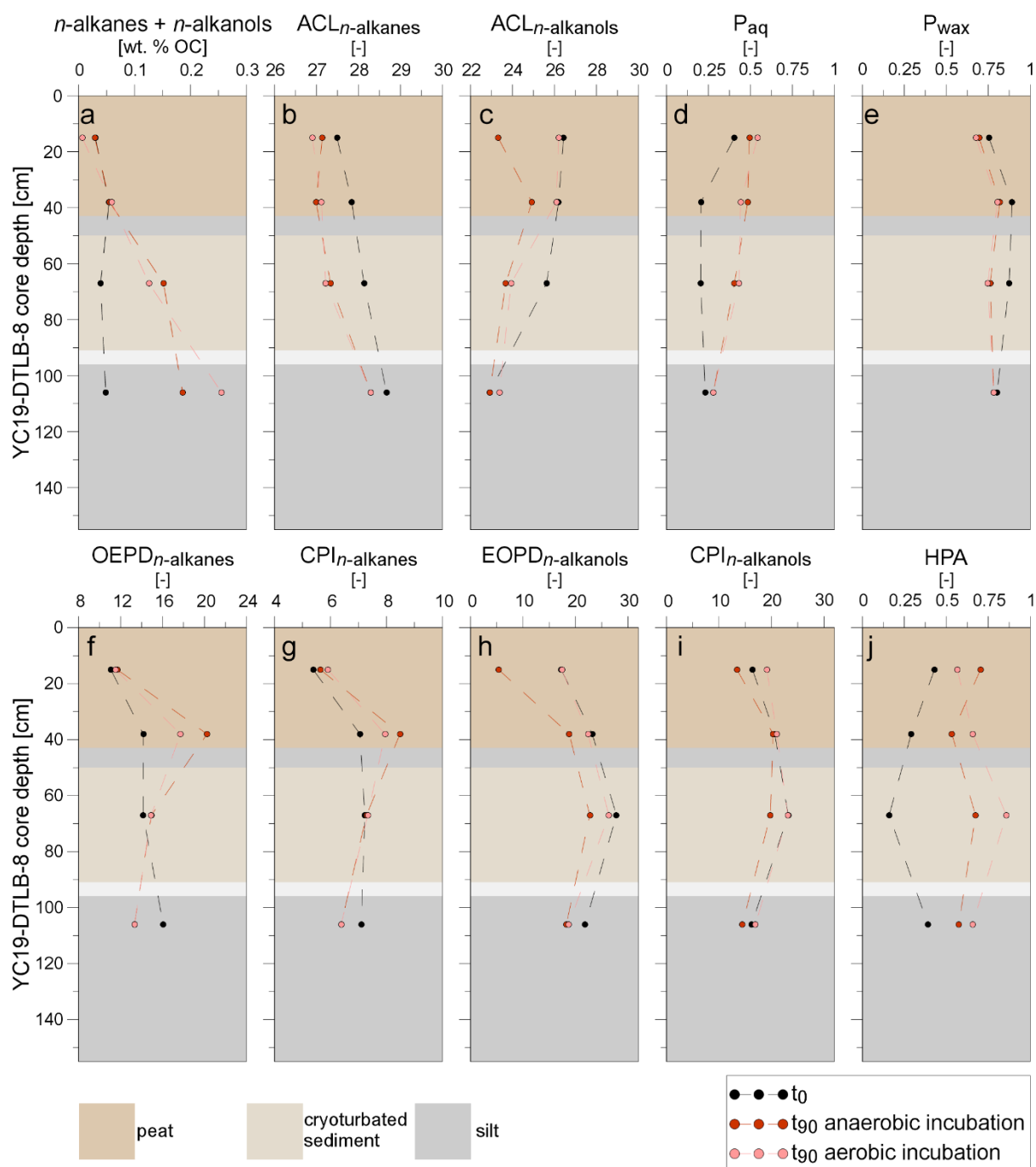
Figure 38: Changes of biomarker indices within the aerobic and anaerobic incubation experiments. Contribution of lipids to the sediment organic carbon content (a) and biomarker indices (b) ACL of n-alkanes, (c) ACL of n-alkanols, (d) P_{aq}, (e) P_{wax}, (f) OEPD of n-alkanes, (g) CPI of n-alkanes, (h) EOPD of n-alkanols, (i) CPI of n-alkanols, and (j) HPA in permafrost sediment core YC19-DTLB-8 at t_0 (black) and at t_{90} of anaerobic (red) and aerobic (pink) incubation.

5.4. Statistical analyses

5.4.1. Pearson's correlation coefficients

We calculated Pearson's correlation coefficient between all geochemical and biomarker parameters with incubation characteristics and reported all statistically significant correlations ($p < 0.05$). Within the samples, soil type parameters TOC, TN and the C:N ratio showed high positive correlations ($r > 0.87$) (Appendix 14). They were further strongly positively correlated to the ice content ($r > 0.79$).

56

All these parameters show strong negative correlation with pH (r < - 0.84). Hence, our organic peat samples tend to be more acidic and ice rich than mineral samples. There is one n.a. value of electrical conductivity in YC19-DTLB-7, but it is observed that eC showed an increasing trend with depth in both YC19-DTLB-7 and YC19-DTLB-8. The C:N ratio and $\delta^{13}C$ signature showed moderate negative correlation with depth. The $\delta^{13}C$ signature does not significantly correlate with any other of the determined geochemical parameters.

The total lipid concentrations (sum of n-alkanes and n-alkanols) per g_{dw} was strongly correlated to TOC, TN, the C:N ratio and the ice content, whereas being negatively correlated with pH and depth, attributed to the overall higher share of OM (Table 12, Appendix 15). Normalized to g_{OC}, positive correlations with TOC, TN, and the ice content were weak and moderate for the C:N ratio. Generally, C:N showed the strongest correlations with geochemical parameters. The share of short-chain n-alkanes was enhanced in mineral sediment samples, as revealed by strong positive correlations to TOC, TN, C:N and ice content. The strong positive correlation of C:N and CPI of n-alkanes and n-alkanols is striking. Naturally, P_{wax} and P_{aq} showed opposing correlation trends.

Table 12: Excerpt of Pearson's correlation coefficients for geochemical parameters and the results of the biomarker analysis. Correlations > 0.7 (in bold) are considered strong. Insignificant correlations (p < 0.05) are omitted.

	TOC	TN	C:N	ice	pH	$\delta^{13}C$	depth
$c_{lipids} \, g_{dw}^{-1}$	**0.93**	**0.85**	**0.93**	**0.81**	**-0.95**		-0.63
$c_{lipids} \, g_{OC}^{-1}$	0.39	0.32	0.52	0.39	-0.38		-0.18
$c_{n\text{-alkanes}} \, g_{OC}^{-1}$	0.44	0.44	0.38	0.45	-0.25		-0.14
$ACL_{n\text{-alkanes}}$			0.49				
Share short-chain n-alkanes	**-0.84**	**-0.82**	**-0.82**	**-0.89**	**0.76**		0.32
P_{wax}	0.63	0.53	**0.76**	0.49	-0.67	-0.40	-0.17
P_{aq}	-0.32	-0.19	-0.62	-0.20	0.37	0.41	
$CPI_{n\text{-alkanes}}$	0.54	0.42	**0.77**	0.44	-0.53		
$OEPD_{n\text{-alkanes}}$	0.40	0.28	0.63	0.31	-0.39		
$c_{n\text{-alkanols}} \, g_{OC}^{-1}$	0.25		0.51	0.24	-0.42		-0.18
$ACL_{n\text{-alkanols}}$		0.48		0.51			
$CPI_{n\text{-alkanols}}$			0.39		-0.25	-0.59	
$EOPD_{n\text{-alkanols}}$						-0.56	
HPA	0.40	0.34	0.46	0.40	-0.36	0.57	-0.46

The CH_4 production per g_{OC} showed weak correlations with bulk geochemical parameters within the anaerobic incubation experiment (Table 13, Appendix 16). The only moderate correlation was a negative correlation with depth. The maximum CO_2 production rate showed strong negative correlation with the soil type characteristics and an opposing strong positive correlation with pH. Further, the decay of CH_4 and CO_2 production rates after the maximum production rate exhibited high negative correlation with the soil type characteristics such as the ice content, TN, TOC, and the C:N

ratio in both sediment cores. In contrast, there was a strong positive correlation with pH for the CO_2 production rate decay. Opposingly, the lag time of maximum CO_2 production rates was positively correlated with the soil type parameters, but negatively with pH and depth. In summary, mineral samples showed more concise peaks, with higher maximum production rates (for CO_2) and stronger production rate decay early on within the anaerobic incubation experiment, as opposed to organic samples.

Table 13: Excerpt of Pearson's correlation coefficients for geochemical parameters and anaerobic incubation characteristics. Correlations above 0.7 (in bold) are considered strong. Insignificant correlations (p < 0.05) are omitted.

	TOC	TN	C:N	ice	pH	$\delta^{13}C$	depth
Carbon release g_{dw}^{-1}	0.62	0.68	0.34	0.65	-0.56	0.32	-0.64
Carbon release g_{OC}^{-1}	0.26	0.33		0.22	-0.26	0.54	-0.68
Carbon loss (wt. % $C_{initial}$)						0.50	-0.56
t_{90} CO_2:CH_4 production ratio	-0.47	-0.46	-0.33	-0.27	0.50	-0.34	**0.75**
t_{90} CH_4 headspace concentration g_{dw}^{-1}	**0.71**	**0.75**	0.45	**0.71**	-0.66	0.33	**-0.71**
t_{90} CH_4 headspace concentration g_{OC}^{-1}	0.39	0.47		0.39	-0.35	0.42	-0.65
Maximum CH_4 production rate						0.48	-0.62
Lag time max CH_4 production rate							
CH_4 production rate decay	**-0.77**	**-0.76**	**-0.76**	**-0.90**	-0.36		0.33
t_{90} CO_2 headspace concentration g_{dw}^{-1}	0.41	0.51		0.50	-0.32	0.29	-0.46
t_{90} CO_2 headspace concentration g_{OC}^{-1}						0.42	-0.36
Maximum CO_2 production rate	**-0.80**	**-0.73**	**-0.89**	**-0.83**	**0.76**		0.22
Lag time maximum CO_2 production rate	**0.73**	0.59	**0.88**	0.55	**-0.84**		-0.60
CO_2 production rate decay	**-0.94**	**-0.96**	**-0.72**	**-0.93**	**0.91**		0.65

Within the anaerobic incubation experiment, total CH_4 production and total CO_2 production were positively linked (r = 0.93), and so were the corresponding maximum production rates (r = 0.57) (Appendix 17). For CH_4, the maximum production rate was strongly positively linked to the total production after 90 days (r = 0.73). This observation was less pronounced for CO_2 (r = 0.40). For CO_2, the lag time until reaching maximum production rates was negatively correlated to the maximum production rate (r = - 0.73) and the production rate decay (r = - 0.63) in conformity with observations above. Correspondingly, maximum CO_2 production and CO_2 production rate decay were positively correlated (r = 0.70).

Within aerobic incubation conditions, Pearson's correlation revealed moderate negative correlation of the cumulative CO_2 production per g_{OC} and soil type parameters TOC, TN, the C:N ratio, and ice content, whereas it showed positive correlation with pH (Table 14, Appendix 18). As observed within the anaerobic incubation, the CO_2 maximum production rate and the following production rate decay showed stronger negative correlations. Both were also strongly postive correlated to pH. The CO_2 production rate decay also appeared to be positively linked with depth. Notably, the lag time of

maximum production rates was not significantly correlated to geochemical parameters, as opposing to anaerobic incubation experiment. Naturally, maximum CO_2 production rates and the production rate decay were positively correlated ($r = 0.68$) (Appendix 19). Again, mineral samples showed more concise peaks, with higher maximum production rates and stronger production rate decay, as opposed to organic samples.

Table 14: Excerpt of Pearson's correlation coefficients for geochemical parameters and aerobic incubation characteristics. Correlations above 0.7 (in bold) are considered strong. Insignificant correlations (p < 0.05) are omitted.

	TOC	TN	C:N	ice	pH	$\delta^{13}C$	depth
Carbon loss (wt. % $C_{initial}$)	-0.58	-0.52	-0.62	-0.50	0.61		0.35
t_{90} cumulative CO_2 production g_{dw}^{-1}	0.68	**0.73**	0.42	**0.73**	-0.58		-0.55
t_{90} cumulative CO_2 production g_{OC}^{-1}	-0.47	-0.42	-0.51	-0.36	0.53		0.34
Maximum CO_2 production rate	**-0.77**	**-0.76**	**-0.75**	**-0.84**	**0.72**		0.25
Lag time maximum CO_2 production rate						-0.69	
CO_2 production rate decay	**-0.95**	**-0.91**	**-0.83**	**-0.83**	**0.95**		**0.78**

5.4.2. Paired t-test

According to the Shapiro-Wilk test, all changes in geochemical parameters were normally distributed ($p > 0.05$), therefore allowed us to perform paired t-tests without data transformation (Appendix 21). Significant changes ($p < 0.05$) in t_0 and t_{90} data sets of geochemical parameters within the anaerobic incubation experiment were observed for TN, TOC as well as for pH (Figure 39).
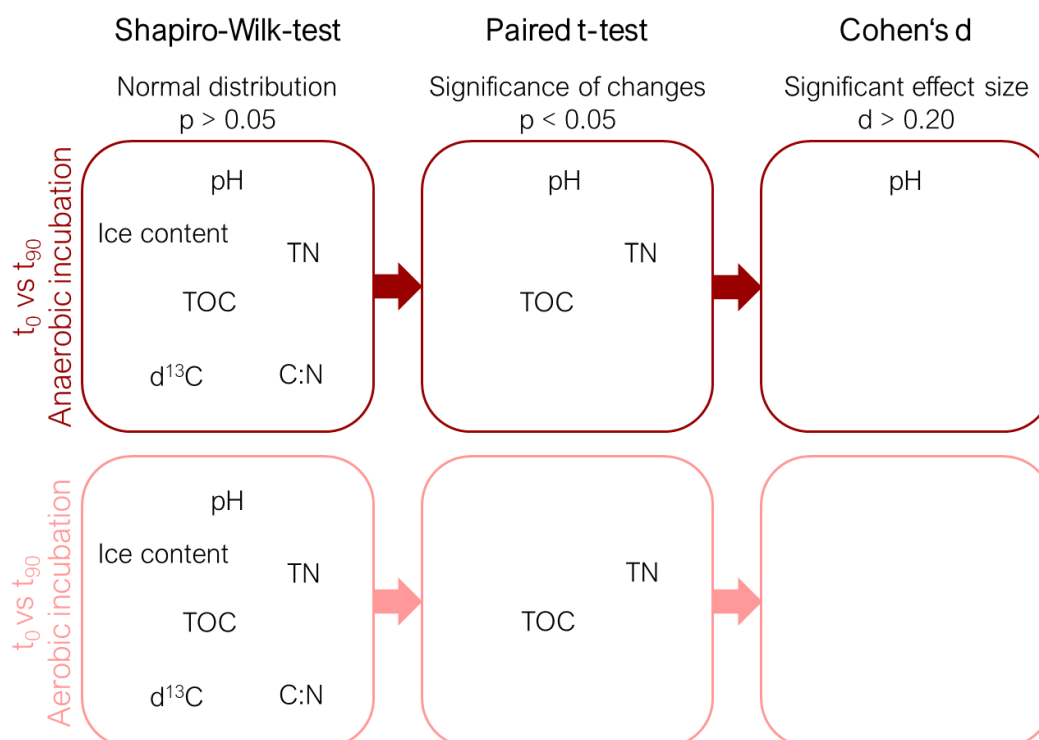
Figure 39: Results of paired t-test for geochemical parameters. Comparison of geochemical data before and after 90 days of anaerobic (top) and aerobic (bottom) incubation. Normal distribution is confirmed by Shapiro-Wilk test p > 0.05, statistical significance of changes is revealed by paired t-test p < 0.05, and the effect size is assessed using Cohen's d.

59

On the contrary, for the C:N ratio and $\delta^{13}C$, p values were > 0.05, implying that changes were not significant. The effect size, according to Cohen's d, was strong for the changes in pH (d > 0.80), but negligible for TOC and TN (d < 0.20).Based on the paired t-test results, we found no statistically significant difference between t_0 and t_{90} data of the aerobic incubation experiment for the pH. Again, changes of TN and TOC were statistically significant, suggesting that the incubation experiment has influenced these parameters. Still, none of these parameter changes were more than negligible according to Cohen's d measure of effect size (d < 0.20).

Without data transformation, all changes in biomarker data sets met the assumption of normality according to the Shapiro-Wilk tests (p > 0.05) (Appendix 22). An array of significant changes in biomarker indices were detected by paired t-tests within 90 days of anaerobic incubation (Figure 40).
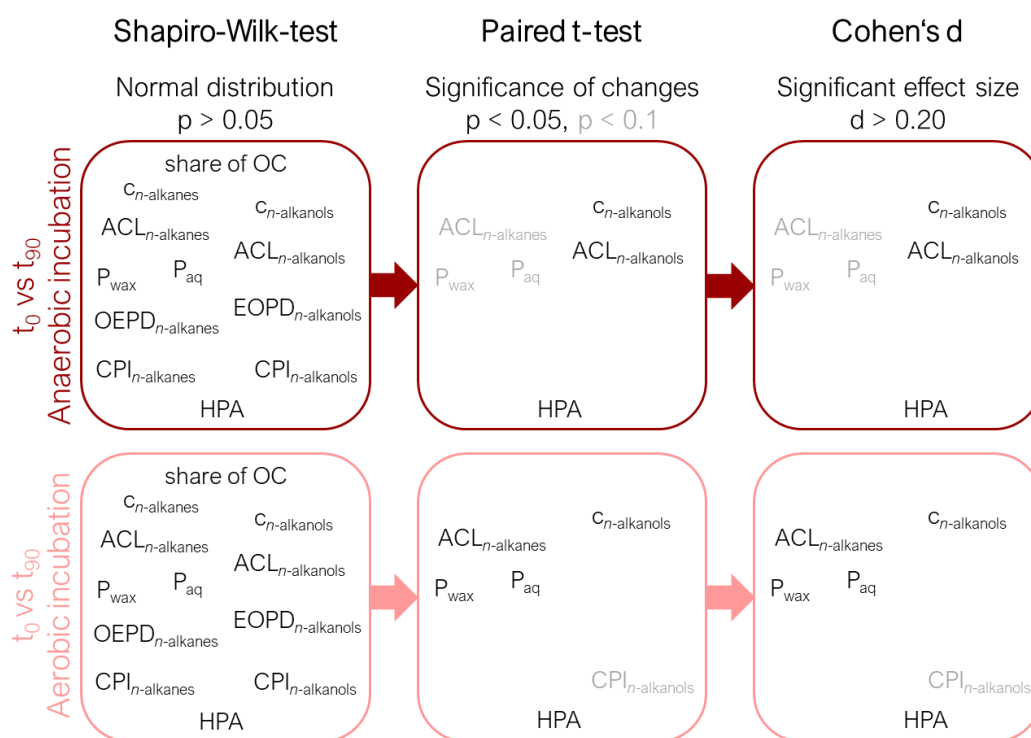
Figure 40: Results of paired t-test for geochemical parameters. Comparison of biomarker data before and after 90 days of anaerobic (top) and aerobic (bottom) incubation. Normal distribution is confirmed by Shapiro-Wilk test p > 0.05, statistical significance of changes is revealed by paired t-test p < 0.05, and the effect size is assessed using Cohen's d.

Anaerobic incubation appeared to primarily affect n-alkanol patterns, as revealed by significant changes in $c_{n\text{-alkanol}}$, $ACL_{n\text{-alkanol}}$ and the HPA, but not in EOPD and $CPI_{n\text{-alkanols}}$ (p > 0.05). When choosing a lower significance level of p < 0.1, changes were also apparent in n-alkane distribution patterns like $ACL_{n\text{-alkane}}$, P_{aq} and P_{wax}. Again, OEPD and $CPI_{n\text{-alkanes}}$ were not significantly affected. Associated effect sizes, revealed by Cohen's d, were larger when compared to the geochemical parameters. A large effect (d > 0.80) was determined by Cohen's d for all n-alkanol parameters ($c_{n\text{-alkanols}}$: d = - 2.10, $ACL_{n\text{-alkanols}}$: d = 1.20, HPA: d = - 3.34), and a medium to large effect for n-alkane parameters ($ACL_{n\text{-alkanes}}$: d = 0.64, P_{aq}: d = - 0.88, P_{wax}: d = 0.61).

Changes of n-alkane patterns were more pronounced within the aerobic incubation experiment. Here, $ACL_{n\text{-alkane}}$, P_{aq} and P_{wax} showed significant changes (p < 0.05) in the paired t-test. Although the

n-alkanol concentration itself significantly changed, n-alkanol related indices failed to meet the paired t-test criterion of $p < 0.05$ for significant changes in t_0 and t_{90} data. Only the higher plant alcohol index (HPA), that comprises both n-alkane and n-alkanol data, showed significant alteration. Again, Cohen's d confirmed large effect sizes for paired t-test results of $ACL_{n\text{-alkane}}$ (d = 0.95), P_{aq} (d = - 1.16), P_{wax} (d = 0.90). The largest effect size was determined for the HPA (d = - 2.32).

5.4.3. Analysis of variance

Analysis of variance (ANOVA) provided insights into the variance of the determined greenhouse gas production potentials among the sediment types (organic, mineral, cryoturbated) well as the permafrost thermal regime (AL, TL, PF). One-way ANOVAs were performed when Shapiro-Wilk-test confirmed normal distribution of the log-transformed data ($p > 0.05$) and Bartlett's test confirmed homogeneity of variances ($p > 0.05$). ANOVA F values display the intergroup variance divided by the intragroup variance (Kim 2017), whereas p values < 0.05 indicate statistical significance.

Within our short-term incubation experiment under anaerobic conditions, one-way ANOVA revealed that the CH_4 production per g_{dw} and per g_{OC} as well as the maximum CH_4 production rate was significantly different among permafrost thermal regimes active layer, transition layer, and permafrost (Table 15). The decay of CH_4 production rates following the maximum production rate, however, was influenced by sediment type. The same accounted for the decay of anaerobic CO_2 production rates.

Table 15: Results of one-way ANOVAs for greenhouse gas production within anaerobic incubation. Only performed if normality confirmed (Shapiro-Wilk > 0.05) for dependent variable and homogeneity of variances confirmed (Bartlett's test > 0.05) for all dependent-independent variable combinations. Significance codes: '' < 0.1 ** < 0.05, *** < 0.01, log-transformed data.*

| | | Shapiro-Wilk test | One-way ANOVA | | | |
| | | | Sediment Type | | Thermal Regime | |
		p	F	p	F	p
Anaerobic incubation	CH_4 production g_{dw}	0.49	3.61	0.107	13.68	0.009***
	CH_4 production g_{OC}	0.35	1.13	0.395	16.15	0.007***
	Max. CH_4 production rate	0.61	1.06	0.415	6.77	0.038**
	Lag time max. CH_4 production rate	0.004				
	CH_4 production rate decay	0.96	12.64	0.011**	0.56	0.602
	CO_2 production g_{dw}	0.008				
	CO_2 production g_{OC}	0.92	0.16	0.857	0.17	0.847
	Max. CO_2 production rate	0.23	3.17	0.129	0.43	0.670
	Lag time max. CO_2 production rate	0.002				
	CO_2 production rate decay	0.30	13.78	0.009***	1.59	0.293
	Carbon loss (wt. % $C_{initial}$)	0.19	0.76	0.513	0.42	0.679
	CO_2:CH_4	0.60	0.79	0.505	6.71	0.038**

Under aerobic conditions, not only the decay of CO_2 production rates, but also the CO_2 production per g_{dw} as well as the maximum CO_2 production rate were affected by the sediment type. Here, no

influence by permafrost thermal regimes was apparent. The lag times of maximum GHG production rates under anaerobic and aerobic conditions were not normally distributed and could not be analysed with ANOVA.

Table 16: Results of one-way ANOVAs for greenhouse gas production within aerobic incubation. Only performed if normality confirmed (Shapiro-Wilk > 0.05) for dependent variable and homogeneity of variances confirmed (Bartlett's test > 0.05) for all dependent-independent variable combinations. Significance codes: '' < 0.1 ** < 0.05, *** < 0.01, log-transformed data.*

| | | Shapiro-Wilk test | One-way ANOVA | | | |
| | | | Sediment Type | | Thermal Regime | |
		p	F	p	F	p
Aerobic incubation	CO_2 production g_{dw}	0.89	4.64	0.073*	0.40	0.689
	CO_2 production g_{OC}	0.25	1.00	0.430	1.94	0.238
	Max. CO_2 production rate	0.22	5.16	0.061*	0.61	0.579
	Lag time max. CO_2 production rate	0.044				
	CO_2 production rate decay	0.60	7.03	0.035**	3.69	0.104
	Carbon loss (wt. % $C_{initial}$)	0.07	1.51	0.307	1.47	0.314

6. Discussion

In a multi-proxy approach, we aimed to (1) evaluate organic matter decomposition in ice-rich drained lake basin (DLB) sediments upon permafrost thaw and to (2) determine the associated greenhouse gas production potential. Our approach included aerobic and anaerobic laboratory incubation experiments, simulating drained and waterlogged conditions in the basins. The study was conducted in two adjacent DLBs on the Yukon coastal plain, Canada, where the two permafrost sediment cores YC19-DTLB-7 and YC19-DTLB-8 were taken during an expedition in spring 2019.

We could confirm that the coastal plain DLB sediments are ice-rich (Jones et al. 2022), and porewater pH is near-neutral to slightly acidic in peat layers (Wolter et al. 2016). Organic and mineral soils are commonly distinguished by TOC values of more than resp. less than 20 wt. % (Schädel et al. 2014). We found that the organic peat layers exhibited very high TOC contents of > 40 wt. %, characteristic of near-surface DLB sediments in the area (Wolter 2016, 2017). Silt layers comprised comparably high TOC contents for mineral sediment of 5 - 10 wt. % (Wolter et al. 2017). Within lake - drained lake basin systems, peat layers accumulate in drained lake basins, while silty mineral sediment layers are potentially indicative of a lacustrine origin (Wolter et al. 2018). However, it has to be regarded that cryoturbation has the potential to alter accumulated sediment layers and overprint the stratigraphy in permafrost sediment (see chapter 2.1.2.), e.g. a high TOC content directly above the permafrost table can be the result of intensified cryoturbation (Ping et al. 1997; Mueller et al. 2015; Beer et al. 2022). Permafrost sediment cores YC19-DTLB-7 and -8 revealed highly heterogenous stratigraphies typical of drained lake basins. Terrestrial conditions prevail in the basins since accumulation of the uppermost peat – silt interface. It was revealed by ^{14}C dating that despite lower peat accumulation of only 21 cm, DTLB-7 appears to be the more mature drained lake basin even though 43 cm of peat accumulated in DTLB-8 since the last potential drainage event. The water-levels were likely fluctuating beforehand. As a viable paleoenvironmental reconstruction in permafrost-affected soils is highly complex due to the influence of cryoturbation, it was deliberately excluded from the research objectives of this thesis.

6.1. Organic matter decomposition

Comprehensive analyses of geochemical parameters and lipid composition were conducted to evaluate the organic matter characteristics of the DLB sediment samples. Correlations were tested using Pearson's r. In order to assess the organic matter decomposition, paired t-tests were performed to test for significant alteration of parameters after the anaerobic and aerobic incubation experiments.

6.1.1. Origin and quality of organic matter before incubation

6.1.1.1. Bulk geochemical parameters

The sediment C:N ratio as well as the carbon stable isotopic composition have long been used to assess the origin and decomposition of organic matter (Meyers 1994; Stevenson 1994; Kuhry & Vitt

1996; Meyers 1997; Gundelwein et al. 2007; Schirrmeister et al. 2011; Tanski et al. 2017; Xia et al. 2021). In our study, the observed low and consistent $\delta^{13}C$ signatures of -27.69 to -28.48 ‰ can be indicative of terrestrial plants using the C3 photosynthetic pathway, freshwater plants or lacustrine algae (- 32 ‰ to - 19 ‰), while C4 plants and marine species would produce less negative $\delta^{13}C$ values (Rullkötter 2003; Still et al. 2003; Kennedy et al. 2010; Martens et al. 2020) (Figure *41*). In combination with high C:N values, an origin of organic matter from terrestrial vascular plants can be assumed (Meyers 1994). Pearson's correlation coefficients indicated that $\delta^{13}C$ signatures were not different in mineral and organic layers (Appendix 14), in line with Dutta et al. (2006), but opposing to observations by Lee et al. (2012). Active layer peats showed highest C:N ratios of approximately 20 (Figure 20 & Figure 21, Appendix 5). The lower C:N ratios in mineral samples (13.31 – 15.70) may indicate a larger input of algal organic matter (Meyers 1994; Paul 2016).
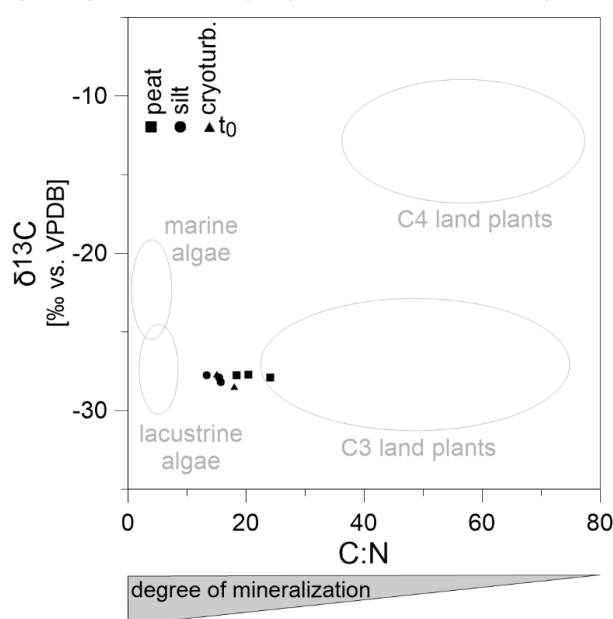
Figure 41: Geochemical proxies C:N ratio and $\delta^{13}C$. Reference areas roughly according to Meyers (1994)*.*

Accompanying the degradation of organic matter, C:N values are known to decrease, whereas the fate of $\delta^{13}C$ values more complex. This will be discussed in detail in chapter 6.1.2. As C:N values were moderately high and both C:N and $\delta^{13}C$ showed moderate negative correlation of with depth (Appendix 14), minor previous decomposition might be reflected. As the C:N ratio and stable carbon isotopic signature both act as indicators of early carbon decomposition in soils, a correlation between the two parameters is assumed. Positive correlation was reported by (Meyers 1997; Hornibrook et al. 2000; Powers & Schlesinger 2002; Zech et al. 2007; Krüger et al. 2014). The correlation of $\delta^{13}C$ and the C:N ratio was not significant in neither of the two studied permafrost cores in this study ($p > 0.05$).

6.1.1.2. Lipid biomarkers

A comprehensive biomarker analysis of extractable lipids offered additional insights into the sedimentary organic matter. Despite generally constituting less than 10 % of the organic matter (Dinel et al. 1990; Meyers 1997), the resilient lipids present various reliable molecular proxies for determining

the origin and decomposition of organic matter (van Bergen et al. 1998; Andersson & Meyers 2012). Generally, the share of OC that was constituted of *n*-alkanes and *n*-alkanols was very low (< 0.06 %) and was only weakly positively correlated with TOC (Table 12, Appendix 15). We could not find a decreasing trend with depth in soil profiles as reported by Dinel et al. (1990), Jongejans et al. (2018), and a synthesis study of *n*-alkane transformation in soils by Thomas et al. (2021), assumably because the sampling depth in our study is generally shallow (< 120 cm).

The average chain lengths (ACL) of *n*-alkanes and *n*-alkanols serve as useful means for identifying the source of organic matter based on characteristic chain length distributions of the main contributing vegetation type (Poynter et al. 1989; Thomas et al. 2021). As all of our samples showed high ACL values (*n*-alkanes: > 27, *n*-alkanols > 22), and the three predominant *n*-alkane homologues n-C_{27}, *n*-C_{29} and *n*-C_{31} constituted for 51 – 78 % of the total *n*-alkane concentrations, we assume an input by terrestrial vascular plant leaf waxes (Eglinton & Hamilton 1967; Bull et al. 2000; Otto & Simpson 2005; Jansen et al. 2006). This finding is supported by high values of land plant proxy P_{wax} of > 0.70 (Zheng et al. 2007). More precisely, c_{max} of most samples in *n*-C_{27} and *n*-C_{29} hint to an OM origin of deciduous trees or, in our setting more likely, from shrubs (Zech et al. 2013). Homologue *n*-C_{31}, indicative of grass species, was the predominant homologue in YC19-DTLB-7 AL1 and YC19-DTLB-8 PF (Zech et al. 2013). Grass species are highly productive pioneer vegetation that establish in recently drained lake basins (Jones et al. 2022). As such, increasing ACL with depth in YC19-DTLB-8 from 27.49 to 28.67 could reflect the vegetation succession from grass to shrub species in the evolving DLB, or the incorporation of fresh organic material into deeper sediment layers by cryoturbation. However, the influence of decomposition, counteracting this trend by lowering ACL, was not yet apparent.

P_{aq} values between 0.1 – 0.4 indicate additional input of organic matter from emergent macrophytes (Ficken et al. 2000; Wang et al. 2014).

Overall, the pioneer peat samples in both cores exhibited the highest terrestrial character as they showed highest P_{wax} and lowest P_{aq}. Further, the share of short-chain *n*-alkanes and soil type parameters TOC, TN and the C:N ratio was strongly negatively correlated (Table 12, Appendix 15), proving either an input of aquatic organic matter or a higher degree of decomposition in mineral samples. Apart from that, biomarker indices predicting the source of organic matter did not appear to differ between mineral and organic samples. This would indicate a similar origin of organic matter input over time, as changes in e.g. the ACL with depth can reveal vegetation shifts over time (Zech et al. 2012; Schaefer et al. 2016; Jongejans et al. 2021).

Further, the distribution of *n*-alkane and *n*-alkanol homologues showed distinctive odd-over-even (*n*-alkanes) and even-over-odd (*n*-alkanols) chain-length predominance, again characteristic for an input by terrestrial vascular plants (Bray & Evans 1961; Kolattukudy 1976; Dinel et al. 1990). High *n*-alkane odd-over-even predominance (OEPD) values of > 10 and carbon preference index (CPI) values of > 5 give further evidence for the high quality of organic matter in our sediment samples and low influence of degradation (Zheng et al. 2007; Jansen & Nierop 2009; Andersson & Meyers 2012).

CPI values of *n*-alkanes progressively decrease with microbial degradation of OM and hence superposition would predict a decreasing trend of CPI with depth (Thomas et al. 2021). Ultimately, even- and odd-numbered *n*-alkanes approach unity as degradation and alteration proceed (Cranwell et al. 1987). This trend of progressing decomposition of organic matter with time is not reflected in CPI values within the incubation period. Pioneer peat samples in both cores were least degraded as revealed by highest CPI. Depth trends of degradation proxies that are commonly observed in biomarker studies are rare in our study. Although we found strong positive correlation of degradation proxies C:N and the CPI of *n*-alkanes and *n*-alkanols (Table 12, Appendix 15), depth trends were not apparent in neither CPI and c_{lipids}. However, moderate negative correlation of HPA and depth indicates that *n*-alkanes are preferentially preserved to *n*-alkanols (Table 12, Appendix 15).

In conclusion, it appears that decomposition has been limited and has not yet significantly altered the original record. High organic matter quality can attributed to the high preservation potential in permafrost-affected soils, where microbial activity is highly restrained (Michaelson & Ping 2003; Dutta et al. 2006). Hence, it can be assumed that biomarker indices and geochemical proxies C:N and $\delta^{13}C$ act as viable proxies for the organic matter origin rather than decomposition in this setting.

6.1.2. Effects of incubation experiments on organic matter

6.1.2.1. Bulk geochemical parameters

C:N ratios in sediments are altered by selective degradation of organic matter components during early diagenesis (Meyers 1994). The C:N ratio records microbes metabolizing permafrost carbon for energy while using released nitrogen as a nutrient to grow (Kuhry & Vitt 1996). As a result, the C:N ratio is progressively decreasing with OM decomposition (Schuur et al. 2015). Therefore, the concept of superposition predicts progressively decreasing C:N ratios with depth (Malmer & Holm 1984; Kuhry & Vitt 1996).

Carbon isotopic signatures can serve as indicators for previous soil conditions and decomposition (Gundelwein et al. 2007). However, consensus on carbon isotopic development with decomposition in soils is lacking (Ågren et al. 1996; Garten Jr. 2006). Several conflicting results have been published on this topic, any direction has previously been reported (Breecker et al. 2015).

A decrease in $\delta^{13}C$ values in soils is potentially induced by selective preservation of isotopically more negative (^{13}C-depleted) compounds like lignin compared to (^{13}C-enriched) hemicellulose or cellulose, thus contributing to a more rapid loss of ^{13}C than ^{12}C (Benner et al. 1987; Nadelhoffer & Fry 1988; Ågren et al. 1996; Boutton 1996; Krull & Retallack 2000; Šantrůčková et al. 2000; Powers & Schlesinger 2002; Alewell et al. 2011). A similar fractionation pattern can be expected in sphagnum peat (Nimz & Tutschek 1977; Rasmussen et al. 1995).

On the other hand, microbial respiration (CH_4 and CO_2) discriminates against the heavy carbon isotope ^{13}C, thereby leaving the residual organic matter enriched in ^{13}C, and hence contributing to increasing $\delta^{13}C$ values in soils (Heyer et al. 1976; Paul 1981; Nadelhoffer & Fry 1988; Melillo et al.

1989; Ågren et al. 1996; Gundelwein et al. 2007; Diochon & Kellman 2008; Campbell et al. 2009; Alewell et al. 2011; Lerch et al. 2011; Acton et al. 2013). However, the reduced carbon turnover under anaerobic conditions resulting from diminished microbial activity limits the extent of these fractionation effects (Stout & Rafter 1978; Krull & Retallack 2000; Alewell et al. 2011; Xia et al. 2021). Hence, slightly decreasing $\delta^{13}C$ values with depth and time have been observed in waterlogged, anaerobic soils (Stout & Rafter 1978; Krull & Retallack 2000). Whereas this selective loss of ^{12}C appears to be undebated for CH_4, several studies claimed that the carbon stable isotopic signature of microbially respired CO_2 equals SOC and plant biomass $\delta^{13}C$ values, thereby not causing fractionation (Deines 1980; Amundson et al. 1998; Ehleringer et al. 2000; Wynn 2007; Breecker et al. 2015; Huang & Hall 2018). Still, pronounced increases in sediment $\delta^{13}C$ signature have been reported in well-drained soils (Nadelhoffer & Fry 1988; Ågren et al. 1996; Balesdent & Mariotti 1996; Boutton 1996; Ehleringer et al. 2000; Garten Jr. et al. 2000; Krull & Retallack 2000; Šantrůčková et al. 2000; Campbell et al. 2009), fuelled by the higher carbon turnover under aerobic conditions.

Minor, non-significant (paired t-test $p > 0.05$) trends of decreasing $\delta^{13}C$ values in anaerobic conditions could be observed in the peaty samples within our study, while opposing slightly increasing values are indicated under aerobic conditions (Figure 39, Figure 42, Appendix 21).
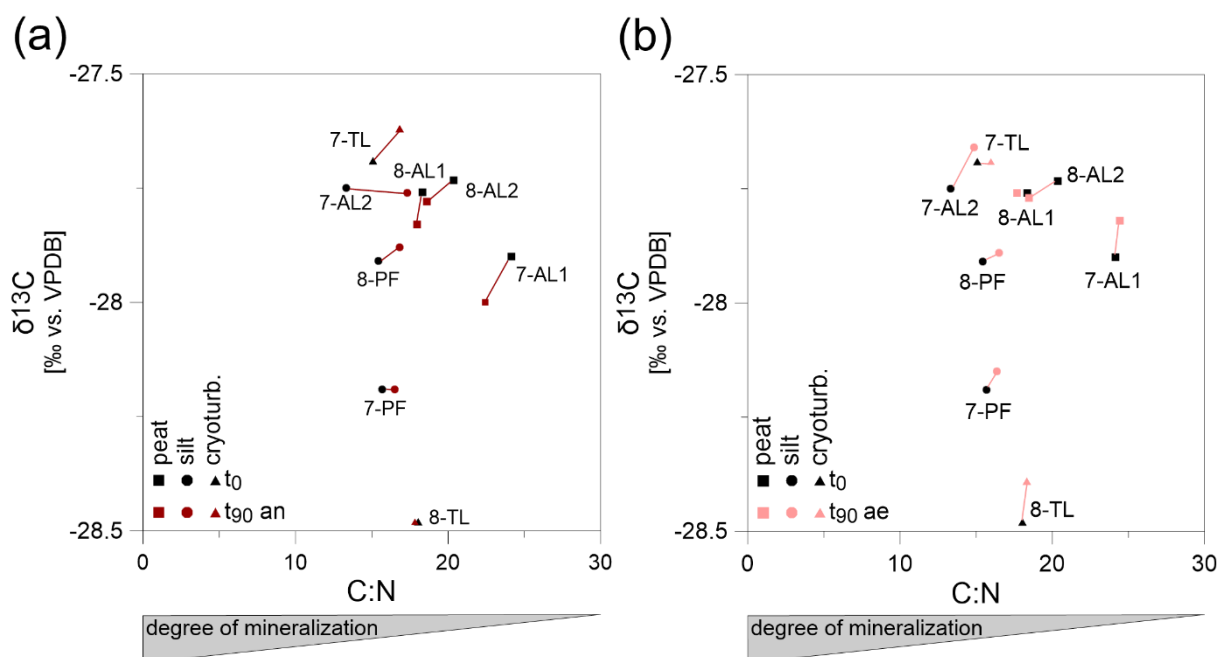
Figure 42: Geochemical proxies C:N ratio and $\delta^{13}C$ after incubation experiments. Laboratory incubation for 90 days at 4 °C under (a) anaerobic and (b) aerobic conditions.

In contrast, the paired t-test confirmed significant changes in TN, TOC, and pH within the anaerobic incubation experiment, but changes in TN and TOC were negligibly small according to Cohen's d. For paired t-test results, it has to be considered that analyses of TOC, TN, C:N and $\delta^{13}C$ include the combustion of material. Hence, the t_0 and t_{90} measurements are not the same sampling material and quality of results relies on meticulous homogenization of sampling material. A drop of pH values is induced by CO_2 dissolution in the water (Haugan & Drange 1996; Millero et al. 2007). The decline

appeared to be higher in silty sediment samples, whereas the peaty top layers remained nearly unaltered. The effect size of pH changes expressed by Cohen's d was higher in anaerobic (d = 0.92) than aerobic (d = - 0.21) conditions.

In summary, the effects of the short-term low-temperature incubation experiments on the organic matter cannot yet be sufficiently depicted by the established geochemical proxies for degradation, the C:N ratio and $\delta^{13}C$.

6.1.2.2. Lipid biomarkers

The analysis of lipids could provide further insights into the transformation of organic matter within the incubation experiments. Assessing the fate of lipids in soil profiles is highly complex. Several studies have reported the reduction and decarboxylation of *n*-alkanoic acids in soils (Eglinton & Hamilton 1967; Lichtfouse 1998; Amelung et al. 2008) (Figure 43). Conversely, other research suggests that *n*-alkanes are oxidized to *n*-alkanols or *n*-methyl ketones and elongated to form *n*-alkanoic (fatty) acids as the lipid decomposition advances (Amblès et al. 1994; Otto & Simpson 2005; Jansen & Nierop 2009; Anokhina et al. 2018). Hence, multiple reaction pathways have been reported for the lipid decomposition in soils. Furthermore, the *n*-alkanoic acids can be oxidized to shorter-chain-length *n*-alkanoic acids by both plants and aerobic bacteria (Dinel et al. 1990). Short chain-length lipids are hence not necessarily source specific biomarkers (Weete 1976; Baker 1982; Harwood and Russell 1984).
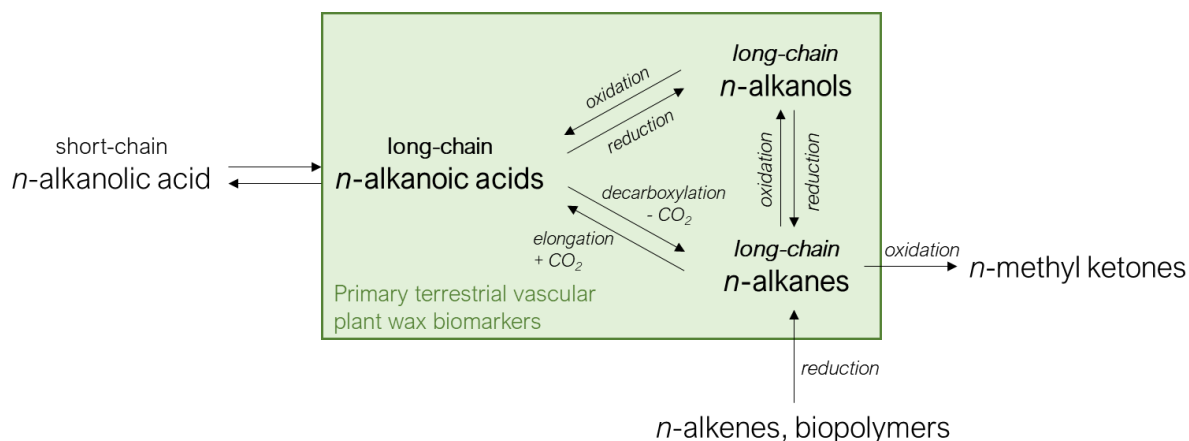
Figure 43: Biosynthetic pathway of long chain n-alkanoic (fatty) acids, n-alkanols and n-alkanes in plant waxes, after (Lichtfouse 1998) according to Kolattukudy (1976), Jansen & Nierop (2009), Killops & Killops (2013), Thomas et al. (2021).

Within our study, we observed significant increases in *n*-alkane and *n*-alkanol concentrations of up to 180 % (*n*-alkanes) and up to 909 % (*n*-alkanols) (Appendix 13). Few other studies reported increases in *n*-alkanes on the short term (Otto & Simpson 2005; Schaefer et al. 2016). Generally decreasing trends of *n*-alkane concentrations over time are expected as a consequence of degradation, as reported in a synthesis paper of lipid biomarker analyses across soil types by Thomas et al. (2021). This increase in *n*-alkane and *n*-alkanol concentration is most likely attributed to the degradation of *n*-fatty acids, though this cannot be assessed within this thesis as results of *n*-fatty acids are not yet available and other pathways of n-alkane and n-alkanol formation in soils are possible (Figure 43). The

accumulation and preservation of *n*-alkanes and *n*-alkanols further appeared to be higher under anaerobic incubation conditions in all samples, except for YC19-DTLB-8 PF (Figure 44). This observation aligns with the generally accepted notion that anaerobic conditions protect reduced organic compounds, such as lipids, from degradation due to lower microbial activity (Fridland 1976; Dinel et al. 1990; Bull et al. 2000).
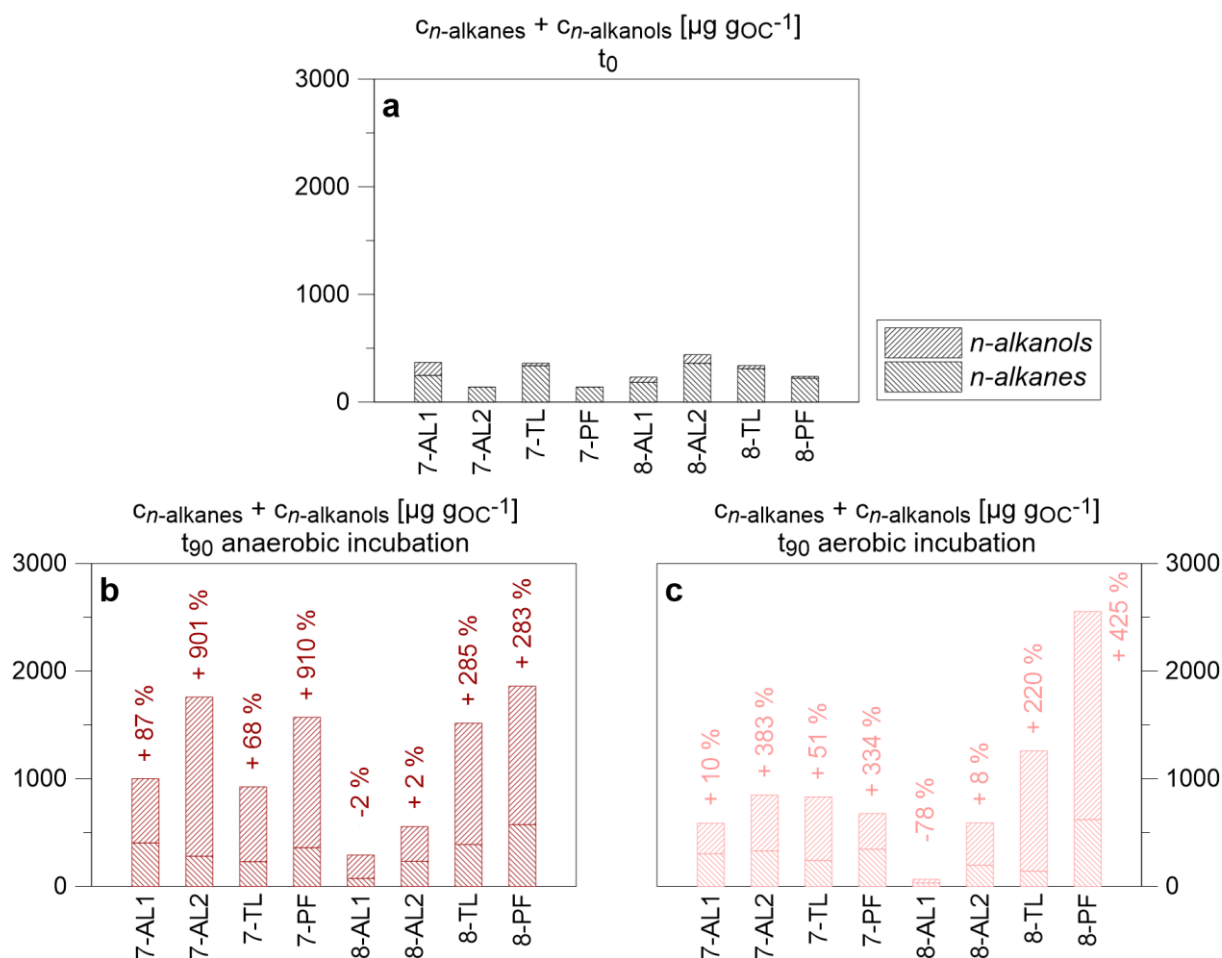
Figure 44: Lipid concentration changes within incubation. (a) Initial n-alkane and n-alkanol concentrations, and changes after 90 days of 4 °C (b) anaerobic and (c) aerobic incubation.

The role of pH as a major control on the fate of extractable lipids in soils and sediment has been highlighted in many studies (Dinel et al. 1990; Bull et al. 2000; Otto & Simpson 2005). Bull et al. (2000) stressed that *n*-alkanes are preferentially preserved under alkaline conditions whereas relative concentrations of *n*-alkanoic acids rise in acidic soils. While we could confirm higher *n*-alkane accumulation in the near-neutral mineral soils compared to more acidic samples (Figure 44, Appendix 13), the enrichment of *n*-alkanols exceeded that of *n*-alkanes in all samples, reflected in significantly increasing HPA. Paired t-tests revealed a significant change in both the *n*-alkanol concentration and the HPA within aerobic and anaerobic incubation conditions (Figure 40, Appendix 22).

Within our study, the dominant *n*-alkane homologue generally either remained the most abundant in the soil or was superseded by an even longer chain length, in accordance with studies by Bull et al. (2000) and Angst et al. (2016). The high *n*-alkanol accumulation came with major, but inconsistent changes of ACL. We observed ACL of *n*-alkanes mostly decreased during aerobic and anaerobic

incubation, and this change is significant according to the paired t-test. It is demonstrated how source-specific patterns can become less pronounced with degradation (Schaefer et al. 2016). As abundant homologues are preferentially degraded, changes in ACL can occur (Zech et al. 2013; Schädel et al. 2016). The same accounts for the observed increase of P_{aq} within incubation, highlighting how microbial organic matter degradation has the potential to distort characteristic leaf wax lipid patterns and may mask the terrestrial origin of OM (Bull et al. 2000; Miltner et al. 2012; Gleixner 2013; Li et al. 2018).

Degradation proxies CPI and OEPD of *n*-alkanes typically decrease with decomposition (Angst et al. 2016; Schaefer et al. 2016; Li et al. 2018; Thomas et al. 2021). The interpretation of the CPI of *n*-alkanols and *n*-alkanoic acids is not as straightforward as of *n*-alkanes (Thomas et al. 2021). Their CPI values can increase with degradation as the result of hydrolysis of other lipids containing long chain acids and alcohols or microbial alteration of other alkyl components (Andersson & Meyers 2012). Although we observed major shifts in lipid composition, a degradation of lipids was not significantly reflected in changing CPI or OEPD values according to results of the paired t-test.

Paired t-test results demonstrated the importance of biomarker analysis to assess carbon characteristics, comprising more significantly changed parameters after the incubation experiments. Further, the effect of changes was higher as compared to simple geochemical metrics like total elemental contents such as TOC or TN. We can conclude that our incubation experiments significantly changed the total concentrations and relative composition of lipid biomarkers, such as the HPA. Still, we stress that a larger sample size and a longer observation period is required to fully assess the fate of lipid biomarkers of our lithological heterogenous sediment cores. Especially as it has to be considered that our study does not cover all extractable lipids and highly important compounds like *n*-alkanoic acids that could distort our observations are missing.

6.2. Greenhouse gas production potential

To address the second research objective, laboratory incubation experiments were carried out in order to assess the greenhouse gas production potential from thawed drained lake basin sediment. Environmental conditions and substrate availability influence greenhouse gas (GHG) production potentials as they are major controls on microbial activity (Dutta et al. 2006; Höfle et al. 2013; Heslop et al. 2015; Faucherre et al. 2018). Consequently, we anticipated finding significantly different GHG production potentials under aerobic and anaerobic incubation conditions, as well as in various soil types and permafrost thermal regimes, within the 90-day low-temperature experiments. Differences among soil types and permafrost thermal regimes were tested in one-way ANOVAs.

The water table usually reflects the border between aerobic and anaerobic regimes in the vertical soil profile. In aerobic soils, carbon mineralization results in CO_2 production, mediated by a range of autotrophic and heterotrophic organisms. Only in anaerobic soils, CH_4 contributes to GHG release as CH_4 is produced solely by anaerobic heterotrophic microorganisms (see chapter 2.3.1.). Therefore,

we expected to detect the carbon turnover only in the form of CO_2 within our aerobic incubation experiment, while CH_4 can contribute to the GHG production potential and fuel the climate forcing effect within anaerobic incubation conditions.

Only a portion of organic carbon accumulated in permafrost soils is susceptible to rapid breakdown upon thaw (Dutta et al. 2006; Zimov et al. 2006a; Elberling et al. 2013). Schädel et al. (2014) highlighted the existence of fast, slow and passive carbon pools in soils, each decomposing with different turnover times (Figure 45). At 5 °C, the labile carbon pool is assumed to decompose within a year, while the slow and passive carbon pools have turnover times of 5 - 15, and > 500 years, respectively (Schädel et al. 2014). Although a carbon pool size analysis was not conducted in our study, our assumption is that in short-term incubation experiments, mainly the labile, fast-cycling carbon pool contributed to observed GHG production potentials (Ping et al. 2015; Vonk et al. 2015). Under aerobic conditions, it is estimated that only 5 – 30 % of the total carbon pool in both organic and mineral permafrost sediment is labile and susceptible to rapid turnover (Shaver et al. 2006; Schädel et al. 2014).
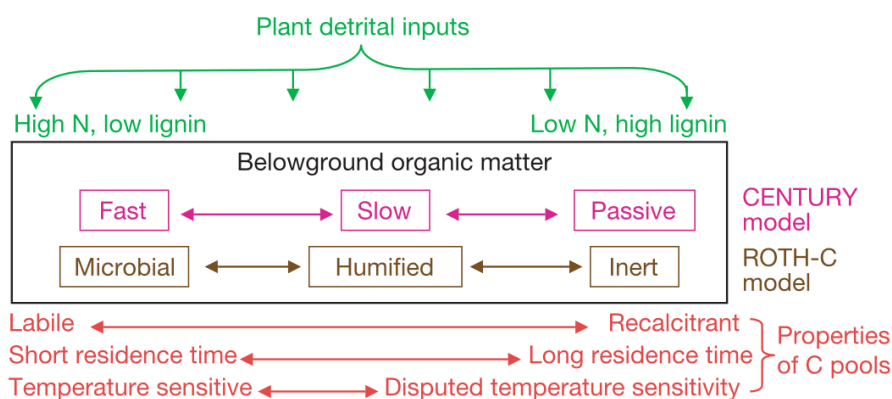
Figure 45: Diagram of properties of conceptual pools of belowground carbon stocks in the CENTURY (Parton et al. 1987) and ROTH-C (Jenkinson 1990) model. Each define three discrete soil carbon pools in the mineral soil that lie roughly along a continuum of decomposability and mean resistance times (MRT) in the soil (Davidson & Janssens 2006).

For all samples, it has to be considered that previous decomposition has taken place. Sediments in drained lake basins may have previously been exposed to aerobic soil conditions (Lee et al. 2012; Jongejans et al. 2021) and may have experienced perennially thawed conditions within a talik underneath a thermokarst lake during lake phases (Jongejans et al. 2021).

6.2.1. Anaerobic incubation experiment

Thermokarst wetlands are known to be one of the most potent sources of CH_4 emissions in permafrost affected environments (Prater et al. 2007; Hodgkins et al. 2014; Treat et al. 2015; Cooper et al. 2017; Wilson et al. 2017). As such, we observed high mineralization of organic carbon to greenhouse gases within the 90-day 4 °C anaerobic incubation experiment. The greenhouse gas production per g_{dw} was related to the content of organic carbon (TOC) (r = 0.62, p < 0.05) and is highest in organic-rich peat sediments, as reported e.g. by Lee et al. (2012), Song et al. (2014), Treat et al. (2015), and Barbato

et al. (2022). Greenhouse gas production per g_{dw} in organic sediment samples was approximately 16 times higher than that in mineral samples, close to values reported in previous studies (Lee et al. 2012: ~ 20).

Even when normalized to g_{OC}, a positive correlation of anaerobic CO_2 and CH_4 production with soil substrate qualities like TOC and TN is expected due to the availability of larger labile C pools and more diverse microbial communities in organic soils compared to mineral soils (Aerts 1997). However, this trend was not very pronounced in our study, and was only statistically significant for CH_4 (r = 0.39, p < 0.05). Many authors that could not encounter a correlation of TOC and C:N with the greenhouse gas production concluded that the projection of methane production from thawing permafrost solely based on soil carbon quality appears to be an oversimplification (Heslop et al. 2015; Holm et al. 2020; Jongejans et al. 2021; Knoblauch et al. 2021). Jongejans et al. (2021) emphasized that the sediment samples have been exposed to different depositional conditions and thaw history since their deposition, which can distort the relations.

All samples remarkably surpassed the median value of the maximum CH_4 production rates in drained lake basins reported in a synthesis study of anoxic Arctic soil incubations by Treat et al., (2015) (Table 17).

Table 17: Comparison of anaerobic incubation characteristics with synthesis study of Treat et al. (2015).

	This study	Treat et al. (2015) Sample count = 7
Site	Drained lake	Drained lake
Temperature [°C]	90 d, 4 °C	4 °C
Max. CH_4 production [µg CH_4-C g_C^{-1} d^{-1}]	1.34 - 23.75	0.6 ± 0.3
Lag time [d]	17 - 34	19 ± 9
Decay [% d^{-1}]	1.80 - 8.77	1.16 ± 0.37
Mean CO_2 production [µg CO_2-C g_C^{-1} d^{-1}]	0.14 - 4.31	125 ± 47
Median CO_2:CH_4 production	0.23 - 2.35	34

Despite the short incubation period, we observed considerable CH_4 production in all samples except for the PF samples (Figure 22, Figure 23, Appendix 6). All samples showed a production rate peak within the incubation period, occurring between day 14 and 34 of the experiment (Table 10, Figure 24). Peak production rates did not surpass inital production rates that are commonly high due to disturbances during sample preparation at the start of the experiment in the PF samples. The encountered longer lag times and low CH_4 production in deeper permafrost layers might be attributed to the delay of methanogen community establishment (Knorr & Blodau 2009; Nilsson & Öquist 2009). This relation was demonstrated by mean lag times of 41 ± 9 days in samples from 0 – 20 cm depth compared to 765 ± 110 days in > 100 cm depth within the synthesis study of Treat et al. (2015).

The absence of an established methanogenic community has previously inhibited CH_4 production in permafrost incubation studies, with significant CH_4 production reported only after several months (Rivkina et al. 2007; Knoblauch et al. 2013) to multiple years (Knoblauch et al. 2018; Walz et al. 2018), or not occuring at all (Walz et al. 2018; Holm et al. 2020). This has led many authors to conclude that the contents of labile carbon and nitrogen are less important drivers of CH_4 compared to CO_2 production (Waldrop et al. 2010; Lee et al. 2012; Knoblauch et al. 2013; Schädel et al. 2014; Holm et al. 2020; Knoblauch et al. 2021). Instead, methanogenesis exhibits a higher sensitivity to unfavourable environmental conditions as only a functionally narrow group of microorganisms is involved in CH_4 production, while a broad range of diverse microorganisms is involved in CO_2 production (Schink 1997; Holm et al. 2020). Therefore, it can be inferred that microbial communities were readily adapted to waterlogged conditions and the analysed drained lake basin sediments readily provided ideal conditions for methanogen species, throughout organic, mineral and cryoturbated layers.

Maximum CO_2 production rates were measured within the first week of the experiment in all samples, reaching up to 139.33 ± 8.61 µg CO_2-C g_{OC}^{-1} d^{-1} in DTLB-7 AL2 and equalling up to 278 times the mean production rate in sample YC19-DTLB-8 TL (Appendix 6). Previous long-term laboratory studies reported that the highest CO_2 production rates occurred within the initial 100 days (Walz et al. 2018). Some samples in this study exhibited fluctuating production rates, potentially indicating shifts in substrate supply (Schädel et al. 2014). Several studies have emphasized the non-linearity of greenhouse gas production rates in anaerobic laboratory incubation studies (Elberling et al. 2013; Knoblauch et al. 2013; Schädel et al. 2014; Walz et al. 2018).

In contrast to the high CH_4 production, the mean CO_2 production rates were magnitudes lower than the median rate of CO_2 production reported in the synthesis of anaerobic incubation studies by Treat et al., (2015) (Table 17). Regarding the high methanogen activity in our samples, these low concentrations potentially arised from *in situ* CO_2 consumption by hydrogenotrophic methanogens (see chapter 2.3.1.).

After initially high CO_2 production rates, a decrease of CO_2 concentrations in the vial headspace was apparent in all samples during early phases of anaerobic incubation (Figure 46). Those negative CO_2 production rates were rarely reported in anaerobic incubation studies. This phenomenon could be attributed to higher CO_2 solubility in water under high pressure that was noticed in the first weeks of the incubation experiment. Unfortunately, this observation could not be supported by pressure data as monitoring vial pressure was not part of the experimental setup. Dissolved CO_2 in the pore water could, in turn, act as a highly accessible source of carbon for methanogens (Hornibrook et al. 1997; Marschner & Kalbitz 2003; Dutta et al. 2006), as the CO_2 reduction pathway for methanogenesis prevails in acidic northern peatlands (Hornibrook et al. 1997; Horn et al. 2003; Lee et al. 2012). However, the observed decrease in CO_2 concentration did not scale with CH_4 production as it was also observed in the PF samples, which only showed very limited CH_4 production. Further,

methanogenesis is typically associated with a rise in CO_2 production (Knoblauch et al. 2013; Holm et al. 2020). It must be regarded that CO_2 and CH_4 production are not the only processes associated with organic matter decomposition in the sediment, and other important processes are not monitored in this study. The effect requires further investigation. The occurrence of this phenomenon is potentially linked to our experimental setup which did not include vial headspace flushing of anaerobic incubation vials. We cannot rule out that because of a later onset of CH_4 production, longer measurement intervals mask decreases in the CO_2 headspace concentration in other studies. This process biases our CO_2 data as the potentially high pressures within the incubation vials and the large interface of gas and porewater phase were not representative of natural conditions. Hence, CO_2 production might be underestimated.

Within the laboratory incubation experiment, three distinct phases of CO_2:CH_4 production rate ratios could be defined over the course of the anaerobic incubation experiment. An initial phase of high CO_2 production and no substantial CH_4 production (CO_2:CH_4 production rate ratio >> 1) lasted approximately 10 - 13 days in active layer samples and 17 - 20 days in the transition layer and permafrost samples (Figure 46). This phase has been reported in other studies (Holm et al. 2020), but typically lasted longer because of longer CH_4 lag time. With ongoing incubation, CO_2:CH_4 production rate ratios decreased, as a larger proportion of anoxic mineralization occurred via methanogenesis (Hodgkins et al. 2014; Holm et al. 2020). In our study, CH_4 production outweighed the CO_2 production during this phase (CO_2:CH_4 production rate ratio < 1), even including negative CO_2 production rates (see above) (Figure 46). Subsequently, a stabilization of production rates appeared to be established within the short incubation period, again reflecting quickly adapting microbial communities (Figure 46). Production rate ratios stabilized at values < 1 for AL and TL and > 1 for PF samples.

The CO_2:CH_4 production ratio is indicative of the oxidation state of the organic carbon and the availability of nitrate, ferric iron or sulfate as alternative electron acceptors (Nilsson & Öquist 2009; Knoblauch et al. 2018). Knoblauch et al., (2018) stated that while optimum conditions for methanogenesis are typically indicated by equal CO_2 and CH_4 production, CO_2:CH_4 ratios can be < 1 in absence of alternative electron acceptors. Instead, reported CO_2:CH_4 production ratios are typically >> 1 (Nilsson & Öquist 2009b; Treat et al. 2015), which Knoblauch et al. (2018) attributed to the underestimation of the long-term CH_4 production potential within short incubation periods.
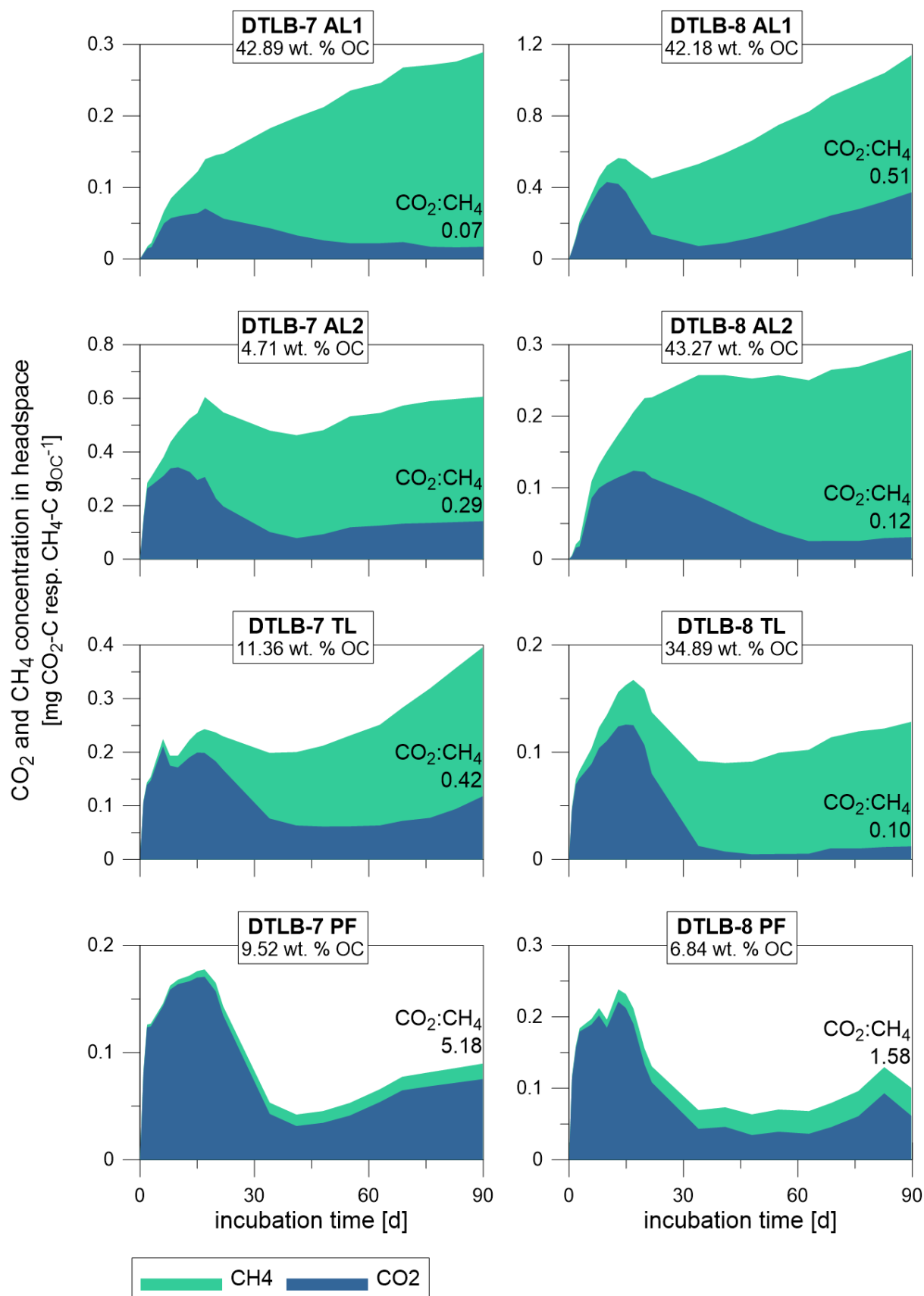
Figure 46: Composition of GHG concentration in vial headspace over time. blue = CO₂, green = CH₄, labels describe rate of produced CO₂:CH₄ at t₉₀, values > 1 indicate higher contribution of CO₂, values < 1 indicate higher contribution of CH₄. Note that shifts in composition not only reflect production, but also decreases in headspace concentration for CO₂.

As a result, the contribution of CH_4 to cumulative GHG production after 90 days of anaerobic incubation ranged from 16.16 – 94.13 % (Figure 46), higher than reported in previous permafrost incubation studies (Table 18). Since low shares of CH_4 contribution have been attributed to lower initial methanogens abundance in permafrost sediments (Waldrop et al. 2010; Knoblauch et al. 2013), we likely encountered a higher initial abundance of methanogens within our samples. This will be investigated in a comprehensive microbial analysis that is not part of this thesis.

Table 18: Comparison of methane contributions to GHG production under anaerobic incubation conditions.

	Thermal regime	Soil type	Incubation setup [°C]	CH_4 contribution to GHG release [%]
This study	AL + PF	mineral	90 d, 4 °C	16.16 – 77.69
	AL	organic	90 d, 4 °C	67.30 – 94.13
Estop-Aragonés et al. (2022)	AL + PF (0 – 6 m)	organic	714 d, 5 °C	0.0002 - 0.77
Knoblauch et al. (2013)	PF (0.6 – 25 m)	mineral	1200 d, 4 °C	29.3 ± 19.7
Knoblauch et al. (2018)	PF (0.6 – 23 m)	mineral	3 a*, 4 °C	~ 50
Lee et al. (2012)	PF (0.4 – 10 m)	mineral	500 d, 15 °C	0.2 – 26.7
	AL	organic	500 d, 15 °C	2.3 – 11.6
Treat et al. (2014)	AL + PF (0 – 1 m)	organic	30 d, 20 °C	0.43 ± 0.017

* after 4 years of pre-incubation until MO community establishment (production of CH_4)

ANOVA of anaerobic CH_4 and CO_2 production revealed no significant differences among soil types ($p > 0.05$) (Figure 47) that were reported by Roy Chowdhury et al. (2015) and Treat et al. (2015). Again, it must be regarded that the CO_2 concentrations at t_{90} are the result of CO_2 production and CO_2 dissolution observed in the incubation vials. Further, it has to be regarded that in our short-term incubation experiment, the CH_4 lag time had a major impact on cumulative GHG production at t_{90}. However, the effect of soil substrate quality parameters on the GHG production was apparent in production rate decay that was observed to be highly negatively correlated with soil type parameters, and ANOVA confirmed signifcant differences of production rate decay between soil types for both CO_2 ($p < 0.01$) and CH_4 ($p < 0.05$). Contrary to previous findings, decay rates within our study appeared to be higher in mineral samples and are not determined by depth (Pearson's correlation: $r = 0.33$, $p < 0.05$) or thermal regime (ANOVA $p > 0.05$) (Treat et al. 2015; Estop-Aragonés et al. 2022). Labile carbon pools in mineral soils appeared to be depleted at faster rates than in organic soils.

Further, CH_4 production and the maximum CH_4 production rate was significantly different between permafrost thermal regimes (AL, TL, PF) (ANOVA $p < 0.01$) and CH_4 production was strongly negatively correlated with depth, aligning with observations by Waldrop et al. (2010), Song et al. (2014), Treat et al. (2015), Jiang et al. (2020), and Estop-Aragonés et al. (2022). The expected distinct trend of longer lag times in mineral compared to organic samples as reported by Treat et al. (2015) could not be tested by ANOVA in our study as values were not normally distributed (Shapiro-Wilk: $p < 0.05$) (Table 15). Pearson's correlation revealed moderate - strong correlation of the CO_2 lag time with soil type parameters TOC, TN and the C:N ratio. However, correlation was only weak – moderate for CH_4 lag times (Table 13). Correlations further implied that maximum production rates of CO_2 per g_{OC} were higher in silty, pH-neutral samples, while the lag time was shorter. However, these differences were not statistically significant according to ANOVA ($p > 0.05$). A correlation of maximum production rates of CO_2 and CH_4 with soil quality substrates was also reported by Holm et al. (2020). The $CO_2:CH_4$ ratio at t_{90} was highly positively correlated with depth (Table 13), aligning with Treat et al. (2015) and Knoblauch et al. (2018). The observation was further supported by ANOVA, revealing significant differences among permafrost thermal regimes ($p < 0.05$). It has to be regarded that within this short-term incubation study, the variation in $CO_2:CH_4$ was highly influenced by the timing of the onset of higher CH_4 production and should be assessed again at a later point in time. Lower anaerobic $CO_2:CH_4$ in mineral soils than in organic soils, as reported by Treat et al. (2015), were not confirmed by ANOVA. Still, a relation was indicated by moderate negative correlation of $CO_2:CH_4$ with soil type parameters TOC, TN and the C:N ratio.

Figure 47: Schematic illustration of the differences of anaerobic GHG production among soil types and permafrost thermal regimes according to one-way ANOVAs.

In conclusion, the anaerobic incubation experiment has demonstrated the high, and highly unfavourable composition of greenhouse gases that could be produced in drained lake basin sediments on the short term. Further, the data supports the conclusion that short-term GHG production potentials in anaerobic conditions cannot be sufficiently predicted by soil type parameters alone (Jongejans et al. 2021).

6.2.2. Aerobic incubation experiment

Carbon mineralization showed high deviation in organic samples, with low CO_2 production in the two pioneer peat samples, where only ~ 0.4 % of initial OC were mineralized within the 90 days of aerobic incubation, while > 2 % of the OC were mineralized in established peat sample YC19-DTLB-8 AL1. Carbon turnover in pioneer peat samples appears to be restricted, showing the lowest carbon loss of all samples despite exhibiting high TOC contents and C:N ratios, commonly interpreted as a proxy for OC availability (Chapin et al., 2012; Gentsch et al., 2015; Malmer & Holm, 1984; Schädel et al., 2014; Weiss et al., 2016). Faucherre et al. (2018) and Schädel et al. (2014) provided the explanation that on the short term, microbial communities can experience a shortage of N as a nutrient necessary for OC mineralization in soils with high C:N ratios (> 25) (Enríquez et al. 1993). Indeed, the pioneer peat samples showed C:N ratios > 20, the highest values within the individual sediment core. As a result, the C_{loss} and the C:N ratio are often negatively correlated in early phases of incubation, aligning with our observations (r = - 0.62, p < 0.05) (Appendix 18). As C:N ratios decrease with progressing decomposition as C is lost and N is retained and recycled (Malmer & Holm 1984; Chapin et al. 2002), a positive correlation is reported on the long term (Schädel et al. 2014; E. Schuur et al. 2015). Carbon mineralization (C_{loss}) under aerobic conditions was within the range of previous studies (Table 19).

Table 19: Comparison of GHG production within laboratory aerobic incubation experiments.

	Thermal regime	Soil type	Incubation setup	C_{loss} [% C_{ini}]
This study	AL	organic	90 d, 4 °C	0.43 - 2.23
	AL+PF	mineral	90 d, 4 °C	1.87 - 2.70
(Dutta et al. 2006)	PF	Yedoma	90 d, 5 °C	2.1 ± 0.2
(Elberling et al. 2013)	Top PF	heath	12 years, 5 °C	55
	Top PF	Wet grassland	12 years, 5 °C	75
(Estop-Aragonés et al. 2022)	AL + PF (0 – 6 m)	peat	714 d, 5 °C	0.21 - 7.79
(Faucherre et al. 2018)	AL	peat	343 d, 5 °C	2.22 ± 2.10
	PF	mineral	343 d, 5 °C	2.54 ± 1.51
(Knoblauch et al. 2013)	PF (0.6 – 25 m)	mineral	1200 d, 4 °C	3.1
(Schädel et al. 2014), (synthesis study)	AL + PF (0 – 1.2 m)	organic	365 d, 5 °C	6
	AL + PF (0 – 22 m)	mineral	365 d, 5 °C	< 5
(Treat et al. 2014)	AL + PF (0 – 1 m)	organic	30 d, 4 °C	0.37

The high carbon turnover of ~ 2 % in mineral permafrost layers, as high as in established surface peat samples, can be attributed to the impact of permafrost freeze-thaw processes. Cryoturbation has the

potential to incorporate large amounts of labile DOC into deep layers (Beer et al. 2022). This incorporation of accessible DOC implies an important proportional increase of the highly available labile C fraction in deep mineral samples compared to organic samples (Weiss et al. 2016). A fast carbon decomposition in mineral soils has been reported by numerous studies and has been attributed to this higher content of intrinsically labile organic matter in syngenetic permafrost before (Dutta et al. 2006; Zimov et al. 2006a; Waldrop et al. 2010; Lee et al. 2012; Jongejans et al. 2021). The high peak production rates detected in mineral samples further indicate the presence of higher relative proportion of the labile carbon pool (Melchert et al. 2022) (Appendix 7). Hence, the deep mineral soil OM has a high potential for being degraded into CO_2. Naturally, this influence is expected to decline with ongoing incubation (Faucherre et al. 2018).

With lag times of only 14 to 45 days, peaks in production rates occurred early on within the aerobic incubation experiment, in conformity with previous incubation studies (Dutta et al. 2006). This also accounts for the silty PF samples, which did not show long time lags to adapt and immediately mineralized significant amounts of carbon to CO_2. Following maximum production rates, rates remained constant for the rest of the 90-day period. Multiple studies reported these steady production rates establishing within the first weeks of aerobic incubation (Dutta et al. 2006; Lee et al. 2012), or the majority of GHG release occuring early on in incubation experiments (Walz et al. (2018): 51 % within 134 days of 1 year, Elberling et al. (2013): 20 % within first 21 months of 12 years). Hence, it can be concluded that aerobic carbon mineralization is less restricted to environmental conditions compared to anaerobic carbon mineralization as overall early GHG production is reported.

A moderate – strong positive correlation with the cumulative CO_2 production per g_{dw} after 90 days of incubation could be observed (Dutta et al. 2006; Song et al. 2014; Knoblauch et al. 2021; Barbato et al. 2022). ANOVA confirmed differences being significantly different among soil types ($p < 0.1$) (Figure 48). Interestingly, the correlations of cumulative CO_2 production per g_{dw} and g_{OC} showed opposing trends. While organic soils showed higher CO_2 production potential per g_{dw} due to their higher TOC content, Pearson's correlation confirmed that mineral soils exhibited higher CO_2 production potential per g_{OC}. In line with observations from the anaerobic incubation experiment, bulk geochemical parameters were highly negatively correlated with the maximum CO_2 production rate and the following production rate decay. Indicating that carbon pools in mineral soils are depleted at faster rates, which is also suggested by ANOVA ($p < 0.1$ for maximum production and $p < 0.05$ for production rate decay) (Figure 48). The decay of production rates further showed strong correlation with depth. However, ANOVA could not confirm any significant differences among permafrost thermal regimes. Correlations with depth were moderate but will likely be more precise after longer incubation, when production peaks are fully covered within the incubation period.
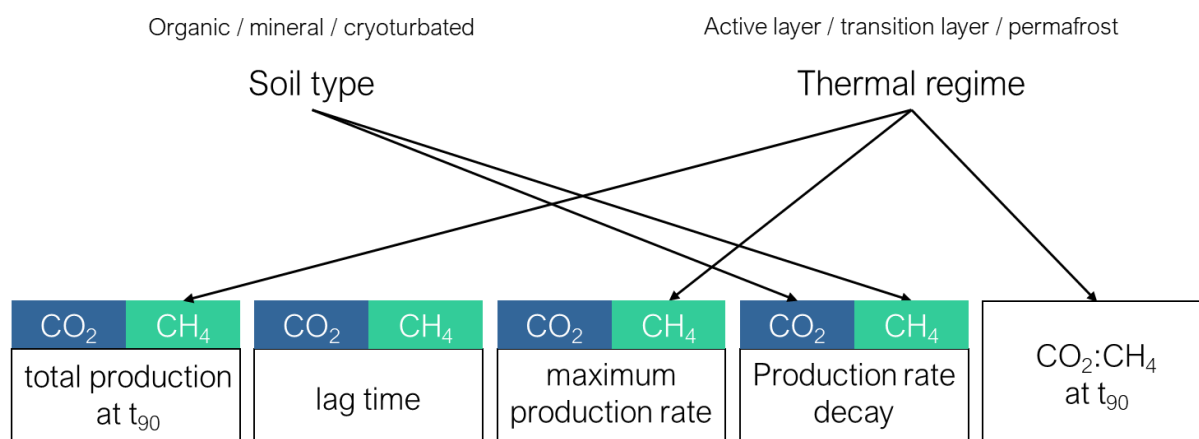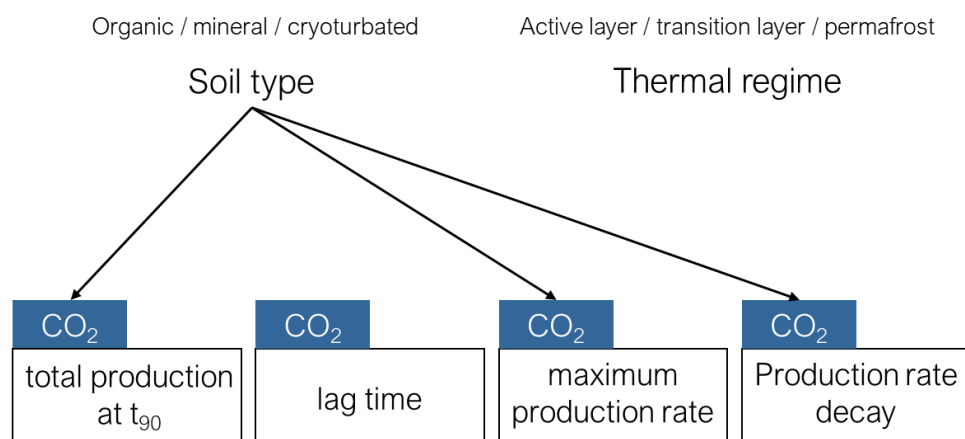
Figure 48: Schematic illustration of the differences of aerobic GHG production among soil types and permafrost thermal regimes according to one-way ANOVAs.

It can be concluded that the sediment cores likely contain diverse or well-established microbial community across all layers, resulting in aerobic decomposition of organic matter being generally less dependent on environmental conditions. High carbon loss and maximum production rates hint to a high labile carbon content in mineral samples in the permafrost layer. In contrast, presumable N limitation retards greenhouse gas production potential of pioneer peat samples.

6.2.3. Comparison of greenhouse gas production potentials

The total greenhouse gas production was orders of magnitude higher under aerobic incubations conditions in all samples covering organic and mineral sediments (Table 20). A higher carbon release under aerobic compared to anaerobic incubation conditions has been reported in multiple studies (Lee et al. 2012; E. Schuur et al. 2015; Schädel et al. 2016; Knoblauch et al. 2018; Estop-Aragonés et al. 2022) as microbial communities take longer to establish and mineralize substantially amounts of carbon under anaerobic conditions. However, Davidson & Janssens (2006) remarked that while anaerobic conditions delay carbon pool mineralization, that does not imply that labile carbon pools transform into recalcitrant passive carbon pools. Hence, we expect that this gap of production under aerobic and anaerobic conditions will decrease with ongoing decomposition on the long term.

In accordance with greenhouse gas production values, the shares of the initial organic carbon content mineralized to GHG was substantially higher under aerobic incubation conditions (0.43 – 2.70 %) compared to anaerobic conditions (0.01 – 0.15 wt. %). Lee et al. (2012) observed a strong correlation of greenhouse gas production under aerobic and anaerobic conditions. So far, the share of OC that is mineralized to GHG under aerobic and anaerobic conditions showed moderate positive correlation ($r = 0.45$, $p < 0.05$) (Appendix 20). It can be assumed that short-term effects such as the delayed methanogen community establishment in anaerobic conditions (see chapter 6.2.1.) or restrained carbon turnover due to N limitation (see chapter 6.2.2.) are constrains on the relation. Similarities in greenhouse gas production behaviour under aerobic and anaerobic conditions are depicted by highly

correlating maximum CO_2 production rates (r = 0.90, p < 0.05) and CO_2 production rate decay (r = 0.80, p < 0.05) (Appendix 20).

Assuming a global warming potential (GWP) of methane of 28 CO_2-equivalents on a 100-year timescale (IPCC 2014), the relative climate forcing (RCF) of each sediment sample on a short timescale is higher under anaerobic conditions compared to aerobic conditions due to the influence of the more potent greenhouse gas methane (Table 20, Figure 49, Figure 50). An exception from this trend are the samples from permafrost layers. For these samples, the relative climate forcing exhibits a large surplus in climate impact under aerobic conditions.

Table 20: Comparison of GHG production potential and climate forcing effect of GHG production under aerobic and anaerobic incubation conditions.

	Soil type	Relative Carbon Release g_{OC}^{-1} t_{90} ae/an	Relative Climate Forcing t_{90} ae/an
YC19-DTLB-7 AL1	Organic	15.6	0.66
YC19-DTLB-7 AL2	Mineral	14.0	0.71
YC19-DTLB-7 TL	Cryoturbated	13.3	0.75
YC19-DTLB-7 PF	Mineral	110.7	22.69
YC19-DTLB-8 AL1	Organic	10.2	0.60
YC19-DTLB-8 AL2	Organic	11.9	0.53
YC19-DTLB-8 TL	Cryoturbated	32.6	1.43
YC19-DTLB-8 PF	Mineral	123.7	12.01
Lee et al. (2012) (500 d, 15 °C)	Organic + Mineral	3.9 - 10.0	1.4 - 7.1
Schädel et al. (2016) (synthesis study)	Organic + Mineral	3.4	2.3
Knoblauch et al. (2018)			~ 0.47

Delayed microbial assemblage can be accounted for the low anaerobic carbon release and hence a low climate forcing potential of anaerobic emissions of permafrost layers on the short term. Hence, depth acts as a factor controlling the anaerobic greenhouse gas production and relative climate forcing on the short term. In contrast, soil type changes do not appear to influence relative carbon release and the relative climate forcing, as the ratios remain approximately constant in all layers. As data was not normally distributed, this observation could not be confirmed by ANOVA.

Depth, or the permafrost thermal regime did not determine greenhouse gas production under aerobic conditions in this study. Here, the availability of organic matter that is dependent on the soil type, generally showed higher influence on the carbon mineralization.
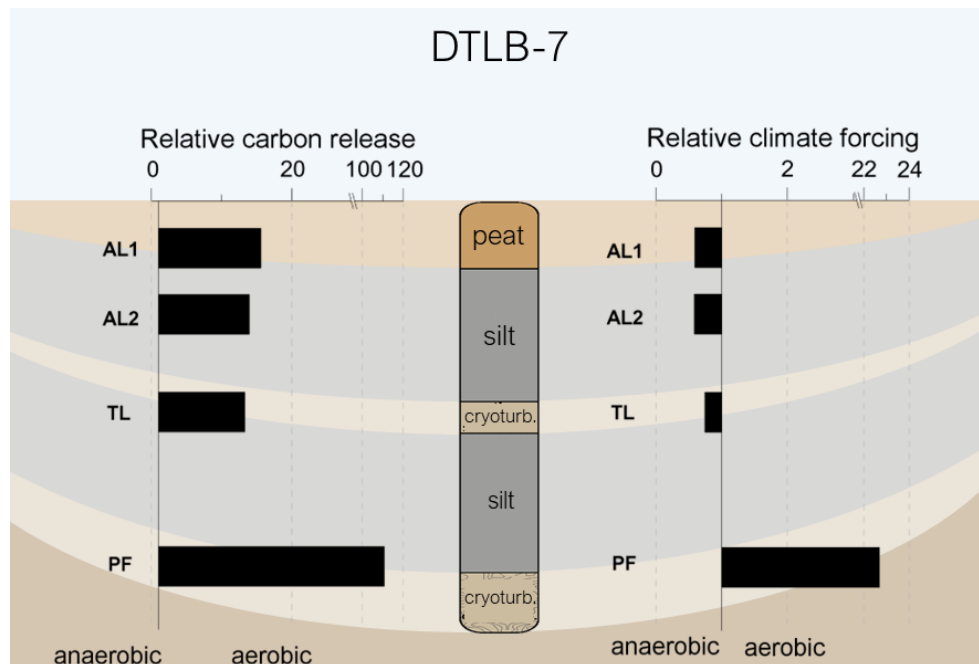
Figure 49: Relative carbon release and relative climate forcing in YC19-DTLB-7.
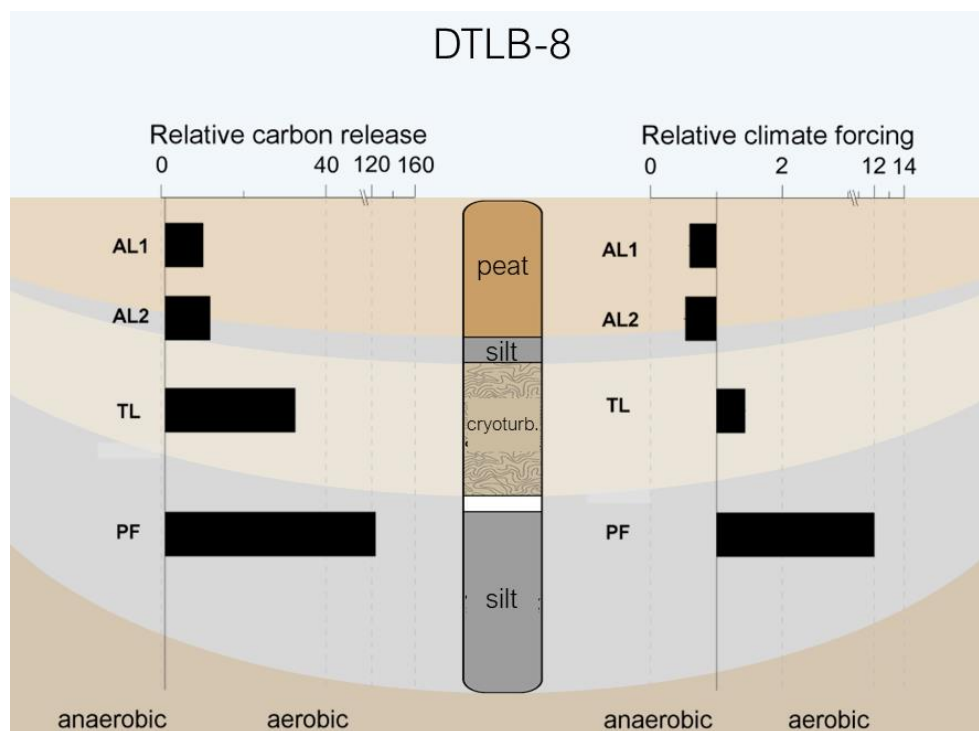
Figure 50: Relative carbon release and relative climate forcing in YC19-DTLB-8.

6.3. Limitations

There are multiple limitations to the validity of results of short-term laboratory incubation studies that have to be considered when interpreting incubation studies on the greenhouse gas production potential. Firstly, it has to be regarded that homogenization and mixing of sampling material, especially of peat samples, likely broke bonds and increased availability of labile OM which is reflected in high production rates starting the incubation experiments (Nilsson & Öquist 2009; Elberling et al. 2013;

Knoblauch et al. 2013; Schädel et al. 2014). The influence of this effect is less significant on longer terms. Therefore, short term production rates are not suitable to be upscaled to long term behaviour, as production rates decline over time.

Further, differing laboratory methods constrain comparability with other published studies.

Importantly, laboratory incubation experiments fail to depict *in situ* conditions regarding effect interactions in multiple ways, e.g. the migration of microbial communities and methane oxidation. The anaerobic methane production potential which should not to be equated with methane emissions to the atmosphere as parts of the produced methane will be trapped, dissolved or consumed in the aerobic zone of surface soils (Knoblauch et al. 2008; Kip et al. 2010; Lee et al. 2012; Knoblauch et al. 2013; Heslop et al. 2015). Long lag times of methane production under anaerobic condtions can also lead to an underestimation of CH_4 production potential in short-term anaerobic incubation studies (Knoblauch et al. 2021). As a result, measured concentrations of anaerobic CH_4 and aerobic CO_2 in laboratory incubation experiments are production potentials that deviate from *in situ* GHG emissions (Knoblauch et al. 2021).

Lastly, assessing the ecosystems sink or source behaviour would require determining carbon uptake by vegetation. Further, long-term responses of permafrost microbial communities to thawing remain unclear (Mackelprang et al., 2011).

Concerning statistical analyses, it has to be taken into account that the small sample count (n = 8) and the lack of organic sediment samples from PF depths in our study are constraints on assessing if our observations align with differences in composition or depth. In summary, the large heterogeneity of our samples is not sufficiently depicted by the low sample count of our study.

7. Conclusion

Drained lake basin environments in the Arctic continuous permafrost region are dynamic ecosystems that have repeatedly experienced major changes in hydrology and vegetation composition. The high productivity of vegetation has led to the incorporation of layers rich in organic carbon (OC) into the sediment stratigraphy. These carbon pools in drained lake basins (DLBs) on the Yukon coastal plain are highly susceptible to thawing in response to climate warming due to high ice contents. The heterogeneous stratigraphies of drained lake basins render it challenging to make a generalized assessment of organic matter decomposition and greenhouse gas production potentials.

In the analyzed sediment samples, high C:N ratios, low $\delta^{13}C$ values and distinctive *n*-alkane and *n*-alkanol distribution patterns, comprising long-chain length and a pronounced odd-over-even resp. even-over-odd predominance, pointed to a high input of terrestrial vascular plant waxes to the organic matter. High values and no apparent depth trends of degradation proxies C:N, CPI or the lipid concentration suggest limited degradation of the organic matter within the permafrost-affected soils in the drained lake basins. Although we cannot report correlation of C:N and $\delta^{13}C$, both parameters appeared to decrease with depth, and a significant positive correlation of C:N and CPI was confirmed.

After 90 days of 4 °C aerobic and anaerobic incubation experiments, we observed high accumulation of *n*-alkanols, particularly in mineral samples and under anaerobic conditions. This does not align with common observation that lipids are decomposed during organic matter degradation and thus, lipid concentrations in sediments decrease. It is important to note that that *n*-alkanes and *n*-alkanols studied in this thesis do not represent the entire lipid concentration. The hypothesis that increasing *n*-alkane and *n*-alkanol concentrations arise from decomposition of *n*-fatty acids could not be investigated as results from *n*-fatty acid biomarker analysis were not yet available.

Despite the observation that geochemical degradation proxies C:N and $\delta^{13}C$, as well as biomarker degradation proxies like the carbon preference index (CPI) of *n*-alkanes were not significantly altered within the incubation experiment, paired t-tests confirmed significant changes in other biomarker parameters like the *n*-alkanol concentration, the average chain length (ACL) and the higher plant alcohol index (HPA). Hence, although organic matter did not experience significant degradation within the short incubation period, the composition of lipids underwent substantial alterations. Therefore, we conclude that even though contributing only minor portions to the organic carbon content, lipid biomarkers are valuable proxies detecting small-scale changes of organic matter within short-term incubation experiments.

The contribution of CH_4 to the greenhouse gas production potential within anaerobic incubation experiments was notably higher in this study compared to findings reported in other studies. The combination of high CH_4 production and short lag times of maximum production rates in our samples suggests that the sediments provided ideal conditions for methanogen species. It appears that that methanogen microbial communities were already well-established in the sediment and were able to adapt to thawed conditions quickly. Moreover, the $CO_2:CH_4$ production rate ratio appeared to stabilize

within the short incubation period at values < 1 within active and transition layers, whereas remaining > 1 permafrost layers. Analysis of variance (ANOVA) confirmed that CH_4 production significantly differed among permafrost thermal regimes. Additionally, the influence of soil type is reflected in the production rate decay of both CH_4 and CO_2 production rates, indicating variations in the size and decomposability of the labile carbon pool.

Greenhouse gas production in the aerobic incubation experiment showed less depth-related influence, with significant CO_2 production observed in samples from all thermal regimes within the short-term incubation period. Even in samples from the currently perenially frozen permafrost layer, organic carbon was very labile and was readily decomposed at 4 °C. The enhanced carbon turnover in permafrost soils may result from the additional incorporation of labile carbon into deeper layers through cryoturbation processes, which has higher relative importance in mineral soils compared to organic soils. This underscores that as thaw progresses, deeper layers, particularly in mineral soils, could rapidly mineralize significant proportions of organic carbon under aerobic conditions. In contrast, microbial carbon turnover in pioneer peats above the organic – mineral interface seemed to be constrained by limited nitrogen (N) availability in the short term. It is hence important to note that carbon turnover in the short term does not simply scale with the organic matter content and quality but is more complex. With lower influence of depth on the greenhouse gas production potential, differences among soil types were more pronounced within aerobic incubation conditions, as confirmed by ANOVA.

It has to be regarded that the determined greenhouse gas production potential in laboratory incubation studies does not reflect the actual GHG emissions as CH_4 will experience consumption when migrating through oxic near-surface soil layers. Further, the potential of drained lake basins to store high amounts of atmospheric carbon in vegetation and peat has to be recognized when assessing the ecosystems sink or source potential.

Regarding the high landscape cover of lake – drained lake basin environments in Arctic lowlands, and considering the reported increased lake drainage in northern wetlands, understanding carbon decomposition in drained lake sediments is highly relevant for the assessment of the circumpolar permafrost carbon feedback. Trajectories of hydrologic conditions in drained lake basin will determine the pace and form of decomposition of the organic carbon pool and hence, the potential greenhouse gas emissions. Thaw depth progression under aerobic conditions in drained soils could cause immediate and high peaks in greenhouse gas production, though initially high production rates are expected to decline over time. It can further be concluded that DLBs could provide perfect conditions for methanogenesis under anaerobic conditions and hence produce a highly unfavourable mix of GHG, even though microbial response to thaw can be expected to show delay.

8. Acknowledgements

References

Acton P., Fox J., Campbell E., Rowe H. & Wilkinson M. 2013. Carbon isotopes for estimating soil decomposition and physical mixing in well-drained forest soils. *Journal of Geophysical Research: Biogeosciences 118*, 1532–1545, doi: 10.1002/2013JG002400.

Aerts R. 1997. Climate, Leaf Litter Chemistry and Leaf Litter Decomposition in Terrestrial Ecosystems: A Triangular Relationship. *Oikos 79*, 439–449, doi: 10.2307/3546886.

Ågren G.I., Bosatta E. & Balesdent J. 1996. Isotope Discrimination during Decomposition of Organic Matter: A Theoretical Analysis. *Soil Science Society of America Journal 60*, 1121–1126, doi: 10.2136/sssaj1996.03615995006000040023x.

Alewell C., Giesler R., Klaminder J., Leifeld J. & Rollog M. 2011. Stable carbon isotopes as indicators for environmental change in palsa peats. *Biogeosciences 8*, 1769–1778, doi: 10.5194/bg-8-1769-2011.

Amante C. & Eakins B.W. 2009. ETOPO1 Global Relief Model converted to PanMap layer format. *NOAA-National Geophysical Data Center*, doi: 10.1594/PANGAEA.769615.

Amblès A., Parlanti E., Jambu P., Mayoungou P. & Jacquesy J.-C. 1994. n-Alkane oxidation in soil. Formation of internal monoalkenes. *Geoderma 64*, 111–124, doi: 10.1016/0016-7061(94)90092-2.

Amelung W., Brodowski S., Sandhage-Hofmann A. & Bol R. 2008. Chapter 6 Combining Biomarker with Stable Isotope Analyses for Assessing the Transformation and Turnover of Soil Organic Matter. *Advances in Agronomy*. Pp. 155–250. Academic Press, doi: 10.1016/S0065-2113(08)00606-8.

Amundson R., Stern L., Baisden T. & Wang Y. 1998. The isotopic composition of soil and soil-respired CO_2. *Geoderma 82*, 83–114, doi: 10.1016/S0016-7061(97)00098-0.

Andersson R.A. & Meyers P.A. 2012. Effect of climate change on delivery and degradation of lipid biomarkers in a Holocene peat sequence in the Eastern European Russian Arctic. *Organic Geochemistry 53*, 63–72, doi: 10.1016/j.orggeochem.2012.05.002.

Angst G., John S., Mueller C.W., Kögel-Knabner I. & Rethemeyer J. 2016. Tracing the sources and spatial distribution of organic carbon in subsoils using a multi-biomarker approach. *Scientific Reports 6*, 29478, doi: 10.1038/srep29478.

Anokhina N.A., Demin V.V. & Zavgorodnyaya Yu.A. 2018. Compositions of n-Alkanes and n-Methyl Ketones in Soils of the Forest-Park Zone of Moscow. *Eurasian Soil Science 51*, 637–646, doi: 10.1134/S1064229318060030.

Arp C.D., Jones B.M., Hinkel K.M., Kane D.L., Whitman M.S. & Kemnitz R. 2020. Recurring outburst floods from drained lakes: an emerging Arctic hazard. *Frontiers in Ecology and the Environment 18*, 384–390, doi: 10.1002/fee.2175.

Arp C.D., Jones B.M., Schmutz J.A., Urban F.E. & Jorgenson M.T. 2010. Two mechanisms of aquatic and terrestrial habitat change along an Alaskan Arctic coastline. *Polar Biology 33*, 1629–1640, doi: 10.1007/s00300-010-0800-5.

Arp C.D., Jones B.M., Urban F.E. & Grosse G. 2011. Hydrogeomorphic processes of thermokarst lakes with grounded-ice and floating-ice regimes on the Arctic coastal plain, Alaska. *Hydrological Processes 25*, 2422–2438, doi: 10.1002/hyp.8019.

Arsham Dr.H. & Lovric M. 2011. Bartlett's Test. *International Encyclopedia of Statistical Science 2*, 20–23, doi: 10.1007/978-3-642-04898-2_132.

Balesdent J. & Mariotti A. 1996. Measurement of Soil Organic Matter Turnover Using 13C Natural Abundance. Pp. 83–111.

Barbato R.A., Jones R.M., Douglas T.A., Doherty S.J., Messan K., Foley K.L., Perkins E.J., Thurston A.K. & Garcia-Reyero N. 2022. Not all permafrost microbiomes are created equal: Influence of permafrost thaw on the soil microbiome in a laboratory incubation study. *Soil Biology and Biochemistry 167*, 108605, doi: 10.1016/j.soilbio.2022.108605.

Barnes M.A. & Barnes W.C. 1978. Organic Compounds in Lake Sediments. In A. Lerman (ed.): *Lakes: Chemistry, Geology, Physics*. Pp. 127–152. New York, NY: Springer, doi: 10.1007/978-1-4757-1152-3_5.

Bartlett M.S. 1936. Statistical information and properties of sufficiency. *Proceedings of the Royal Society of London, Series A 154*, 124–137.

Beer C., Knoblauch C., Hoyt A.M., Hugelius G., Palmtag J., Mueller C.W. & Trumbore S. 2022. Vertical pattern of organic matter decomposability in cryoturbated permafrost-affected soils. *Environmental Research Letters 17*, 104023, doi: 10.1088/1748-9326/ac9198.

Benner R., Fogel M.L., Sprague E.K. & Hodson R.E. 1987. Depletion of 13C in lignin and its implications for stable carbon isotope studies. *Nature 329*, 708–710, doi: 10.1038/329708a0.

Bergstedt H., Jones B.M., Hinkel K., Farquharson L., Gaglioti B.V., Parsekian A.D., Kanevskiy M., Ohara N., Breen A.L., Rangel R.C., Grosse G. & Nitze I. 2021. Remote Sensing-Based Statistical Approach for Defining Drained Lake Basins in a Continuous Permafrost Region, North Slope of Alaska. *Remote Sensing 13*, 2539, doi: 10.3390/rs13132539.

Bischoff J., Mangelsdorf K., Gattinger A., Schloter M., Kurchatova A.N., Herzschuh U. & Wagner D. 2013. Response of methanogenic archaea to Late Pleistocene and Holocene climate changes in the Siberian Arctic. *Global Biogeochemical Cycles 27*, 305–317, doi: 10.1029/2011GB004238.

Biskaborn B.K., Smith S.L., Noetzli J., Matthes H., Vieira G., Streletskiy D.A., Schoeneich P., Romanovsky V.E., Lewkowicz A.G., Abramov A., Allard M., Boike J., Cable W.L., Christiansen H.H., Delaloye R., Diekmann B., Drozdov D., Etzelmüller B., Grosse G., Guglielmin M., Ingeman-Nielsen T., Isaksen K., Ishikawa M., Johansson M., Johannsson H., Joo A., Kaverin D., Kholodov A., Konstantinov P., Kröger T., Lambiel C., Lanckman J.-P., Luo D., Malkova G., Meiklejohn I., Moskalenko N., Oliva M., Phillips M., Ramos M., Sannel A.B.K., Sergeev D., Seybold C., Skryabin P., Vasiliev A., Wu Q., Yoshikawa K., Zheleznyak M. & Lantuit H. 2019. Permafrost is warming at a global scale. *Nature Communications 10*, 264, doi: 10.1038/s41467-018-08240-4.

Blasco S.M., Fortin G., Hill P.R., O'Connor M.J. & Brigham-Grette J. 1990. The late Neogene and Quaternary stratigraphy of the Canadian Beaufort continental shelf. In A. Grantz, L. Johnson & J.F. Sweeney (eds.): *The Arctic Ocean Region*. P. 0. Geological Society of America, doi: 10.1130/DNAG-GNA-L.491.

Bockheim J.G. 2007. Importance of Cryoturbation in Redistributing Organic Carbon in Permafrost-Affected Soils. *Soil Science Society of America Journal 71*, 1335–1342, doi: 10.2136/sssaj2006.0414N.

Boreddy S.K.R., Haque Md.M., Kawamura K., Fu P. & Kim Y. 2018. Homologous series of n-alkanes (C19-C35), fatty acids (C12-C32) and n-alcohols (C8-C30) in atmospheric aerosols from central Alaska: Molecular distributions, seasonality and source indices. *Atmospheric Environment 184*, 87–97, doi: 10.1016/j.atmosenv.2018.04.021.

Bouchard F., Fortier D., Paquette M., Boucher V., Pienitz R. & Laurion I. 2020. Thermokarst lake inception and development in syngenetic ice-wedge polygon terrain during a cooling climatic trend, Bylot Island (Nunavut), eastern Canadian Arctic. *The Cryosphere 14*, 2607–2627, doi: 10.5194/tc-14-2607-2020.

Bouchard F., MacDonald L.A., Turner K.W., Thienpont J.R., Medeiros A.S., Biskaborn B.K., Korosi J., Hall R.I., Pienitz R. & Wolfe B.B. 2017. Paleolimnology of thermokarst lakes: a window into permafrost landscape evolution. *Arctic Science 3*, 91–117, doi: 10.1139/as-2016-0022.

Boutton T.W. 1996. Stable carbon isotope ratios of soil organic matter and their use as indicators of vegetation and climate change. *Mass spectrometry of soils.*, 47–82.

Bowden W.B. 2010. Climate Change in the Arctic – Permafrost, Thermokarst, and Why They Matter to the Non-Arctic World. *Geography Compass 4*, 1553–1566, doi: 10.1111/j.1749-8198.2010.00390.x.

Bowman J. 2006. The methanotrophs - the families Methylococcaceae and Methylocystaceae. *The Prokaryotes: An Evolving Electronic Resource for the Microbiological Community*, 431–445.

Box J., Colgan W., Christensen T.R., Schmidt N., Lund M., Parmentier F.-J., Brown R., Bhatt U., Euskirchen E., Romanovsky V., Walsh J., Overland J., Wang M., Corell R., Meier W., Wouters B., Mernild S., Mård J., Pawlak J. & Olsen M. 2019. Key indicators of Arctic climate change: 1971–2017. *Environmental Research Letters 14*, 045010, doi: 10.1088/1748-9326/aafc1b.

Bray E.E. & Evans E.D. 1961. Distribution of n-paraffins as a clue to recognition of source beds. *Geochimica et Cosmochimica Acta 22*, 2–15, doi: 10.1016/0016-7037(61)90069-2.

Breecker D.O., Bergel S., Nadel M., Tremblay M.M., Osuna-Orozco R., Larson T.E. & Sharp Z.D. 2015. Minor stable carbon isotope fractionation between respired carbon dioxide and bulk soil organic matter during laboratory incubation of topsoil. *Biogeochemistry 123*, 83–98, doi: 10.1007/s10533-014-0054-3.

Bring A., Fedorova I., Dibike Y., Hinzman L., Mård J., Mernild S.H., Prowse T., Semenova O., Stuefer S.L. & Woo M.-K. 2016. Arctic terrestrial hydrology: A synthesis of processes, regional effects, and research challenges. *Journal of Geophysical Research: Biogeosciences 121*, 621–649, doi: 10.1002/2015JG003131.

Brosius L.S., Anthony K.M.W., Treat C.C., Lenz J., Jones M.C., Bret-Harte M.S. & Grosse G. 2021. Spatiotemporal patterns of northern lake formation since the Last Glacial Maximum. *Quaternary Science Reviews 253*, 106773, doi: 10.1016/j.quascirev.2020.106773.

Brown R. & Kupsch W. 1974. *Permafrost Terminology*. Ottawa,Ontario, Canada: National Research Council of Canada.

Brown R.J.E. 1966. Relation between mean annual air and ground temperatures in the permafrost region of Canada. *Proceedings: Permafrost International Conference*, 241–246.

Bull I.D., Bergen P.F. van, Nott C.J., Poulton P.R. & Evershed R.P. 2000. Organic geochemical studies of soils from the Rothamsted classical experiments—V. The fate of lipids in different long-term experiments. *Organic Geochemistry 31*, 389–408, doi: 10.1016/S0146-6380(00)00008-5.

Burn C. 2011. Cryostratigraphy, paleogeography, and climate change during the early Holocene warm interval, western Arctic coast, Canada. *Canadian Journal of Earth Sciences 34*, 912–925, doi: 10.1139/e17-076.

Burn C.R. 1997. Cryostratigraphy, paleogeography, and climate change during the early Holocene warm interval, western Arctic coast, Canada. *Canadian Journal of Earth Sciences 34*, 912–925, doi: 10.1139/e17-076.

Burn C.R. 1994. Permafrost, tectonics, and past and future regional climate change, Yukon and adjacent Northwest Territories. *Canadian Journal of Earth Sciences 31*, 182–191, doi: 10.1139/e94-015.

Burn C.R. 1998. The active layer: two contrasting definitions. *Permafrost and Periglacial Processes 9*, 411–416, doi: 10.1002/(SICI)1099-1530(199810/12)9:4<411::AID-PPP292>3.0.CO;2-6.

Burn C.R. & Kokelj S.V. 2009. The environment and permafrost of the Mackenzie Delta area. *Permafrost and Periglacial Processes 20*, 83–105, doi: 10.1002/ppp.655.

Burn C.R. & Smith M.W. 1990. Development of thermokarst lakes during the holocene at sites near Mayo, Yukon territory. *Permafrost and Periglacial Processes 1*, 161–175, doi: 10.1002/ppp.3430010207.

Burn C.R. & Zhang Y. 2009. Permafrost and climate change at Herschel Island (Qikiqtaruq), Yukon Territory, Canada. *Journal of Geophysical Research: Earth Surface 114*, doi: 10.1029/2008JF001087.

Calib 8.2. Accessed on the internet at http://calib.org/calib/calib.html on 9 November 2023.

Camill P. 2005. Permafrost Thaw Accelerates in Boreal Peatlands During Late-20th Century Climate Warming. *Climatic Change 68*, 135–152, doi: 10.1007/s10584-005-4785-y.

Campbell J.E., Fox J.F., Davis C.M., Rowe H.D. & Thompson N. 2009. Carbon and Nitrogen Isotopic Measurements from Southern Appalachian Soils: Assessing Soil Carbon Sequestration under Climate and Land-Use Variation. *Journal of Environmental Engineering 135*, 439–448, doi: 10.1061/(ASCE)EE.1943-7870.0000008.

Carroll J.J., Slupsky J.D. & Mather A.E. 1991. The Solubility of Carbon Dioxide in Water at Low Pressure. *Journal of Physical and Chemical Reference Data 20*, 1201–1209, doi: 10.1063/1.555900.

Chadburn S.E., Burke E.J., Cox P.M., Friedlingstein P., Hugelius G. & Westermann S. 2017. An observation-based constraint on permafrost loss as a function of global warming. *Nature Climate Change 7*, 340–344, doi: 10.1038/nclimate3262.

Chapin F.S., Matson P.A. & Mooney H.A. (eds.). 2002. Terrestrial Decomposition. *Principles of Terrestrial Ecosystem Ecology*. Pp. 151–175. New York, NY: Springer, doi: 10.1007/0-387-21663-4_7.

Chapin F.S., Shaver G.R., Giblin A.E., Nadelhoffer K.J. & Laundre J.A. 1995. Responses of Arctic Tundra to Experimental and Observed Changes in Climate. *Ecology 76*, 694–711, doi: 10.2307/1939337.

Chapin F.S., Woodwell G.M., Randerson J.T., Rastetter E.B., Lovett G.M., Baldocchi D.D., Clark D.A., Harmon M.E., Schimel D.S., Valentini R., Wirth C., Aber J.D., Cole J.J., Goulden M.L., Harden J.W., Heimann M., Howarth R.W., Matson P.A., McGuire A.D., Melillo J.M., Mooney H.A., Neff J.C., Houghton R.A., Pace M.L., Ryan M.G., Running S.W., Sala O.E., Schlesinger W.H. & Schulze E.D. 2006. Reconciling carbon-cycle concepts, terminology, and methods. *Ecosystems 9*, 1041–1050, doi: 10.1007/s10021-005-0105-7.

Chen Y., Liu F., Kang L., Zhang D., Kou D., Mao C., Qin S., Zhang Q. & Yang Y. 2021. Large-scale evidence for microbial response and associated carbon release after permafrost thaw. *Global Change Biology 27*, 3218–3229, doi: 10.1111/gcb.15487.

Christensen T.R. & Cox P. 1995. Response of methane emission from arctic tundra to climatic change: results from a model simulation. *Tellus B: Chemical and Physical Meteorology 47*, 301–309, doi: 10.3402/tellusb.v47i3.16049.

Ciais P., Sabine C., Bala G., Bopp L., Brovkin V., Canadell J., Chhabra A., DeFries R., Galloway J., Heimann M., Jones C., Le Quéré C., Myneni R.B., Piao S. & Thornton P. 2014. Carbon and other biogeochemical cycles. *Climate Change 2013: The Physical Science Basis. Contribution of Working Group I to the Fifth Assessment Report of the Intergovernmental Panel on Climate Change*. Pp. 465–570. Cambridge University Press. Accessed on the internet at https://hdl.handle.net/11858/00-001M-0000-0023-E5DD-A on 7 November 2023.

Cohen J. 1988. *Statistical power analysis for the behavioral sciences*. 2nd ed. Hillsdale, N.J: L. Erlbaum Associates.

Conrad R. 2005. Quantification of methanogenic pathways using stable carbon isotopic signatures: a review and a proposal. *Organic Geochemistry 36*, 739–752, doi: 10.1016/j.orggeochem.2004.09.006.

Conrad R. 2009. The global methane cycle: recent advances in understanding the microbial processes involved. *Environmental Microbiology Reports 1*, 285–292, doi: 10.1111/j.1758-2229.2009.00038.x.

Conrad R. & Klose M. 1999. Anaerobic conversion of carbon dioxide to methane, acetate and propionate on washed rice roots. *FEMS Microbiology Ecology 30*, 147–155, doi: 10.1111/j.1574-6941.1999.tb00643.x.

Conrad R., Mayer H.-P. & Wüst M. 1989. Temporal change of gas metabolism by hydrogen-syntrophic methanogenic bacterial associations in anoxic paddy soil. *FEMS Microbiology Ecology 5*, 265–273, doi: 10.1111/j.1574-6968.1989.tb03701.x.

Coolen M.J.L. & Orsi W.D. 2015. The transcriptional response of microbial communities in thawing Alaskan permafrost soils. *Frontiers in Microbiology 6*. Accessed on the internet at https://www.frontiersin.org/articles/10.3389/fmicb.2015.00197 on 27 September 2023.

Coolen M.J.L., van de Giessen J., Zhu E.Y. & Wuchter C. 2011. Bioavailability of soil organic matter and microbial community dynamics upon permafrost thaw. *Environmental Microbiology 13*, 2299–2314, doi: 10.1111/j.1462-2920.2011.02489.x.

Cooper M.D.A., Estop-Aragonés C., Fisher J.P., Thierry A., Garnett M.H., Charman D.J., Murton J.B., Phoenix G.K., Treharne R., Kokelj S.V., Wolfe S.A., Lewkowicz A.G., Williams M. & Hartley I.P. 2017. Limited contribution of permafrost carbon to methane release from thawing peatlands. *Nature Climate Change 7*, 507–511, doi: 10.1038/nclimate3328.

Couture N. 2010. Fluxes of soil organic carbon from eroding permafrost coasts, Canadian Beaufort Sea.

Couture N.J., Irrgang A., Pollard W., Lantuit H. & Fritz M. 2018. Coastal Erosion of Permafrost Soils Along the Yukon Coastal Plain and Fluxes of Organic Carbon to the Canadian Beaufort Sea. *Journal of Geophysical Research: Biogeosciences 123*, 406–422, doi: 10.1002/2017JG004166.

Couture N.J. & Pollard W.H. 2017. A Model for Quantifying Ground-Ice Volume, Yukon Coast, Western Arctic Canada. *Permafrost and Periglacial Processes 28*, 534–542, doi: 10.1002/ppp.1952.

Cranwell P.A. 1981. Diagenesis of free and bound lipids in terrestrial detritus deposited in a lacustrine sediment. *Organic Geochemistry 3*, 79–89, doi: 10.1016/0146-6380(81)90002-4.

Cranwell P.A. 1984. Lipid geochemistry of sediments from Upton Broad, a small productive lake. *Organic Geochemistry 7*, 25–37, doi: 10.1016/0146-6380(84)90134-7.

Cranwell P.A., Eglinton G. & Robinson N. 1987. Lipids of aquatic organisms as potential contributors to lacustrine sediments—II. *Organic Geochemistry 11*, 513–527, doi: 10.1016/0146-6380(87)90007-6.

D'Agostino R. 1986. *Goodness-of-Fit-Techniques*. New York: Routledge, doi: 10.1201/9780203753064.

D'Amico S., Collins T., Marx J.-C., Feller G., Gerday C. & Gerday C. 2006. Psychrophilic microorganisms: challenges for life. *EMBO reports 7*, 385–389, doi: 10.1038/sj.embor.7400662.

Davidson E.A. & Janssens I.A. 2006. Temperature sensitivity of soil carbon decomposition and feedbacks to climate change. *Nature 440*, 165–173, doi: 10.1038/nature04514.

Deines P. 1980. Handbook of Environmental Isotope Geochemistry. *(No Title) 1*, 329.

Deshpande B.N., Maps F., Matveev A. & Vincent W.F. 2017. Oxygen depletion in subarctic peatland thaw lakes. *Arctic Science 3*, 406–428, doi: 10.1139/as-2016-0048.

Dinel H., Schnitzer M. & Mehuys G.R. 1990. Soil lipids: origin, nature, content, decomposition, and effect on soil physical properties. *Soil biochemistry. Volume 6.*, 397–429.

Diochon A. & Kellman L. 2008. Natural abundance measurements of 13C indicate increased deep soil carbon mineralization after forest disturbance. *Geophysical Research Letters 35*, doi: 10.1029/2008GL034795.

Dobinski W. 2011. Permafrost. *Earth-Science Reviews 108*, 158–169, doi: 10.1016/j.earscirev.2011.06.007.

Dorrepaal E., Toet S., van Logtestijn R.S.P., Swart E., van de Weg M.J., Callaghan T.V. & Aerts R. 2009. Carbon respiration from subsurface peat accelerated by climate warming in the subarctic. *Nature 460*, 616–619, doi: 10.1038/nature08216.

Duk-Rodkin A. 1999. Glacial Limits Map of Yukon.

Duk-Rodkin A. & Hughes O.L. 1995. *Quaternary geology of the northeastern part of the central Mackenzie Valley corridor, District of Mackenzie, Northwest Territories*. Ottawa: Geological Survey of Canada.

Dutta K., Schuur E. a. G., Neff J.C. & Zimov S.A. 2006. Potential carbon release from permafrost soils of Northeastern Siberia. *Global Change Biology 12*, 2336–2351, doi: 10.1111/j.1365-2486.2006.01259.x.

Dylik J. & Rybczynska E. 1964. Le thermokarst, phénomène négligé dans les études du Pléistocène. *Annales de Géographie 73*, 513–523.

Eglinton G. & Hamilton R.J. 1967. Leaf Epicuticular Waxes. *Science 156*, 1322–1335, doi: 10.1126/science.156.3780.1322.

Ehleringer J.R., Buchmann N. & Flanagan L.B. 2000. Carbon Isotope Ratios in Belowground Carbon Cycle Processes. *Ecological Applications 10*, 412–422, doi: 10.1890/1051-0761(2000)010[0412:CIRIBC]2.0.CO;2.

Elberling B., Michelsen A., Schädel C., Schuur E.A.G., Christiansen H.H., Berg L., Tamstorf M.P. & Sigsgaard C. 2013. Long-term CO2 production following permafrost thaw. *Nature Climate Change 3*, 890–894, doi: 10.1038/nclimate1955.

Enríquez S., Duarte C.M. & Sand-Jensen K. 1993. Patterns in decomposition rates among photosynthetic organisms: the importance of detritus C:N:P content. *Oecologia 94*, 457–471, doi: 10.1007/BF00566960.

Ernakovich J.G., Barbato R.A., Rich V.I., Schädel C., Hewitt R.E., Doherty S.J., Whalen E.D., Abbott B.W., Barta J., Biasi C., Chabot C.L., Hultman J., Knoblauch C., Vetter M.C.Y.L., Leewis M.-C., Liebner S., Mackelprang R., Onstott T.C., Richter A., Schütte U.M.E., Siljanen H.M.P., Taş N., Timling I., Vishnivetskaya T.A., Waldrop M.P. & Winkel M. 2022. Microbiome assembly in thawing permafrost and its feedbacks to climate. *Global Change Biology 28*, 5007–5026, doi: 10.1111/gcb.16231.

Estop-Aragonés C., Heffernan L., Knorr K.-H. & Olefeldt D. 2022. Limited Potential for Mineralization of Permafrost Peatland Soil Carbon Following Thermokarst: Evidence From Anoxic Incubation and Priming Experiments. *Journal of Geophysical Research: Biogeosciences 127*, e2022JG006910, doi: 10.1029/2022JG006910.

Faucherre S., Jørgensen C.J., Blok D., Weiss N., Siewert M.B., Bang-Andreasen T., Hugelius G., Kuhry P. & Elberling B. 2018. Short and Long-Term Controls on Active Layer and Permafrost Carbon Turnover Across the Arctic. *Journal of Geophysical Research: Biogeosciences 123*, 372–390, doi: 10.1002/2017JG004069.

Ficken K.J., Li B., Swain D.L. & Eglinton G. 2000. An n-alkane proxy for the sedimentary input of submerged/floating freshwater aquatic macrophytes. *Organic Geochemistry 31*, 745–749, doi: 10.1016/S0146-6380(00)00081-4.

Forbes D.L. 1980. Late Quaternary sea level changes in the southern Beaufort Sea. *Geological Survey of Canada: Current Research*, 75–78.

French H. 2013. The Periglacial Environment, Third Edition. Pp. 186–215, doi: 10.1002/9781118684931.ch8.

French H. & Shur Y. 2010. The principles of cryostratigraphy. *Earth-Science Reviews 101*, 190–206, doi: 10.1016/j.earscirev.2010.04.002.

French H.M. 1987. Periglacial geomorphology in North America: current research and future trends. *Progress in Physical Geography: Earth and Environment 11*, 533–551, doi: 10.1177/030913338701100404.

French H.M. 2007. *The Periglacial Environment*. 3rd edition. Chichester, England ; Hoboken, NJ: John Wiley &Sons.

French H.M. 2017. *The Periglacial Environment*. 4th edition. John Wiley & Sons.

Fridland V.M. 1976. Pattern of the soil cover. *Pattern of the soil cover.* Accessed on the internet at https://www.cabdirect.org/cabdirect/abstract/19831979057 on 19 October 2023.

Gagosian R.B., Peltzer E.T. & Zafiriou O.C. 1981. Atmospheric transport of continentally derived lipids to the tropical North Pacific. *Nature 291*, 312–314, doi: 10.1038/291312a0.

Galley R.J., Babb D., Ogi M., Else B.G.T., Geilfus N.-X., Crabeck O., Barber D.G. & Rysgaard S. 2016. Replacement of multiyear sea ice and changes in the open water season duration in the Beaufort Sea since 2004. *Journal of Geophysical Research: Oceans 121*, 1806–1823, doi: 10.1002/2015JC011583.

Garten Jr. C.T. 2006. Relationships among forest soil C isotopic composition, partitioning, and turnover times. *Canadian Journal of Forest Research 36*, 2157–2167, doi: 10.1139/x06-115.

Garten Jr. C.T., Cooper L.W., Post III W.M. & Hanson P.J. 2000. Climate Controls on Forest Soil C Isotope Ratios in the Southern Appalachian Mountains. *Ecology 81*, 1108–1119, doi: 10.1890/0012-9658(2000)081[1108:CCOFSC]2.0.CO;2.

Gelpi E., Schneider H., Mann J. & Oró J. 1970. Hydrocarbons of geochemical significance in microscopic algae. *Phytochemistry 9*, 603–612, doi: 10.1016/S0031-9422(00)85700-3.

Gignac G.E. & Szodorai E.T. 2016. Effect size guidelines for individual differences researchers. *Personality and Individual Differences 102*, 74–78, doi: 10.1016/j.paid.2016.06.069.

Gleixner G. 2013. Soil organic matter dynamics: a biological perspective derived from the use of compound-specific isotopes studies. *Ecological Research 28*, 683–695, doi: 10.1007/s11284-012-1022-9.

Glombitza C., Mangelsdorf K. & Horsfield B. 2009. Maturation related changes in the distribution of ester bound fatty acids and alcohols in a coal series from the New Zealand Coal Band covering diagenetic to catagenetic coalification levels. *Organic Geochemistry 40*, 1063–1073, doi: 10.1016/j.orggeochem.2009.07.008.

Government of Canada. 2011. Canadian Climate Normals - Climate - Environment and Climate Change Canada. Accessed on the internet at https://climate.weather.gc.ca/climate_normals/index_e.html on 10 September 2023.

Graversen R.G., Mauritsen T., Tjernström M., Källén E. & Svensson G. 2008. Vertical structure of recent Arctic warming. *Nature 451*, 53–56, doi: 10.1038/nature06502.

Grosse G., Jones B. & Arp C. 2013. 8.21 Thermokarst Lakes, Drainage, and Drained Basins. In J.F. Shroder (ed.): *Treatise on Geomorphology*. Pp. 325–353. San Diego: Academic Press, doi: 10.1016/B978-0-12-374739-6.00216-5.

Gundelwein A., Müller-Lupp T., Sommerkorn M., Haupt E.T.K., Pfeiffer E.-M. & Wiechmann H. 2007. Carbon in tundra soils in the Lake Labaz region of arctic Siberia. *European Journal of Soil Science 58*, 1164–1174, doi: 10.1111/j.1365-2389.2007.00908.x.

Harden J.W., Koven C.D., Ping C.-L., Hugelius G., David McGuire A., Camill P., Jorgenson T., Kuhry P., Michaelson G.J., O'Donnell J.A., Schuur E.A.G., Tarnocai C., Johnson K. & Grosse G. 2012. Field information links permafrost carbon to physical vulnerabilities of thawing. *Geophysical Research Letters 39*, doi: 10.1029/2012GL051958.

Harwood J.L. & Russell N.J. 1984. Distribution of lipids. In J.L. Harwood & N.J. Russell (eds.): *Lipids in Plants and Microbes*. Pp. 35–70. Dordrecht: Springer Netherlands, doi: 10.1007/978-94-011-5989-0_3.

Haugan P.M. & Drange H. 1996. Effects of CO2 on the ocean environment. *Energy Conversion and Management 37*, 1019–1022, doi: 10.1016/0196-8904(95)00292-8.

He X., He K.S. & Hyvönen J. 2016. Will bryophytes survive in a warming world? *Perspectives in Plant Ecology, Evolution and Systematics 19*, 49–60, doi: 10.1016/j.ppees.2016.02.005.

Heginbottom J.A., Brown J., Melnikov E.S. & Ferrians Jr. O.J. 1993. Circumarctic Map of Permafrost and Ground Ice Conditions. Permafrost: Sixth International Conference. Pp. 1132–1136. Wushan, Guangzhou, China: South China University Press.

Héquette A., Desrosiers M. & Barnes P.W. 1995. Sea ice scouring on the inner shelf of the southeastern Canadian Beaufort Sea. *Marine Geology 128*, 201–219, doi: 10.1016/0025-3227(95)00095-G.

Heslop J., Walter Anthony K., Sepulveda-Jauregui A., Martinez-Cruz K., Bondurant A., Grosse G. & Jones M. 2015. Thermokarst-lake methanogenesis along a complete talik profile. *Biogeosciences 12*, 4317–4331, doi: 10.5194/bg-12-4317-2015.

Heslop J.K., Walter Anthony K.M., Winkel M., Sepulveda-Jauregui A., Martinez-Cruz K., Bondurant A., Grosse G. & Liebner S. 2020. A synthesis of methane dynamics in thermokarst lake environments. *Earth-Science Reviews 210*, 103365, doi: 10.1016/j.earscirev.2020.103365.

Heyer J., Hübner H. & Maaβ I. 1976. Isotopenfraktionierung des Kohlenstoffs bei der mikrobiellen Methanbildung. *Isotopenpraxis Isotopes in Environmental and Health Studies 12*, 202–205, doi: 10.1080/10256017608543912.

Hill P.R. 1990. Coastal geology of the King Point area, Yukon Territory, Canada. *Marine Geology 91*, 93–111, doi: 10.1016/0025-3227(90)90135-7.

Hill P.R., Blasco S.M., Harper J.R. & Fissel D.B. 1991. Sedimentation on the Canadian Beaufort Shelf. *Continental Shelf Research 11*, 821–842, doi: 10.1016/0278-4343(91)90081-G.

Hinkel K., Jones B., Eisner W., Cuomo C., Beck R., Frohn R. & Hinkel C. 2007. Methods to Assess Natural and Anthropogenic Thaw Lake Drainage on the Western Arctic Coastal Plain of Northern Alaska. *Journal of Geophysical Research 112*, doi: 10.1029/2006JF000584.

Hinkel K.M., Eisner W.R., Bockheim J.G., Nelson F.E., Peterson K.M. & Dai X. 2003. Spatial Extent, Age, and Carbon Stocks in Drained Thaw Lake Basins on the Barrow Peninsula, Alaska. *Arctic, Antarctic, and Alpine Research 35*, 291–300.

Hinkel K.M., Frohn R.C., Nelson F.E., Eisner W.R. & Beck R.A. 2005. Morphometric and spatial analysis of thaw lakes and drained thaw lake basins in the western Arctic Coastal Plain, Alaska. *Permafrost and Periglacial Processes 16*, 327–341, doi: 10.1002/ppp.532.

Hinzman L.D., Kane D.L., Gieck R.E. & Everett K.R. 1991. Hydrologic and thermal properties of the active layer in the Alaskan Arctic. *Cold Regions Science and Technology 19*, 95–110, doi: 10.1016/0165-232X(91)90001-W.

Hobbie S.E., Miley T.A. & Weiss M.S. 2002. Carbon and Nitrogen Cycling in Soils from Acidic and Nonacidic Tundra with Different Glacial Histories in Northern Alaska. *Ecosystems 5*, 0761–0774, doi: 10.1007/s10021-002-0185-6.

Hodgkins S.B., Tfaily M.M., McCalley C.K., Logan T.A., Crill P.M., Saleska S.R., Rich V.I. & Chanton J.P. 2014. Changes in peat chemistry associated with permafrost thaw increase greenhouse gas production. *Proceedings of the National Academy of Sciences 111*, 5819–5824, doi: 10.1073/pnas.1314641111.

Höfle S., Rethemeyer J., Mueller C.W. & John S. 2013. Organic matter composition and stabilization in a polygonal tundra soil of the Lena Delta. *Biogeosciences 10*, 3145–3158, doi: 10.5194/bg-10-3145-2013.

Holm S., Walz J., Horn F., Yang S., Grigoriev M.N., Wagner D., Knoblauch C. & Liebner S. 2020. Methanogenic response to long-term permafrost thaw is determined by paleoenvironment. *FEMS Microbiology Ecology 96*, fiaa021, doi: 10.1093/femsec/fiaa021.

Hopkins D.M. 1949. Thaw Lakes and Thaw Sinks in the Imuruk Lake Area, Seward Peninsula, Alaska. *The Journal of Geology*, doi: 10.1086/625591.

Horn M.A., Matthies C., Küsel K., Schramm A. & Drake H.L. 2003. Hydrogenotrophic Methanogenesis by Moderately Acid-Tolerant Methanogens of a Methane-Emitting Acidic Peat. *Applied and Environmental Microbiology 69*, 74–83, doi: 10.1128/AEM.69.1.74-83.2003.

Hornibrook E.R.C., Longstaffe F.J. & Fyfe W.S. 1997. Spatial distribution of microbial methane production pathways in temperate zone wetland soils: Stable carbon and hydrogen isotope evidence. *Geochimica et Cosmochimica Acta 61*, 745–753, doi: 10.1016/S0016-7037(96)00368-7.

Hornibrook E.R.C., Longstaffe F.J., Fyfe W.S. & Bloom Y. 2000. Carbon-isotope ratios and carbon, nitrogen and sulfur abundances in flora and soil organic matter from a temperate-zone bog and marsh. *Geochemical Journal 34*, 237–245, doi: 10.2343/geochemj.34.237.

Hsu H. & Lachenbruch P.A. 2005. Paired t Test. *Encyclopedia of Biostatistics*. John Wiley & Sons, Ltd, doi: 10.1002/0470011815.b2a15112.

Huang W. & Hall S.J. 2018. Large impacts of small methane fluxes on carbon isotope values of soil respiration. *Soil Biology and Biochemistry 124*, 126–133, doi: 10.1016/j.soilbio.2018.06.003.

Hudak D.R. & Young J.M.C. 2002. Storm climatology of the Southern Beaufort sea. *Atmosphere-Ocean 40*, 145–158, doi: 10.3137/ao.400205.

Hugelius G., Bockheim J.G., Camill P., Elberling B., Grosse G., Harden J.W., Johnson K., Jorgenson T., Koven C.D., Kuhry P., Michaelson G., Mishra U., Palmtag J., Ping C.-L., O'Donnell J., Schirrmeister L., Schuur E. a. G., Sheng Y., Smith L.C., Strauss J. & Yu Z. 2013. A new data set for estimating organic carbon storage to 3 m depth in soils of the northern circumpolar permafrost region. *Earth System Science Data 5*, 393–402, doi: 10.5194/essd-5-393-2013.

Hugelius G., Strauss J., Zubrzycki S., Harden J.W., Schuur E.A.G., Ping C.L., Schirrmeister L., Grosse G., Michaelson G.J., Koven C.D., O'Donnell J.A., Elberling B., Mishra U., Camill P., Yu Z., Palmtag J. & Kuhry P. 2014. Estimated stocks of circumpolar permafrost carbon with quantified uncertainty ranges and identified data gaps. *Biogeosciences 11*, 6573–6593, doi: 10.5194/bg-11-6573-2014.

Hughes O.L., Harington C.R., Janssens J.A., Matthews J.V., Morlan R.E., Rutter N.W. & Schweger C.E. 1981. Upper Pleistocene Stratigraphy, Paleoecology, and Archaeology of the Northern Yukon Interior, Eastern Beringia 1. Bonnet Plume Basin. *Arctic 34*, 329–365.

in 't Zandt M.H., Liebner S. & Welte C.U. 2020. Roles of Thermokarst Lakes in a Warming World. *Trends in Microbiology 28*, 769–779, doi: 10.1016/j.tim.2020.04.002.

IPCC (ed.). 2014. Anthropogenic and Natural Radiative Forcing. *Climate Change 2013 – The Physical Science Basis: Working Group I Contribution to the Fifth Assessment Report of the Intergovernmental Panel on Climate Change*. Pp. 659–740. Cambridge: Cambridge University Press, doi: 10.1017/CBO9781107415324.018.

IPCC. 2013. *Climate Change 2013 – The Physical Science Basis: Working Group I Contribution to the Fifth Assessment Report of the Intergovernmental Panel on Climate Change*. Cambridge: Cambridge University Press, doi: 10.1017/CBO9781107415324.

IPCC, Watson R.T., Albritton D.L., Barker T., Bashmakov I., Canziani O.F., Christ R., Cubasch U., Davidson O.R., Gitay H., Griggs D.J., Halsnaes K., Houghton J.T., House J.I., Kundzewicz Z.W., Lal M., Leary N., Magadza C., McCarthy J.J., Mitchell J.F.B., Moreira J.R., Munasinghe M., Noble I., Pachauri R.K., Pittock B., Prather M.J., Richels R.G., Robinson J.B., Sathaye J., Schneider S., Scholes R., Stocker T., Sundararaman N., Swart R.J., Taniguchi T. & Zhou D.W. 2001. *Climate Change 2001: Synthesis Report. A Contribution of Working Groups I, II and III to the Third Assessment Report of the Intergovernmental Panel on Climate Change*. Cambridge University Press. Accessed on the internet at https://research.monash.edu/en/publications/climate-change-2001-synthesis-report-a-contribution-of-working-gr on 28 October 2022.

Jansen B. & Nierop K.G.J. 2009. Methyl ketones in high altitude Ecuadorian Andosols confirm excellent conservation of plant-specific n-alkane patterns. *Organic Geochemistry 40*, 61–69, doi: 10.1016/j.orggeochem.2008.09.006.

Jansen B., Nierop K.G.J., Hageman J.A., Cleef A.M. & Verstraten J.M. 2006. The straight-chain lipid biomarker composition of plant species responsible for the dominant biomass production along two altitudinal transects in the Ecuadorian Andes. *Organic Geochemistry 37*, 1514–1536, doi: 10.1016/j.orggeochem.2006.06.018.

Jenkinson D.S. 1990. The turnover of organic carbon and nitrogen in the soil. *Philosophical Transactions of the Royal Society B-Biological Sciences 329*, 361–368, doi: 10.1098/rstb.1990.0177.

Jiang L., Song Y., Sun L., Song C., Wang X., Ma X., Liu C. & Gao J. 2020. Effects of warming on carbon emission and microbial abundances across different soil depths of a peatland in the permafrost region under anaerobic condition. *Applied Soil Ecology 156*, 103712, doi: 10.1016/j.apsoil.2020.103712.

Jobbágy E.G. & Jackson R.B. 2000. The Vertical Distribution of Soil Organic Carbon and Its Relation to Climate and Vegetation. *Ecological Applications 10*, 423–436, doi: 10.1890/1051-0761(2000)010[0423:TVDOSO]2.0.CO;2.

Jones B.M. & Arp C.D. 2015. Observing a Catastrophic Thermokarst Lake Drainage in Northern Alaska. *Permafrost and Periglacial Processes 26*, 119–128, doi: 10.1002/ppp.1842.

Jones B.M., Arp C.D., Grosse G., Nitze I., Lara M.J., Whitman M.S., Farquharson L.M., Kanevskiy M., Parsekian A.D., Breen A.L., Ohara N., Rangel R.C. & Hinkel K.M. 2020. Identifying historical and future potential lake drainage events on the western Arctic coastal plain of Alaska. *Permafrost and Periglacial Processes 31*, 110–127, doi: 10.1002/ppp.2038.

Jones B.M., Arp C.D., Jorgenson M.T., Hinkel K.M., Schmutz J.A. & Flint P.L. 2009. Increase in the rate and uniformity of coastline erosion in Arctic Alaska. *Geophysical Research Letters 36*, doi: 10.1029/2008GL036205.

Jones B.M., Grosse G., Arp C.D., Jones M.C., Walter Anthony K.M. & Romanovsky V.E. 2011. Modern thermokarst lake dynamics in the continuous permafrost zone, northern Seward Peninsula, Alaska. *Journal of Geophysical Research: Biogeosciences 116*, doi: 10.1029/2011JG001666.

Jones B.M., Grosse G., Farquharson L.M., Roy-Léveillée P., Veremeeva A., Kanevskiy M.Z., Gaglioti B.V., Breen A.L., Parsekian A.D., Ulrich M. & Hinkel K.M. 2022. Lake and drained lake basin systems in lowland permafrost regions. *Nature Reviews Earth & Environment 3*, 85–98, doi: 10.1038/s43017-021-00238-9.

Jones M.C., Grosse G., Jones B.M. & Walter Anthony K. 2012. Peat accumulation in drained thermokarst lake basins in continuous, ice-rich permafrost, northern Seward Peninsula, Alaska. *Journal of Geophysical Research: Biogeosciences 117*, doi: 10.1029/2011JG001766.

Jongejans L.L., Liebner S., Knoblauch C., Mangelsdorf K., Ulrich M., Grosse G., Tanski G., Fedorov A.N., Konstantinov P.Y., Windirsch T., Wiedmann J. & Strauss J. 2021. Greenhouse gas production and lipid biomarker distribution in Yedoma and Alas thermokarst lake sediments in Eastern Siberia. *Global Change Biology 27*, 2822–2839, doi: 10.1111/gcb.15566.

Jongejans L.L., Strauss J., Lenz J., Lenz J., Peterse F., Mangelsdorf K., Fuchs M., Fuchs M., Grosse G. & Grosse G. 2018. Organic matter characteristics in yedoma and thermokarst deposits on Baldwin Peninsula, west Alaska. *Biogeosciences 15*, 6033–6048, doi: 10.5194/bg-15-6033-2018.

Jorgenson M., Shur Y. & Pullman E. 2006. Abrupt increase in permafrost degradation in Arctic Alaska. *Geophys. Res. Lett 33*, doi: 10.1029/2005GL024960.

Jorgenson M.T. & Grosse G. 2016. Remote Sensing of Landscape Change in Permafrost Regions. *Permafrost and Periglacial Processes 27*, 324–338, doi: 10.1002/ppp.1914.

Jorgenson M.T. & Shur Y. 2007. Evolution of lakes and basins in northern Alaska and discussion of the thaw lake cycle. *Journal of Geophysical Research: Earth Surface 112*, doi: 10.1029/2006JF000531.

Kennedy H., Beggins J., Duarte C.M., Fourqurean J.W., Holmer M., Marbà N. & Middelburg J.J. 2010. Seagrass sediments as a global carbon sink: Isotopic constraints. *Global Biogeochemical Cycles 24*, doi: 10.1029/2010GB003848.

Killops S.D. & Killops V.J. 2013. *Introduction to Organic Geochemistry*. John Wiley & Sons.

Killops S.D. & Killops V.J. 2009. *Introduction to Organic Geochemistry*. Wiley.

Kim T.K. 2015. T test as a parametric statistic. *Korean Journal of Anesthesiology 68*, 540–546, doi: 10.4097/kjae.2015.68.6.540.

Kim T.K. 2017. Understanding one-way ANOVA using conceptual figures. *Korean Journal of Anesthesiology 70*, 22–26, doi: 10.4097/kjae.2017.70.1.22.

Kip N., van Winden J.F., Pan Y., Bodrossy L., Reichart G.-J., Smolders A.J.P., Jetten M.S.M., Damsté J.S.S. & Op den Camp H.J.M. 2010. Global prevalence of methane oxidation by symbiotic bacteria in peat-moss ecosystems. *Nature Geoscience 3*, 617–621, doi: 10.1038/ngeo939.

Knief C. 2019. Diversity of Methane-Cycling Microorganisms in Soils and Their Relation to Oxygen. *Current Issues in Molecular Biology 33*, 23–56, doi: 10.21775/cimb.033.023.

Knoblauch C., Beer C., Liebner S., Grigoriev M.N. & Pfeiffer E.-M. 2018. Methane production as key to the greenhouse gas budget of thawing permafrost. *Nature Climate Change 8*, 309–312, doi: 10.1038/s41558-018-0095-z.

Knoblauch C., Beer C., Schuett A., Sauerland L., Liebner S., Steinhof A., Rethemeyer J., Grigoriev M.N., Faguet A. & Pfeiffer E.-M. 2021. Carbon Dioxide and Methane Release Following Abrupt Thaw of

Pleistocene Permafrost Deposits in Arctic Siberia. *Journal of Geophysical Research: Biogeosciences 126*, e2021JG006543, doi: 10.1029/2021JG006543.

Knoblauch C., Beer C., Sosnin A., Wagner D. & Pfeiffer E.-M. 2013. Predicting long-term carbon mineralization and trace gas production from thawing permafrost of Northeast Siberia. *Global Change Biology 19*, 1160–1172, doi: 10.1111/gcb.12116.

Knoblauch C., Zimmermann U., Blumenberg M., Michaelis W. & Pfeiffer E.-M. 2008. Methane turnover and temperature response of methane-oxidizing bacteria in permafrost-affected soils of northeast Siberia. *Soil Biology and Biochemistry 40*, 3004–3013, doi: 10.1016/j.soilbio.2008.08.020.

Knorr K.-H. & Blodau C. 2009. Impact of experimental drought and rewetting on redox transformations and methanogenesis in mesocosms of a northern fen soil. *Soil Biology and Biochemistry 41*, 1187–1198, doi: 10.1016/j.soilbio.2009.02.030.

Kobabe S., Wagner D. & Pfeiffer E.-M. 2004. Characterisation of microbial community composition of a Siberian tundra soil by fluorescence in situ hybridisation. *FEMS Microbiology Ecology 50*, 13–23, doi: 10.1016/j.femsec.2004.05.003.

Koch J.C., Gurney K. & Wipfli M.S. 2014. Morphology-Dependent Water Budgets and Nutrient Fluxes in Arctic Thaw Ponds. *Permafrost and Periglacial Processes 25*, 79–93, doi: 10.1002/ppp.1804.

Kokelj S.V., Smith C. a. S. & Burn C.R. 2002. Physical and chemical characteristics of the active layer and permafrost, Herschel Island, western Arctic Coast, Canada. *Permafrost and Periglacial Processes 13*, 171–185, doi: 10.1002/ppp.417.

Kolattukudy P.E. 1976. Chemistry and biochemistry of natural waxes. *(No Title)*. Accessed on the internet at https://cir.nii.ac.jp/crid/1130282270452776704 on 18 October 2023.

Kolattukudy P.E. & Espelie K.E. 1989. Chemistry, Biochemistry, and Function of Suberin and Associated Waxes. In J.W. Rowe (ed.): *Natural Products of Woody Plants: Chemicals Extraneous to the Lignocellulosic Cell Wall*. Springer Series in Wood Science. Pp. 304–367. Berlin, Heidelberg: Springer, doi: 10.1007/978-3-642-74075-6_11.

Koven C., Ringeval B., Friedlingstein P., Ciais P., Cadule P., Khvorostyanov D., Krinner G. & Tarnocai C. 2011. Permafrost carbon-climate feedbacks accelerate global warming. *Proceedings of the National Academy of Sciences 108*, 14769–14774, doi: 10.1073/pnas.1103910108.

Krüger J.P., Leifeld J. & Alewell C. 2014. Degradation changes stable carbon isotope depth profiles in palsa peatlands. *Biogeosciences 11*, 3369–3380, doi: 10.5194/bg-11-3369-2014.

Krull E.S. & Retallack G.J. 2000. δ13C depth profiles from paleosols across the Permian-Triassic boundary: Evidence for methane release. *GSA Bulletin 112*, 1459–1472, doi: 10.1130/0016-7606(2000)112<1459:CDPFPA>2.0.CO;2.

Kuhry P. & Vitt D.H. 1996. Fossil Carbon/Nitrogen Ratios as a Measure of Peat Decomposition. *Ecology 77*, 271–275, doi: 10.2307/2265676.

Kwon M.J., Beulig F., Ilie I., Wildner M., Küsel K., Merbold L., Mahecha M.D., Zimov N., Zimov S.A., Heimann M., Schuur E.A.G., Kostka J.E., Kolle O., Hilke I. & Göckede M. 2017. Plants, microorganisms, and soil temperatures contribute to a decrease in methane fluxes on a drained Arctic floodplain. *Global Change Biology 23*, 2396–2412, doi: 10.1111/gcb.13558.

Lachenbruch A.H. 1962. *Mechanics of Thermal Contraction Cracks and Ice-Wedge Polygons in Permafrost*. Geological Society of America.

Lafrenière M.J. & Lamoureux S.F. 2019. Effects of changing permafrost conditions on hydrological processes and fluvial fluxes. *Earth-Science Reviews 191*, 212–223, doi: 10.1016/j.earscirev.2019.02.018.

Lantuit H. & Pollard W. 2007. Fifty years of coastal erosion and retrogressive thaw slump activity on Herschel Island, Southern Beaufort Sea, Yukon Territory, Canada. *Geomorphology 95*, doi: 10.1016/j.geomorph.2006.07.040.

Lantuit H. & Pollard W.H. 2005. Temporal stereophotogrammetric analysis of retrogressive thaw slumps on Herschel Island, Yukon Territory. *Natural Hazards and Earth System Sciences 5*, 413–423, doi: 10.5194/nhess-5-413-2005.

Lawrence D.M., Koven C.D., Swenson S.C., Riley W.J. & Slater A.G. 2015. Permafrost thaw and resulting soil moisture changes regulate projected high-latitude high-latitude CO2 and CH4 emissions. *Environmental Research Letters 10*, 094011, doi: 10.1088/1748-9326/10/9/094011.

Lawrence D.M., Slater A.G., Romanovsky V.E. & Nicolsky D.J. 2008. Sensitivity of a model projection of near-surface permafrost degradation to soil column depth and representation of soil organic matter. *Journal of Geophysical Research: Earth Surface 113*, doi: 10.1029/2007JF000883.

Lee H., Schuur E.A.G., Inglett K.S., Lavoie M. & Chanton J.P. 2012. The rate of permafrost carbon release under aerobic and anaerobic conditions and its potential effects on climate. *Global Change Biology 18*, 515–527, doi: 10.1111/j.1365-2486.2011.02519.x.

Lehner B. & Döll P. 2004. Development and validation of a global database of lakes, reservoirs and wetlands. *Journal of Hydrology 296*, 1–22, doi: 10.1016/j.jhydrol.2004.03.028.

Lenz J., Wetterich S., Jones B.M., Meyer H., Bobrov A. & Grosse G. 2016. Evidence of multiple thermokarst lake generations from an 11 800-year-old permafrost core on the northern Seward Peninsula, Alaska. *Boreas 45*, 584–603, doi: 10.1111/bor.12186.

Lerch T.Z., Nunan N., Dignac M.-F., Chenu C. & Mariotti A. 2011. Variations in microbial isotopic fractionation during soil organic matter decomposition. *Biogeochemistry 106*, 5–21, doi: 10.1007/s10533-010-9432-7.

Li X., Anderson B.J., Vogeler I. & Schwendenmann L. 2018. Long-chain n-alkane and n-fatty acid characteristics in plants and soil - potential to separate plant growth forms, primary and secondary grasslands? *Science of The Total Environment 645*, 1567–1578, doi: 10.1016/j.scitotenv.2018.07.105.

Lichtfouse E. 1998. Isotope and biosynthetic evidence for the origin of long-chain aliphatic lipids in soils. *Die Naturwissenschaften 85*, 76–77, doi: 10.1007/s001140050456.

Liebner S., Zeyer J., Wagner D., Schubert C., Pfeiffer E.-M. & Knoblauch C. 2011. Methane oxidation associated with submerged brown mosses reduces methane emissions from Siberian polygonal tundra. *Journal of Ecology 99*, 914–922, doi: 10.1111/j.1365-2745.2011.01823.x.

Lindgren P.R., Farquharson L.M., Romanovsky V.E. & Grosse G. 2021. Landsat-based lake distribution and changes in western Alaska permafrost regions between the 1970s and 2010s. *Environmental Research Letters 16*, 025006, doi: 10.1088/1748-9326/abd270.

Ling F. & Zhang T. 2003. Numerical simulation of permafrost thermal regime and talik development under shallow thaw lakes on the Alaskan Arctic Coastal Plain. *Journal of Geophysical Research: Atmospheres 108*, doi: 10.1029/2002JD003014.

Loiko S., Klimova N., Kuzmina D. & Pokrovsky O. 2020. Lake Drainage in Permafrost Regions Produces Variable Plant Communities of High Biomass and Productivity. *Plants 9*, 867, doi: 10.3390/plants9070867.

Loisel J., Yu Z., Beilman D.W., Camill P., Alm J., Amesbury M.J., Anderson D., Andersson S., Bochicchio C., Barber K., Belyea L.R., Bunbury J., Chambers F.M., Charman D.J., Vleeschouwer F.D., Fialkiewicz-Koziel B., Finkelstein S.A., Galka M., Garneau M., Hammarlund D., Hinchcliffe W., Holmquist J., Hughes P., Jones M.C., Klein E.S., Kokfelt U., Korhola A., Kuhry P., Lamarre A.,

Lamentowicz M., Large D., Lavoie M., MacDonald G., Magnan G., Makila M., Mallon G., Mathijssen P., Mauquoy D., McCarroll J., Moore T.R., Nichols J., O'Reilly B., Oksanen P., Packalen M., Peteet D., Richard P.J.H., Robinson S., Ronkainen T., Rundgren M., Sannel A.B.K., Tarnocai C., Thom T., Tuittila E.-S., Turetsky M., Valiranta M., Linden M. van der, Geel B. van, Bellen S. van, Vitt D., Zhao Y. & Zhou W. 2014. A database and synthesis of northern peatland soil properties and Holocene carbon and nitrogen accumulation. *The Holocene 24*, 1028–1042, doi: 10.1177/0959683614538073.

Lovley D.R. & Klug M.J. 1986. Model for the distribution of sulfate reduction and methanogenesis in freshwater sediments. *Geochimica et Cosmochimica Acta 50*, 11–18, doi: 10.1016/0016-7037(86)90043-8.

Lunardini V.J. 1995. *Permafrost formation time*. [Hanover, N.H] : [Springfield, Va: US Army Corps of Engineers, Cold Regions Research & Engineering Laboratory ; Available from NTIS.

Luo Y., Wan S., Hui D. & Wallace L.L. 2001. Acclimatization of soil respiration to warming in a tall grass prairie. *Nature 413*, 622–625, doi: 10.1038/35098065.

Mackay J.R. 1981. An experiment in lake drainage, Richards Island, Northwest Territories; a progress report. *An experiment in lake drainage, Richards Island, Northwest Territories; a progress report*.

Mackay J.R. 1988. Catastrophic lake drainage, Tuktoyaktuk Peninsula area, District of Mackenzie. *Paper - Geological Survey of Canada 881*, 83–90.

Mackay J.R. 1978. Freshwater shelled invertebrate indicators of paleoclimate in northwestern Canada during late glacial times: Discussion. *Canadian Journal of Earth Sciences 15*, 461–462, doi: 10.1139/e78-052.

Mackay J.R. 1963. Notes on the Shoreline Recession along the Coast of the Yukon Territory. *Arctic 16*, 195–197.

Mackelprang R., Waldrop M.P., DeAngelis K.M., David M.M., Chavarria K.L., Blazewicz S.J., Rubin E.M. & Jansson J.K. 2011. Metagenomic analysis of a permafrost microbial community reveals a rapid response to thaw. *Nature 480*, 368–371, doi: 10.1038/nature10576.

MacKenzie W.H., Kennedy C.E. & Flynn N. 2022. *Ecosystems of the Yukon Arctic Region: a guide to identification*. Whitehorse, Yukon: Department of Environment, Fish and Wildlife Branch, Government of Yukon.

Malmer N. & Holm E. 1984. Variation in the C/N-Quotient of Peat in Relation to Decomposition Rate and Age Determination with 210 Pb. *Oikos 43*, 171–182, doi: 10.2307/3544766.

Manson G.K. & Solomon S.M. 2007. Past and future forcing of Beaufort Sea coastal change. *Atmosphere-Ocean 45*, 107–122, doi: 10.3137/ao.450204.

Marschner B. & Kalbitz K. 2003. Controls of bioavailability and biodegradability of dissolved organic matter in soils. *Geoderma 113*, 211–235, doi: 10.1016/S0016-7061(02)00362-2.

Marsh P. & Neumann N.N. 2001. Processes controlling the rapid drainage of two ice-rich permafrost-dammed lakes in NW Canada. *Hydrological Processes 15*, 3433–3446, doi: 10.1002/hyp.1035.

Marsh P., Russell M., Pohl S., Haywood H. & Onclin C. 2009. Changes in thaw lake drainage in the Western Canadian Arctic from 1950 to 2000. *Hydrological Processes 23*, 145–158, doi: 10.1002/hyp.7179.

Martens J., Wild B., Muschitiello F., O'Regan M., Jakobsson M., Semiletov I., Dudarev O.V. & Gustafsson Ö. 2020. Remobilization of dormant carbon from Siberian-Arctic permafrost during three past warming events. *Science Advances 6*, eabb6546, doi: 10.1126/sciadv.abb6546.

Marzi R., Torkelson B.E. & Olson R.K. 1993. A revised carbon preference index. *Organic Geochemistry 20*, 1303–1306, doi: 10.1016/0146-6380(93)90016-5.

Masson-Delmotte V.P., Zhai P., Pirani A., Conors S.L., Péan C., Berger S., Caud N., Chen Y., Goldfarb L., Gomis M.I., Huang M., Leitzell K., Lonnoy E., Matthews J.B.R., Maycock T.K., Waterfield T., Yelekçi O., Yu R. & Zhou B. 2021. *Climate Change 2021: The Physical Science Basis. Contribution of Working Group I to the Sixth Assessment Report of the Intergovernmental Panel on Climate Change*. IPCC (ed.). Cambridge, United Kingdom and New York, NY, USA: Cambridge University Press. Accessed on the internet at doi:10.1017/9781009157896 on .

Matveev A., Laurion I., Deshpande B.N., Bhiry N. & Vincent W.F. 2016. High methane emissions from thermokarst lakes in subarctic peatlands. *Limnology and Oceanography 61*, S150–S164, doi: 10.1002/lno.10311.

McGuire A.D., Anderson L.G., Christensen T.R., Dallimore S., Guo L., Hayes D.J., Heimann M., Lorenson T.D., Macdonald R.W. & Roulet N. 2009. Sensitivity of the carbon cycle in the Arctic to climate change. *Ecological Monographs 79*, 523–555, doi: 10.1890/08-2025.1.

McGuire A.D., Lawrence D.M., Koven C., Clein J.S., Burke E., Chen G., Jafarov E., MacDougall A.H., Marchenko S., Nicolsky D., Peng S., Rinke A., Ciais P., Gouttevin I., Hayes D.J., Ji D., Krinner G., Moore J.C., Romanovsky V., Schädel C., Schaefer K., Schuur E.A.G. & Zhuang Q. 2018. Dependence of the evolution of carbon dynamics in the northern permafrost region on the trajectory of climate change. *Proceedings of the National Academy of Sciences 115*, 3882–3887, doi: 10.1073/pnas.1719903115.

Melchert J.O., Wischhöfer P., Knoblauch C., Eckhardt T., Liebner S. & Rethemeyer J. 2022. Sources of CO2 Produced in Freshly Thawed Pleistocene-Age Yedoma Permafrost. *Frontiers in Earth Science 9*. Accessed on the internet at https://www.frontiersin.org/articles/10.3389/feart.2021.737237 on 19 September 2023.

Melillo J.M., Aber J.D., Linkins A.E., Ricca A., Fry B. & Nadelhoffer K.J. 1989. Carbon and nitrogen dynamics along the decay continuum: Plant litter to soil organic matter. *Plant and Soil 115*, 189–198, doi: 10.1007/BF02202587.

Meyers P.A. 1997. Organic geochemical proxies of paleoceanographic, paleolimnologic, and paleoclimatic processes. *Organic Geochemistry 27*, 213–250, doi: 10.1016/S0146-6380(97)00049-1.

Meyers P.A. 1994. Preservation of elemental and isotopic source identification of sedimentary organic matter. *Chemical Geology 114*, 289–302, doi: 10.1016/0009-2541(94)90059-0.

Michaelson G.J. & Ping C.L. 2003. Soil organic carbon and CO2 respiration at subzero temperature in soils of Arctic Alaska. *Journal of Geophysical Research: Atmospheres 108*, ALT 5-1-ALT 5-10, doi: 10.1029/2001JD000920.

Millero F., Huang F., Graham T. & Pierrot D. 2007. The dissociation of carbonic acid in NaCl solutions as a function of concentration and temperature. *Geochimica et Cosmochimica Acta 71*, 46–55, doi: 10.1016/j.gca.2006.08.041.

Miltner A., Bombach P., Schmidt-Brücken B. & Kästner M. 2012. SOM genesis: microbial biomass as a significant source. *Biogeochemistry 111*, 41–55, doi: 10.1007/s10533-011-9658-z.

Mueller C.W., Rethemeyer J., Kao-Kniffin J., Löppmann S., Hinkel K.M. & G. Bockheim J. 2015. Large amounts of labile organic carbon in permafrost soils of northern Alaska. *Global Change Biology 21*, 2804–2817, doi: 10.1111/gcb.12876.

Nadelhoffer K.J. & Fry B. 1988. Controls on Natural Nitrogen-15 and Carbon-13 Abundances in Forest Soil Organic Matter. *Soil Science Society of America Journal 52*, 1633–1640, doi: 10.2136/sssaj1988.03615995005200060024x.

Natali S.M., Schuur E.A.G., Webb E.E., Pries C.E.H. & Crummer K.G. 2014. Permafrost degradation stimulates carbon loss from experimentally warmed tundra. *Ecology 95*, 602–608, doi: 10.1890/13-0602.1.

Neubauer S.C. & Megonigal J.P. 2015. Moving Beyond Global Warming Potentials to Quantify the Climatic Role of Ecosystems. *Ecosystems 18*, 1000–1013, doi: 10.1007/s10021-015-9879-4.

Nguyen T.-N., Burn C.R., King D.J. & Smith S.L. 2009. Estimating the extent of near-surface permafrost using remote sensing, Mackenzie Delta, Northwest Territories. *Permafrost and Periglacial Processes 20*, 141–153, doi: 10.1002/ppp.637.

Nilsson M. & Öquist M. 2009a. Partitioning Litter Mass Loss into Carbon Dioxide and Methane in Peatland Ecosystems. *Carbon Cycling in Northern Peatlands*. Pp. 131–144. American Geophysical Union (AGU), doi: 10.1029/2008GM000819.

Nilsson M. & Öquist M. 2009b. Partitioning Litter Mass Loss into Carbon Dioxide and Methane in Peatland Ecosystems. *Carbon Cycling in Northern Peatlands*. Pp. 131–144. American Geophysical Union (AGU), doi: 10.1029/2008GM000819.

Nimz H.H. & Tutschek R. 1977. Kohlenstoff-13-NMR-Spektren von Ligninen, 7. Zur Frage des Ligningehalts von Moosen (Sphagnum magellanicum Brid.). *31*, 101–106, doi: 10.1515/hfsg.1977.31.4.101.

Nitze I., Grosse G., Jones B.M., Arp C.D., Ulrich M., Fedorov A. & Veremeeva A. 2017. Landsat-Based Trend Analysis of Lake Dynamics across Northern Permafrost Regions. *Remote Sensing 9*, 640, doi: 10.3390/rs9070640.

Nitze I., Grosse G., Jones B.M., Romanovsky V.E. & Boike J. 2018. Remote sensing quantifies widespread abundance of permafrost region disturbances across the Arctic and Subarctic. *Nature Communications 9*, 5423, doi: 10.1038/s41467-018-07663-3.

Obu J., Lantuit H., Fritz M., Pollard W.H., Sachs T. & Günther F. 2016. Relation between planimetric and volumetric measurements of permafrost coast erosion: a case study from Herschel Island, western Canadian Arctic. *Polar Research 35*, 30313, doi: 10.3402/polar.v35.30313.

Obu J., Westermann S., Bartsch A., Berdnikov N., Christiansen H.H., Dashtseren A., Delaloye R., Elberling B., Etzelmüller B., Kholodov A., Khomutov A., Kääb A., Leibman M.O., Lewkowicz A.G., Panda S.K., Romanovsky V., Way R.G., Westergaard-Nielsen A., Wu T., Yamkhin J. & Zou D. 2019. Northern Hemisphere permafrost map based on TTOP modelling for 2000–2016 at 1 km2 scale. *Earth-Science Reviews 193*, 299–316, doi: 10.1016/j.earscirev.2019.04.023.

Oechel W.C., Hastings S.J., Vourlrtis G., Jenkins M., Riechers G. & Grulke N. 1993. Recent change of Arctic tundra ecosystems from a net carbon dioxide sink to a source. *Nature 361*, 520–523, doi: 10.1038/361520a0.

Oechel W.C., Vourlitis G.L., Hastings S.J., Ault Jr. R.P. & Bryant P. 1998. The effects of water table manipulation and elevated temperature on the net CO2 flux of wet sedge tundra ecosystems. *Global Change Biology 4*, 77–90, doi: 10.1046/j.1365-2486.1998.00110.x.

Oechel W.C., Vourlitis G.L., Hastings S.J., Zulueta R.C., Hinzman L. & Kane D. 2000. Acclimation of ecosystem CO2 exchange in the Alaskan Arctic in response to decadal climate warming. *Nature 406*, 978–981, doi: 10.1038/35023137.

Olefeldt D., Goswami S., Grosse G., Hayes D., Hugelius G., Kuhry P., McGuire A.D., Romanovsky V.E., Sannel A.B.K., Schuur E. a. G. & Turetsky M.R. 2016. Circumpolar distribution and carbon storage of thermokarst landscapes. *Nature Communications 7*, 13043, doi: 10.1038/ncomms13043.

Olefeldt D., Heffernan L., Jones M.C., Sannel A.B.K., Treat C.C. & Turetsky M.R. 2021. Permafrost Thaw in Northern Peatlands: Rapid Changes in Ecosystem and Landscape Functions. In J.G. Canadell &

R.B. Jackson (eds.): *Ecosystem Collapse and Climate Change*. Ecological Studies. Pp. 27–67. Cham: Springer International Publishing, doi: 10.1007/978-3-030-71330-0_3.

Olefeldt D., Turetsky M.R., Crill P.M. & McGuire A.D. 2013. Environmental and physical controls on northern terrestrial methane emissions across permafrost zones. *Global Change Biology 19*, 589–603, doi: 10.1111/gcb.12071.

Otto A. & Simpson M.J. 2005. Degradation and Preservation of Vascular Plant-derived Biomarkers in Grassland and Forest Soils from Western Canada. *Biogeochemistry 74*, 377–409, doi: 10.1007/s10533-004-5834-8.

Palmtag J., Hugelius G., Lashchinskiy N., Tamstorf M.P., Richter A., Elberling B. & Kuhry P. 2015. Storage, Landscape Distribution, and Burial History of Soil Organic Matter in Contrasting Areas of Continuous Permafrost. *Arctic, Antarctic, and Alpine Research 47*, 71–88, doi: 10.1657/AAAR0014-027.

Parton W.J., Schimel D.S., Cole C.V. & Ojima D.S. 1987. Analysis of Factors Controlling Soil Organic Matter Levels in Great Plains Grasslands. *Soil Science Society of America Journal 51*, 1173–1179, doi: 10.2136/sssaj1987.03615995005100050015x.

Paul E.A. 1981. *Soil Biochemistry*. CRC Press.

Paul E.A. 2016. The nature and dynamics of soil organic matter: Plant inputs, microbial transformations, and organic matter stabilization. *Soil Biology and Biochemistry 98*, 109–126, doi: 10.1016/j.soilbio.2016.04.001.

Ping C.L., Jastrow J.D., Jorgenson M.T., Michaelson G.J. & Shur Y.L. 2015. Permafrost soils and carbon cycling. *SOIL 1*, 147–171, doi: 10.5194/soil-1-147-2015.

Ping C.L., Michaelson G.J. & Kimble J.M. 1997. Carbon storage along a latitudinal transect in Alaska. *Nutrient Cycling in Agroecosystems 49*, 235–242, doi: 10.1023/A:1009731808445.

Plug L.J. & West J.J. 2009. Thaw lake expansion in a two-dimensional coupled model of heat transfer, thaw subsidence, and mass movement. *Journal of Geophysical Research: Earth Surface 114*, doi: 10.1029/2006JF000740.

Polishchuk Y.M., Bryksina N.A. & Polishchuk V.Y. 2015. Remote analysis of changes in the number of small thermokarst lakes and their distribution with respect to their sizes in the cryolithozone of Western Siberia, 2015. *Izvestiya, Atmospheric and Oceanic Physics 51*, 999–1006, doi: 10.1134/S0001433815090145.

Pollard W.H. 1990. The nature and origin of ground ice in the Herschel Island area, Yukon Territory. *Proceedings, Fifth Canadian Permafrost Conference, Québec*. Pp. 23–30.

Popp T.J., Chanton J.P., Whiting G.J. & Grant N. 2000. Evaluation of methane oxidation in the rhizosphere of a Carex dominated fen in northcentral Alberta, Canada. *Biogeochemistry 51*, 259–281, doi: 10.1023/A:1006452609284.

Powers J.S. & Schlesinger W.H. 2002. Geographic and vertical patterns of stable carbon isotopes in tropical rain forest soils of Costa Rica. *Geoderma 109*, 141–160, doi: 10.1016/S0016-7061(02)00148-9.

Poynter J.G., Farrimond P., Robinson N. & Eglinton G. 1989. Aeolian-Derived Higher Plant Lipids in the Marine Sedimentary Record: Links with Palaeoclimate. In M. Leinen & M. Sarnthein (eds.): *Paleoclimatology and Paleometeorology: Modern and Past Patterns of Global Atmospheric Transport*. NATO ASI Series. Pp. 435–462. Dordrecht: Springer Netherlands, doi: 10.1007/978-94-009-0995-3_18.

Prater J.L., Chanton J.P. & Whiting G.J. 2007. Variation in methane production pathways associated with permafrost decomposition in collapse scar bogs of Alberta, Canada. *Global Biogeochemical Cycles 21*, doi: 10.1029/2006GB002866.

R development team. 2022. R: A language and environment for statistical computing. Accessed on the internet at https://www.R-project.org/ on .

Radke Matthias., Willsch Helmut. & Welte D.H. 1980. Preparative hydrocarbon group type determination by automated medium pressure liquid chromatography. *Analytical Chemistry 52*, 406–411, doi: 10.1021/ac50053a009.

Rampton V. 1982. Quaternary Geology of the Yukon Coastal Plain. *Quaternary Geology of the Yukon Coastal Plain*.

Rasmussen S., Wolff C. & Rudolph H. 1995. Compartmentalization of phenolic constituents in sphagnum. *Phytochemistry 38*, 35–39, doi: 10.1016/0031-9422(94)00650-I.

Reimer P.J. 2020. Composition and consequences of the IntCal20 radiocarbon calibration curve. *Quaternary Research 96*, 22–27, doi: 10.1017/qua.2020.42.

Rieley G., Collier R.J., Jones D.M., Eglinton G., Eakin P.A. & Fallick A.E. 1991. Sources of sedimentary lipids deduced from stable carbon-isotope analyses of individual compounds. *Nature 352*, 425–427, doi: 10.1038/352425a0.

Ritchie J.C. 1984. Past and Present Vegetation of the Far Northwest of Canada. *Past and Present Vegetation of the Far Northwest of Canada*. University of Toronto Press, doi: 10.3138/9781487580353.

Rivkina E., Gilichinsky D., Wagener S., Tiedje J. & McGrath J. 1998. Biogeochemical activity of anaerobic microorganisms from buried permafrost sediments. *Geomicrobiology Journal 15*, 187–193, doi: 10.1080/01490459809378075.

Rivkina E., Shcherbakova V., Laurinavichius K., Petrovskaya L., Krivushin K., Kraev G., Pecheritsina S. & Gilichinsky D. 2007. Biogeochemistry of methane and methanogenic archaea in permafrost. *FEMS Microbiology Ecology 61*, 1–15, doi: 10.1111/j.1574-6941.2007.00315.x.

Romanovsky V.E., Smith S.L. & Christiansen H.H. 2010. Permafrost thermal state in the polar Northern Hemisphere during the international polar year 2007–2009: a synthesis. *Permafrost and Periglacial Processes 21*, 106–116, doi: 10.1002/ppp.689.

Roslev P. & King G.M. 1996. Regulation of methane oxidation in a freshwater wetland by water table changes and anoxia. *FEMS Microbiology Ecology 19*, 105–115, doi: 10.1111/j.1574-6941.1996.tb00203.x.

Roy Chowdhury T., Herndon E.M., Phelps T.J., Elias D.A., Gu B., Liang L., Wullschleger S.D. & Graham D.E. 2015. Stoichiometry and temperature sensitivity of methanogenesis and CO_2 production from saturated polygonal tundra in Barrow, Alaska. *Global Change Biology 21*, 722–737, doi: 10.1111/gcb.12762.

Roy-Leveillee P. & Burn C.R. 2017. Near-shore talik development beneath shallow water in expanding thermokarst lakes, Old Crow Flats, Yukon. *Journal of Geophysical Research: Earth Surface 122*, 1070–1089, doi: 10.1002/2016JF004022.

Rullkötter J. 2003. Geochemistry, Organic. In R.A. Meyers (ed.): *Encyclopedia of Physical Science and Technology (Third Edition)*. Pp. 549–574. New York: Academic Press, doi: 10.1016/B0-12-227410-5/00282-9.

Rustad L., Campbell J., Marion G., Norby R., Mitchell M., Hartley A., Cornelissen J., Gurevitch J., & GCTE-NEWS. 2001. A meta-analysis of the response of soil respiration, net nitrogen mineralization, and

aboveground plant growth to experimental ecosystem warming. *Oecologia 126*, 543–562, doi: 10.1007/s004420000544.

Šantrůčková H., Bird M.I. & Lloyd J. 2000. Microbial processes and carbon-isotope fractionation in tropical and temperate grassland soils. *Functional Ecology 14*, 108–114, doi: 10.1046/j.1365-2435.2000.00402.x.

Schädel C., Bader M.K.-F., Schuur E.A.G., Biasi C., Bracho R., Čapek P., De Baets S., Diáková K., Ernakovich J., Estop-Aragones C., Graham D.E., Hartley I.P., Iversen C.M., Kane E., Knoblauch C., Lupascu M., Martikainen P.J., Natali S.M., Norby R.J., O'Donnell J.A., Chowdhury T.R., Šantrůčková H., Shaver G., Sloan V.L., Treat C.C., Turetsky M.R., Waldrop M.P. & Wickland K.P. 2016. Potential carbon emissions dominated by carbon dioxide from thawed permafrost soils. *Nature Climate Change 6*, 950–953, doi: 10.1038/nclimate3054.

Schädel C., Schuur E.A.G., Bracho R., Elberling B., Knoblauch C., Lee H., Luo Y., Shaver G.R. & Turetsky M.R. 2014. Circumpolar assessment of permafrost C quality and its vulnerability over time using long-term incubation data. *Global Change Biology 20*, 641–652, doi: 10.1111/gcb.12417.

Schaefer I.K., Lanny V., Franke J., Eglinton T.I., Zech M., Vysloužilová B. & Zech R. 2016. Leaf waxes in litter and topsoils along a European transect. *SOIL 2*, 551–564, doi: 10.5194/soil-2-551-2016.

Schaefer K., Lantuit H., Romanovsky V.E., Schuur E.A.G. & Witt R. 2014. The impact of the permafrost carbon feedback on global climate. *Environmental Research Letters 9*, 085003, doi: 10.1088/1748-9326/9/8/085003.

Schaefer K., Zhang T., Bruhwiler L. & Barrett A.P. 2011. Amount and timing of permafrost carbon release in response to climate warming. *Tellus B 63*, 165–180, doi: 10.1111/j.1600-0889.2011.00527.x.

Schink B. 1997. Energetics of syntrophic cooperation in methanogenic degradation. *Microbiology and Molecular Biology Reviews 61*, 262–280, doi: 10.1128/mmbr.61.2.262-280.1997.

Schirrmeister L., Grosse G., Wetterich S., Overduin P.P., Strauss J., Schuur E.A.G. & Hubberten H.-W. 2011. Fossil organic matter characteristics in permafrost deposits of the northeast Siberian Arctic. *Journal of Geophysical Research: Biogeosciences 116*, doi: 10.1029/2011JG001647.

Schulte S., Mangelsdorf K. & Rullkötter J. 2000. Organic matter preservation on the Pakistan continental margin as revealed by biomarker geochemistry. *Organic Geochemistry 31*, 1005–1022, doi: 10.1016/S0146-6380(00)00108-X.

Schuur E., McGuire A.D., Schädel C., Grosse G., Harden J.W., Hayes D.J., Hugelius G., Koven C.D., Kuhry P., Lawrence D.M., Natali S.M., Olefeldt D., Romanovsky V.E., Schaefer K., Turetsky M.R., Treat C.C. & Vonk J.E. 2015. Climate change and the permafrost carbon feedback. *Nature 520*, 171–179, doi: 10.1038/nature14338.

Schuur E.A.G., Abbott B.W., Bowden W.B., Brovkin V., Camill P., Canadell J.G., Chanton J.P., Chapin F.S., Christensen T.R., Ciais P., Crosby B.T., Czimczik C.I., Grosse G., Harden J., Hayes D.J., Hugelius G., Jastrow J.D., Jones J.B., Kleinen T., Koven C.D., Krinner G., Kuhry P., Lawrence D.M., McGuire A.D., Natali S.M., O'Donnell J.A., Ping C.L., Riley W.J., Rinke A., Romanovsky V.E., Sannel A.B.K., Schädel C., Schaefer K., Sky J., Subin Z.M., Tarnocai C., Turetsky M.R., Waldrop M.P., Walter Anthony K.M., Wickland K.P., Wilson C.J. & Zimov S.A. 2013. Expert assessment of vulnerability of permafrost carbon to climate change. *Climatic Change 119*, 359–374, doi: 10.1007/s10584-013-0730-7.

Schuur E.A.G., Bockheim J., Canadell J.G., Euskirchen E., Field C.B., Goryachkin S.V., Hagemann S., Kuhry P., Lafleur P.M., Lee H., Mazhitova G., Nelson F.E., Rinke A., Romanovsky V.E., Shiklomanov N., Tarnocai C., Venevsky S., Vogel J.G. & Zimov S.A. 2008. Vulnerability of Permafrost Carbon to Climate Change: Implications for the Global Carbon Cycle. *BioScience 58*, 701–714, doi: 10.1641/B580807.

Schuur E. A.G., McGuire A.D., Schädel C., Grosse G., Harden J.W., Hayes D.J., Hugelius G., Koven C.D., Kuhry P., Lawrence D.M., Natali S.M., Olefeldt D., Romanovsky V.E., Schaefer K., Turetsky M.R., Treat C.C. & Vonk J.E. 2015. Climate change and the permafrost carbon feedback. *Nature 520*, 171–179, doi: 10.1038/nature14338.

Seppälä M. 1986. The Origin of Palsas. *Geografiska Annaler: Series A, Physical Geography 68*, 141–147, doi: 10.1080/04353676.1986.11880167.

Sepulveda-Jauregui A., Walter Anthony K.M., Martinez-Cruz K., Greene S. & Thalasso F. 2015. Methane and carbon dioxide emissions from 40 lakes along a north–south latitudinal transect in Alaska. *Biogeosciences 12*, 3197–3223, doi: 10.5194/bg-12-3197-2015.

Shapiro S.S. & Wilk M.B. 1965. An Analysis of Variance Test for Normality (Complete Samples). *Biometrika 52*, 591–611, doi: 10.2307/2333709.

Shaver G.R., Giblin A.E., Nadelhoffer K.J., Thieler K.K., Downs M.R., Laundre J.A. & Rastetter E.B. 2006. Carbon turnover in Alaskan tundra soils: effects of organic matter quality, temperature, moisture and fertilizer. *Journal of Ecology 94*, 740–753, doi: 10.1111/j.1365-2745.2006.01139.x.

Shur Y., Hinkel K.M. & Nelson F.E. 2005. The transient layer: implications for geocryology and climate-change science. *Permafrost and Periglacial Processes 16*, 5–17, doi: 10.1002/ppp.518.

Sistla S.A., Moore J.C., Simpson R.T., Gough L., Shaver G.R. & Schimel J.P. 2013. Long-term warming restructures Arctic tundra without changing net soil carbon storage. *Nature 497*, 615–618, doi: 10.1038/nature12129.

Smith C.A.S., Meikle J.C. & Roots C.F. 2004. *Ecoregions of the Yukon Territory: Biophysical properties of Yukon landscapes*. Summerland, British Columbia, Canada: Yukon Geological Survey. Accessed on the internet at https://data.geology.gov.yk.ca/Reference/67942#InfoTab on .

Smith L.C., Sheng Y., MacDonald G.M. & Hinzman L.D. 2005. Disappearing Arctic Lakes. *Science 308*, 1429–1429, doi: 10.1126/science.1108142.

Song C., Wang X., Miao Y., Wang J., Mao R. & Song Y. 2014. Effects of permafrost thaw on carbon emissions under aerobic and anaerobic environments in the Great Hing'an Mountains, China. *Science of The Total Environment 487*, 604–610, doi: 10.1016/j.scitotenv.2013.09.083.

Ståhle L. & Wold S. 1989. Analysis of variance (ANOVA). *Chemometrics and Intelligent Laboratory Systems 6*, 259–272, doi: 10.1016/0169-7439(89)80095-4.

Stevenson F.J. 1994. *Humus Chemistry: Genesis, Composition, Reactions*. John Wiley & Sons.

Still C.J., Berry J.A., Collatz G.J. & DeFries R.S. 2003. Global distribution of C3 and C4 vegetation: Carbon cycle implications. *Global Biogeochemical Cycles 17*, 6-1-6–14, doi: 10.1029/2001GB001807.

Stout J.D. & Rafter T.A. 1978. *The 13C/12C isotopic ratios of some New Zealand tussock grassland soils*. New Zealand: DSIR Science Information Division.

Strauss J., Schirrmeister L., Grosse G., Fortier D., Hugelius G., Knoblauch C., Romanovsky V., Schädel C., Schneider von Deimling T., Schuur E.A.G., Shmelev D., Ulrich M. & Veremeeva A. 2017. Deep Yedoma permafrost: A synthesis of depositional characteristics and carbon vulnerability. *Earth-Science Reviews 172*, 75–86, doi: 10.1016/j.earscirev.2017.07.007.

Strauss J., Schirrmeister L., Mangelsdorf K., Eichhorn L., Wetterich S. & Herzschuh U. 2015. Organic-matter quality of deep permafrost carbon – a study from Arctic Siberia. *Biogeosciences 12*, 2227–2245, doi: 10.5194/bg-12-2227-2015.

Stroeve J.C., Markus T., Boisvert L., Miller J. & Barrett A. 2014. Changes in Arctic melt season and implications for sea ice loss. *Geophysical Research Letters 41*, 1216–1225, doi: 10.1002/2013GL058951.

Stuiver M., Reimer P.J. & Braziunas T.F. 1998. High-Precision Radiocarbon Age Calibration for Terrestrial and Marine Samples. *Radiocarbon 40*, 1127–1151, doi: 10.1017/S0033822200019172.

Sushama L., Laprise R., Caya D., Verseghy D. & Allard M. 2007. An RCM projection of soil thermal and moisture regimes for North American permafrost zones. *Geophysical Research Letters 34*, doi: 10.1029/2007GL031385.

Swanson D.K. 2019. Thermokarst and precipitation drive changes in the area of lakes and ponds in the National Parks of northwestern Alaska, 1984–2018. *Arctic, Antarctic, and Alpine Research 51*, 265–279, doi: 10.1080/15230430.2019.1629222.

Tanski G., Lantuit H., Ruttor S., Knoblauch C., Radosavljevic B., Strauss J., Wolter J., Irrgang A.M., Ramage J. & Fritz M. 2017. Transformation of terrestrial organic matter along thermokarst-affected permafrost coasts in the Arctic. *Science of The Total Environment 581–582*, 434–447, doi: 10.1016/j.scitotenv.2016.12.152.

Tarnocai C., Canadell J.G., Schuur E. a. G., Kuhry P., Mazhitova G. & Zimov S. 2009. Soil organic carbon pools in the northern circumpolar permafrost region. *Global Biogeochemical Cycles 23*, doi: 10.1029/2008GB003327.

Thomas C.L., Jansen B., van Loon E.E. & Wiesenberg G.L.B. 2021. Transformation of *n*-alkanes from plant to soil: a review. *SOIL 7*, 785–809, doi: 10.5194/soil-7-785-2021.

Treat C.C. & Jones M.C. 2018. Near-surface permafrost aggradation in Northern Hemisphere peatlands shows regional and global trends during the past 6000 years. *The Holocene 28*, 998–1010, doi: 10.1177/0959683617752858.

Treat C.C., Jones M.C., Alder J., Sannel A.B.K., Camill P. & Frolking S. 2021. Predicted Vulnerability of Carbon in Permafrost Peatlands With Future Climate Change and Permafrost Thaw in Western Canada. *Journal of Geophysical Research: Biogeosciences 126*, e2020JG005872, doi: 10.1029/2020JG005872.

Treat C.C., Natali S.M., Ernakovich J., Iversen C.M., Lupascu M., McGuire A.D., Norby R.J., Roy Chowdhury T., Richter A., Šantrůčková H., Schädel C., Schuur E.A.G., Sloan V.L., Turetsky M.R. & Waldrop M.P. 2015. A pan-Arctic synthesis of CH4 and CO2 production from anoxic soil incubations. *Global Change Biology 21*, 2787–2803, doi: 10.1111/gcb.12875.

Treat C.C., Wollheim W.M., Varner R.K., Grandy A.S., Talbot J. & Frolking S. 2014. Temperature and peat type control CO2 and CH4 production in Alaskan permafrost peats. *Global Change Biology 20*, 2674–2686, doi: 10.1111/gcb.12572.

Turetsky M.R., Abbott B.W., Jones M.C., Anthony K.W., Olefeldt D., Schuur E.A.G., Grosse G., Kuhry P., Hugelius G., Koven C., Lawrence D.M., Gibson C., Sannel A.B.K. & McGuire A.D. 2020. Carbon release through abrupt permafrost thaw. *Nature Geoscience 13*, 138–143, doi: 10.1038/s41561-019-0526-0.

van Bergen P.F., Nott C.J., Bull I.D., Poulton P.R. & Evershed R.P. 1998. Organic geochemical studies of soils from the Rothamsted Classical Experiments—IV. Preliminary results from a study of the effect of soil pH on organic matter decay. *Organic Geochemistry 29*, 1779–1795, doi: 10.1016/S0146-6380(98)00188-0.

van Everdingen R.O. 1998. *Multi-language Glossary of Permafrost and related Ground-Ice terms*. Accessed on the internet at http://globalcryospherewatch.org/reference/glossary_docs/Glossary_of_Permafrost_and_Ground-Ice_IPA_2005.pdf on .

van Huissteden J. 2020. Permafrost Carbon Quantities and Fluxes. In J. van Huissteden (ed.): *Thawing Permafrost: Permafrost Carbon in a Warming Arctic*. Pp. 179–274. Cham: Springer International Publishing, doi: 10.1007/978-3-030-31379-1_4.

van Huissteden J., Berrittella C., Parmentier F.J.W., Mi Y., Maximov T.C. & Dolman A.J. 2011. Methane emissions from permafrost thaw lakes limited by lake drainage. *Nature Climate Change 1*, 119–123, doi: 10.1038/nclimate1101.

Vishnivetskaya T.A., Liebner S., Wilhelm R. & Wagner D. 2011. Microbial Carbon Cycling in Permafrost. *Polar Microbiology*. Pp. 181–199. John Wiley & Sons, Ltd, doi: 10.1128/9781555817183.ch9.

Voigt C., Lamprecht R.E., Marushchak M.E., Lind S.E., Novakovskiy A., Aurela M., Martikainen P.J. & Biasi C. 2017. Warming of subarctic tundra increases emissions of all three important greenhouse gases – carbon dioxide, methane, and nitrous oxide. *Global Change Biology 23*, 3121–3138, doi: 10.1111/gcb.13563.

Vonk J.E., Tank S.E., Mann P.J., Spencer R.G.M., Treat C.C., Striegl R.G., Abbott B.W. & Wickland K.P. 2015. Biodegradability of dissolved organic carbon in permafrost soils and aquatic systems: a meta-analysis. *Biogeosciences 12*, 6915–6930, doi: 10.5194/bg-12-6915-2015.

Wagner D. 2008. Microbial Communities and Processes in Arctic Permafrost Environments. In P. Dion & C.S. Nautiyal (eds.): *Microbiology of Extreme Soils*. Soil Biology. Pp. 133–154. Berlin, Heidelberg: Springer, doi: 10.1007/978-3-540-74231-9_7.

Wagner D. & Liebner S. 2009. Global Warming and Carbon Dynamics in Permafrost Soils: Methane Production and Oxidation. In R. Margesin (ed.): *Permafrost Soils*. Soil Biology. Pp. 219–236. Berlin, Heidelberg: Springer, doi: 10.1007/978-3-540-69371-0_15.

Waldrop M.P., Wickland K.P., White Iii R., Berhe A.A., Harden J.W. & Romanovsky V.E. 2010. Molecular investigations into a globally important carbon pool: permafrost-protected carbon in Alaskan soils. *Global Change Biology 16*, 2543–2554, doi: 10.1111/j.1365-2486.2009.02141.x.

Walker D.A., Epstein H.E., Gould W.A., Kelley A.M., Kade A.N., Knudson J.A., Krantz W.B., Michaelson G., Peterson R.A., Ping C.-L., Raynolds M.K., Romanovsky V.E. & Shur Y. 2004. Frost-boil ecosystems: complex interactions between landforms, soils, vegetation and climate. *Permafrost and Periglacial Processes 15*, 171–188, doi: 10.1002/ppp.487.

Walter Anthony K., Daanen R., Anthony P., Schneider von Deimling T., Ping C.-L., Chanton J.P. & Grosse G. 2016. Methane emissions proportional to permafrost carbon thawed in Arctic lakes since the 1950s. *Nature Geoscience 9*, 679–682, doi: 10.1038/ngeo2795.

Walter Anthony K., Schneider von Deimling T., Nitze I., Frolking S., Emond A., Daanen R., Anthony P., Lindgren P., Jones B. & Grosse G. 2018. 21st-century modeled permafrost carbon emissions accelerated by abrupt thaw beneath lakes. *Nature Communications 9*, 3262, doi: 10.1038/s41467-018-05738-9.

Walter Anthony K.M., Zimov S.A., Grosse G., Jones M.C., Anthony P.M., Iii F.S.C., Finlay J.C., Mack M.C., Davydov S., Frenzel P. & Frolking S. 2014. A shift of thermokarst lakes from carbon sources to sinks during the Holocene epoch. *Nature 511*, 452–456, doi: 10.1038/nature13560.

Walter K.M., Chanton J.P., Chapin III F.S., Schuur E. a. G. & Zimov S.A. 2008. Methane production and bubble emissions from arctic lakes: Isotopic implications for source pathways and ages. *Journal of Geophysical Research: Biogeosciences 113*, doi: 10.1029/2007JG000569.

Walter K.M., Edwards M.E., Grosse G., Zimov S.A. & Chapin F.S. 2007. Thermokarst Lakes as a Source of Atmospheric CH4 During the Last Deglaciation. *Science 318*, 633–636, doi: 10.1126/science.1142924.

Walter K.M., Zimov S.A., Chanton J.P., Verbyla D. & Chapin F.S. 2006. Methane bubbling from Siberian thaw lakes as a positive feedback to climate warming. *Nature 443*, 71–75, doi: 10.1038/nature05040.

Walvoord M.A. & Kurylyk B.L. 2016. Hydrologic Impacts of Thawing Permafrost—A Review. *Vadose Zone Journal 15*, vzj2016.01.0010, doi: 10.2136/vzj2016.01.0010.

Walz J., Knoblauch C., Tigges R., Opel T., Schirrmeister L. & Pfeiffer E.-M. 2018. Greenhouse gas production in degrading ice-rich permafrost deposits in northeastern Siberia. *Biogeosciences 15*, 5423–5436, doi: 10.5194/bg-15-5423-2018.

Wang N., Zong Y., Brodie C.R. & Zheng Z. 2014. An examination of the fidelity of n-alkanes as a palaeoclimate proxy from sediments of Palaeolake Tianyang, South China. *Quaternary International 333*, 100–109, doi: 10.1016/j.quaint.2014.01.044.

Washburn A.L. 1979. *Geocryology: a survey of periglacial processes and environments.* London: Edward Arnold.

Weete J.D. 1976. Algal and fungal Waxes. *Chemistry and Biochemistry of Natural Waxes*, 349–418.

Weiss N., Blok D., Elberling B., Hugelius G., Jørgensen C.J., Siewert M.B. & Kuhry P. 2016. Thermokarst dynamics and soil organic matter characteristics controlling initial carbon release from permafrost soils in the Siberian Yedoma region. *Sedimentary Geology 340*, 38–48, doi: 10.1016/j.sedgeo.2015.12.004.

West J.J. & Plug L.J. 2008. Time-dependent morphology of thaw lakes and taliks in deep and shallow ground ice. *Journal of Geophysical Research: Earth Surface 113*, doi: 10.1029/2006JF000696.

Whalen S.C. & Reeburgh W.S. 2000. Methane Oxidation, Production, and Emission at Contrasting Sites in a Boreal Bog. *Geomicrobiology Journal 17*, 237–251, doi: 10.1080/01490450050121198.

Whiting G.J. & Chanton J.P. 2001. Greenhouse carbon balance of wetlands: methane emission versus carbon sequestration. *Tellus B: Chemical and Physical Meteorology 53*, 521–528, doi: 10.3402/tellusb.v53i5.16628.

Williams P.J. & Smith M.W. 1991a. *The Frozen Earth: Fundamentals of Geocryology*. Cambridge University Press.

Williams P.J. & Smith M.W. 1991b. *The Frozen Earth: Fundamentals of Geocryology*. Cambridge University Press.

Wilson R.M., Fitzhugh L., Whiting G.J., Frolking S., Harrison M.D., Dimova N., Burnett W.C. & Chanton J.P. 2017. Greenhouse gas balance over thaw-freeze cycles in discontinuous zone permafrost. *Journal of Geophysical Research: Biogeosciences 122*, 387–404, doi: 10.1002/2016JG003600.

Wolter J., Lantuit H., Fritz M., Macias-Fauria M., Myers-Smith I. & Herzschuh U. 2016. Vegetation composition and shrub extent on the Yukon coast, Canada, are strongly linked to ice-wedge polygon degradation. *Polar Research 35*, 27489, doi: 10.3402/polar.v35.27489.

Wolter J., Lantuit H., Herzschuh U., Stettner S. & Fritz M. 2017. Tundra vegetation stability versus lake-basin variability on the Yukon Coastal Plain (NW Canada) during the past three centuries. *The Holocene 27*, 1846–1858, doi: 10.1177/0959683617708441.

Wolter J., Lantuit H., Wetterich S., Rethemeyer J. & Fritz M. 2018. Climatic, geomorphologic and hydrologic perturbations as drivers for mid- to late Holocene development of ice-wedge polygons in the western Canadian Arctic. *Permafrost and Periglacial Processes 29*, 164–181, doi: 10.1002/ppp.1977.

Woodwell G.M. & Whittaker R.H. 1968. Primary Production in Terrestrial Ecosystems. *American Zoologist 8*, 19–30, doi: 10.1093/icb/8.1.19.

Wynn J.G. 2007. Carbon isotope fractionation during decomposition of organic matter in soils and paleosols: Implications for paleoecological interpretations of paleosols. *Palaeogeography, Palaeoclimatology, Palaeoecology 251*, 437–448, doi: 10.1016/j.palaeo.2007.04.009.

Xia S., Song Z., Li Q., Guo L., Yu C., Singh B.P., Fu X., Chen C., Wang Y. & Wang H. 2021. Distribution, sources, and decomposition of soil organic matter along a salinity gradient in estuarine wetlands characterized by C:N ratio, δ13C-δ15N, and lignin biomarker. *Global Change Biology 27*, 417–434, doi: 10.1111/gcb.15403.

Yamamoto S., Alcauskas J.B. & Crozier T.E. 1976. Solubility of methane in distilled water and seawater. *Journal of Chemical & Engineering Data 21*, 78–80, doi: 10.1021/je60068a029.

Yao Y., Huang Y., Zhao J., Wang L., Ran Y., Liu W. & Cheng H. 2021. Permafrost thaw induced abrupt changes in hydrology and carbon cycling in Lake Wudalianchi, northeastern China. *Geology 49*, 1117–1121, doi: 10.1130/G48891.1.

Zech Michael, Krause T., Meszner S. & Faust D. 2013. Incorrect when uncorrected: Reconstructing vegetation history using n-alkane biomarkers in loess-paleosol sequences – A case study from the Saxonian loess region, Germany. *Quaternary International 296*, 108–116, doi: 10.1016/j.quaint.2012.01.023.

Zech M., Rass S., Buggle B., Löscher M. & Zöller L. 2012. Reconstruction of the late Quaternary paleoenvironments of the Nussloch loess paleosol sequence, Germany, using n-alkane biomarkers. *Quaternary Research 78*, 226–235, doi: 10.1016/j.yqres.2012.05.006.

Zech M., Zech R. & Glaser B. 2007. A 240,000-year stable carbon and nitrogen isotope record from a loess-like palaeosol sequence in the Tumara Valley, Northeast Siberia. *Chemical Geology 242*, 307–318, doi: 10.1016/j.chemgeo.2007.04.002.

Zech Roland, Zech M., Marković S., Hambach U. & Huang Y. 2013. Humid glacials, arid interglacials? Critical thoughts on pedogenesis and paleoclimate based on multi-proxy analyses of the loess–paleosol sequence Crvenka, Northern Serbia. *Palaeogeography, Palaeoclimatology, Palaeoecology 387*, 165–175, doi: 10.1016/j.palaeo.2013.07.023.

Zhang T., Barry R.G., Knowles K., Heginbottom J.A. & Brown J. 2008. Statistics and characteristics of permafrost and ground-ice distribution in the Northern Hemisphere. *Polar Geography 31*, 47–68, doi: 10.1080/10889370802175895.

Zhang T., Barry R.G., Knowles K., Heginbottom J.A. & Brown J. 1999. Statistics and characteristics of permafrost and ground-ice distribution in the Northern Hemisphere. *Polar Geography 23*, 132–154, doi: 10.1080/10889379909377670.

Zheng Y., Zhou W., Meyers P.A. & Xie S. 2007. Lipid biomarkers in the Zoigê-Hongyuan peat deposit: Indicators of Holocene climate changes in West China. *Organic Geochemistry 38*, 1927–1940, doi: 10.1016/j.orggeochem.2007.06.012.

Zimov S., Voropaev Y., Semiletov I., Davydov S., Prosiannikov S., Chapin III F.S., Chapin M., Trumbore S. & Tyler S. 1997. North Siberian Lakes: A Methane Source Fueled by Pleistocene Carbon. *Science 277*, 800–802, doi: 10.1126/science.277.5327.800.

Zimov S.A., Davydov S.P., Zimova G.M., Davydova A.I., Schuur E. a. G., Dutta K. & Chapin III F.S. 2006a. Permafrost carbon: Stock and decomposability of a globally significant carbon pool. *Geophysical Research Letters 33*, doi: 10.1029/2006GL027484.

Zimov S.A., Schuur E.A.G. & Chapin F.S. 2006b. Permafrost and the Global Carbon Budget. *Science 312*, 1612–1613, doi: 10.1126/science.1128908.

Zona D., Lipson D., T P., Oberbauer S., Olivas P., Gioli B. & Oechel W. 2012. Increased CO2 loss from vegetated drained lake tundra ecosystems due to flooding. *Global Biogeochemical Cycles*, doi: 10.1029/2011GB004037.

Zona D., Oechel W.C., Peterson K.M., Clements R.J., Paw U K.T. & Ustin S.L. 2010. Characterization of the carbon fluxes of a vegetated drained lake basin chronosequence on the Alaskan Arctic Coastal Plain. *Global Change Biology 16*, 1870–1882, doi: 10.1111/j.1365-2486.2009.02107.x.

Appendix

Appendix 1: Grain size classification according to ISO 14688-1:2017.

Grain size	Descriptive terminology	
> 64 mm		Boulder
< 64 mm	Very coarse	
< 32 mm	Coarse	
< 16 mm	Medium	Gravel
< 8 mm	Fine	
< 4 mm	Very fine	
< 2 mm	Very coarse	
< 1 mm	Coarse	
< 500 µm	Medium	Sand
< 250 µm	Fine	
< 125 µm	Very fine	
< 63 µm	Very coarse	
< 31 µm	Coarse	
< 16 µm	Medium	Silt
< 8 µm	Fine	
< 4 µm	Very fine	
< 2 µm		Clay

Appendix 2: Calculation of dissociation constants of carbon acids for determining c_{DIC} according to Millero et al. (2007).

pK1   Potentiometric measurements as a function of molality and temperature
pK2   Potentiometric measurements as a function of molality and temperature

$$pK_1 = -114.3106 + \frac{5773.67}{T} + 17.779524 \ln T$$

$$pK_2 = -83.2997 + \frac{4821.38}{T} + 13.5962 \ln T$$

$$pK_1^* - pK_1 = 35.2911m^{0.5} + 0.8491m - 0.32m^{1.5} + 0.055m^2 + \frac{-1583.09m^{0.5}}{T} + (-5.4366m^{0.5}) \ln T$$

$$pK_2^* - pK_2 = 38.2746m^{0.5} + 1.6057m - 0.647m^{1.5} + 0.113m^2 + \frac{-1738.16m^{0.5}}{T} + (-6.0346m^{0.5}) \ln T$$

$$K_1 = 10^{-((pK_1^* - pK_1) + pK_1)}$$

$$K_2 = 10^{-((pK_2^* - pK_2) + pK_2)}$$

Appendix 3: Characteristic n-alkane chain lengths in organisms after Zheng et al. (2007) and Schäfer et al. (2016).

n-alkane		Reference
C_{17}	Aquatic algae and photosynthetic bacteria	(e.g., Giger et al., 1980; Cranwell et al., 1987)
Max at C_{21}, C_{23} or C_{25}	Submerged and floating macrophytes	(Cranwell, 1984; Ficken et al., 2000)
> C_{25}	epicuticular leaf waxes, higher terrestrial plants	Eglinton et al., 1962; Eglinton and Hamilton, 1967; Otto and Simpson, 2005
C_{27} and C_{29}	leaf waxes of trees and shrubs	Maffei, 1996; Maffei et al., 2004; Rommerskirchen et al., 2006; Zech et al., 2009; Lei et al., 2010; Kirkels et al., 2013
C_{27}, C_{29} and C_{31}	Vascular land plants and emergent macrophytes	(Eglinton and Hamilton, 1967; Cranwell, 1973; Cranwell et al., 1987; Rieley et al., 1991; Ficken et al., 2000
C_{31} and C_{33}	grasses and herbs	Maffei, 1996; Maffei et al., 2004; Rommerskirchen et al., 2006; Zech et al., 2009; Lei et al., 2010; Kirkels et al., 2013

n-alkanoic acid		Reference
C_{16} and C_{18}	Aquatic algae and photosynthetic bacteria	(e.g., Robinson et al., 1984; Volkman et al., 1999)
> C_{20}	epicuticular leaf waxes, higher terrestrial plants	Eglinton et al., 1962; Eglinton and Hamilton, 1967; Otto and Simpson, 2005
$C_{24} - C_{30}$	Vascular land plants and emergent macrophytes	Cranwell, 1974; Wiesenberg and Schwark, 2006

n-alkanol		Reference
$C_{16} - C_{22}$	Aquatic algae and photosynthetic bacteria	(e.g., Robinson et al., 1984; Volkman et al., 1999)
C_{22} and C_{24}	Submerged and floating macrophytes	(Ficken et al., 1998a)
$C_{22} - C_{30}$	Vascular land plants and emergent macrophytes	Eglinton and Hamilton, 1967; Rieley et al., 1991

Appendix 4: Calibrated radiocarbon ages of YC19-DTLB-7 and YC19-DLB-8

	Median radiocarbon age	Age range (2 σ)	Relative area under probability distribution
	[cal a BP]	[cal a BP]	[-]
YC19-DTLB-7 19.5 – 21 cm	949	788 – 1 071	0.994
YC19-DTLB-7 64 – 65.5 cm	1 619	1 526 – 1 730	1.000
YC19-DTLB-7 132 – 134.5 cm	2 989	2 876 – 3 075	0.986
YC19-DTLB-8 41 – 42.5 cm	600	529 – 659	1.000
YC19-DTLB-8 51 – 52.5 cm	504	474 – 526	1.000
YC19-DTLB-8 86.5 – 88 cm	1 213	1 174 – 1 295	0.765
YC19-DTLB-8 150 – 151.5 cm	8 105	8 027 – 8 176	1.000

Appendix 5: Raw data of sedimentological and biogeochemical parameters at t0.

Sample ID	ice content	TC	TOC	TN	C:N	δ¹³C	pH	eC
	[wt.%]	[wt.%]	[wt.%]	[wt.%]	[-]	[‰ vs. VPDB]	[-]	[μS/cm]
YC19-DTLB-7 AL1	83.65		42.89	1.78	24.14	-27.90	4.75	-
YC19-DTLB-7 AL2	39.31		4.71	0.35	13.31	-27.75	6.23	62.4
YC19-DTLB-7 TL	63.57		11.36	0.75	15.07	-27.69	6.28	73.0
YC19-DTLB-7 PF	62.79		9.52	0.61	15.70	-28.19	6.31	172
YC19-DTLB-8 AL1	91.74		42.18	2.30	18.34	-27.76	5.06	34.9
YC19-DTLB-8 AL2	83.68		43.27	2.12	20.37	-27.73	4.59	52.8
YC19-DTLB-8 TL	81.85		34.89	1.93	18.05	-28.48	5.43	55.9
YC19-DTLB-8 PF	55.17		6.84	0.44	15.45	-27.91	6.50	102.9

Appendix 5: Raw data of sedimentological and biogeochemical parameters at t0.

Appendix 6: Anaerobic incubation results of CH_4 and CO_2 (90 days, 4 °C, N_2 atmosphere).

Sample ID	CH_4 production t_{90}	Mean CH_4 production rate	maximum CH_4 production rate	max:mean CH_4 production rate ratio	Lag time
	[mg CH_4-C g_{TOC}^{-1}]	[µg CH_4-C g_{TOC}^{-1} d^{-1}]	[µg CH_4-C g_{OC}^{-1} d^{-1}]	[-]	[d]
YC19-DTLB-7 AL1	0.27 ± 0.03	3.02 ± 0.38	5.05 ± 0.40	1.67	20
YC19-DTLB-7 AL2	0.49 ± 0.02	5.87 ± 0.77	23.75 ± 4.16	4.05	17
YC19-DTLB-7 TL	0.28 ± 0.00	3.09 ± 0.05	4.68 ± 0.07	1.51	34
YC19-DTLB-7 PF	0.01 ± 0.00	0.16 ± 0.01	1.34 ± 0.28	8.29	2
YC19-DTLB-8 AL1	0.77 ± 0.02	8.54 ± 0.22	19.24 ± 0.45	2.25	17
YC19-DTLB-8 AL2	0.26 ± 0.03	2.91 ± 0.29	6.31 ± 0.24	2.16	22
YC19-DTLB-8 TL	0.12 ± 0.00	1.29 ± 0.04	3.06 ± 0.10	2.37	22
YC19-DTLB-8 PF	0.04 ± 0.00	0.43 ± 0.02	1.84 ± 0.08	4.24	2

Sample ID	CO_2 production t_{90}	Mean CO_2 production rate	Maximum CO_2 production rate	Max:mean CO_2 production rate ratio	Lag time
	[mg CO_2-C g_{TOC}^{-1}]	[µg CO_2-C g_{TOC}^{-1} d^{-1}]	[µg CO_2-C g_{OC}^{-1} d^{-1}]	[-]	[d]
YC19-DTLB-7 AL1	0.02 ± 0.01	0.19 ± 0.12	8.11 ± 2.29	42.96	6
YC19-DTLB-7 AL2	0.14 ± 0.01	2.37 ± 1.40	139.33 ± 8.61	58.86	2
YC19-DTLB-7 TL	0.12 ± 0.01	1.31 ± 0.12	76.71 ± 1.30	58.42	2
YC19-DTLB-7 PF	0.08 ± 0.01	0.84 ± 0.07	66.59 ± 9.29	79.57	2
YC19-DTLB-8 AL1	0.37 ± 0.02	4.91 ± 0.20	68.51 ± 10.85	15.90	3
YC19-DTLB-8 AL2	0.03 ± 0.00	0.34 ± 0.04	16.12 ± 3.49	46.92	6
YC19-DTLB-8 TL	0.01 ± 0.00	0.14 ± 0.05	37.87 ± 4.05	277.54	2
YC19-DTLB-8 PF	0.06 ± 0.00	0.69 ± 0.05	83.70 ± 10.48	121.78	2

Appendix 7: Aerobic incubation results CO_2.

Sample ID	cumulative CO_2 production t_{90}	Mean CO_2 production rate	Maximum CO_2 production rate	Max:mean CO_2 production rate ratio	Lag time
	[mg CO_2-C g_{TOC}^{-1}]	[µg CO_2-C g_{TOC}^{-1} d^{-1}]	[µg CO_2-C g_{TOC}^{-1} d^{-1}]	[-]	[d]
YC19-DTLB-7 AL1		50.37 ± 1.98	88.82 ± 4.20	1.76	13
YC19-DTLB-7 AL2		97.89 ± 0.73	452.94 ± 1.14	4.63	1
YC19-DTLB-7 TL		58.77 ± 2.76	210.96 ± 26.03	3.59	1
YC19-DTLB-7 PF		110.76 ± 3.61	189.86 ± 103.26	1.71	29
YC19-DTLB-8 AL1		129.79 ± 5.35	211.30 ± 11.89	1.63	22
YC19-DTLB-8 AL2		38.78 ± 1.56	92.35 ± 2.09	2.38	15
YC19-DTLB-8 TL		46.58 ± 24.20	80.13 ± 1.94	1.72	1
YC19-DTLB-8 PF		138.66 ± 10.85	416.07 ± 17.04	3.00	1

Appendix 8: Greenhouse gas production potential and climate forcing effect of emissions.

Sample ID	Aerobic incubation		Anaerobic incubation		RCF
	Greenhouse gas production	Climate forcing effect	Greenhouse gas production	Climate forcing effect	
	[mg CO_2-C + CH_4-C g_{OC}^{-1}]	[mg CO_2-eq g_{OC}^{-1}]	[mg CO_2-C + CH_4-C g_{OC}^{-1}]	[mg CO_2-eq g_{OC}^{-1}]	[-]
YC19-DTLB-7-AL1	4.51 ± 0.18	4.52 ± 0.18	0.29 ± 0.02	6.82 ± 0.86	0.66
YC19-DTLB-7-AL2	8.78 ± 0.07	9.04 ± 0.11	0.63 ± 0.02	1.72 ± 0.00	5.11
YC19-DTLB-7-TL	5.27 ± 0.27	5.34 ± 0.27	0.40 ± 0.01	7.06 ± 0.13	0.75
YC19-DTLB-7-PF	9.93 ± 0.32	9.99 ± 0.32	0.09 ± 0.01	0.44 ± 0.03	22.69
YC19-DTLB-8-AL1	11.65 ± 0.46	11.71 ± 0.46	1.14 ± 0.02	19.56 ± 0.57	0.60
YC19-DTLB-8-AL2	3.48 ± 0.14	3.49 ± 0.14	0.29 ± 0.03	6.57 ± 0.65	0.53
YC19-DTLB-8-TL	4.18 ± 2.17	4.20 ± 2.17	0.13 ± 0.01	2.92 ± 0.10	1.43
YC19-DTLB-8-PF	12.45 ± 0.97	12.49 ± 0.97	0.10 ± 0.01	1.04 ± 0.05	12.01

Appendix 9: Raw data of sedimentological and biogeochemical parameters at t$_{90}$ of incubation experiments.

t$_{90}$ of Anaerobic incubation								
Sample ID	ice content	TC	TOC	TN	C:N	δ^{13}C	pH	eC
	[wt.%]	[wt.%]	[wt.%]	[wt.%]	[-]	[‰ vs. VPDB]	[-]	[µS/cm]
DTLB-7 AL1	86.49		45.58	2.03	22.44	-28.00	4.85	225
DTLB-7 AL2	45.27		6.17	0.36	17.30	-27.76	4.95	N.A.
DTLB-7 TL	68.03		15.60	0.93	16.83	-27.62	5.55	1 398
DTLB-7 PF	73.33		10.26	0.62	16.50	-28.19	5.42	1 745
DTLB-8 AL1	94.59		41.87	2.33	17.98	-27.83	5.02	1 221
DTLB-8 AL2	85.83		43.30	2.33	18.62	-27.78	4.66	274
DTLB-8 TL	83.67		38.51	2.16	17.81	-28.48	4.91	694
DTLB-8 PF	67.76		8.15	0.48	16.83	-27.88	5.43	1 956

t$_{90}$ of Aerobic incubation								
Sample ID	ice content	TC	TOC	TN	C:N	δ^{13}C	pH	eC
	[wt.%]	[wt.%]	[wt.%]	[wt.%]	[-]	[‰ vs. VPDB]	[-]	[µS/cm]
DTLB-7 AL1	84.83		45.60	1.87	24.42	- 27.82	5.21	N.A.
DTLB-7 AL2	39.19		5.07	0.34	14.83	- 27.66	6.10	N.A.
DTLB-7 TL	64.38		14.14	0.87	16.33	- 27.69	6.26	N.A.
DTLB-7 PF	70.14		11.16	0.68	16.34	- 28.15	6.82	N.A.
DTLB-8 AL1	92.36		41.88	2.37	17.68	- 27.76	5.32	231
DTLB-8 AL2	84.92		44.14	2.39	18.48	- 27.77	4.98	N.A.
DTLB-8 TL	82.31		37.99	2.08	18.31	- 28.39	5.28	N.A.
DTLB-8 PF	60.14		7.65	0.46	16.49	- 27.89	6.38	120.5

Appendix 10: Raw data of lipid composition and lipid biomarker indices at t_0

	n-alkanes						
Sample ID	c $_{n\text{-alkanes}}$	c $_{n\text{-alkanes}}$	ACL $_{C23\text{-}C33}$	P_{aq}	P_{wax}	OEPD	CPI
	[µg/g$_{dw}$]	[µg/g$_{OC}$]	[-]	[-]	[-]	[-]	[-]
DTLB-7 AL1	106.91	249.27	28.92	0.15	0.89	16.26	8.21
DTLB-7 AL2	6.52	138.49	27.78	0.32	0.76	10.45	5.07
DTLB-7 TL	38.33	337.52	27.67	0.36	0.73	10.35	5.28
DTLB-7 PF	13.41	139.70	27.79	0.28	0.80	10.72	5.46
DTLB-8 AL1	77.71	184.23	27.49	0.40	0.75	11.08	5.38
DTLB-8 AL2	156.22	361.08	27.84	0.21	0.89	14.17	7.06
DTLB-8 TL	108.60	311.27	28.13	0.20	0.87	14.16	7.23
DTLB-8 PF	15.17	221.76	28.67	0.23	0.80	16.06	7.10

	n-alkanols					
Sample ID	c $_{n\text{-alkanols}}$	c $_{n\text{-alkanols}}$	ACL	EOPD	CPI	HPA
	[µg/g$_{dw}$]	[µg/g$_{OC}$]	[-]	[-]	[-]	[-]
DTLB-7 AL1	122.36	285.29	24.76	30.09	19.16	0.43
DTLB-7 AL2	1.75	37.21	24.58	24.89	13.15	0.17
DTLB-7 TL	24.24	213.47	25.75	22.57	12.33	0.34
DTLB-7 PF	1.52	15.82	26.62	27.44	13.47	0.09
DTLB-8 AL1	48.25	114.38	26.44	17.32	11.13	0.43
DTLB-8 AL2	80.05	185.02	26.20	23.22	14.69	0.29
DTLB-8 TL	28.69	82.21	25.63	27.81	15.83	0.16
DTLB-8 PF	18.08	264.19	22.91	21.84	13.49	0.39

Appendix 11: Raw data of lipid composition and lipid biomarker indices at t_{90} of anaerobic incubation

			n-alkanes				
Sample ID	c $_{n\text{-alkanes}}$	c $_{n\text{-alkanes}}$	$ACL_{C23\text{-}C33}$	P_{aq}	P_{wax}	OEPD	CPI
	$[\mu g/g_{dw}]$	$[\mu g/g_{OC}]$	[-]	[-]	[-]	[-]	[-]
DTLB-7 AL1	184.05	403.63	28.45	0.21	0.85	19.31	8.77
DTLB-7 AL2	17.25	279.54	28.33	0.24	0.82	11.56	5.65
DTLB-7 TL	35.82	229.62	27.47	0.39	0.73	10.40	5.22
DTLB-7 PF	36.96	360.26	27.54	0.35	0.77	12.22	5.74
DTLB-8 AL1	31.14	74.38	27.14	0.49	0.69	11.70	5.64
DTLB-8 AL2	101.25	233.84	26.99	0.48	0.82	20.24	8.48
DTLB-8 TL	149.98	389.45	27.33	0.41	0.76	14.94	7.29
DTLB-8 PF	46.72	573.42	28.29	0.28	0.78	13.33	6.38

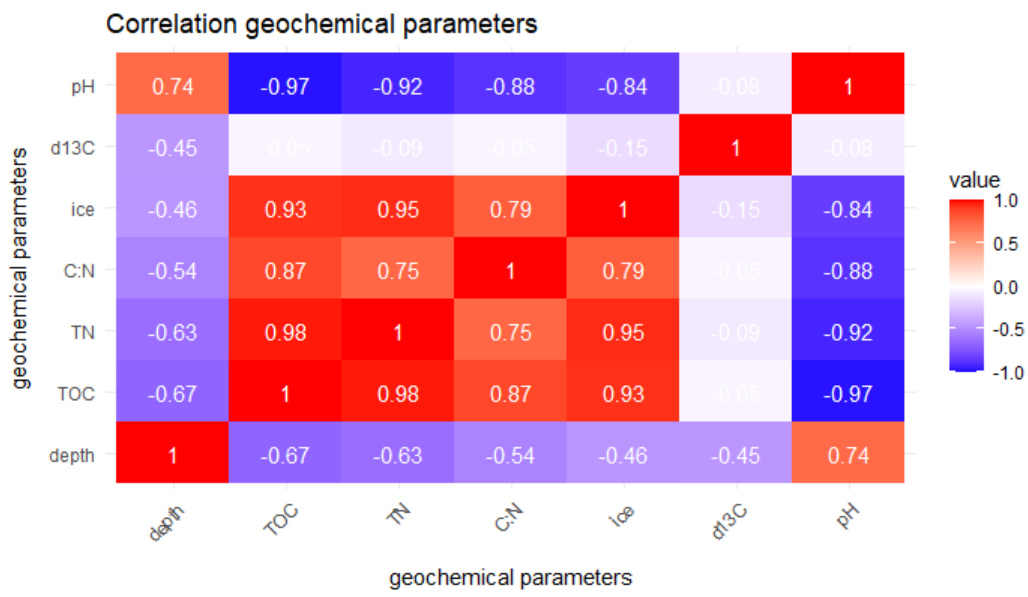|						
			n-alkanols			
Sample ID	c $_{n\text{-alkanols}}$	c $_{n\text{-alkanols}}$	ACL	EOPD	CPI	HPA
	$[\mu g/g_{dw}]$	$[\mu g/g_{OC}]$	[-]	[-]	[-]	[-]
DTLB-7 AL1	272.07	596.87	26.63	29.33	27.35	0.60
DTLB-7 AL2	91.21	1 479.17	22.96	28.40	23.92	0.74
DTLB-7 TL	108.38	694.91	22.99	23.46	19.33	0.63
DTLB-7 PF	124.21	1 210.29	23.27	27.57	22.18	0.67
DTLB-8 AL1	91.00	217.34	23.32	5.37	13.44	0.70
DTLB-8 AL2	139.39	321.90	24.93	18.83	20.35	0.53
DTLB-8 TL	434.11	1 127.41	23.68	22.75	19.81	0.67
DTLB-8 PF	104.79	1 286.21	22.91	18.27	14.48	0.57

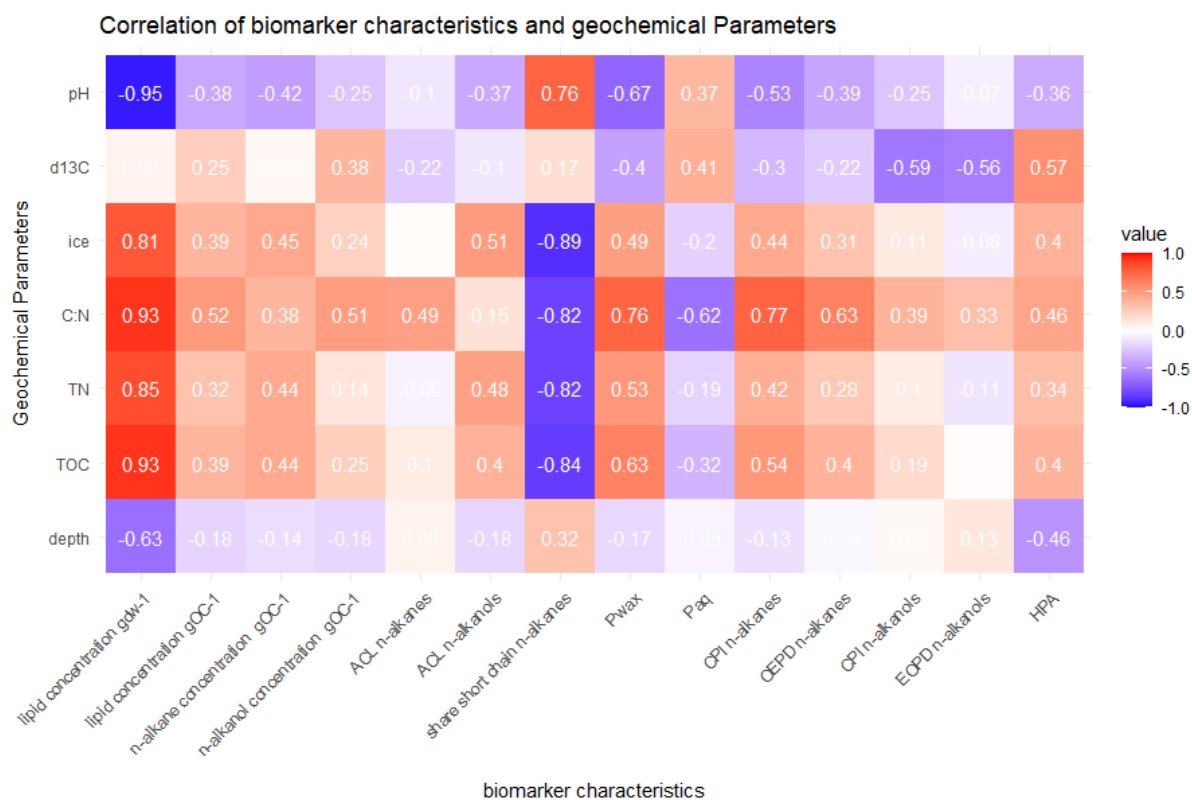*Appendix 12: Raw data of lipid composition and lipid biomarker indices at t_{90} of aerobic incubation*

			n-alkanes				
Sample ID	$c_{\text{n-alkanes}}$	$c_{\text{n-alkanes}}$	$\text{ACL}_{\text{C23-C33}}$	P_{aq}	P_{wax}	OEPD	CPI
	[µg/g$_{dw}$]	[µg/g$_{OC}$]	[-]	[-]	[-]	[-]	[-]
DTLB-7 AL1	137.79	302.17	27.94	0.28	0.81	16.93	7.73
DTLB-7 AL2	16.77	330.71	28.07	0.28	0.79	10.93	5.37
DTLB-7 TL	34.07	240.93	27.52	0.39	0.72	9.87	5.01
DTLB-7 PF	38.58	345.68	27.48	0.35	0.77	11.14	5.50
DTLB-8 AL1	13.52	32.28	26.90	0.54	0.68	11.53	5.91
DTLB-8 AL2	86.71	196.44	27.12	0.44	0.80	17.70	7.95
DTLB-8 TL	54.39	143.18	27.22	0.43	0.75	14.92	7.33
DTLB-8 PF	47.49	620.74	28.29	0.28	0.78	13.33	6.38

|			*n*-alkanols			
Sample ID	$c_{\text{n-alkanols}}$	$c_{\text{n-alkanols}}$	ACL	EOPD	CPI	HPA
	[µg/g$_{dw}$]	[µg/g$_{OC}$]	[-]	[-]	[-]	[-]
DTLB-7 AL1	129.87	284.81	27.98	28.17	29.52	0.50
DTLB-7 AL2	26.24	517.97	24.43	29.74	25.08	0.54
DTLB-7 TL	83.60	591.09	23.61	25.33	20.73	0.60
DTLB-7 PF	36.73	329.18	25.44	27.67	21.28	0.40
DTLB-8 AL1	13.91	33.22	26.20	17.42	19.15	0.57
DTLB-8 AL2	173.70	393.50	26.09	22.41	21.03	0.66
DTLB-8 TL	423.50	1 114.85	23.94	26.36	23.13	0.86
DTLB-8 PF	147.90	1 932.53	23.38	18.72	16.97	0.66

*Appendix 13: changes of lipid concentrations after aerobic and anaerobic incubation*

	Anaerobic incubation			Aerobic incubation		
	Changes $C_{n\text{-alkanes}}$ [%]	Changes $C_{n\text{-alkanols}}$ [%]	Changes $C_{n\text{-alkanes}} + C_{n\text{-alkanols}}$ [%]	Changes $C_{n\text{-alkanes}}$ [%]	Changes $C_{n\text{-alkanols}}$ [%]	Changes $C_{n\text{-alkanes}} + C_{n\text{-alkanols}}$ [%]
YC19-DTLB-7 AL1	+ 61.92	+ 109.22	+ 87.16	+ 21.22	- 0.17	+ 9.81
YC19-DTLB-7 AL2	+ 56.58	+ 3 875.03	+ 900.94	+ 138.79	+ 1 291.95	+ 383.01
YC19-DTLB-7 TL	- 43.29	+ 225.53	+ 67.79	- 28.62	+ 176.89	+ 51.00
YC19-DTLB-7 PF	+ 88.48	+ 7 550.45	+ 909.86	+ 147.44	+ 1 980.77	+ 333.93
YC19-DTLB-8 AL1	- 44.07	+ 90.01	- 2.31	- 82.48	- 70.96	- 78.07
YC19-DTLB-8 AL2	- 51.05	+ 73.98	+ 1.76	- 45.60	+ 112.68	+ 8.03
YC19-DTLB-8 TL	+ 31.36	+ 1 271.33	+ 285.50	- 54.00	+ 1 256.03	+ 219.72
YC19-DTLB-8 PF	+ 141.07	+ 386.84	+ 282.67	+ 179.91	+ 631.49	+ 425.41

Appendix 14: Pearson's correlation coefficients (r) geochemical parameters.

Correlation geochemical parameters

	depth	TOC	TN	C:N	ice	d13C	pH
pH	0.74	-0.97	-0.92	-0.88	-0.84	-0.08	1
d13C	-0.45	-0.05	-0.09	-0.05	-0.15	1	-0.08
ice	-0.46	0.93	0.95	0.79	1	-0.15	-0.84
C:N	-0.54	0.87	0.75	1	0.79	-0.05	-0.88
TN	-0.63	0.98	1	0.75	0.95	-0.09	-0.92
TOC	-0.67	1	0.98	0.87	0.93	-0.05	-0.97
depth	1	-0.67	-0.63	-0.54	-0.46	-0.45	0.74

geochemical parameters (y-axis)

geochemical parameters (x-axis)

value
1.0
0.5
0.0
-0.5
-1.0

Appendix 15: Pearson's correlation coefficients (r) geochemical parameters - biomarker indices.

Correlation of biomarker characteristics and geochemical Parameters

Geochemical Parameters	lipid concentration gdw-1	lipid concentration gOC-1	n-alkane concentration gOC-1	n-alkanol concentration gOC-1	ACL n-alkanes	ACL n-alkanols	share short chain n-alkanes	Pwax	Paq	CPI n-alkanes	OEPD n-alkanes	CPI n-alkanols	EOPD n-alkanols	HPA
pH	-0.95	-0.38	-0.42	-0.25	-0.1	-0.37	0.76	-0.67	0.37	-0.53	-0.39	-0.25	-0.07	-0.36
d13C	0.06	0.25	0.04	0.38	-0.22	-0.1	0.17	-0.4	0.41	-0.3	-0.22	-0.59	-0.56	0.57
ice	0.81	0.39	0.45	0.24		0.51	-0.89	0.49	-0.2	0.44	0.31	0.11	-0.08	0.4
C:N	0.93	0.52	0.38	0.51	0.49	0.15	-0.82	0.76	-0.62	0.77	0.63	0.39	0.33	0.46
TN	0.85	0.32	0.44	0.14	-0.06	0.48	-0.82	0.53	-0.19	0.42	0.28	0.1	-0.11	0.34
TOC	0.93	0.39	0.44	0.25	0.1	0.4	-0.84	0.63	-0.32	0.54	0.4	0.19		0.4
depth	-0.63	-0.18	-0.14	-0.18	0.08	-0.18	0.32	-0.17	-0.05	-0.13	-0.04	0.02	0.13	-0.46

value
1.0
0.5
0.0
-0.5
-1.0

biomarker characteristics

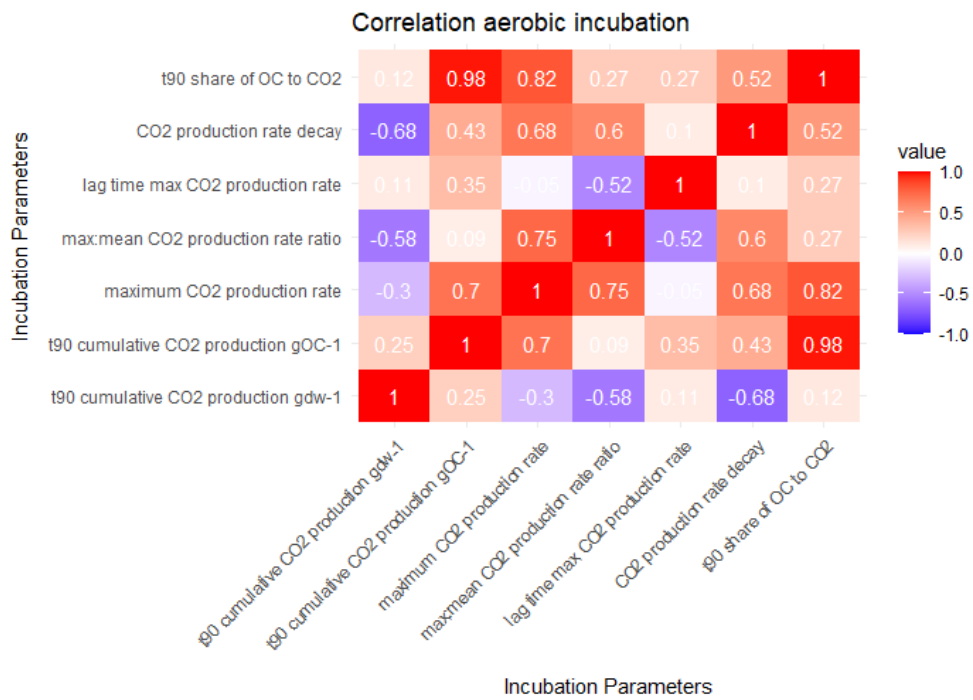*Appendix 16: Pearson's correlation coefficients (r) geochemical parameters - anaerobic incubation characteristics.*

Correlation Geochemical Parameters - anaerobic Incubation Parameters
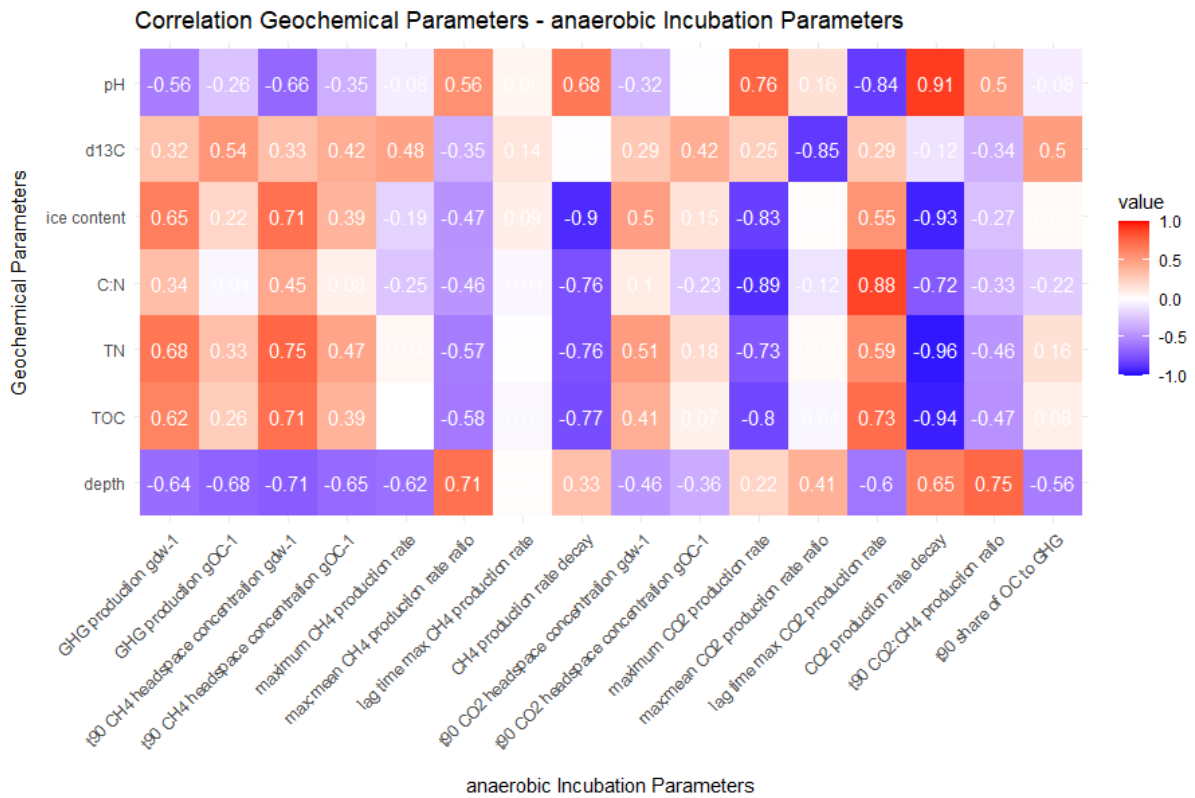
Appendix 17: Pearson's correlation coefficients (r) anaerobic incubation characteristics.

Correlation anaerobic incubation
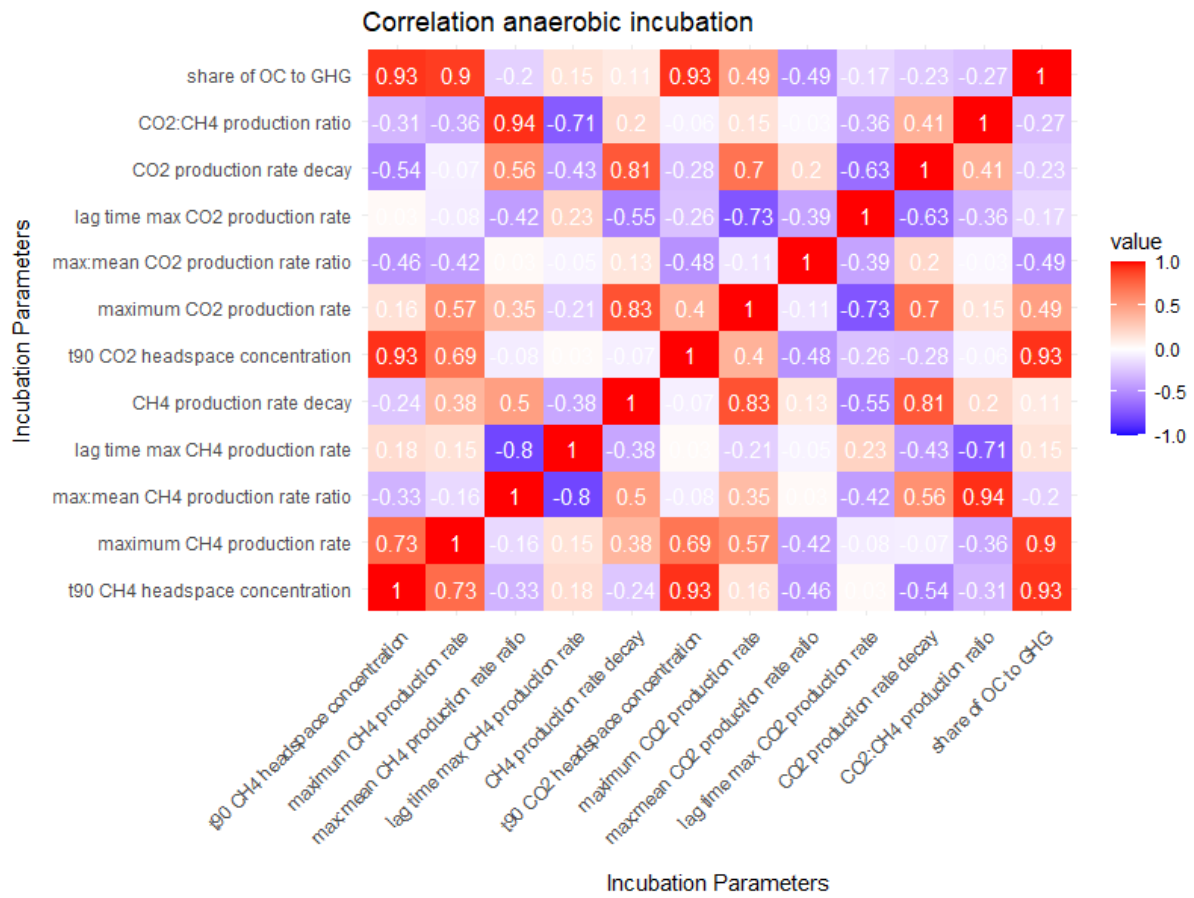
Appendix 18: Pearson's correlation coefficients (r) geochemical parameters - aerobic incubation characteristics.
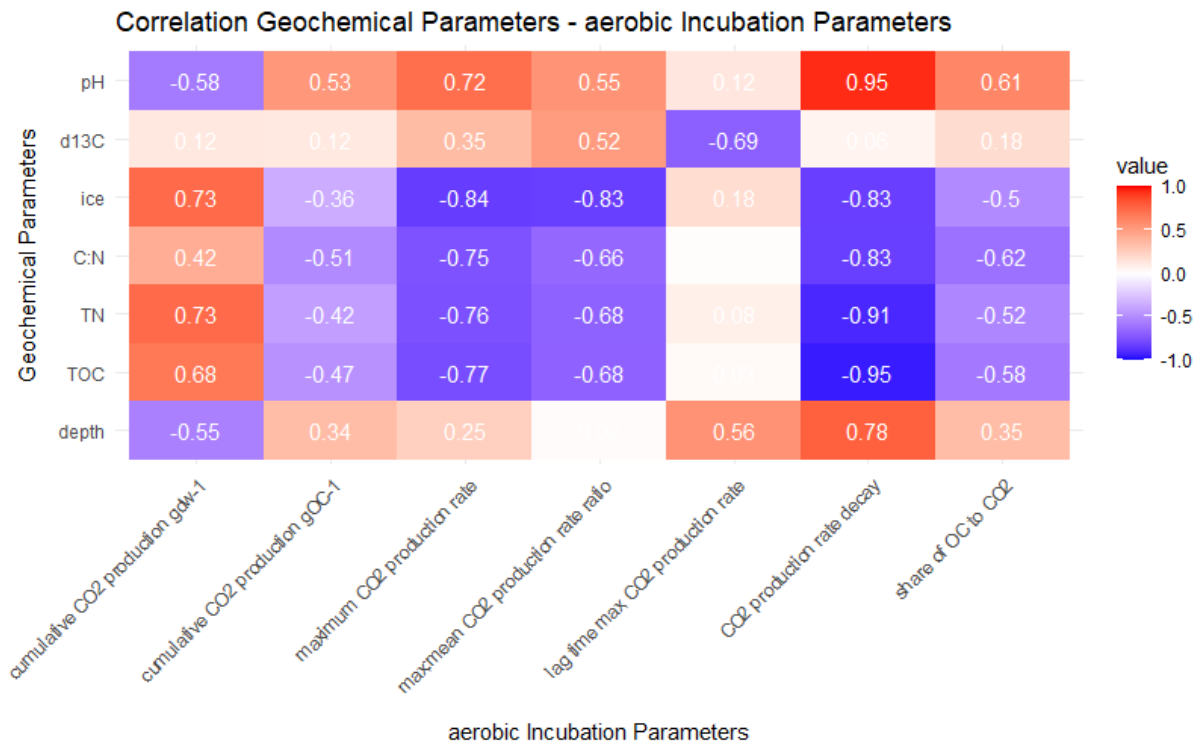
Appendix 19: Pearson's correlation coefficients (r) aerobic incubation characteristics.

Appendix 20: Pearson's correlation coefficients anaerobic vs aerobic incubation.

Correlation between Anaerobic and Aerobic Incubation

Appendix 21: Paired t-test results of geochemical analysis at t_0 and t_{90} of anaerobic incubation.

	Anaerobic incubation			
Geochemical parameter	Shapiro-Wilk p	Paired t-test t	Paired t-test p	Cohen's d effect size
pH	**0.36**	2.87	**0.024**	**0.92**
Ice content	**0.06**	- 3.76	0.07	**- 0.32**
TOC	**0.62**	- 2.92	**0.022**	- 0.10
TN	**0.08**	- 3.11	**0.017**	- 0.14
C:N	**0.63**	- 0.72	0.50	- 0.17
δ¹³C	**0.94**	- 0.84	0.43	- 0.06

Bold text denotes significant p-values (p > 0.05 for Shapiro-Wilk-test, p < 0.05 for paired t-test)
Bold text denotes significant effect size (d > 0.20)

	Aerobic incubation			
Geochemical parameter	Shapiro-Wilk test p	Paired t-test t	Paired t-test p	Cohen's d effect size
pH	**0.08**	- 1.49	0.18	**- 0.21**
Ice content	0.01	- 2.21	0.06	**- 0.12**
TOC	**0.44**	- 3.34	**0.012**	- 0.08
TN	**0.50**	- 3.18	**0.015**	- 0.11
C:N	**0.35**	- 0.77	0.46	- 0.10
δ¹³C	**0.36**	2.05	0.08	0.13

Bold text denotes significant p-values (p > 0.05 for Shapiro-Wilk-test, p < 0.05 for paired t-test)
Bold text denotes significant effect size (d > 0.20)

Appendix 22: Paired t-test results of biomarker analysis at t_0 and t_{90} of anaerobic incubation.

Anaerobic incubation				
Biomarker Parameter	Shapiro-Wilk p	Paired t-test t	Paired t-test p	Cohen's d effect size
C $_{n\text{-alkanes}}$	0.34	- 1.21	0.27	-0.62
C $_{n\text{-alkanols}}$	0.29	- 3.91	**0.01**	**-2.10**
Share of OC	0.24	- 1.49	0.18	**-0.38**
ACL $_{n\text{-alkane}}$	0.21	2.27	0.06	**0.64**
ACL $_{n\text{-alkanols}}$	0.35	2.46	**0.04**	**1.20**
P$_{aq}$	0.53	- 2.21	0.06	**- 0.88**
P$_{wax}$	0.91	2.01	0.08	**0.61**
OEPD $_{n\text{-alkanes}}$	0.57	- 1.47	0.19	**- 0.41**
CPI $_{n\text{-alkane}}$	0.78	- 1.37	0.22	**-0.23**
EOPD $_{n\text{-alkanols}}$	0.62	1.58	0.16	**0.43**
CPI $_{n\text{-alkanols}}$	0.23	- 1.71	0.13	**- 0.66**
HPA	0.07	- 5.75	**0.001**	**- 3.34**
Share C_{10} - C_{20}	0.10	2.15	0.07	**0.56**

Bold text denotes significant p-values (p > 0.05 for Shapiro-Wilk-test, p < 0.05 for paired t-test)
Bold text denotes significant effect size (d > 0.20)

Aerobic incubation				
Biomarker Parameter	Shapiro-Wilk p	Paired t-test t	Paired t-test p	Cohen's d effect size
C $_{n\text{-alkanes}}$	0.17	- 0.44	0.67	**- 0.24**
C $_{n\text{-alkanols}}$	0.15	- 2.43	**0.045**	**-1.15**
Share of OC	0.05	-1.24	0.26	**-0.35**
ACL $_{n\text{-alkane}}$	0.80	3.16	**0.016**	**0.95**
ACL $_{n\text{-alkanols}}$	0.23	0.38	0.71	0.16
P$_{aq}$	0.69	- 3.09	**0.017**	**- 1.16**
P$_{wax}$	0.79	2.92	**0.022**	**0.90**
OEPD $_{n\text{-alkanes}}$	0.14	- 0.64	0.54	- 0.14
CPI $_{n\text{-alkane}}$	0.99	-0.26	0.80	-0.04
EOPD $_{n\text{-alkanols}}$	0.55	-0.09	0.93	-0.02
CPI $_{n\text{-alkanols}}$	0.79	- 1.89	**0.1**	**- 0.76**
HPA	0.34	-4.64	**0.002**	**- 2.32**
Share C_{10} - C_{20}	0.63	1.61	0.15	**0.34**

Bold text denotes significant p-values (p > 0.05 for Shapiro-Wilk-test, p < 0.05 for paired t-test)
Bold text denotes significant effect size (d > 0.20)